# Synthesis of Lactone-based Conjugated Polymers for Recently Emerging n-type Organic Thermoelectrics and Electrochemical Transistors

A thesis submitted in partial fulfilment of the requirement
for the degree of Doctor of Philosophy


Maryam Abdulhadi Alsufyani

New College

Oxford

Michaelmas term

2023

# I Declaration

The work described in this thesis was carried out in the Department of Chemistry at the University of Oxford and the Chemistry program at King Abdullah University of Science and Technology between September 2018 and June 2023 under the supervision of Professor Iain McCulloch, and is my own work except where otherwise specified.

Maryam Alsufyani, June 2023

# II Copyright Declaration

# III Acknowledgment

First and foremost, I would like to express my gratitude to Professor Iain McCulloch for his supervision, guidance, and constant encouragement throughout my DPhil studies. I am truly grateful for the opportunity he has provided me to pursue my studies at the University of Oxford. I am thankful for his encouragement and belief in my abilities, as well as the opportunities he provided for me to learn and grow throughout my PhD, intellectually and personally.

I would also like to thank the member of the McCulloch group, especially i) Dr. Rawad Hallani for training me when I joined the lab, and for helping me advance my projects. ii) Prof. Xingxing Chen and Prof. Hu Chen who continuously advised me and helped me with my experiments, and for creating the encouraging and positive work atmosphere. I would also like to thank KAUST group members Dr. Weimin Zhang, Dr. Rajendar Sheelamanthula, Dr. Balaji Purushothaman, Dr. Mindaugas Kirkus, for their continuous support and advice. Also, Imperial college group member Dr. Cameron Jellett for being around when I did my first polymerization, his advice and support. Finally, Oxford group members Dr. Helen Bristow, Dr. Xiaolei Zhao, Dr, Zeinab Hamid, Dr. Yunseul Kim, Dr. Yuanbao Lin and Dr. Jin Yang, Junfu Tian, and Yuyun Yao for their support.

Next, I would like to thank all collaborators for the thermoelectric projects, (Prof. Simone Fabiano, Dr. Suhao Wang and Dr. Marc-Antoine Stoeckel at Linköping University), the organic electrochemical transistor project, (Prof. Jonathan Rivnay, Dr. Reem Rachid, Dilara Meli, Ruiheng Wu, and Dr. Bryan Paulsen at Northwestern University, and Prof. Alexandra Paterson, and Dr. Maryam Shahi at University of Kentucky), for putting the time and efforts to make the projects happen, and for the great discussions and useful insights.

I would like to also extend my gratitude to Dr. Will Myers and Prof. Claudia Tait at the University of Oxford for their generosity and constant advice, useful insights, and assistance during my EPR experiments. I would also like to thank Prof. Hu Chen at KAUST and Dr. Karl Thorley at the University of Kentucky for conducting computational DFT simulations. I would like to thank Dr. Khrystyna Regeta, and Dr. Craig Combe at KAUST for conducting energy levels measurements (UPS, LE-IPES, and PESA). I would like to thank Prof. Kim Ji-Seon and Dr. Katherine Stewart at Imperial College London for helping us with the in-situ Raman experiments.

I would also like to thank Prof James Durrant and his group for hosting me at Imperial College London and for their invaluable contributions to my projects. I'm particularly grateful to Dr. Benjamin Moss for specifying the time to train me for potential decay spectroscopy experiment and for helping me analyze the data.

Now, I would like to thank those friends who made an impact during my PhD. I would like to thank Afnan Shirbini who continuously inspired me and encouraged me to move forward. I would also like to thank Abdullah Alshehri, Abdullah Alyami, and Abdullah Dahwa for their support.

Finally, I would like to thank my parents, for believing in me and supporting me throughout my studies. Also, my siblings for their advice and support.

# IV Abbreviations

| | |
|---|---|
| °C | Degrees Celsius |
| Å | Angstrom |
| C* | Volumetric capacitance |
| CB | Chlorobenzene |
| $CHCl_3$ | Chloroform |
| CP | Conjugated polymer |
| CV | Cyclic voltammetry |
| d | Channel thickness |
| DCB | Dichlorobenzene |
| DCM | Dichloromethane |
| DFT | Density functional theory |
| Diglyme | Diethylene glycol dimethyl ether |
| DMF | Dimethylformamide |
| DMPO | 5,5-dimethyl-1-pyrroline N-oxide |
| DMPO-$OO^-$ | DMPO-superoxide adduct |
| DPP | Diketopyrrolopyrrole |
| EA | Electron affinity |
| EDL | Electrical double layer |
| $E_g$ | Band gap |
| EG-OFET | Electrolyte gated organic field effect transistor |
| EIS | Electrochemical impedance spectroscopy |
| EPR | Electron paramagnetic resonance spectroscopy |
| eV | Electron volt |
| EWG | Electron-withdrawing group |
| F4TCNQ | 2,3,5,6-tetrafluoro-tetracyanoquinodimethane |
| GIWAXS | Grazing incidence wide-angle X-ray scattering |
| $g_m$ | Transconductance |
| GPC/SEC | Gel permeation chromatography-size exclusion chromatography |
| $H_2O_2$ | Hydrogen peroxide |

| | |
|---|---|
| HOMO | Highest occupied molecular orbital |
| I | Current |
| $I_D$ | Drain current |
| $I_{on/off}$ | Current on/off ratio |
| IP | Ionisation potential |
| ITO | Indium tin oxide |
| L | Channel length |
| LE-IPES | Low energy inverse photoelectron spectroscopy |
| LUMO | Lowest unoccupied molecular orbital |
| m/z | Mass to charge |
| MeCN | Acetonitrile |
| Mn | Number average molecular weight |
| MS | Mass spectrometry |
| Mw | Weight average molecular weight |
| n | Charge carrier concentration |
| NBS | N-bromosuccinimide |
| NDI | Naphthalene diimide |
| N-DMBI | 4-(2,3-Dihydro-1,3-dimethyl-1H-benzimidazol-2-yl)-N,N-dimethylbenzenamine |
| NIR | Near-infrared |
| NMR | Nuclear magnetic resonance |
| $O_2^{\bullet-}$ | Superoxide radical |
| OECT | Organic electrochemical transistor |
| OFET | Organic field-effect transistor |
| OLED | Organic light-emitting diodes |
| OMIEC | Organic mixed ionic−electronic conductor |
| OPV | Organic photovoltaics |
| ORR | Oxygen reduction reaction |
| OSC | Organic semiconductor |
| OTE | Organic thermoelectric |
| P3HT | Poly(3-hexylthiophene) |
| PEDOT | Poly(3,4-ethylenedioxythiophene) |
| PESA | Photoelectron spectroscopy in air |

| | |
|---|---|
| PF | Power factor |
| PTSA | P-toluenesulfonic acid |
| q | Elemental charge |
| rpm | Revolutions per minute |
| S | Seebeck coefficient |
| SEC | Spectroelectrochemistry |
| SOMO | Singly occupied molecular orbital |
| TAM | Triaminomethane |
| TBAF | Tetrabutylammonium fluoride |
| $TBAPF_6$ | Tetrabutylammonium hexafluorophosphate |
| TDAE | Tetrakis(dimethylamino)ethylene |
| TGA | Thermogravimetric analysis |
| THF | Tetrahydrofuran |
| UPS | Ultraviolet photoelectron spectroscopy |
| UV-vis | UV-visible absorption spectroscopy |
| V | Voltage |
| $V_D$ | Drain voltage |
| $V_G$ | Gate voltage |
| $V_{th}$ | Threshold voltage |
| W | Channel width |
| $\delta$ | Chemical shift |
| $\lambda$ | Wavelength |
| $\mu$ | Mobility |
| $\mu_e$ | Electron mobility |
| $\sigma$ | Electrical conductivity |

# V Abstract

Conjugated polymers (CPs) have demonstrated remarkable potential as electroactive components for various electronic applications over the past decades. Electron-transporting (n-type) materials, in particular, have been recognized to be essential in recently emerging i) clean energy conversion applications for developing efficient thermoelectric generators and ii) in bioelectronics for metabolite sensing that rely on electron generation or for developing complementary circuits. However, current n-type materials have limited scope and poor performance when compared to their p-type counterparts. This work explores enhancing the performance of n-type materials for organic thermoelectrics (OTEs) and organic electrochemical transistors (OECTs), through strategic chemical design, and structure-property relationship elucidation. The polymer series designed in this work consists of electron deficient lactam and lactone building blocks, with a particular focus on the significance of the lactone unit on the polymer electron affinity (EA). The first two studies are dedicated to exploring and optimizing the thermoelectric performance of a series of six lactone-based n-type polymers. This was achieved through chemical design modulation of acene ring size, and side chain length/polarity, resulting in n-type polymers with a state-of-the-art thermoelectric performance. The third study investigates the implementation of the earlier developed polymers in OECTs, particularly, focusing on the role of superoxide formation from electron transfer during polaron transport. This study demonstrates that turning off the thermodynamic favorability of this reaction prevents superoxide formation, leading to more stable and higher performing devices. The work of this thesis will offer guidance to the field, by demonstrating the advantages that can arise from designing n-type semiconducting polymers with high electron affinity, in the fields of OTEs and OECTs.

# Contents

# Chapter 1

# Introduction

## 1.1 Organic electronics

Organic electronics has gained considerable attention in the past decades, in both academia and industry. This is because of their ability to provide cost-effective, flexible, light-weight, and roll-to-roll printed electronics over large-areas by means of easy processability from solution at low-temperatures, which is important for industrial purposes. The current advancements in organic electronics have also benefited from structure-property investigation at the molecular level in academia. Technologies such as organic light-emitting diodes (OLED), organic solar cells or organic photovoltaics (OPV), and organic field-effect transistors (OFETs) actively utilize the semiconducting properties of organic molecules, and are already available in global market and offer opportunities for the development of displays, renewable energy, and internet of things (IoT).[1, 2] The breakthroughs achieved in the application described above has opened opportunities for more exciting applications in the field of organic bioelectronics which take advantage of mixed ionic/electronic transport in the organic active layer,[3] also in the field of energy harvesting organic thermoelectrics for waste heat recovery,[4] which take advantage of the non-toxic, lightweight, flexible, and low thermal conductivity of the organic material to offer the next-generation affordable, on-body wearable, near-room temperature energy generation modules.

What keeps the field of organic electronics vibrant is its multidisciplinary promising applications as described above ranging from rollable photovoltaics, flexible displays, wearable electronics for energy harvesting and healthcare applications. Not only is it a multidisciplinary field but it is also interdisciplinary, where researchers from several disciplines (chemists, physicists, material scientists, electrical engineers, and bio scientists) are collaborating to develop the next generation materials and devices to deliver state-of-the-art electronics applications.

This thesis covers the recently emerging organic electronic applications, namely organic thermoelectrics (OTEs) and a common module of organic bioelectronics called organic electrochemical transistors (OECTs). We address the relationship between the chemical properties of the active layer component (a conjugated polymer), its physical properties, thin film microstructure, and how these factors affect the device performance of the selected application. A visual representation of the investigation process from polymer design to application is depicted in (Figure 1).

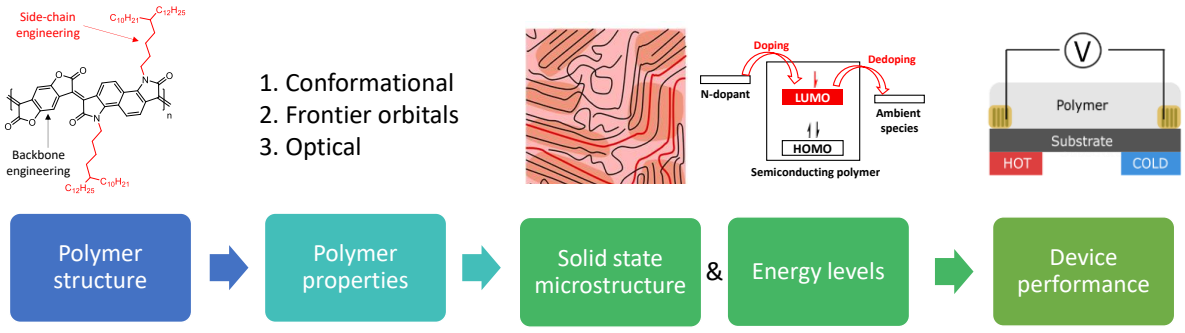


Figure 1. Structure-property relationship from polymer chemical structure to device performance.

### 1.1.1 Conjugated polymers

Conjugated polymers comprise $sp^2$-hybridized carbon atoms, where three electrons engage in sigma bonding, creating two C-C sigma bonds and one C-H sigma bond. The remaining electron localizes in a $p_z$-orbital and forms a π-bond with the adjacent $sp^2$-carbon atom. These carbon centers go along a path of alternating single and double bonds.[5] The overlap between unhybridised $p_z$ orbitals perpendicular to the σ-framework gives rise to delocalized π-orbitals. (Figure. 2a). Extended conjugation enhances the extent of interaction between atomic orbitals resulting in a broadening of the highest occupied and lowest unoccupied molecular orbitals

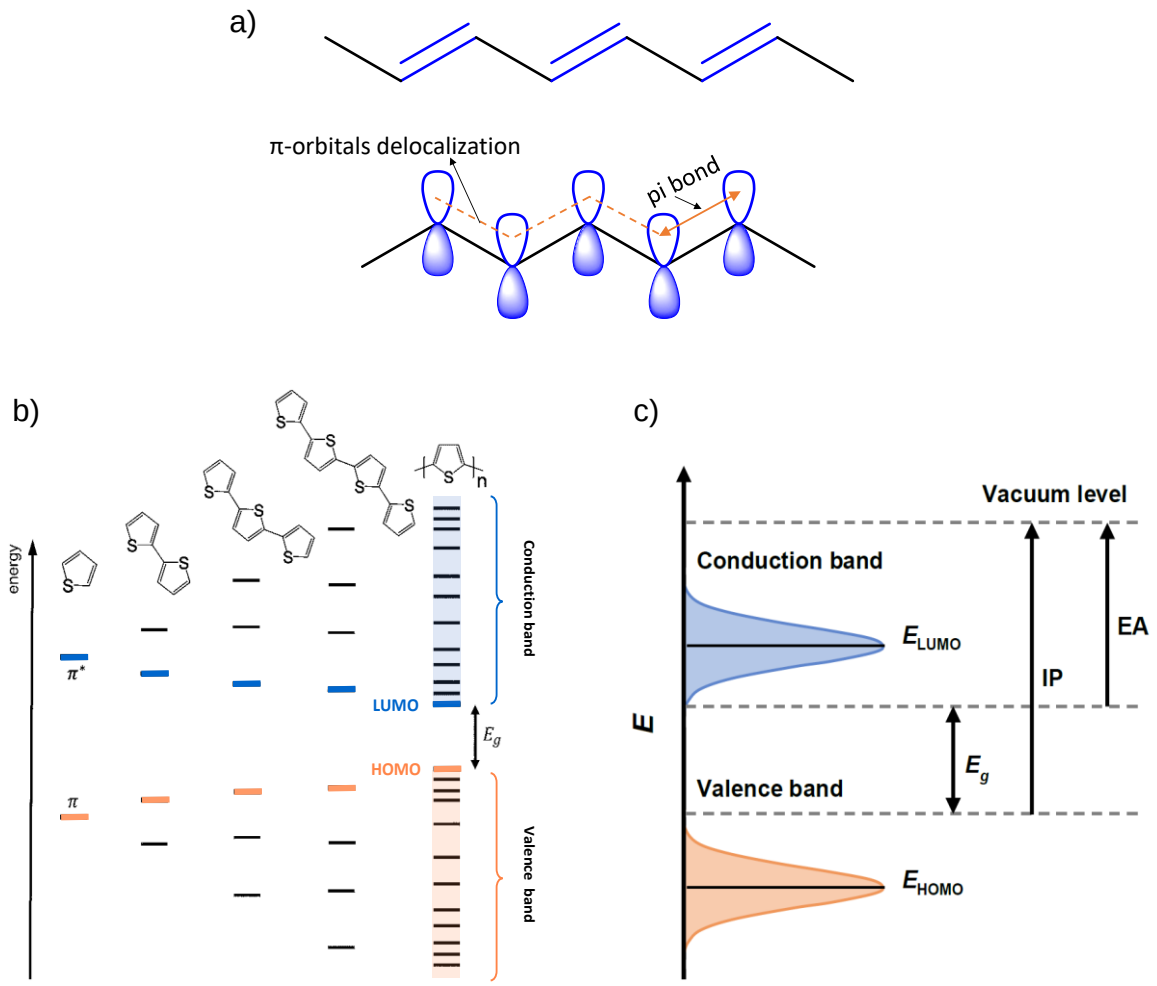


Figure 2. a) Conjugated system of p-orbitals with alternating double and single bonds enabling p-orbitals overlapping in poly(acetylene). b) Evolution of the HOMO and LUMO levels as the number of thiophene repeat units is increasing, resulting in valence and conduction bands for polythiophene with a narrow band gap, $E_g$ c) Schematic illustration of the energy level diagram that can be considered in organic semiconductors. $E_g$, IP, and EA refer to band gap, ionization potential, and electron affinity, respectively. Figure b) adapted with permission from ref. 14, and Figure c) reproduced with permission from ref. 6.

(HOMO and LUMO) into narrower semiconducting-like electronic bands. (See Figure 2b).[6] In inorganic semiconductors, these bands are referred to as occupied valence band (or highest occupied molecular orbital HOMO) and unoccupied conduction band (or lowest unoccupied molecular orbital LUMO), which are separated by a band gap ($E_g$). (See Figure 2c) The delocalization of π-electronic density can also occur between neighboring molecules. This interplay of both intra- and inter-molecular delocalization plays a crucial role in influencing the optical and charge transport properties used in a variety of organic electronic applications.

Conjugated polymers are inherently not conductive and have been recognized as insulating materials. Not until 1977, when Shirakawa, MacDiarmid, and Heeger made a significant breakthrough (Nobel Prize in Chemistry in 2000) by demonstrating a dramatic increase in electrical conductivity of polyacetylene through chemical doping by iodine.[7, 8] Following this, conjugated polymers have attracted a lot of attention for use in optoelectronic devices as an alternative to inorganic electronic materials because of their low-cost and solution proccessable properties which allow roll-to-roll printed, light weight, and flexible devices. Adding to this, the physical properties (solubility, crystallinity) and electronic properties (charge transport) of conjugated polymers can be tuned and optimized by means of organic synthesis.[9, 10] This has enabled conjugated polymers to be applied in multiple organic electronic applications.

## 1.2 Electrical conductivity of conjugated polymers

In all electronic applications, charge carrier concentration and transport are required in order for the device to function. For example, in organic photovoltaics (OPVs) and organic light-emitting diodes (OLEDs), the transport of charge carriers through thin films is the key property of both devices, where charge carriers can either flow from the contacts to the active zone in

OLEDs or the reverse in OSCs. To minimize any kind of loss in this flow, a highly conductive active layer (conjugated polymer) is preferred.[11] A similar concept is present in transistor based devices, organic field effect transistors (OFETs), and organic electrochemical transistors (OECTs),[12] where the transport of injected charge carriers takes place from source electrode to drain electrode, where they get extracted, and current can be modulated. Along this route, a highly conductive polymer is therefore needed to minimize charge losses through charge traps. Also in thermoelectric devices, where charge transport takes place from hot end to cold end when a thermal gradient is applied.[13] The electrical conductivity (σ) is a measure of a material's ability to conduct an electric current and is defined as:

$$\sigma = qn\mu \quad (1)$$

Where n is the carrier concentration, q is electric charge, μ is the charge carrier mobility. As shown in the equation, the electrical conductivity strongly depends on n (which increases by doping) and on μ (which depends on the polymer microstructure).[14] The two following sections will discuss optimizing each parameter in order to enhance the electrical conductivity.

### 1.2.1 Introducing Charge Carriers: Doping

In general, conjugated polymers (in their pristine/undoped form) are nearly insulators with very low electrical conductivities ($10^{-6}$–$10^{-11}$ S cm$^{-1}$), and a bandgap lying in the range of 2-3 eV.[15] In the late seventies, a significant breakthrough was made by demonstrating that poly(acetylene) could acquire conductivity through a redox reaction when exposed to iodine vapors. As a result the electrical conductivity increased from $10^{-9}$ to $10^{5}$ S cm$^{-1}$.[7, 8, 16] Such process is referred to as "doping", and it involves intentionally introducing charge carriers to the conjugated backbone to regulate the charge carrier concentration and hence electrical

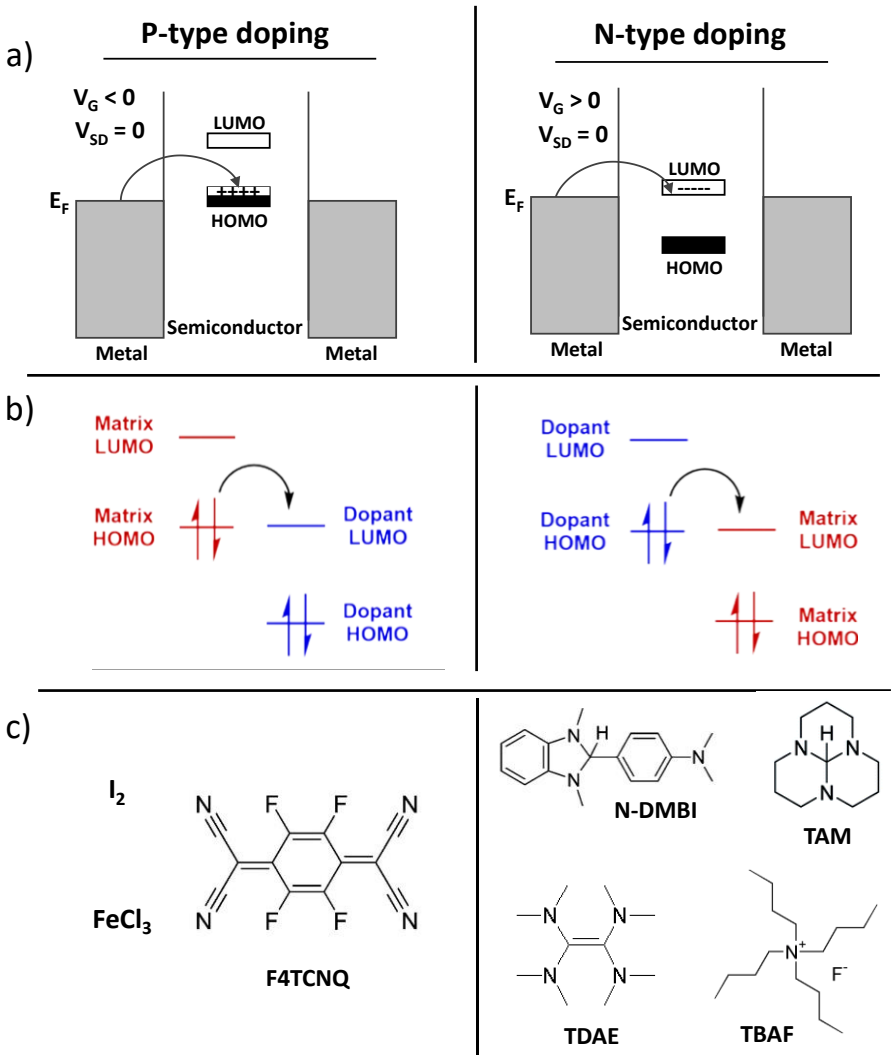


Figure 3. Schematic illustration of charge carrier generation mechanism by a) injection from metal electrodes (e.g., field effect doping in OFETs, demonstrating hole injection in p-type doping and electron injection in n-type doping, prior to charge transport. $V_G$ is gate voltage, $V_{SD}$ is drain voltage), b) molecular doping by a typical integer charge transfer mechanism, and c) most common p-type and n-type dopants. Figure a) is adapted from ref. 19. Figure b) is reproduced with permission from ref. 20.

conductivity. This technique has opened up new opportunities for all organic electronic devices since its discovery, allowing for the development of organic electronic devices with unprecedented performances. Current doping approaches include electrochemical doping and molecular doping.[13, 17] Schematic illustration of the corresponding doping methods is depicted in Figure 3a and b.

In the case of electrochemical doping, a transistor geometry is typically used. The conjugated polymer is in contact with two metal electrodes (source and drain, from which extra charge carriers are provided). This layer (source-semiconductor-drain) is separated from a third

metal electrode, known as the gate, by a thin dielectric or an electrolyte. In conventional electrochemical processes, the voltage applied between the gate and the channel (polymer) causes field-effect oxidation or reduction of the conjugated polymer layer, but only near the dielectric interface. This is a typical description of organic field effect transistors (OFETs).[18] (Figure 5b). Electrolyte-gated transistors such as organic electrochemical transistors (OECTs), have a similar working principle of (OFETs) except that when gate voltage is applied, ions are injected from the electrolyte into the conjugated polymer layer, and oxidation or reduction takes place throughout the entire volume of the polymer channel. (Figure 5c) In both transistors, charge carriers are injected (doping) from metal electrodes (see Figure 3a) by means of a redox reaction, and charges with opposite charge from electrolyte (in OECTs) or dielectric (in OFETs) can stabilize the injected charges.[3, 19] More on the working principle of OFETs and OECTs will be discussed in Section 1.3.2. A schematic representation of electrochemical doping methods are summarized in Figure 5a-c. In general, electrochemical doping offers advantages of i) controllable doping level by electrode potential adjustment. ii) Due to electrode injection, doping and de-doping are reversible with no additional chemical reagents in the process. [17]

Molecular doping occurs through a redox reaction. In this context, electron donors or acceptors are added to the host conjugated polymers to generate mobile charge carriers. As a result, the polymer is either oxidized (p-type doping) or reduced (n-type doping). As described in Figure 3b, p-type dopants accept electrons from the highest occupied molecular orbital (HOMO) states of the host polymer, resulting in a positive polaron ($P^{\bullet+}$) on the host polymer, and a negative counterion (i.e. anion) on the dopant, which neutralizes the positive charge introduced in the polymer's π-electron system. Conversely, n-type dopants donate electrons to the lowest unoccupied molecular orbital (LUMO) of the host polymer, resulting in a negative polaron ($P^{\bullet-}$) on the host polymer, and a positive counterion (i.e. cation) on the dopant to

neutralize the negatively charged conjugated polymer[17, 20] Molecular doping is typically used to realize high performing organic thermoelectric devices. P-type dopants such as $I_2$,[21] $FeCl_3$[22] and small molecules such as F4TCNQ are commonly used as p-type dopants.[17] Among these, F4TCNQ derivatives are currently the most used dopant due to their high electron affinity (-4.6 to -5.2 eV) that lies around the ionization potential of common p-type polymers such as P3HT and PBTTT.[23, 24] P-type doping is regarded as a stable process in ambient conditions because energy levels of dopant and host polymer are below the energy levels of hole traps such as oxygen and water (-4.8 eV).[25] Given that this thesis focuses primarily on n-type polymers, we will not delve deeply into the complexities of p-type doping. Compared to p-type doping, n-type doping process has suffered from ambient instability due to i) shallow LUMO level of most n-type polymers (lying within potential electron traps, $O_2$ and $H_2O$).[26] Further elaboration on this topic can be found in Section 1.4.1. ii) Finding air-stable n-dopants with dopant HOMO levels which are shallow enough to drive n-type doping in OSCs is challenging due to their increased vulnerability to oxidation by ambient species. The commonly employed n-dopants include a limited selection of dopants such as 4-(1,3-dimethyl-2,3-dihydro-1*H*-benzoimidazol-2-yl)-*N*,*N*-dimethylaniline (N-DMBI),[27] tetrakis(dimethylamino)ethylene (TDAE),[28] tetrabutylammonium fluoride (TBAF),[29] and triaminomethane (TAM).[30] (see Figure 3c for dopant structures). More on efficient n-doping processes will be discussed later in Section 1.4.2.

As doping causes a significant increase in electrical conductivity, it is also accompanied by drastic changes in the electronic, optical, magnetic, and structural properties of the polymer.[14] The generation of polaronic/bipolaronic charge carriers upon doping introduces new electronic states within the polymer's bandgap. Figure 4 depicts an example of an n-type and p-type doping process that generates negative/positive polaron (radical anion/cation) and bipolaron (dianion/dication). The acceptance/removal of an electron by/from the π-system of the

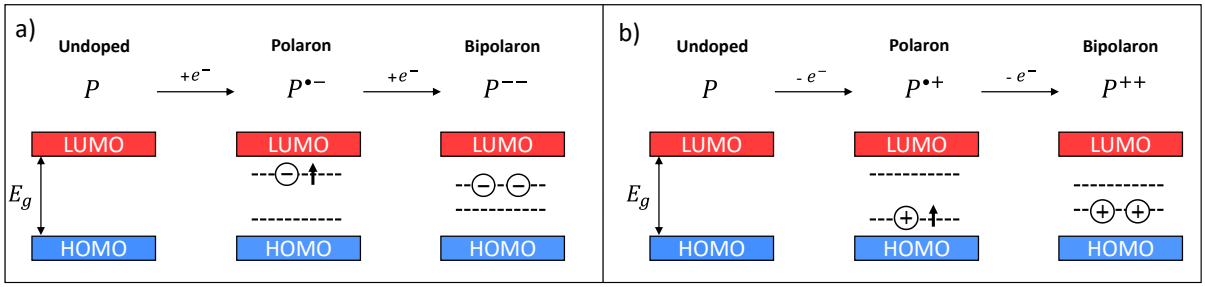


Figure 4. A schematic representation of neutral polymer; polaron states; and bipolaron states induced by a) n-doping and b) p-doping process. Adapted from ref. 14

conjugated backbone results in the formation of free radical and a negative/positive charge. Further coupling of the two leads to the formation of a negative/positive polaron (a radical anion/cation having a spin 1/2). Further addition/removal of an electron give rise to a spin-less bipolaron. Both polaronic/bipolaronic charges are associated with lattice distortion and are delocalized over the polymer backbone. Lattice distortion can be understood chemically as the formation of "quinoid" structures with more planar conformation.[31] Formation of polarons and bipolaron and thus doping of a conjugated polymer can be monitored by i) Optical UV-vis-NIR spectroscopy as they're associated with new optical transitions observable as a broad infrared absorption. ii) Electron paramagnetic spectroscopy (EPR), where spin polarons are EPR-active, while spin-less bipolarons are EPR-silent.[5]

Back to molecular doping, deposition methods of the doped conjugated polymer have an important influence on the solid-state microstructure.[32] Due to its simplicity and suitability for large scale processing, "solution doping" is the most widely used deposition method. As depicted in Figure 5d, solution doping simply involves directly admixing polymer and dopant solutions followed by co-deposition by spin-coating (widely used for more uniform films) or drop-casting (less uniform films). A wide range of dopant concentrations can be obtained. However, high dopant concentrations was found to negatively affect the polymer's morphology due to dopant aggregation, which lead to phase separation thus disturbing the packing behavior and ultimately charge transport. Another disadvantage of this method is that the dopant remains after doping, potentially hindering the polymer from developing the desired highly ordered

microstructure essential for high carrier mobility, resulting in low conductivity of the doped polymer. Overall, this method enables the exploration of various dopant concentrations to find the doping level that achieves a beneficial balance of electrical conductivity, desired film morphology, and charge carrier mobility, and is thus controllable. [17, 33]

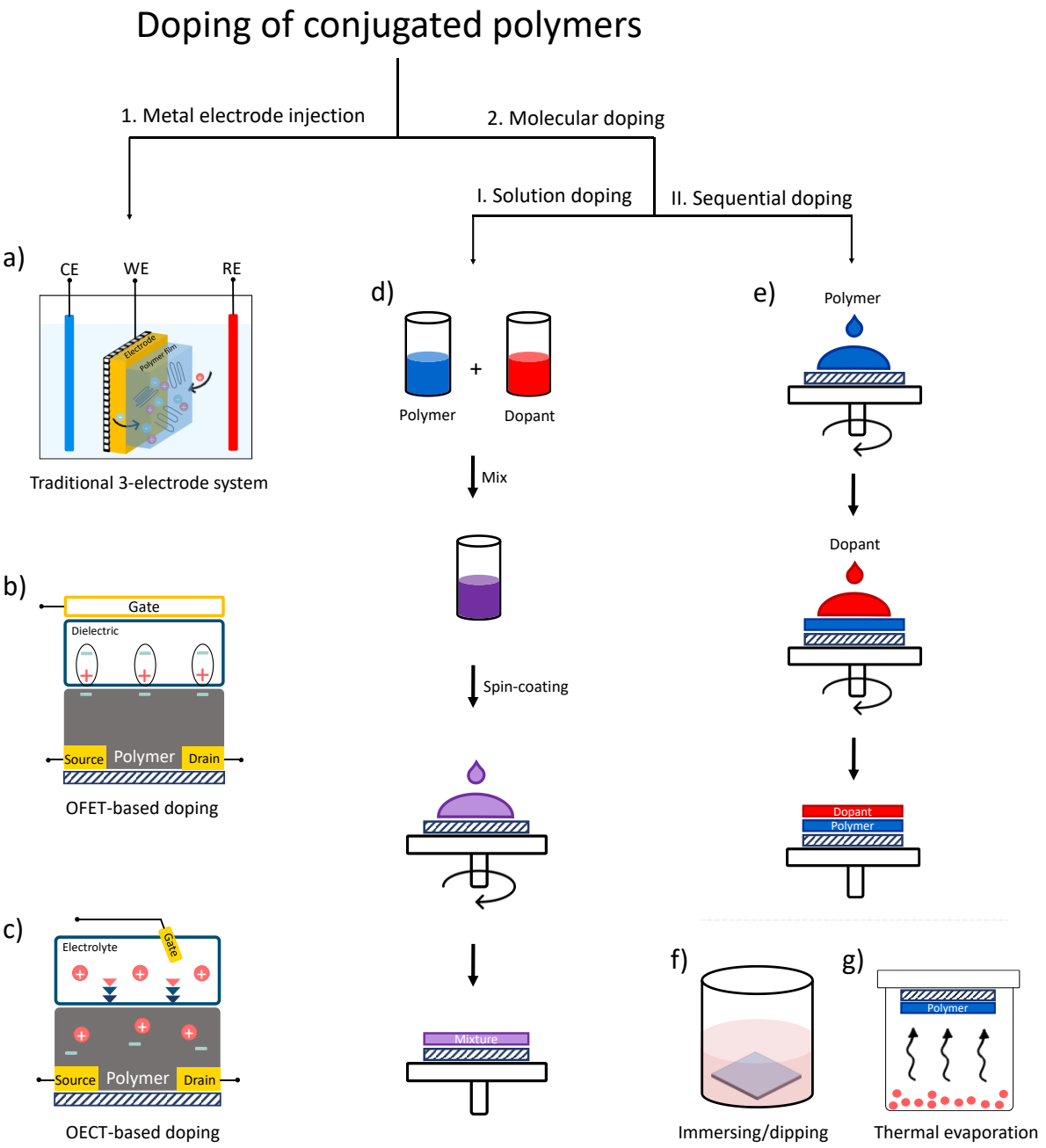


Figure 5. A summary of doping methods and film deposition techniques in molecular doping. Adapted from ref. 17 and 33.

To avoid the above drawbacks of "solution doping", another common deposition method is developed known as "sequential doping". As demonstrated in Figure 5e-g, in sequential doping, the pristine (undoped) polymer film is first prepared by solution deposition (spin-coating or drop-casting), and then the dopant solution is deposited on the pre-cast polymer film. (Figure 5e). Another sequential methods involve introducing the dopant into the pre-cast polymer film via immersion/dipping the substrate with the deposited polymer film in pre-prepared dopant solution. (Figure 5f) In the two above methods, the dopant will not dissolve the polymer film if it is deposited or immersed with an orthogonal solvent, which could present an issue if an orthogonal solvent is not found. Dissolving away the polymer film can be avoided by thermal evaporation, which involves infusing the dopant to the pre-cast polymer film via thermal sublimation. (Figure 5g). Small dopants can enter the polymer film through sequential doping, which has little effect on the crystalline domains and preserves the film's mobility.[32]

### 1.2.2 Charge Carrier Transport in Conjugated Polymers

In the last section, we have discussed the first factor to increase the electrical conductivity by increasing the carrier concentration, (n), by "doping". It is now time to discuss charge carrier transport behaviour after doping, which leads us to the second factor in optimizing the electrical conductivity of conjugated polymers, charge carrier mobility (μ) (see eq. 1). The transport mechanism of charge carriers in the bulk of the conjugated polymer can be described as a combination of intrachain transport across the polymer chain, or interchain transport across adjacent polymer chains. The former is facilitated by delocalization of π-orbitals along the polymer, and the latter is facilitated by π- π stacking and is known as 'hopping' between polymer chains.[34] The charge carrier mobility (μ) is a measure of how fast charge carriers can move when an electric field is applied, and charge carrier mobility values can be used to

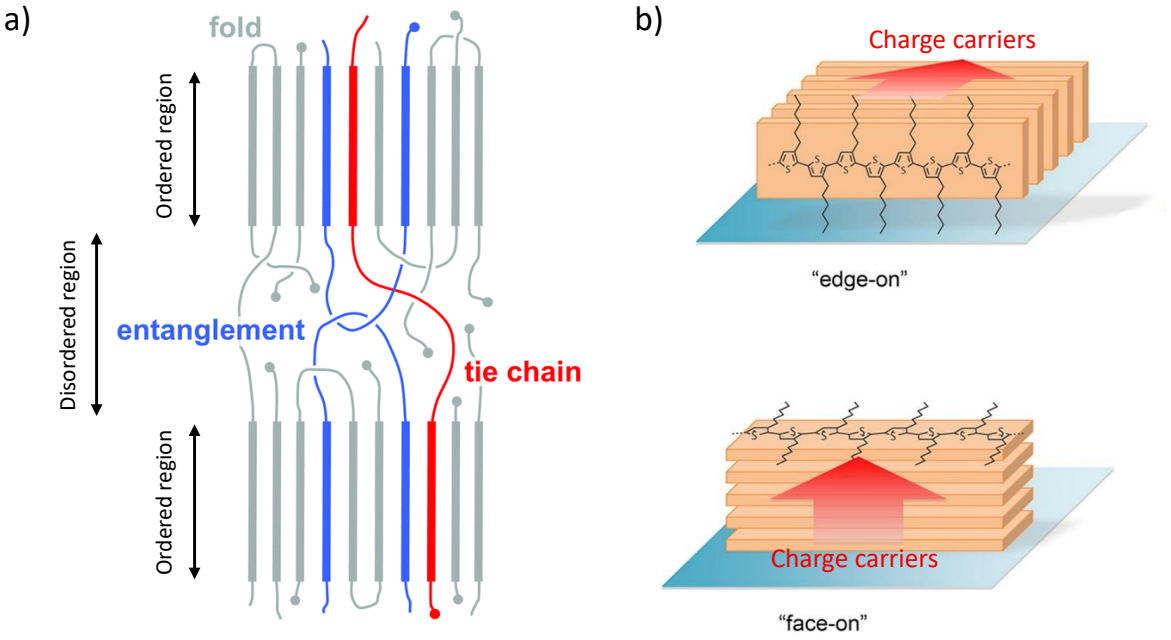


Figure 6. Charge transport process in conjugated polymer thin films. a) Connection between crystallites by entanglements and tie chains. b) Crystallite orientation with respect to substrate. Figure a) reproduced with permission from ref. 14. Figure b) reproduced and modified with permission from ref. 43.

estimate the extent of charge delocalization.[35] In thin films, semi-crystalline polymers comprise both ordered (crystalline) and disordered (amorphous) domains.[36] Charge transport within crystallites is fastest along the polymer backbone (intra-chain) which can be facilitated by increasing coplanarity of the conjugated backbone,[37] then second fastest in the π-stacking direction (inter-chain), which can also benefit from backbone planarity and rigidity to enable more efficient π-π stacking,[38] and finally absent in the side-chain stacking direction.[39] Crystalline and amorphous domains are interconnected through entanglements and tie chains.[14, 40] (Figure 6a). Sufficiently long and rigid polymer chains are able to form tie chains that connect the neighboring crystallites so that inter-crystallite charge transport can take place and a macroscopic charge transport between the ordered regions throughout the film can be realized.[41, 42]

Charge transport efficiency is also related to crystalline texture, which is the out-of-plane crystallite preferential orientation with respect to the substrate. Some crystallites are preferentially oriented "edge-on", some are "face-on", and some exhibit a mixture of the two.[43]

(Figure 6b). Because intermolecular charge transport is favored in the direction of π -stacking, in-plane and out-of-plane mobilites tend to be distinct. In OPVs, where charges are transported out-of-plane, a preferred face-on texture is desired.[44] While "edge-on" orientation is more beneficial for in-plane charge transport such as OFETs.[45] This implies that the interchain transport and/or crystallite interconnectivity is generally the limiting step of charge transport in conjugated polymer thin films. The degree of solid-state ordering of conjugated polymer thin films can be strongly influenced by i) molecular structure (molecular weight and solubilizing side chains), and ii) processing conditions (solvent, temperature, and deposition method).[46] More on optimizing charge carrier transport will be discussed in details in Section 1.4 for electron transporting (n-type) polymers.

## 1.3. Recently emerging organic electronic applications

Conjugated polymers have been crucial in the progress of various technologies such as organic light-emitting diodes (OLEDs), organic photovoltaics (OPVs), and thin-film transistors (OTFTs), as discussed in Section 1. The advances in the aforementioned applications, which were achieved through extensive multidisciplinary research including molecular design rules, processing techniques, and structure-property relationships, are now being exploited for the emergence of two promising fields: organic thermoelectrics (OTEs) and organic electrochemical transistors (OECTs). In the following sections, we will discuss each application separately, and subsequently explore materials that can be strategically designed to serve both applications simultaneously, providing a dual advantage.

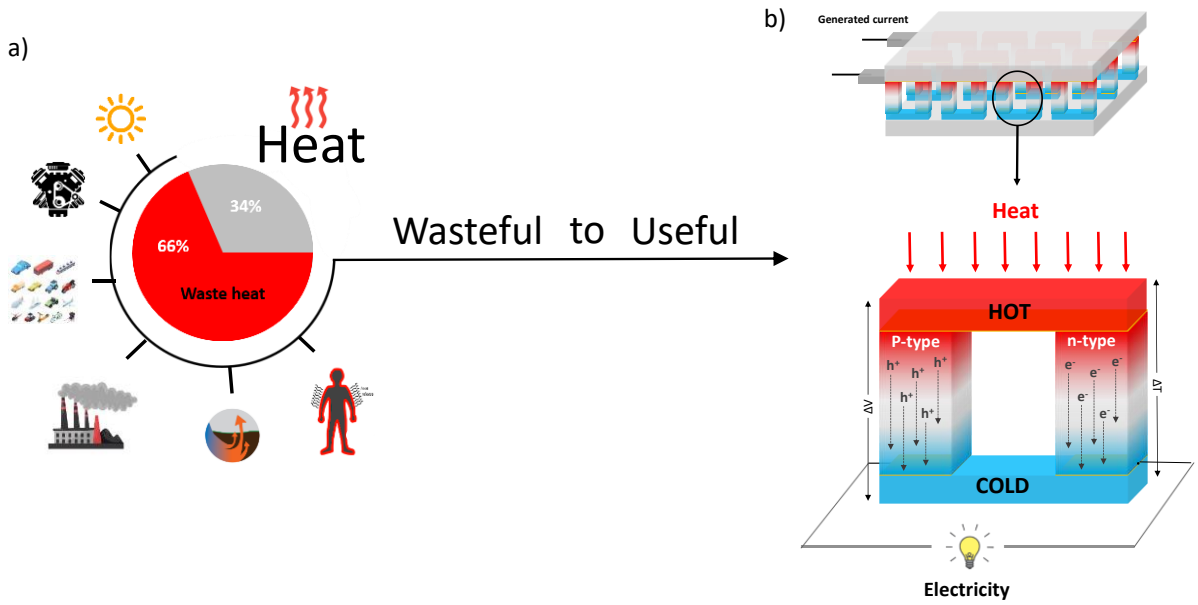


Figure 7. Schematic diagram of a) the approximated parentage of wasted heat and b) the internal component of a vertical thermoelectric generator, comprising both p-type and n-type semiconductors. Adapted from ref. 51 and 14.

### 1.3.1. Organic thermoelectrics (OTEs)

Efficient energy conversion that can reduce the usage of fossil fuels and greenhouse gas emissions have become of paramount concern due to the global trend of industrialization and growing population which demand high energy consumption. Driven by that, researchers have been dedicated to convert diverse clean energy sources, including sunlight, wind, and nuclear power, into usable electricity. Delivering safe, efficient, and affordable clean energy conversion devices is also desirable. A new track of clean energy application has recently emerged, where the potential to recycle and use waste heat is recognized.[47] Heat is abundant, however a considerable amounts of it (more than 60%) is wasted into the environment from a range of different energy producing sources like vehicles, industrial processes, human activities and also more interestingly, the human body.[4, 48] (Figure 7a). There has been an increased interest in harvesting/recycling this wasted energy into useful electricity in the form of thermoelectric generators. Thermoelectric generators (TEGs) are solid-state devices employed for the direct conversion of thermal energy into electrical power by applying a thermal gradient

across a conductive material (called a thermoelectric material).[47] (Figure 7b). Thermoelectric generators are particularly attractive for their ability to function within solid-state device in a quite manner, requiring no moving mechanical parts, hence allowing operation for long periods of time with minimum maintenance.[49]

Currently, state-of-art thermoelectric materials are inorganic metal alloys. However, metal alloys are constituted of atomic elements such as tellurium, lead, and antimony, which are i) present with low natural abundance, ii) operate at high temperature (peak performance of $Bi_2Te_3$ is at ~380 K)[50] thus rendering the commercial viability of thermoelectric technologies difficult due to high manufacturing cost. [51] The aforementioned drawbacks of inorganic thermoelectric materials are hindering the widespread adoption of thermoelectric technologies. This is where organic materials (mostly conjugated polymers), once more, offer solutions towards flexible fabrication and manufacturing, cost-effective technologies. In contrast to inorganic materials, organic materials are of higher natural abundance and allow operation at low temperatures, even at near-room temperature, thus enable manufacturing at much lower cost. Moreover, their solution-based processing allow deposition on flexible substrates with variety of shapes, allowing for waste heat recovery from lightweight and wearable thermoelectrics.[4]

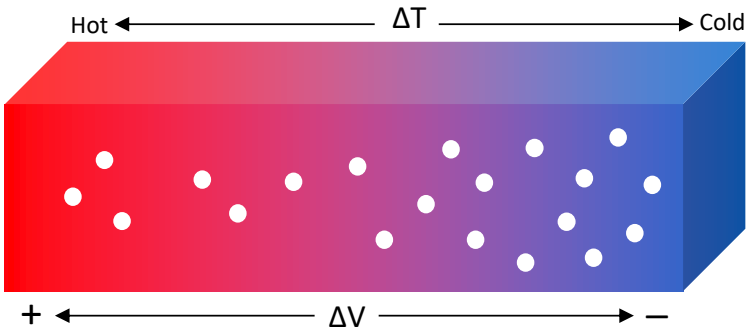


Figure 8. Charge carrier movement from the hot side to the colder side in response to applied temperature difference. Adapted from ref. 13.

Thermoelectric generators (TEGs) working principle is based on the Seebeck effect, which was discovered in the 1820s by Thomas Johann Seebeck. A temperature difference across a semiconductor causes the diffusion of charge carriers (electrons or holes) from the hot side to the cold side, creating a buildup of charge and thus voltage difference (Figure 8). The magnitude of the voltage induced (thermal voltage) in response to temperature difference across the material defines the Seebeck coefficient, also called the thermal power, and has a unit of ($\mu V\ K^{-1}$).[4 52]

$$\alpha = \frac{\Delta V}{\Delta T} \tag{2}$$

In Figure 7b, the standard layout of a thermoelectric generator is presented. A single (unicouple) thermoelectric generator (TEG) is typically comprised of p-type and n-type semiconductor legs that are electrically connected though electrodes. Connecting multiple unicouples electrically in series and thermally in parallel form the thermoelectric module. The efficiency of a thermoelectric generator is governed by the dimensionless figure of merit ZT (see eq. 2), where T is temperature, *S* is Seebeck coefficient, $\sigma$ is electrical conductivity, and $\kappa$ is thermal conductivity of the material.

$$ZT = \frac{S^2\sigma}{\kappa} \tag{3}$$

The sign of Seebeck indicates the majority of charge carriers, electrons in n-type semiconductors or holes in p-type semiconductors. The efficiency of a thermoelectric device is determined by the properties of the semiconducting material constituting it. So, to get a high ZT, we must maximize the numerator and minimize the denominator. In other words, an ideal thermoelectric material should be a good electrical conductor (high $\sigma$) and a poor thermal conductor (low κ). Due to their intrinsic low thermal conductivity (0.3–1.0 $Wm^{-1}K^{-1}$) compared to inorganic materials,[53] conjugated polymers have emerged as potential candidates as

thermoelectric materials. This has prompted researchers in the field to focus on maximizing the nominator, known as the power factor (PF), which is frequently used to assess the thermoelectric performance of conjugated polymers. (See eq.3) The power factor comprises two leading thermoelectric parameters of organic thermoelectrics, Seebeck coefficient (α) and electrical conductivity ($\sigma$). As the carrier concentration increases, electrical conductivity increases accordingly. On the other hand, the Seebeck coefficient decreases with increasing carrier concentration. This indicates that the Seebeck coefficient and electrical conductivity are interdependent. As a result, an optimal doping level must be considered in order to maximize the power factor (PF).

$$PF = S^2\sigma \tag{4}$$

Since Seebeck optimization appears to be difficult and poorly understood,[39] the field has shifted its focus towards enhancing electrical conductivity, where the optimization of its

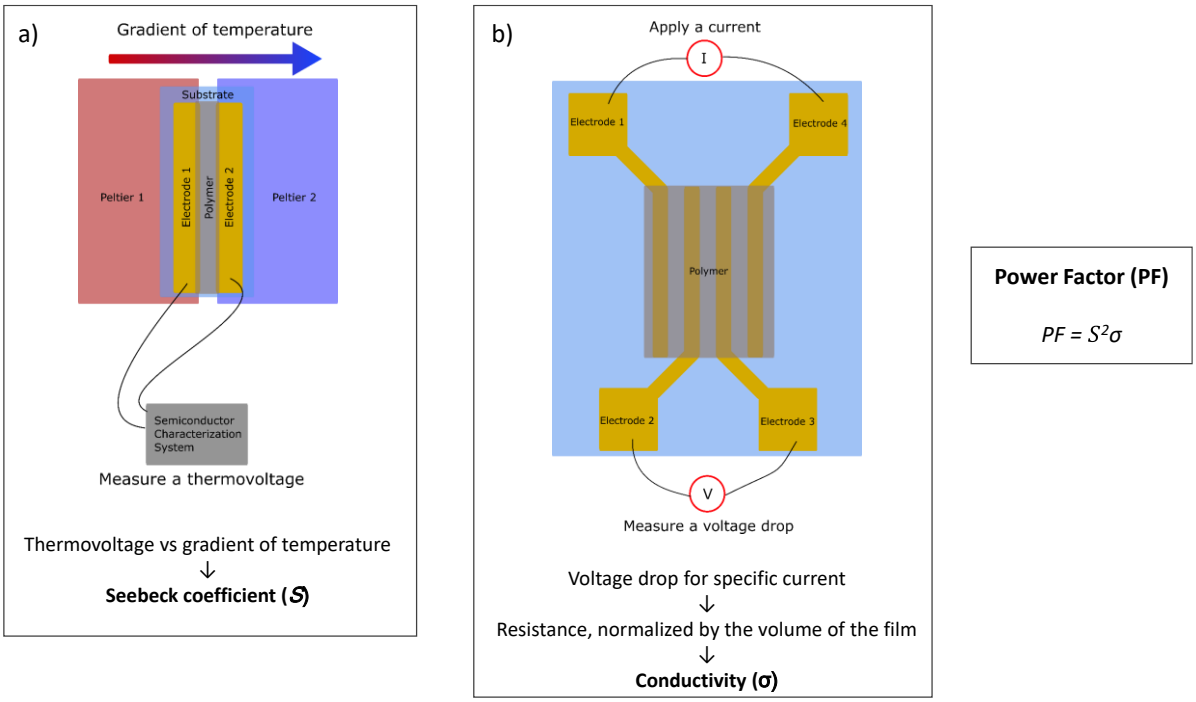


Figure 9. a) A setup illustration for measuring the Seebeck coefficient in which the thermovoltage (ΔV) is measured across a thermal gradient ((ΔT). b) four-probe setup for electrical resistivity measurements. Setup illustrations were provided by thermoelectric collaborator in this work, Marc-Antoine Stockel.

parameters, charge carrier mobility and carrier concentration is well established (see eq.1, Section 1.2). As mentioned above, organic thermoelectrics, in addition to their low thermal conductivity, offer compatibility with solution-based processing for large-area production, light weight, low toxicity, and high mechanical flexibility. These intrinsic properties make organic thermoelectrics promising for the development of next-generation energy harvesting devices that are flexible, wearable, and can operate at low temperature (<200°C).

Typically, the Seebeck coefficient and electrical conductivity of an OTE material are measured separately, in the in-plane direction. Seebeck coefficient (α) measurements involve the use of two Peltier modules to achieve a temperature gradient (ΔT) across the polymer film, and the thermovoltage (ΔV) is tested between two electrodes. (Figure 9a). The electrical conductivity ($\sigma$) is most commonly measured by, also called 4-point method [54]. (Figure 9b), in which a current is passed through the outer probes and the drop voltage across the inner probes is measured, and the resistivity (the inverse of electrical conductivity) is therefore calculated. After obtaining both Seebeck coefficient (α) and electrical conductivity($\sigma$), the Power factor (PF) can be therefore obtained from eq. 3.

Ultimately, in order to obtain efficient thermoelectric generators (practical thermoelectric applications), both p-type and n-type legs must be in comparable thermoelectric performance. However, this is not the case with the current p- and n-type materials. Champion p-type materials include PEDOT:PSS with electrical conductivity reaching 1000 S $cm^{-1}$ , PF of 470 $\mu W.m^{-1}.K^{-2}$ and $ZT$ = ± 0.42 at 297 K.[55, 56] On the other hand, n-type materials are lagging behind their p-type counterparts. In recent years, significant research efforts have been devoted to addressing the challenges that hinder n-type polymers from achieving high performance. More on the challenges of n-type thermoelectrics will be discussed in Section 1.4.

### 1.3.2 Organic electrochemical transistors (OECTs)

Another emerging application that gained a considerable interest involves coupling electronics with biology. Organic bioelectronics aim to fulfill the present and future healthcare and diagnostic need of the biomedical community. In this regard, organic electrochemical transistors (OECTs) have demonstrated their capability to meet these demands effectively.[3] Organic electrochemical transistor (OECT) leverages the mixed transport of ions and electrons within the organic semiconductor (mostly conjugated polymers, and recently have been referred to as organic mixed ionic−electronic conductors (OMIECs)).[57] In this thesis, conjugated polymers used for OECT applications will be called OECT materials and/or OECT channel/OECT active layer.

Before delving into the working principle and benefits of OECTs, it is necessary to review OFETs. This is because the widespread use of OFETs inspired the development of OECTs, pioneered by Wrighton and colleagues in 1984.[58] OFET is a three-terminal transistor with a gate electrode, and two metal electrodes, source and drain between which the OECT active layer is deposited to create a channel through which carriers can flow from the source to the drain. (Figure 10a). In OFETs, a solid dielectric layer is vertically sandwiched between the OSC layer and gate electrode. Two potentials are applied at the gate and drain electrodes, respectively, with a grounded source electrode, and therefore two voltages are produced: the gate-source voltage ($V_{GS}$) and the drain-source voltage ($V_{DS}$). This process is the foundation of an OFET's operational principle. OFET is in its “OFF” state without the application of gate bias. By applying a negative or positive voltage between the gate and source ($V_{GS}$), the dielectric becomes polarized and a layer of charge carriers accumulates at the dielectric-semiconductor interface, turning OFET “ON”. Further application of voltage between the source and drain ($V_{DS}$), will drive the accumulated charge carriers at the OSC active layer to flow from source to drain, from which charge carriers will be collected and drain current will

be generated ($I_D$). This buildup of electrostatic charges at the interface, caused by the gate voltage, regulates the conductivity of the OSC channel, and the extent of the conductivity is

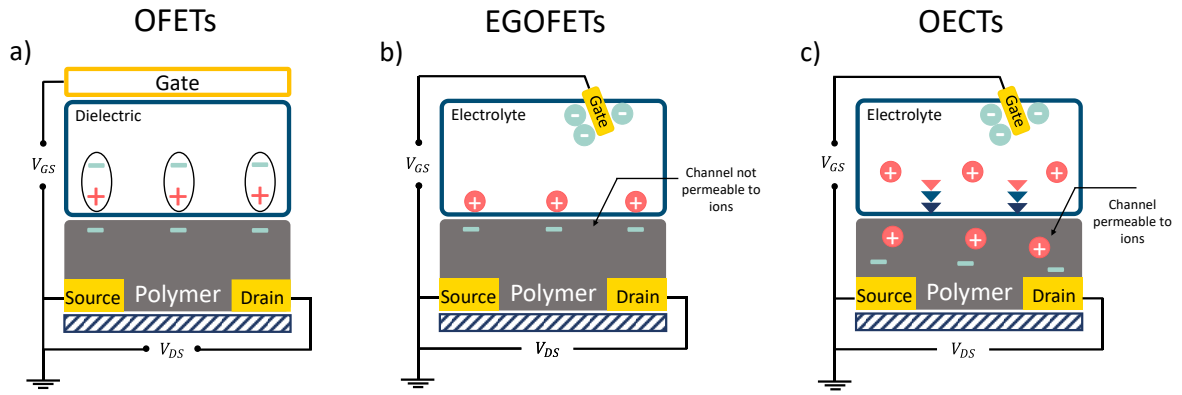


Figure 10. Schematic representation of a) OFETs, b) EG-OFETs, and c) OECTs, in their "ON" state, operating with n-type active layer. $V_{GS}$ is the voltage between gate and source. $V_{DS}$ is the voltage applied between drain and source. Adapted from ref. 33 and 59.

monitored by the generated drain current ($I_D$), which can be tuned by the extent of applied field.[12] Replacing the dielectric layer with an electrolyte layer, resulted in the emergence of a new category of OFETs, known as electrolyte-gated organic field effect transistors (EG-OFETs),[59] presented in Figure 10b. Similar to OFETs, EG-OFETs operate by a gate voltage switch to regulate the number of charge carriers at the OSC layer interface. However, in the case of EG-OFET, the generated charge carriers in the OSC active layer are compensated by ion of opposite charge from the electrolyte which accumulate at the OSC layer interface upon gate voltage switch. As a result, an electrical double layer (EDL) forms along the electrolyte/semiconductor interface, which enhances the capacitance (C) and enables operation at lower voltages compared to OFETs.[60] When the OSC active layer is permeable to ions, charge accumulation becomes no longer limited to OSC channel-electrolyte interface, and ions can permeate throughout the polymer's entire volume (Figure 10c), leading to a remarkable regulation of the polymer film's doping state, increasing its conductivity. This 3D interaction between the active material and the electrolyte, is the distinctive characteristic of OECTs, giving them a significant advantage over EG-OFETs, and OFETs by means of volumetric capacitance ($C^*$) that can be orders of magnitude larger than the electrical double layer

capacitance in EG-OFETs.[59] As a result, this leads to greater current amplification compared to equivalent biasing conditions and geometries in conventional transistors. Furthermore, it allows for operation at low voltage levels, making OECTs well-suited for biological applications. This is especially important in cases where the aqueous media's limited electrochemical window limits applied potentials to about 1.2 V.[60]

Similar to OFETs and EG-OFETs, the operation of an OECT is initiated by a gate voltage ($V_G$) switch (input), allowing substantial modulation in the drain current (output) at low-gate voltage, thereby making OECTs efficient switches and potent amplifiers, because it allows large current modulation in response to low gate voltage switch, (small input-large output). This characteristic makes OECTs a promising technology for flexible and ultra-sensitive bioelectronic interfaces for healthcare related applications. Being composed of organic materials, OECTs can offer technological pathways to cost-, power-effective, and compact devices, enabling rapid advances in organic bioelectronics for bio-sensing.[61]

OECTs have two working modes, depletion mode (when the OECT layer is inherently conductive, such as PEDOT:PSS) and accumulation mode (when the OECT layer is semiconductor with low conductivity).[3] Since most conjugated polymers are semiconductors with low electrical conductivity, an accumulation mode is most commonly used, in which the current is typically OFF and is switched ON by applying a gate voltage. Accumulation mode OECTs are also of particular interest for sensing applications, since they consume little power because they are normally turned off and only turn on when an analyte is present.[62] In Figure 11, the typical structure of an OECT is presented with an accumulation mode operation of n-type OECT materials. In the absence of applied bias, the OECT device is in its “OFF” state. (Figure 11a). Applying a gate-source voltage ($V_{GS}$) will induce two simultaneous processes. The first one involves electron injection from the source electrode, which are stabilized by cations from the electrolyte. (Figure 11b). After applying a drain-source voltage ($V_{DS}$), charge

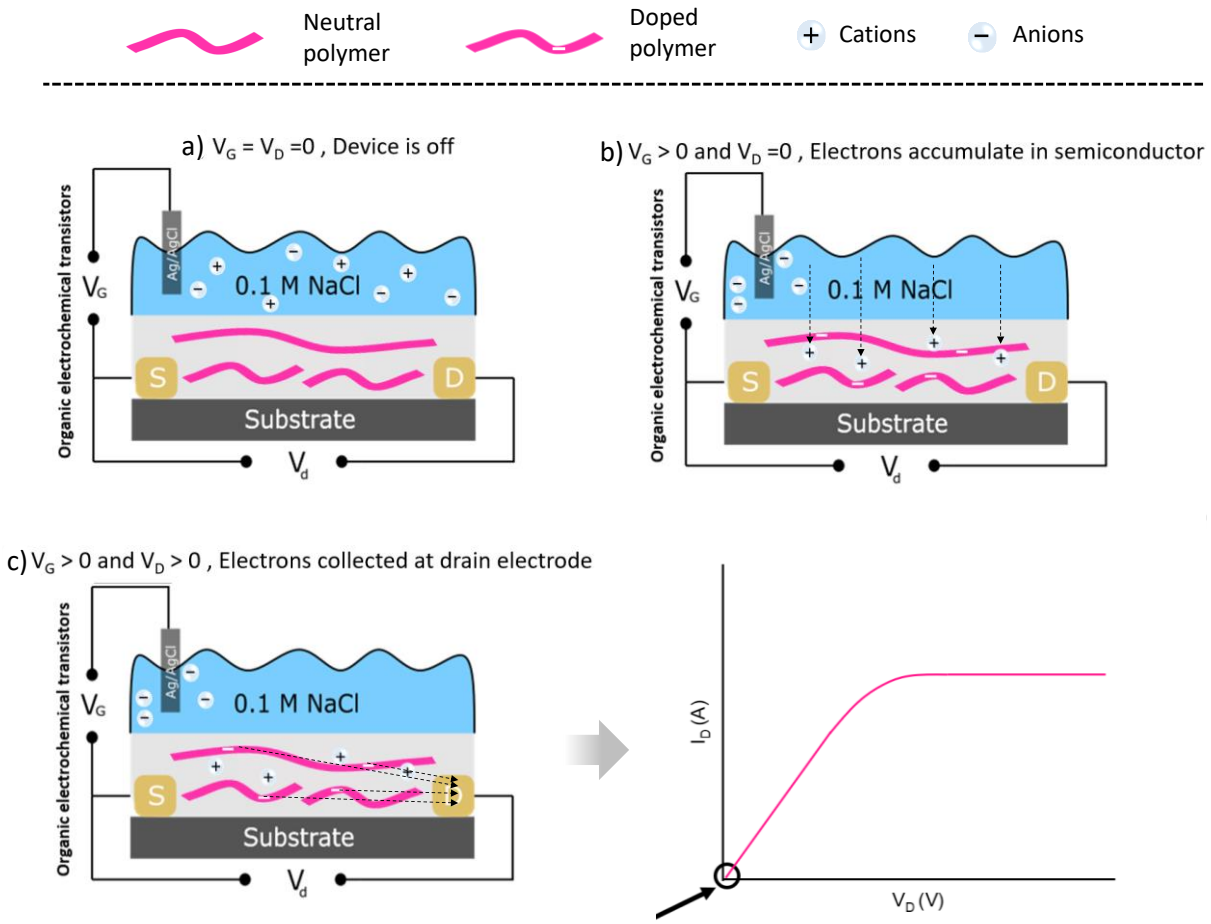


Figure 11. Operation of an n-type accumulation mode OECT. a) Gate voltage ($V_G$) is off, and so is the OECT device. b) A positive gate-source voltage is applied ($V_{GS} > 0$), injecting electrons into OECT layer from source electrode, stabilized by cations from electrolyte. c) Applying drain-source voltage ($V_{DS} > 0$) will cause the charge carriers to transport across the polymer to drain electrode, leading to drain current ($I_D$).

carriers will transfer from the OECT layer to the drain electrode by means of hopping and transport across the polymer layer. (Figure 11c). The current-voltage characteristics of OECTs are represented using output and transfer plots. (Figure 12) The output curve shows the drain currents ($I_D$) resulted from the modulation of drain-source voltage ($V_{DS}$) at constant gate voltage ($V_G$), and is scanned over different gate voltages, showing both linear and saturation regimes. (Figure 12a). The transfer curve is derived from the output curve and shows the drain currents ($I_D$) as a function of gate voltage ($V_G$) at a particular drain voltage ($V_D$) in the saturation regime, and describes the transduction of small gate voltage signals into large drain currents. The efficiency of this transduction (or the ability of an OECT device to amplify a small input signal) is measured by the first derivative of the transfer curve, namely,

transconductance, $g_m = \partial I_D/\partial V_G$, as seen in Figure 12b, which is the first important figure of merit of an OECT device. Because of the volumetric nature of their response, OECTs have very high transconductance values, on the order of millisiemens for micrometre-scale devices. Another parameter that can be derived from the transfer curve and is also used to evaluate the OECT performance, is the threshold voltage ($V_{th}$), which is the minimum gate voltage that is needed to fill trap states and produce mobile charge carriers, thus turning the device on. The device's threshold voltage can be derived from the transfer curve by extrapolating a graph of $\sqrt{I_D}$ against $V_G$, as illustrated in Figure 12c.[63]

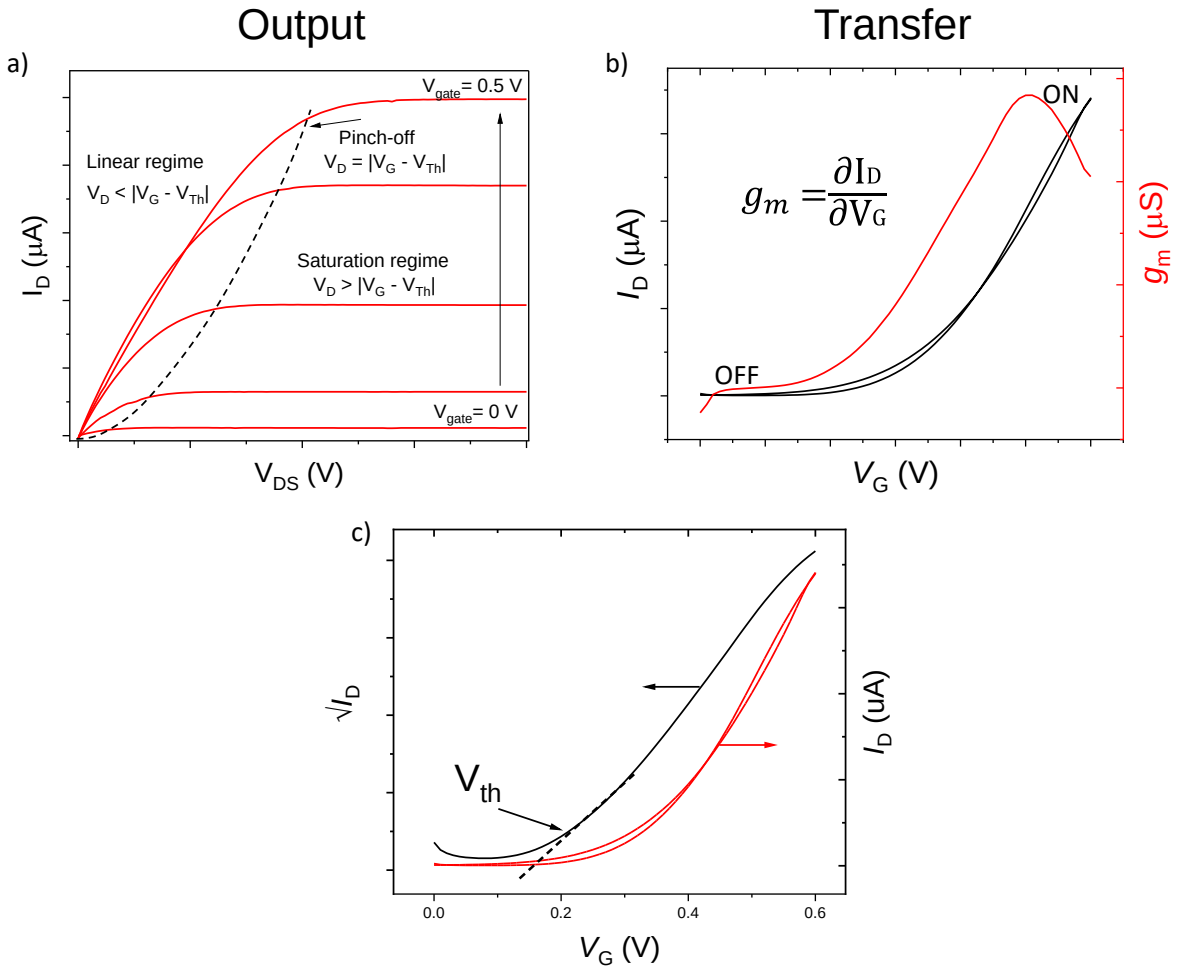


Figure 12. Illustration of characteristic of accumulation mode n-type OECT device. a) Output curve presenting the drain current as a function of source drain voltage for different gate voltages and b) Transfer curve of the saturated regime showing the drain current as a function of gate voltage, defining the transconductance, and c) drain current as a square root, showing the threshold voltage ($V_{th}$).

A commonly employed model by Bernards and Malliaras divides the OECT into two circuits [64], i) an electronic circuit, which involves the flow of electronic charge in the source-channel-drain direction, and ii) an ionic circuit that involves the flow of ions in the gate-electrolyte-channel direction. The Bernards-Malliaras model is therefore suitable for evaluating the output characteristics of OECT devices and enables quantification of transconductance ($g_m$). In the saturation regime, transconductance is defined as follows:

$$g_m = \frac{Wd}{L}\mu C^*\left(V_g - V_{th}\right) \quad (4)$$

Where W is the channel width, d is the channel thickness, L the channel length, μ is the electronic charge carrier mobility, $C^*$ is the volumetric capacitance, $V_g$ is the gate voltage, and $V_{th}$ is the threshold voltage. As illustrated in equation 4, since $g_m$ is dependent on the channel volume (Wd/L), it is often represented as geometry-normalized transconductance ($g_{m,norm} = g_m \frac{L}{Wd}$), for fair comparison between different reported $g_m$ values. Additionally, $g_m$ is directly dependent on charge carrier mobility, μ, (transport of electronic charge) and volumetric capacitance, $C^*$, (store of ionic charge). Both parameters define another key figure of merit, called product of charge-carrier mobility and volumetric capacitance [$\mu C^*$], as proposed by Sahika Inal and colleagues.[65] The authors highlight that this product can be directly calculated from the transconductance according to equation 4. Alternatively, [$\mu C^*$] can be found by calculating each parameter separately. The volumetric capacitance (C*) can be analysed by measuring the capacitance by electrochemical impedance measurements (EIS) at a certain offset voltage. The next section will focus on the design requirements for n-type polymers to maximize the performance of n-type OTE and OECT devices.

## 1.4. Electron-transporting n-type conjugated polymers

Current literature on conjugated polymers for various organic electronic applications is dominated by hole-transporting p-type materials. Electron transporting n-type materials, on the other hand, have lagged behind their p-type counterparts. This discrepancy becomes apparent in charge carrier mobility records in organic field effect transistor (OFETs), with p-type conjugated polymers making significant progress, beginning with hole mobilities of $10^{-5}$ $cm^2$ $V^{-1}$ $s^{-1}$ in 1986[66] and eventually reaching high hole mobilities over 40 $cm^2$ $V^{-1}$ $s^{-1}$.[67, 68] On the other hand, n-type conjugated polymers have yet to exceed the benchmark mobility of 10 $cm^2$ $V^{-1}$ $s^{-1}$.[69] In organic thermoelectrics (OTEs), p-type polymers exhibited excellent electrical conductivities (σ) of 1000 S $cm^{-1}$,[51] while most n-type polymers struggle to exceed electrical conductivities of 1 S $cm^{-1}$ with few examples achieving values in the order of $10^1$ S $cm^{-1}$.[51] The same trend applies in organic electrochemical transistors (OECTs), with transconductance ($g_m$) and ($\mu C^*$) over 200 S $cm^{-1}$, and 500 F $cm^{-1}$ $V^{-1}$ $s^{-1}$, respectively, recorded for p-type polymers, and only few n-type polymers achieved figure of merit values over 10.[70] This disparity in electrical performance has prompted researchers to investigate the factors responsible for the poor performance of n-type polymers, commencing with fundamental aspects such as molecular design of the semiconducting polymer. Several factors have been found to influence the n-type polymer's performance. Some factors are exclusive for particular applications, while others have been found to be problematic across various applications. In the following section, limitations concerning organic thermoelectrics (OTEs), and organic electrochemical transistors (OECTs), will be addressed. It should be noted that the hole and electron transport mechanisms are theoretically identical and are not the limiting factor in the lower performance of n-type materials.[46] When designing electron-transporting materials, one must consider desirable characteristics, such as high mobility, high conductivity, ease of synthesis, material air stability, and efficient charge injection at interfaces. While efforts can be made to enhance these

characteristics through molecular design optimization, it's essential to recognize that certain characteristics are not intrinsic to the material itself, but also dependent on device properties.[46] Typically, charge transport characteristics are used to compare the efficiency of newly designed semiconducting polymers. The efficiency of charge transport in semiconducting polymers is governed by multiple factors, some are related to inherent properties of the polymer such as polymer molecular weight (MW) and side chain composition. For example, increasing the molecular weight of conjugated polymers has been found to substantially enhance the field-effect mobility, which was explained by longer polymer chains bridging separate crystallite within the solid microstructure, facilitating charge transport.[71] [72]Longer chains also allow charge carriers to travel further before having to hop to another chain, which can increase carrier mobility. It must be noted however, that an opposite trend was found in a n-type polymer, P(NDI2OD-T2), with electron mobility decreasing with increasing MW, which was explained by the lack of aggregation prior to polymer deposition in low MW polymers favoring long range ordering, as opposed to observed aggregation in high MW polymer, which was found to form crystalline films with poor interconnectivity between crystallites.[73] Side chains which are usually incorporated to assist solubility, have also been found a useful tool to modulate crystallinity. Multiple studies revealed the effects of side-chain engineering on crystallinity. Control of side-chain size,[74] length,[75] branching point position from the backbone,[76] and regio-position on the backbone,[77] have all been found to affect polymer torsional conformation leading to higher mobilites.[77, 78] Energetic disorders have been shown to impact charge transport, and are usually imposed by the presence of chemical impurities and structural defects, such as kinks in the polymer chain, which might break the conjugation. Such defects lead to energetic disorders.[12, 46] Trap-limited transport can occur by impurities with energy levels distributed in the band gap of the semiconducting polymer, thus acting as trapping sites and hindering charge transport. Energetic disorder can also be caused by energy

distributions due to the fluctuations of frontier molecular orbital energies within the polymer, which stems from the different segments within the polymer with varying conjugation length and consequently different energies. Polymer conformation could also contribute to energy level distribution by fluctuations of torsional angles between the polymers building blocks across the polymer chain.

Device related factors that could potentially affect charge transport is charge injection/extraction barrier at metal/semiconductor interface.[69] Also, polymer processing conditions have a substantial impact on solid-state microstructure. It was found that the solvent from which the polymer is deposited can influence the degree of pre-aggregation in solution (polymer self-assembly), and eventually the film microstructure, and that high degree of pre-aggregation can cause domain boundaries that limit charge transport in spite of the highly ordered stacking within one aggregate, which is explained by the lack of connectivity between crystalline domains.[79] Other extrinsic factors such as charge trapping during device operation by ambient species have been recognized as one of the limiting factors in achieving high-mobility n-type polymers.

In summary, charge transport can be influenced by efficient polymer packing and frontier molecular orbitals (energy levels and distribution). Factors that can affect both properties include molecular weight,[71, 72, 73, 80] side-chain engineering,[74, 75, 76, 77] chain aggregation behaviour in solution,[79] polymer conformation (backbone planarity and rigidity),[74, 81, 82, 83] quality of the synthesized polymer (minimizing residual impurities),[84] and energy levels of the polymer (trap-free transport and injection barriers).[26] Considering the above factors are crucial when designing new p-and n-type polymer semiconductors. Nevertheless, when it comes to designing new n-type polymers, precise design rules need to be employed to tackle the main challenges that restrict the developments of high-performing n-type polymers. The challenges include ambient instability, charge carrier generation, charge transport, and

therefore electrical conductivity. More on these limitations will be discussed in the following section, starting with joint limitations for both OTEs and OECTs, then delving into limitations concerning each application individually.

### 1.4.1 Importance and limitation of n-type polymers for OTEs and OECTs

Before discussing the constraints associated with n-type polymer along with the efforts made to address those challenges, it is necessary to explain why high-performance n-type materials are needed in the first place. Despite the inferior performance of electron-transporting (n-type) semiconducting polymers, they are highly desired. For example, for practical organic thermoelectric applications, and for a thermoelectric module to operate efficiently, both n-type and p-type constituting semiconductors must be of comparable performance, which is difficult to achieve due to the existing performance gap. In OECTs, electron-transporting (n-type) materials are of paramount need for i) direct-electron-transfer-based biological sensors,[85, 86] ii) complementary logic circuits, where they can be paired with p-type polymers, which carry the benefit towards reduced power consumption, improved switching speeds and operational stability,[59, 80, 87] and iii) cathodes for lithium or sodium ion batteries.[88, 89, 90] However, the mismatch between n-type and p-type performance in both OTEs and OECTs is restricting the development of next-generation thermoelectric and bioelectronic technologies.

The low electron affinity (shallow LUMO level) is commonly recognized as the constraining factor in the realization of high-performing n-type polymers, giving rise to ambient instability. Unlike n-type polymers, most p-type conjugated polymers function within an energetically stable suitable window, with ionization energy (IE) ranging from 4.9–6.0 eV, lying deeper than energy levels of common charge traps like oxygen and water.[25] Most common n-type polymers on the other hand, exhibit electron affinities (EA) that reside within an electrochemical window of potential electron traps (oxygen/water). In 1996, De Leeuw et

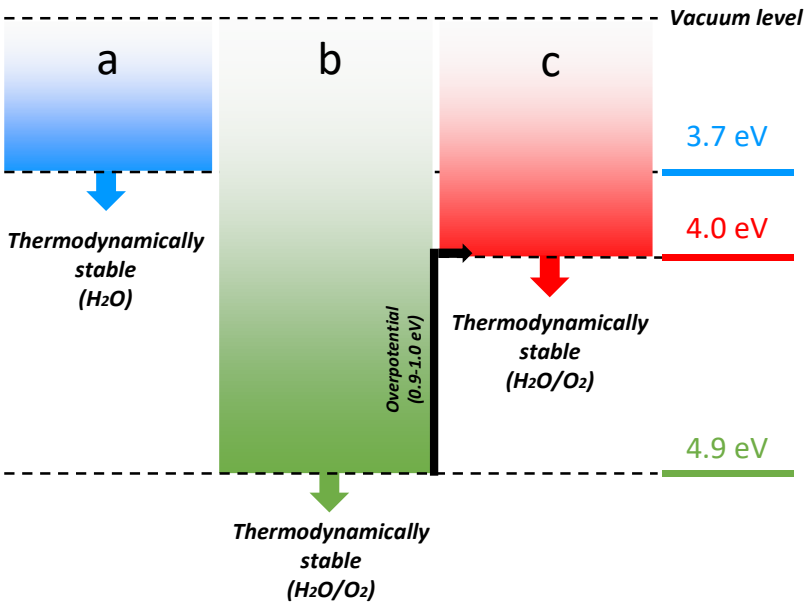


Figure 13. A visual representation of the EA requirements for the stability of an n-type material, showing the thermodynamical stability against a) water, b) wet oxygen, and c) water and oxygen after taking into account an overpotential of 0.9–1.0 eV, which is associated with the activation free energy needed for the redox reaction to proceed, requiring an excess voltage above the theoretically predicted values. The LUMO levels that correspond to these redox potentials have been estimated using the equation $E_{LUMO} = E_{red} + 4.4$ V. Adapted from ref 94 and 95

al. addressed the issue of ambient stability of n-doped polymers for the first time. He described the air sensitivity of these materials is due to a redox reaction of electron-carrying (n-doped) polymer with atmospheric water and/or oxygen, and demonstrated a thermodynamic stability to redox reactions involving these ambient species can be achieved by tuning the energy of the LUMO level, with a shallow n-doped LUMO at risk of oxidation by oxygen or water (through an electron transfer from polymer radical anions to neutral $H_2O/O_2$).[26] It should be noted that that air-instability of n-type polymers does not stem from an intrinsic chemical instability, but rather an ambient instability of the polymer radical anions generated after n-doping and the susceptibility of the latter to be trapped by ambient species, leading to degradation under device operation.[91] It has been demonstrated both theoretically and experimentally that a LUMO energy of -4.00 eV or deeper is required for an n-type organic semiconductor to exhibit a stable electron transport.[59, 92, 93] An electrochemical guide towards avoiding oxidation by ambient species was elaborated as follows: i) in order to prevent polymer radical anions from oxidation

by $H_2O$, an n-type polymer must possess a reduction potential higher than -0.658 V versus standard calomel electrode (SCE) at pH=7, which corresponds to a LUMO level of (-3.7 eV), and is the potential where water reduction occurs according to the following equation ($2H_2O + 2e^- \rightleftharpoons H_2 + 2OH^-$). (Figure. 13a) ii) Under identical conditions, oxygen (wet $O_2$) can undergo two-electron reduction by polymers radical anions to form hydrogen peroxide, at reduction potential + 0.024 V (-4.4 eV), ($O_2 + 2H^+ + 2e^- \rightleftharpoons H_2O_2$). Oxygen also undergoes four-electron reduction at reduction potential + 0.571 V (-4.9 eV) in presence of water, ($O_2 + 2H_2O + 4e^- \rightleftharpoons 4OH^-$). So, in order for an n-doped polymer to be stable in wet oxygen, it must possess a reduction potential higher than +0.024 V, and +0.571 V. This concludes the LUMO level of an n-type polymer must be below -3.7 eV to avoid oxidation by water, and below -4.4 eV and -4.9 eV to avoid oxidation by both oxygen and water. (Figure 13b). The above values are approximated assuming pH 7 and an overpotential of 0.0 V.

Several n-type polymers surpass -3.7 eV, and therefore develop resistance to oxidation by water. However, since most of the current n-type polymers acquire LUMO levels ≤ -4.00 eV, they are still unable to meet the requirements for avoiding oxidation by oxygen. Nevertheless, experimentally, a couple of non-fluorinated n-type materials with LUMO levels ~ -4 eV were able to show air stable OFET-based device operation.[91] This can be explained by overpotentials, which is the free energy of activation required for the redox reaction to proceed, requiring an excess voltage beyond the theoretically predicted values, serves to provide this free energy.[26] An overpotential or excess voltage is estimated to range between 0.9−1.0 V based on studies involving various n-type materials.[26, 91, 92, 93] Therefore, by accounting for these overpotentials, it is concluded that a LUMO of ~ -4 eV would be sufficient to enable an air-stable electron transport. (Figure 13c) This energetic threshold has been supported by experimental observations and became a widely utilized rule for assessing the stability of n-type materials.[91, 92, 93, 94, 95] Nevertheless, there are complications that needs to be considered in

my opinion, and are outlined as follows: i) as raised by De Leeuw,[26] the estimated reduction potentials of $H_2O/O_2$ that he reported holds for aqueous solutions, while most conjugated polymers are processed in non-aqueous solvents. ii) Oxygen reduction reactions (ORR) reported by De Leeuw only considered the two and four electron transfer of n-doped polymer to oxygen, which corresponds to LUMO threshold values of -4.4 and -4.9 eV, respectively to avoid this reaction. However, the first step of ORR (one-electron transfer) to form superoxide radical was ignored,[96] with the explanation that the reduction potential for superoxide formation (-0.9 V vs SCE) was determined in aprotic media and does not fit with his goal of investigation in ambient conditions. Nevertheless, reduction potential of oxygen to superoxide has been reported by others to occur in aqueous solution at pH 7 with reduction potential of -0.33 $V_{SHE}$ equivalent to a LUMO of -4.11 eV.[96] This LUMO level lies within the proposed LUMO required for an air stable electron transport (~ -4 eV), and therefore suggest that the reduction potential of first product of ORR reaction requires serious consideration. iii) In the context of OECTs, apart from electrochemical degradations driven by energetics (thermodynamic instability), one must also consider chemical degradation that results from the thermodynamic instability. For example, during OECT operation, latent ORR products such as $H_2O_2$ could react with the n-doped polymer leading to its chemical degradation, with potential corrosive damage during OECT operation.[97, 98]

Aside from achieving thermodynamic stability towards oxygen and water, another approach towards ambient stability can be achieved kinetically. For example, by designing fluoroalkyl-based semiconductors which sufficiently pack in dense thin films creating kinetic barrier against ambient species penetration,[91, 92, 99] or by device encapsulation in inert atmosphere. However, in the case of the former, a balance between crystallinity and solubility must be found to ensure easy processing from solution; in the case of the latter, it should be noted that encapsulation is not sufficient for practical applications.

A deep LUMO of the n-type polymer also favored to lower the electron injection barrier at the source-drain/semiconductor interface, which is the difference between the metal electrode Fermi level ($E_F$) and the semiconductor LUMO energy. Gold is commonly used as the metal electrode with work function of -5.1 eV. Considering that most common n-type polymers exhibit a span of LUMO between -3.7 and -4.1 eV, a high injection barrier is therefore created. It was found that deepening the LUMO level facilitates electron injection and transport. [93]

Ongoing investigations on the factors contributing to the low LUMO values of n-type polymers has prompted researchers to re-assess charge transport in n-type polymers. As mentioned before, charge transport itself is similar in both p-type and n-type polymers, and the inferior performance of the latter was ascribed to air instability. Therefore, researchers were attempted to increase the electron affinity (deepen the LUMO) by introducing electron-withdrawing functional groups (directly to the conjugated backbone, such as CN, C=O, X: Cl, Br, F) to provide thermodynamic stabilization, or by incorporating fluoroalkyl side chains to provide kinetic stabilization against $H_2O/O_2$ penetration. In the former case, however, it was found that incorporating electron-withdrawing group (EWG) was not sufficient by itself to enhance the electron affinity (EA). Interestingly, the reason behind that was the poor delocalization of LUMO orbital along the conjugated backbone, required for sufficient electron transport. While high-performing p-type polymers consist of all donor, electron rich aromatic rings, HOMO is more readily delocalized giving rise to high mobility. This was not the case in most (early) n-type polymers, which have donor-acceptor moieties on their backbone, and the large torsional angle between donor and acceptor building blocks caused LUMO orbitals to be localized on the acceptor. Charge localization reduces mobility and thus device performance, while also preventing high electron affinity.[39, 100]

To summarize, the design of high performing n-type polymers necessitates the consideration of several key characteristics in order to achieve air-stable electron transport: i) the synthesis of an electron-deficient backbone by incorporating EWGs. ii) rigid/planar backbone for efficient charge delocalization and solid-state packing, iii) achieving i and ii together will enable deep LUMO levels required for air stability and efficient charge injection at electrodes. These characteristics apply for OFETs, OECTs and OTEs. However, doping in OECTs takes place electrochemically, while in OTEs the doping is chemical. As a result, both technologies show a difference in the challenges they present in order to achieve i) efficient charge carrier generation, ii) efficient charge transport, and iii) ambient stability. These different challenges are the topic of the next section."

### 1.4.2 Key design considerations for high performance n-type OTEs and OECT: limiting factors and molecular design strategies

In this section, we will discuss the design strategies that have been adopted to fulfill the three challenges in n-type polymers, namely i) charge carrier generation, ii) charge carrier transport, and iii) ambient stability. Each challenge will be separately addressed for OTEs and OECTs, focusing on the limiting factors in optimizing their parameters and the molecular design strategies employed to overcome those limitations. The advantage of designing n-type materials for both OTEs and OECTs is their "joint" molecular design requirements, allowing them to serve both applications, thereby expanding the scope of application for the synthesized n-type polymer, as will be discussed below. Because deepening LUMO levels is important for air stable n-type materials, it is also a used strategy to improve charge injection/chemical doping (charge carrier generation challenge), and deep LUMO levels were achieved in some cases while attempting to improve intramolecular charge delocalization (charge carrier

transport challenge). As a result, general chemical design strategies for deepening LUMO levels will be discussed first.

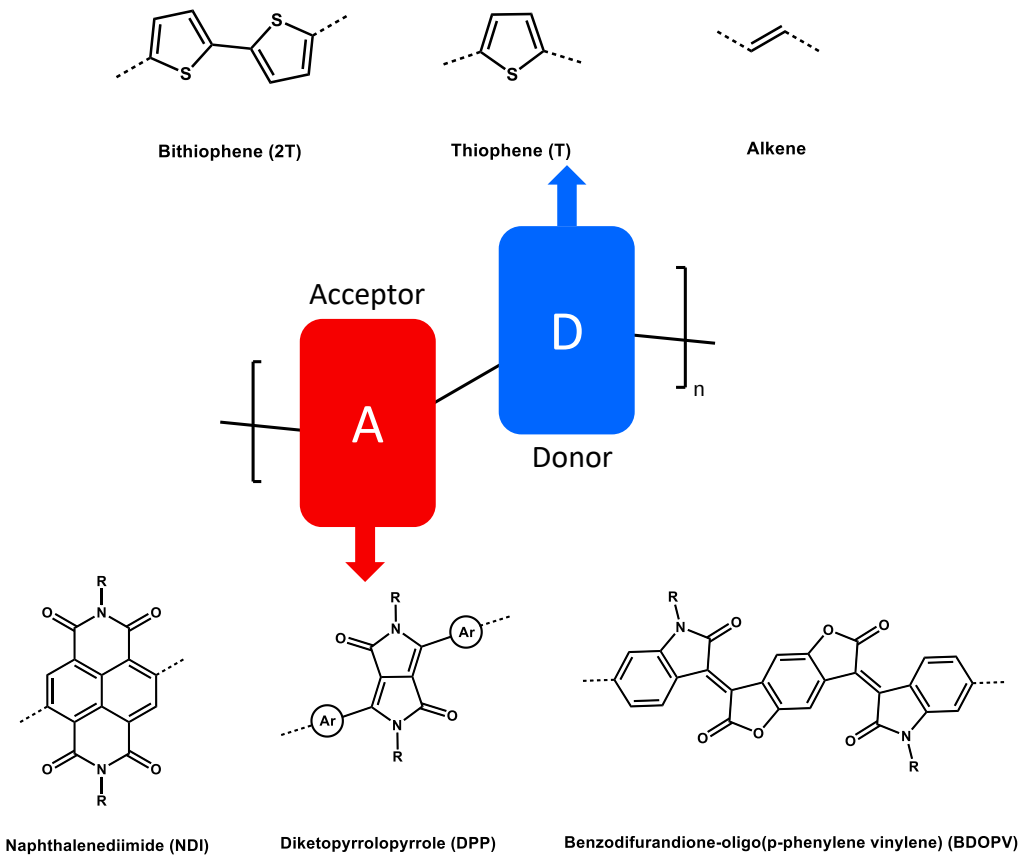


Figure 14. Schematic representation of D-A polymers with examples of early developed D-A building blocks.

## a) Ambient stability

First, the most common electron-deficient building blocks that constitutes an n-type material will be listed. The early examples of n-type polymers are composed of alternating electron rich "donor" and electron deficient "acceptor" building blocks, and known as (D-A) polymers. Common acceptor building blocks include, naphthalenediimide (NDI),[101, 102] diketopyrrolopyrrole (DPP),[103] and benzodifurandione-based poly(p-phenylene vinylene) (BDPPV),[104] and when polymerized with "unodified" donor building blocks, the resultant copolymers exhibit LUMO levels ranging between (3.7-4.00 eV).[83, 105, 106] (Figure 14). The

synthetic techniques that have been adopted to further enhance the electron affinity (deepening LUMO levels) of n-type polymers include the incorporation of electron-withdrawing groups, such as F, Cl, CN. For example, when hydrogen atom in BDPPV (with LUMO -4.01 eV, and $\sigma$ = 0.26 S $cm^{-1}$), was replaced by fluorine atom, (see Figure 15a), FBDPPV showed enhanced electron affinity (with LUMO -4.17 eV, and $\sigma$ = 14 S $cm^{-1}$).[107] Other strategies to deepen LUMO levels were applied on the widely used NDI-based polymer, P(NDI2OD-T2), or sometimes called N2200. For example, replacing the sulfur chalcogen atom with selenium was found to improve orbital overlap (induced by larger p-orbital in selenium), and thus lower LUMO level by 0.10 eV, thus the selenium-containing polymer exhibited higher electron mobility than the sulfur-containing polymer.[108, 109] (Figure 15b). In the same polymer class, extending the core of NDI unit by adding two fused thiophene rings, was found beneficial towards deepening the LUMO by 0.13 eV.[110, 111, 112] (Figure 15c). This was explained by the enhanced planarization induced by reducing the torsional angles between the monomer, which in turn has enabled better electron mobility. Finally, backbone rigidification induced by non-covalent electrostatic interactions was found to benefit deep LUMO levels. A good example is represented in BDOPV based polymers,[113]when sp2-nitrogen atoms were embedded in BDOPV-2T, resulting in a stronger electron-deficient building block, diaza-BDOPV (AzaBDOPV-2T). (Figure 15c) The resulting polymer exhibited a more planar backbone, a lower LUMO by 0.13 eV than BDOPV-2T, and an electron mobility that was twice as high, 3.22 $cm^2\ V^{-1}\ s^{-1}$. Although the above strategies proved efficient to deepen LUMO levels, only FBDPPV was exhibiting air-stable performance. Despite the moderate LUMO level (-4.17 eV), the air stability in FBDPPV was kinetically driven by the dense packing provided by the fluorine atoms. This insufficient deepening of LUMO levels by D-A polymers has encouraged researchers to design all acceptor, or acceptor-acceptor (A-A) in an attempt to achieve highly electron-deficient n-type

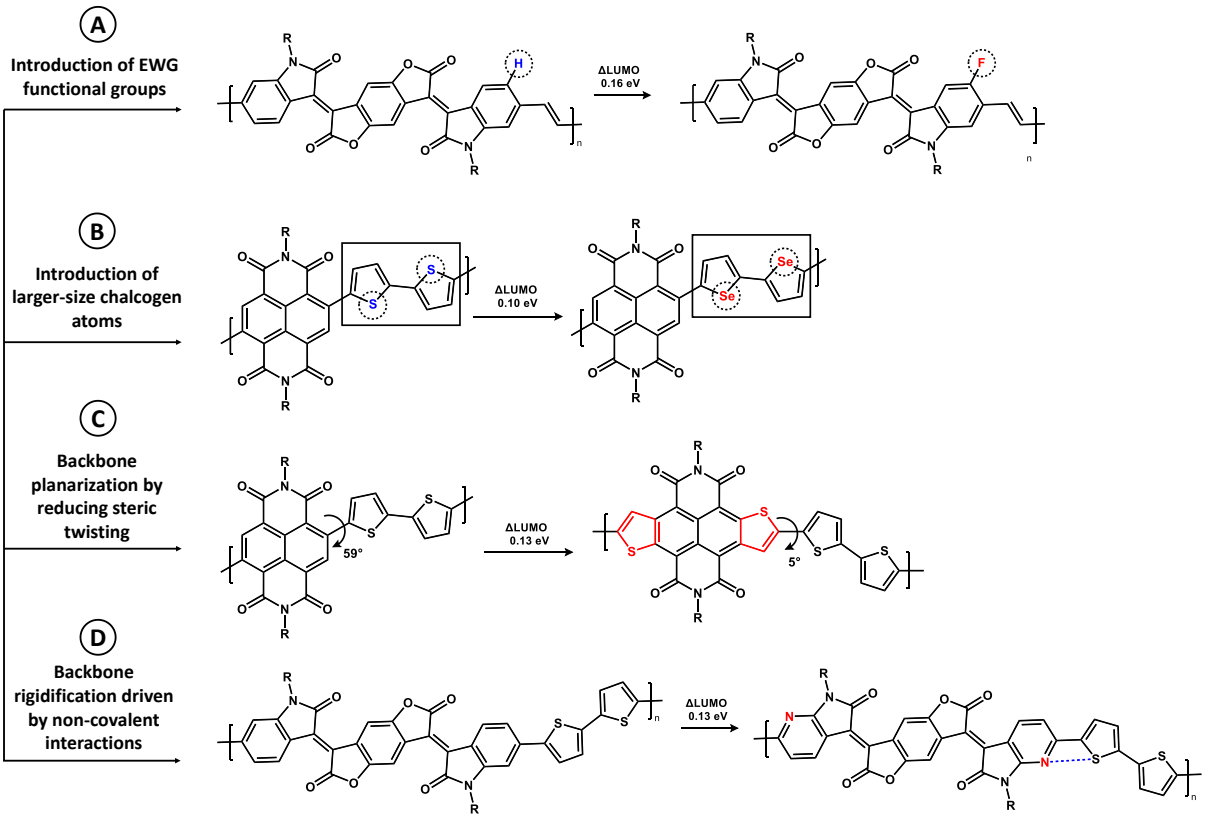


Figure 15. Examples of synthetic techniques to deepen LUMO levels in D-A polymers.

polymers. By taking notes from the above design strategies, the recently emerged n-type polymers have a shared property of a fused backbone with an all acceptor or A-A building blocks. A very good example of a fully rigid n-type polymer is the ladder-type polymer polybenzimidazobenzophenanthroline, (BBL). (Figure 16a). BBL exhibit a torsion-free backbone, with LUMO level of (-4.15 eV).[38] Although its LUMO level does not provide thermodynamic stability in air, BBL demonstrated air stable performance. This was ascribed to its rigidity that promoted close packing of the polymer chains with a crystalline thin film, which act as a kinetic barrier to oxygen diffusion. Another class of all acceptor (A-A) polymers are the fused lactam polymers, (Figure 16b), which comprise electron deficient bioxindole and bis-isatin monomers, connected together by a double bond to allow a locked conformation with nearly no free rotation, and hence low energetic disorders.[74] Most n-type

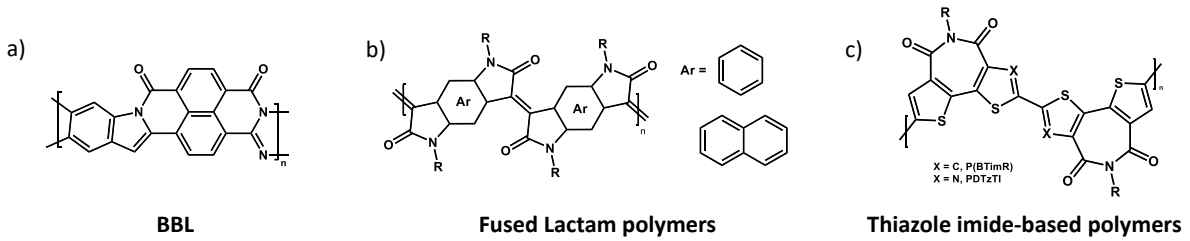


Figure 16. Chemical structures of polymeric materials containing an acceptor–acceptor (A–A) motifs.

polymers are polymerized by metal-catalyzed polymerization which link aromatic groups through single bonds, [14] and give rise to conformational and energetic disorders due to rotation around these single bonds (with barrier for full rotation in the range of 2−8 kcal $mol^{-1}$).[74] Unlike conventional D-A n-type polymers, these fused lactam polymers are polymerized through aldol condensation to result in double-bond linkage between the monomers (with barrier for full rotation in the order of 25 kcal $mol^{-1}$), allowing a locked conformation with low torsional angles, enabling charge delocalization over the acceptor lactam unit which give rise to deep LUMO levels, and eventually an air-stable electron transport. Another class of A-A polymers, are fused thiazole imide homo polymers (Figure 16c), with electron-withdrawing imide groups, contributing to the electron acceptor character. The parent polymer (P(BTimR)), has fused electron-rich thiophene core, which leads to shallow LUMO levels (-3.47 eV) which are detrimental to its ambient stability.[74] Replacing the fused thiophene rings with electron-deficient thiazole rings (PDTzTI),[114] has led to a more planar backbone induced by intramolecular noncovalent N···S interactions, leading to high electron mobility, 1.61 $cm^2\ V^{-1}\ s^{-1}$, and also enhanced the polymer EA (- 3.77 eV). However, the shallow LUMO level of PDTzTI, is still hindering its ambient stability.

b) Charge carrier generation

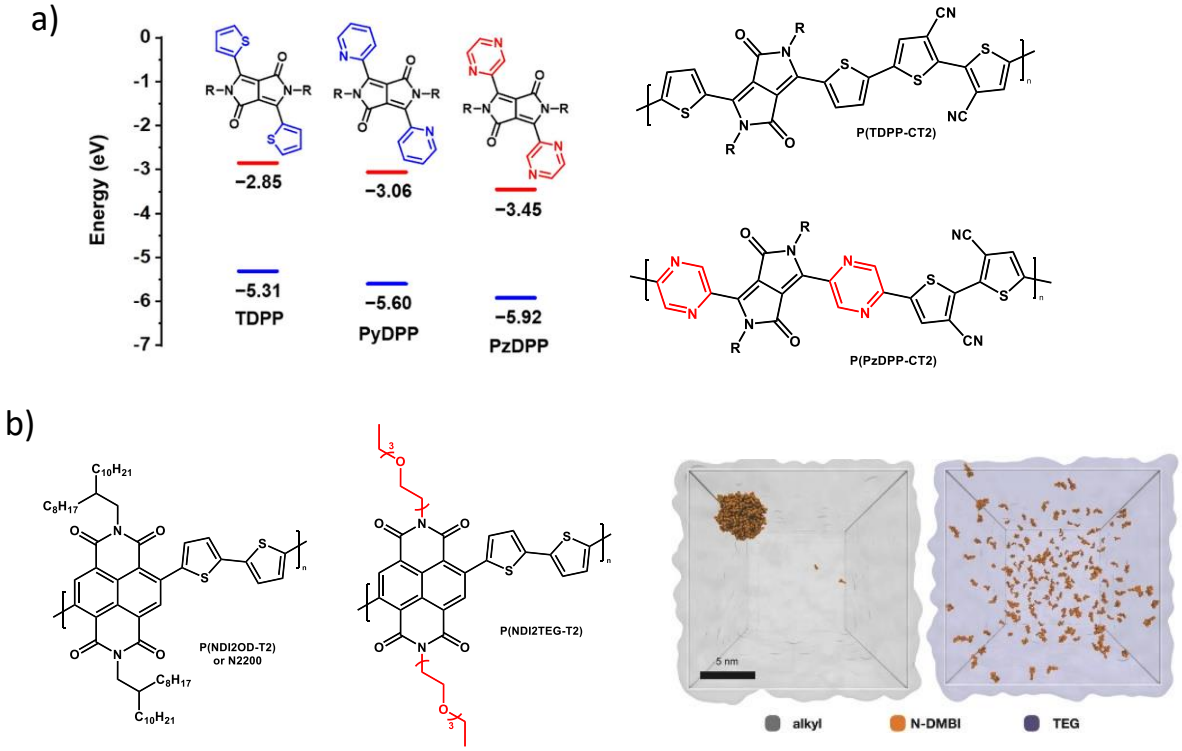


Figure 17. Enhancing n-doping efficiency by a) deepening LUMO level, and b) polymer-dopant miscibility. Reproduced with permission from ref 83 and 116.

In OTEs, charge carrier generation is achieved by chemical doping to increase the charge carrier density, and thus electrical conductivity. Chemical n-doping of n-type polymers is achieved by introducing small-molecule donors (as discussed earlier and shown in Figure 3c). Once admixed with an n-type polymer, a redox process takes place by an electron transfer from the dopant HOMO to the polymer's LUMO. (Figure 3b). Increasing the dopant concentrations leads to modulation of the charge carrier density. Factors that can limit the n-doping efficiency in OTEs are i) energy level mismatch between dopant HOMO to the polymer's LUMO that could hinder the energetically driven electron transfer, and ii) polymer-dopant miscibility, where both should be in proximity to enable effective electron transfer, and it was found the different polarities of the two can lead to phase segregation by forming aggregates on the film, limiting the doping process.[39, 115] The former factor can be achieved by lowering the LUMO of the n-type polymer, to match the deep HOMO of the dopant. For an effective n-doping, the

dopant's HOMO should be higher than the polymer's LUMO. Shallowing the dopant HOMO increases its vulnerability to oxidation by ambient species, thus deep HOMO n-dopants (such as N-DMBI, HOMO is -4.4 eV) are commonly used to maintain air stability.[27] Therefore, lowering the LUMO of the n-type polymer (below -4.00 eV) is the common strategy used to enhance energy level offset between the polymer and the dopant. For example, in D-A polymers, modifying the electron-deficiency of the donor moiety can increase the electron affinity of the D-A polymer. Yan, X et al. reported the design of pyrazine-flanked DPP (PzDPP) acceptor which was polymerized with an electron-deficient donor moiety, 3,3′-dicyano-2,2′-bithiophene to yield P(PzDPP-CT2). (Figure 17a).[83] When compared to a thiophene-flanked DPP polymer (LUMO -3.7 eV), P(TDPP-CT2), the polymer P(PzDPP-CT2) exhibited better planarity and stronger electron affinity (LUMO -4.03 eV). P(PzDPP-CT2) film showed higher doping level upon doping with a widely employed dopant N-DMBI, resulting in a remarkable 20-fold enhancement in electrical conductivity. The second factor, polymer-dopant miscibility, is most commonly achieved by matching the polarity between the polymer and the dopant. For example, Liu et al, reported a remarkable 200-fold increase in electrical conductivity within P(NDI2TEG-T2) polymer compared to P(NDI2OD-T2) polymer, achieved by substituting the conventional alkyl side chains with ethylene-glycol based polar side chains, and was supported by MD simulations that polar side chains favor dopant dispersion into the polymer matrix compared to alkyl chains.[116] (Figure 17b).

In OECTs, doping of organic semiconductor is achieved electrochemically, while both electron injection and ion injection needs to be considered and carefully balanced. Factors that can limit electronic charge injection is large injection barrier (discussed in the last section), which originate from mismatch between the polymer's LUMO and the metal's work function. Ion injection, on the other hand, can be limited by the polymer's hydrophobic nature, which prevents ions from penetrating the bulk of the polymer channel and thus lower the volumetric

capacitance that defines the OECT device. Facile electron injection can be achieved by reducing the barrier height with respect to the metal electrode, the commonly used metal electrode is (Au), which has a high-working function (5.1 eV). So, designing n-type materials with low-lying LUMO levels could be a good strategy, although still challenging. Alternatively, the use of metal electrodes with low work function such as aluminum is preferable. However, such metals tend to get oxidized in air, thus limit the benefit of lower injection barrier.[59] Ion injection and penetration has been improved by replacing alkyl side chains with polar side chains on the same backbone. For example, changing the alkyl:glycol chain ratio has enabled a customization on an NDI-T2 backbone to facilitate either 2D operation in OFETs, or 3D operation in OECTs. (Figure 18a). When functionalized with alkyl side chains, n-type NDI-T2 backbone will perform well in OFETs. However, its hydrophobicity prevents it from functioning with mixed electronic-ionic transport. Therefore, by introducing a range of ratios of ethylene-glycol side chains to the alkylated NDI-T2, electrochemical doping and ionic transport is facilitated, (enhanced charging at lower reduction potentials as the ratio of glycol-side chains is increased), allowing operation in OECTs.[117] Interestingly, the optimum ratio was found to be 90% glycol and 10% alkyl, the polymer known as P-90, and one of the most reported n-type OECT materials. (Figure 18b). Although swelling (the degree of ion uptake) was enhanced by increasing the glycol chain ratio, and therefore ion transport, but that came at the expense of charge transport properties. A drop of electron mobility was found as the alkyl chain ratio decreases.[117] Also in another study, over-swelling was found to limit electrochemical reversibility,[118]as shown in Figure 18c, suggesting a careful control of the alkyl:glycol ratio to favor ion injection, electron transport, and electrochemical reversibility simultaneously.

c) charge carrier transport

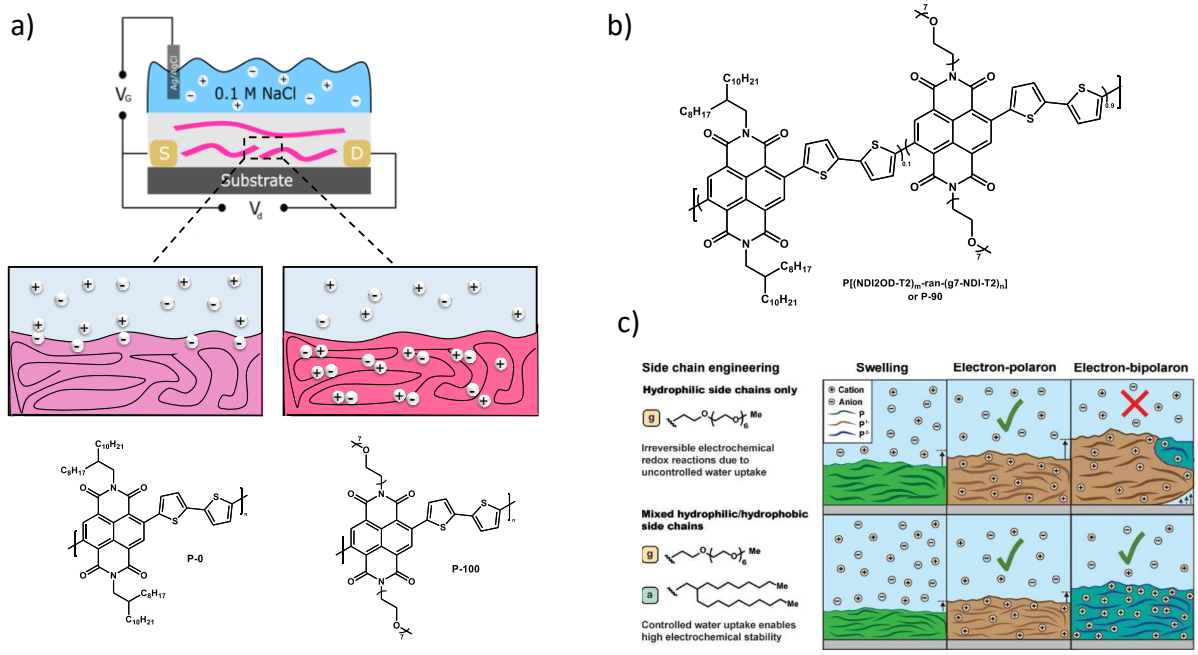


Figure 18. Improving ion injection in n-type polymers. a) Structures of the all alkyl material (P-0) and all glycol material (P-100) and schematic illustrations of their operation. b) Polymer structure of mixed alkyl-glycol polymer (P-90). c) Schematic illustration of the electrochemical reversibility of all glycol vs mixed alkyl-glycol NDI-based polymers. Figure a) is adapted from ref. 94. Figure c) is reproduced with permission from ref. 118.

Factors affecting charge transport (intrinsic polymer properties and device-processing parameters) have been extensively discussed in Section 1.4.1. In both OTEs and OECTs, charge delocalization is required for an efficient electron transport. Early developed n-type polymers are composed of D-A building blocks. As mentioned earlier, because of the large torsional angle between the donor and acceptor building blocks, LUMO orbitals were localized on the acceptor unit, which hinder both charge delocalization and achieving deep LUMO levels. To enhance charge delocalization, donor engineering is one of the effective strategies. For example, modifying the donor moiety to feature functional groups that would promote backbone planarity through intra-chain van der wall interactions. For example, by replacing the bithiophene (2T) in the typical NDI polymer, P(NDI2OD-T2), with bithiazole (2Zt), have resulted in less steric repulsion between the two monomers, giving rise to greater backbone planarity, and hence enhanced intermolecular interactions. (Figure 19a). Also, bithiazole

enhances the electron affinity and therefore reduces the D-A character. When n-doped, P(NDI2OD-Tz2) yielded higher electrical conductivities and power factors than those of analogous P(NDI2OD-T2).[28] Another approach to backbone planarity was achieved by extending the core of (NDI) unit to naphthodithiophene diimide (NDTI), the resulting polymer showed a more planar backbone and closer polymer packing, leading to more than two orders of magnitude higher electron mobility in OECTs. (Figure 19b). The backbone planarity, which promotes charge delocalization, also comes with the benefit of lowering the LUMO level, which therefore also enabled a stable OECT performance.[112] While reducing D-A character as well as enhancing backbone coplanarity has proven to enhance the electrical conductivity in NDI-based polymer, another class of polymers has facilitated charge delocalization in n-type polymers by means of a rigid/fused backbone. For example, ladder-type polymer polybenzimidazobenzophenanthroline, (BBL) shows high electrical conductivity in thermoelectrics up to 2.4 S $cm^{-1}$, when n-doped. When compared with the widely used P(NDI2ODT2) polymer, BBL exhibited a more extended polaron delocalization length due to its nearly torsion-free backbone.[38] BBL has also shown to be an efficient n-type OECT material, delivering a normalized transconductance ($g_m$) that surpasses that of the most high-performing NDI-based polymers with similar thickness by a factor of 2.5, and the highest reported volumetric capacitance to date, with a value of 930 F $cm^{-3}$.[87] (Figure 19c). This was ascribed to the absence of side chains which allows the material to store charge closer to the backbone, when compared with side-chain composed NDI-based polymers. Moreover, the high rigidity has enabled high electron affinity (-4.15 eV),[119] and therefore, BBL-based OECT devices have shown water stable operation. However, due to lack of side-chains, BBL requires film deposition using aggressive solvents such as methanesulfonic acid (MSA), which requires careful purification to remove residual acids. A new approach to achieve rigidity, solubility, all A-A character, and high electron affinity, was reported by the McCulloch group in 2018.

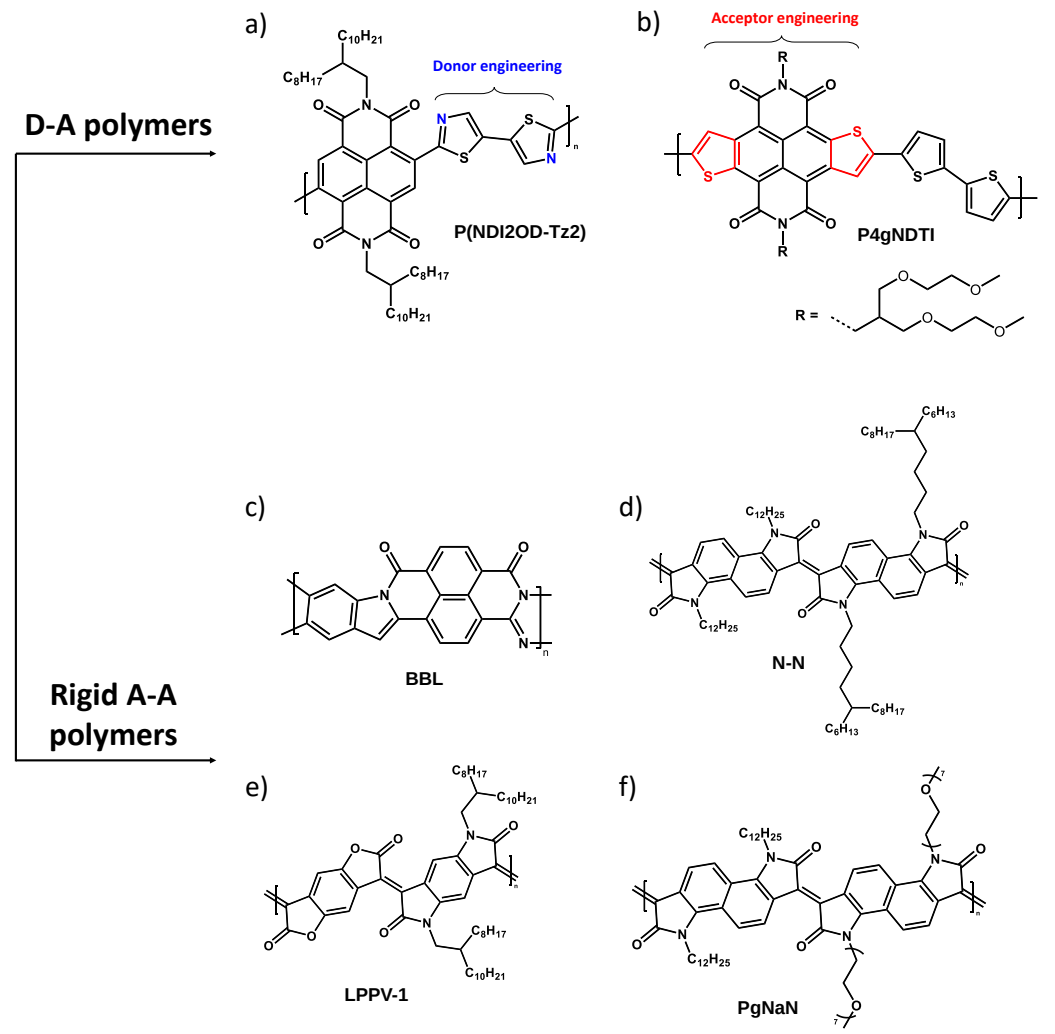


Figure 19. Design strategies to enhance polaron delocalization in D-A and A-A polymers

The report involved a series of fused lactam n-type polymers featuring air stable electron transport in OFETs. These polymer are composed of electron-deficient bis-lactam units, connected together by a double bond to allow a locked conformation with nearly no free rotation, and hence low energetic disorders. The first example of fused lactam polymers in OTEs, were reported by Chen Hu et. al, exhibiting electrical conductivities and power factors as high as 0.65 S $cm^{-1}$ , and 3.2 μW $m^{-1}$ $K^{-2}$, respectively for N-N polymer.[120] (Figure 19d). When a mixture of fused lactam and lactone were polymerized, LPVV-1 exhibited high conductivity and power factor of up to 1.1 S $cm^{-1}$ , and 1.96 μW $m^{-1}$ $K^{-2}$, respectively, retaining 90% of the thermoelectric performance after 7 days of exposure to air, due to deep

LUMO level of -4.5 eV.[82] (Figure 19e). In OECT, the first example of fused lactam polymer, PgNaN, with a mixture of alkylated and glycolated side chains, have delivered a state-of-the-art OECT performance, with normalized transconductance ($g_m$) of 0.2 S $cm^{-1}$, and $\mu C^*$of 0.66 F $cm^{-1}$ $s^{-1}$, near the performance of state-of-the-art, BBL. [121] (Figure 19f).

One more factor that limit charge transport in OTEs, is counterion effect. After doping with molecular dopants, the transport of generated polarons/bipolarons could be hindered by the columbic attractions between the ionized dopant and polaron/bipolarons, also known as carrier-dopant interactions. Unfortunately, these attractions are strong due to the low dielectric constant of organic semiconductors, such that columbic interactions might act as a trap of charge carriers, thus hindering mobility, and thus high conductivity. Efforts to overcome this limitation involved the control of dopant location within the polymer. One example is reported by J. A. Koster group, where they found an enhanced number of free charge carriers by a deliberate control of polymer packing density to overcome columbic interaction. (Figure 20a) This was enabled by (PDTzTI), a recently developed acceptor–acceptor (A–A) homopolymer.[122] Unlike P(NDI2ODT2), PDTzTI chains was found to pack into larger crystalline domains, which keep the ionized dopants far from the polaron/bipolarons on the polymer chains, leading to counter-ion-trap-free interchain transport. This strategy has enabled PDTzTI with 500 times higher electrical conductivity, with power factors as high as 7.6 μW $m^{-1}$ $K^{-2}$. Another way to control the dopant location, by keeping away from the charge-carrying polymer chain, was achieved by tailoring the side chains. J. A. Koster group, developed NDI-based polymers with amphipathic side chain that contains an alkyl chain as a spacer between the polymer backbone and an ethylene glycol type chain. (Figure 20b). The use of this alkyl spacer helped control the dopant sites away from the backbone, thus minimizing the influence of counterions.[123] This approach was used to enhance the thermoelectric performance by selectively increasing the Seebeck coefficient, which enabled power factors of 18 μW $m^{-1}$ $K^{-2}$.

## Design strategies to overcome columbic interactions (controlling dopant location)

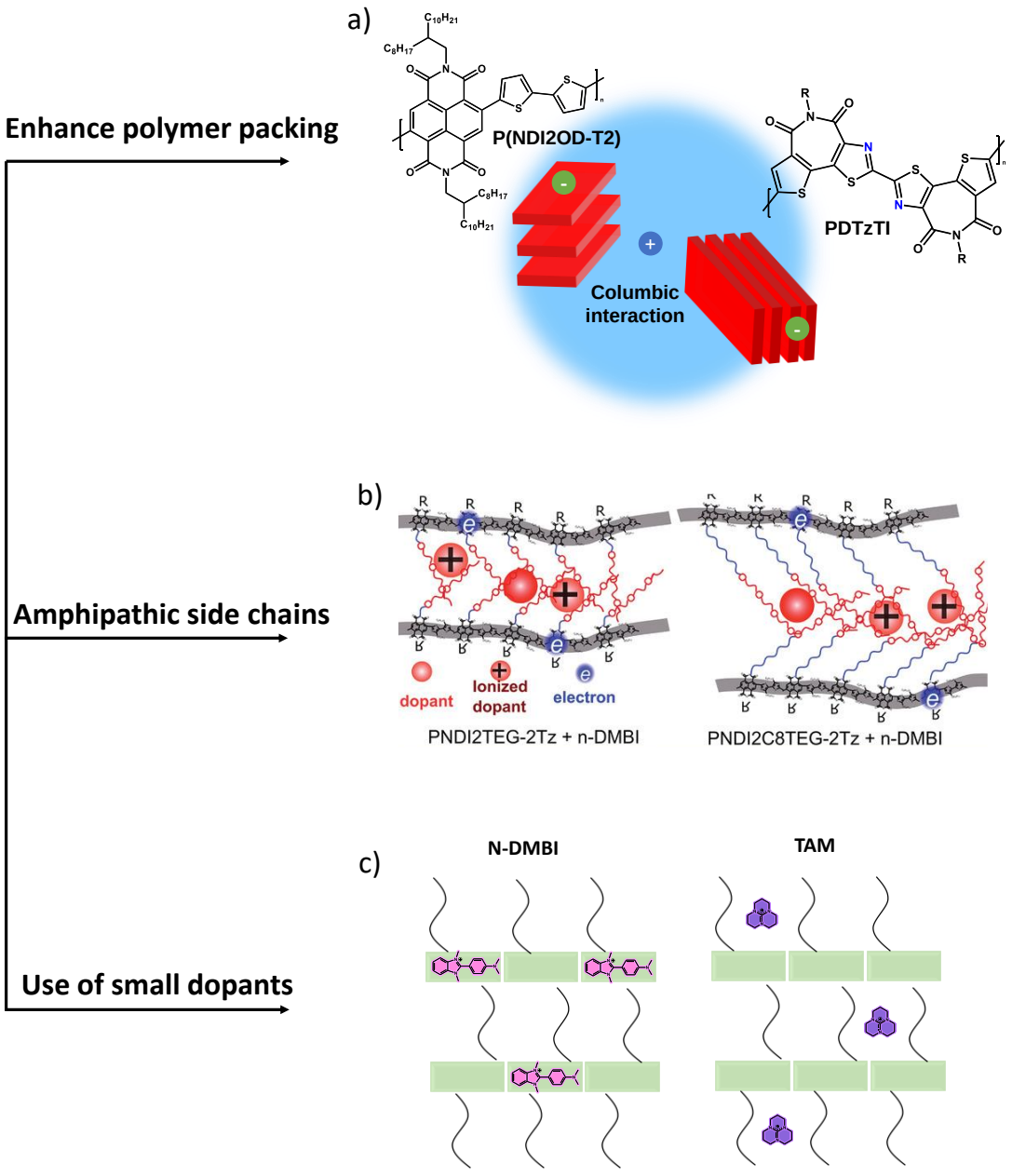


Figure 20. Summary of chemical design strategies to overcome columbic interactions. Figures a and c are adapted from ref. 122 and 82. Figure b is reproduced with permission from ref 123.

A similar target of keeping the dopant away from the backbone, was accomplished by Jian Pei's group, by the use of small dopant (TAM).[82] Unlike the widely used n-dopant, N-DMBI, TAM was found to negligibly perturb the polymer microstructure and ordering. After doping,

the ionized dopant exhibited weak affinity to the π-backbone, but strong affinity to side chains. Thus, reducing polymer-dopant columbic interactions, enabling excellent conductivity of up to 22 S $cm^{-1}$ and a power factor of 80 μ$Wm^{-1}$ $K^{-2}$, without sacrificing the Seebeck coefficient. (Figure 20c). In summary, the above approaches provides a route to overcome the trade-off between electrical conductivity and the Seebeck coefficient, resulting in a higher power factor. A summary of the joint chemical design strategies to optimize the performance of both OTEs and OECTs are summarized in Table. 1.

Table 1. A summary of joint design approaches for OTEs and OECTs

| | **Factors to consider** | | **Joint design approach** |
|---|---|---|---|
| **Challenge** | **OTEs** | **OECTs** | |
| **Charge carrier generation** | • Polymer-dopant energy level match<br>• Dopant miscibility | • Electron injection<br>• Ion Injection | • Lower LUMO<br>• Enhance hydrophilicity/polarity |
| | | | |
| **Charge carrier transport** | • Counterion effect (columbic attractions)<br>• Charge delocalization | Charge delocalization | • Locking conformation (Backbone planarity) |
| | | | |
| **Ambient stability** | Charge delocalization | Charge delocalization | • Locking conformation (Backbone planarity)<br>• Lower LUMO |
| | | | |

## 1.5. Thesis aims and overview

The overall aim of this work is to develop n-type conjugated polymers with high electrical conductivities for organic thermoelectric applications and for bioelectronics applications based on organic electrochemical transistors (OECTs). High performing n-type conjugated polymers are of crucial importance in organic thermoelectrics in order to develop efficient thermoelectric generators where both p-type and n-type operating elements are of equal performance. The

inferior performance of n-type polymers has also limited the development of electron-transfer based biosensors and complementary circuits in bioelectronics. When this project was initiated, the field was missing n-type polymers with high conductivities, which was mainly ascribed to the EA of the literature n-type materials, and to the poor charge delocalization. Therefore, this work aimed to tackle those challenges by synthesizing and investigating a series of n-type polymers while establishing structure-property relationships. The polymer series investigated in this work are comprised of A-A motifs, with a highly rigid backbone. The polymers are synthesized using metal-free aldol condensation polymerization that eliminate the use of toxic organostannane and the expensive palladium catalysts used in cross-coupling polymerizations. This aldol polymerization has only water as the by-product, with no need for complex subsequent purifications steps. This class of polymers are therefore ideal candidates for applications in biological interfaces, and human-body interactive wearable electronics. The main aim of this work is to enhance the electrical conductivity of n-type polymers by developing n-type polymers with high electron affinity. This goal was pursued by introducing the lactone unit into the recently developed fused polymer based on lactam, in order to enhance the electron-deficiency of the conjugated backbone. While doing so, an understanding of the effect of backbone core extension/contraction and side chain engineering on achieving the desired high EA and charge delocalization was developed.

**Chapter 2** presents a series of three fused electron-deficient copolymers, where the electron withdrawing lactone unit was first incorporated along the backbone. In the parent fused lactam series paper, it was concluded that an aromatic core extension from phenyl to naphthalene has enhanced the transport properties. This chapter examines the effect of the core extension of the lactone unit on the EA, combined with exploring the effect of side chain length on the polymer film microstructure, and how both ultimately impact the thermoelectric performance.

**Chapter 3** takes notes from the findings in chapter 2 and in literature, by developing three random copolymers with a rational chemical design to further optimize backbone planarity, which will improve the extent of charge delocalization, and the latter's effect on enhancing EA and air stability. Also enhancing the doping efficiency through glycol side-chain functionalization. This chapter presents new insights into material design guidelines for the future development of high performing n-type organic thermoelectrics with improved air stability.

The design strategies presented in the first two chapters attempted to improve thermoelectric performance while focusing on maximizing the electrical conductivity to enhance thermoelectric power factor (PF). Optimizing Seebeck coefficient does not lie within the scope of this work.

**Chapter 4** leverages the progress made in chapter 1 and 2, and explores the employment of the developed materials in bioelectronic applications. A key challenge in the development of n-type conjugated polymers for high performance electrochemical transistors, is their stable performance in ambient conditions. In this chapter, we evaluate the impact of one of the reactions of electrons with molecular oxygen, namely the formation of superoxide radical anions, on the OECT performance. This chapter demonstrates a general design methodology for avoiding detrimental parasitic reactions under ambient conditions, as well as the benefits that result in improved OECT performance.

## 1.6. References


1. Koch N. Organic electronic devices and their functional interfaces. *Chemphyschem* 2007, **8**(10)**:** 1438-1455.

2. Santato C, Cicoira F. Organic Electronics Emerging Concepts and Technologies Preface. *Organic Electronics: Emerging Concepts and Technologies* 2013**:** Xiii-Xiii.

3. Rivnay J, Inal S, Salleo A, Owens RM, Berggren M, Malliaras GG. Organic electrochemical transistors. *Nature Reviews Materials* 2018, **3**(2).

4. Russ B, Glaudell A, Urban JJ, Chabinyc ML, Segalman RA. Organic thermoelectric materials for energy harvesting and temperature control. *Nature Reviews Materials* 2016, **1**(10).

5. Bubnova O, Crispin X. Towards polymer-based organic thermoelectric generators. *Energy & Environmental Science* 2012, **5**(11).

6. Maria IP. Developing organic semiconductors with mixed ionic and electronic transport for organic bioelectronics. 2020.

7. Chiang CK, Fincher CR, Park YW, Heeger AJ, Shirakawa H, Louis EJ, *et al.* Electrical-Conductivity in Doped Polyacetylene. *Physical Review Letters* 1977, **39**(17)**:** 1098-1101.

8. Shirakawa H. The discovery of polyacetylene film: The dawning of an era of conducting polymers (Nobel lecture). *Angew Chem-Int Edit* 2001, **40**(14)**:** 2575-2580.

9. Bronstein H, Nielsen CB, Schroeder BC, McCulloch I. The role of chemical design in the performance of organic semiconductors. *Nature Reviews Chemistry* 2020.

10. Ding L, Yu ZD, Wang XY, Yao ZF, Lu Y, Yang CY, *et al.* Polymer Semiconductors: Synthesis, Processing, and Applications. *Chemical Reviews* 2023, **123**(12)**:** 7421-7497.

11. Lussem B, Riede M, Leo K. Doping of organic semiconductors. *Phys Status Solidi A* 2013, **210**(1)**:** 9-43.

12. Blom PW. Polymer electronics: To be or not to be? *Advanced Materials Technologies* 2020, **5**(6)**:** 2000144.

13. Li JT, Lei T. Recent Progress on Addressing the Key Challenges in Organic Thermoelectrics. *Chem Asian J* 2021, **16**(12)**:** 1508-1518.

14. Kroon R, Mengistie DA, Kiefer D, Hynynen J, Ryan JD, Yu L, *et al.* Thermoelectric plastics: from design to synthesis, processing and structure-property relationships. *Chem Soc Rev* 2016, **45**(22)**:** 6147-6164.

15. Goel M, Thelakkat M. Polymer Thermoelectrics: Opportunities and Challenges. *Macromolecules* 2020, **53**(10)**:** 3632-3642.

16. Heeger AJ. Semiconducting and metallic polymers: The fourth generation of polymeric materials. *Journal of Physical Chemistry B* 2001, **105**(36)**:** 8475-8491.

17. Zhao W, Ding J, Zou Y, Di CA, Zhu D. Chemical doping of organic semiconductors for thermoelectric applications. *Chem Soc Rev* 2020, **49**(20)**:** 7210-7228.

18. Kergoat L, Piro B, Berggren M, Horowitz G, Pham M-C. Advances in organic transistor-based biosensors: from organic electrochemical transistors to electrolyte-gated organic field-effect transistors. *Analytical and bioanalytical chemistry* 2012, **402:** 1813-1826.

19. Singh TB, Sariciftci NS. Progress in plastic electronics devices. *Annual Review of Materials Research* 2006, **36:** 199-230.

20. Cowen LM, Atoyo J, Carnie MJ, Baran D, Schroeder BC. Review—Organic Materials for Thermoelectric Energy Generation. *ECS Journal of Solid State Science and Technology* 2017, **6**(3)**:** N3080-N3088.

21. Boyle CJ, Upadhyaya M, Wang PJ, Renna LA, Lu-Diaz M, Jeong SP, *et al.* Tuning charge transport dynamics via clustering of doping in organic semiconductor thin films. *Nature Communications* 2019, **10**.

22. Yamamoto J, Furukawa Y. Electronic and Vibrational Spectra of Positive Polarons and Bipolarons in Regioregular Poly(3-hexylthiophene) Doped with Ferric Chloride. *Journal of Physical Chemistry B* 2015, **119**(13)**:** 4788-4794.

23. Hynynen J, Kiefer D, Muller C. Influence of crystallinity on the thermoelectric power factor of P3HT vapour-doped with F4TCNQ. *RSC Adv* 2018, **8**(3)**:** 1593-1599.

24. Patel SN, Glaudell AM, Peterson KA, Thomas EM, O'Hara KA, Lim E, *et al.* Morphology controls the thermoelectric power factor of a doped semiconducting polymer. *Science Advances* 2017, **3**(6).

25. Jia H, Lei T. Emerging research directions for n-type conjugated polymers. *Journal of Materials Chemistry C* 2019, **7**(41)**:** 12809-12821.

26. deLeeuw DM, Simenon MMJ, Brown AR, Einerhand REF. Stability of n-type doped conducting polymers and consequences for polymeric microelectronic devices. *Synthetic Metals* 1997, **87**(1)**:** 53-59.

27. Wei P, Oh JH, Dong GF, Bao ZN. Use of a 1H-Benzoimidazole Derivative as an n-Type Dopant and To Enable Air-Stable Solution-Processed n-Channel Organic Thin-Film Transistors. *Journal of the American Chemical Society* 2010, **132**(26)**:** 8852-+.

28. Wang SH, Sun HD, Erdmann T, Wang G, Fazzi D, Lappan U, *et al.* A Chemically Doped Naphthalenediimide-Bithiazole Polymer for n-Type Organic Thermoelectrics. *Advanced Materials* 2018, **30**(31).

29. Kim J, Khim D, Baeg KJ, Park WT, Lee SH, Kang M, *et al.* Systematic Study of Widely Applicable N-Doping Strategy for High-Performance Solution-Processed Field-Effect Transistors. *Advanced Functional Materials* 2016, **26**(43)**:** 7886-7894.

30. Yang CY, Ding YF, Huang DZ, Wang J, Yao ZF, Huang CX, *et al.* A thermally activated and highly miscible dopant for n-type organic thermoelectrics. *Nature Communications* 2020, **11**(1).

31. Bredas JL, Street GB. Polarons, Bipolarons, and Solitons in Conducting Polymers. *Accounts of Chemical Research* 1985, **18**(10)**:** 309-315.

32. Xiong M, Wang J-Y, Pei J. Controlling the Film Microstructure in Organic Thermoelectrics. *Organic Materials* 2021, **03**(01)**:** 001-016.

33. Scaccabarozzi AD, Basu A, Anies F, Liu J, Zapata-Arteaga O, Warren R, *et al.* Doping Approaches for Organic Semiconductors. *Chem Rev* 2022, **122**(4)**:** 4420-4492.

34. Fratini S, Nikolka M, Salleo A, Schweicher G, Sirringhaus H. Charge transport in high-mobility conjugated polymers and molecular semiconductors. *Nature Materials* 2020, **19**(5)**:** 491-502.

35. Zhao XG, Zhan XW. Electron transporting semiconducting polymers in organic electronics. *Chem Soc Rev* 2011, **40**(7)**:** 3728-3743.

36. Rivnay J, Mannsfeld SCB, Miller CE, Salleo A, Toney MF. Quantitative Determination of Organic Semiconductor Microstructure from the Molecular to Device Scale. *Chemical Reviews* 2012, **112**(10)**:** 5488-5519.

37. Nakano M, Sawamoto M, Yuki M, Takimiya K. N,N '-Unsubstituted Naphthodithiophene Diimide: Synthesis and Derivatization via N-Alkylation and -Arylation. *Organic Letters* 2016, **18**(15)**:** 3770-3773.

38. Wang S, Sun H, Ail U, Vagin M, Persson PO, Andreasen JW, *et al.* Thermoelectric Properties of Solution-Processed n-Doped Ladder-Type Conducting Polymers. *Adv Mater* 2016, **28**(48)**:** 10764-10771.

39. Lu Y, Wang J-Y, Pei J. Strategies To Enhance the Conductivity of n-Type Polymer Thermoelectric Materials. *Chemistry of Materials* 2019, **31**(17)**:** 6412-6423.

40. McDermott AG, DesLauriers PJ, Fodor JS, Jones RL, Snyder CR. Measuring Tie Chains and Trapped Entanglements in Semicrystalline Polymers. *Macromolecules* 2020, **53**(13)**:** 5614-5626.

41. Himmelberger S, Vandewal K, Fei ZP, Heeney M, Salleo A. Role of Molecular Weight Distribution on Charge Transport in Semiconducting Polymers. *Macromolecules* 2014, **47**(20)**:** 7151-7157.

42. Gu KC, Loo YL. The Polymer Physics of Multiscale Charge Transport in Conjugated Systems. *J Polym Sci Pol Phys* 2019, **57**(23)**:** 1559-1571.

43. Osaka I, Takimiya K. Backbone orientation in semiconducting polymers. *Polymer* 2015, **59:** A1-A15.

44. Skrypnychuk V, Wetzelaer GJAH, Gordiichuk PI, Mannsfeld SCB, Herrmann A, Toney MF, *et al.* Ultrahigh Mobility in an Organic Semiconductor by Vertical Chain Alignment. *Advanced Materials* 2016, **28**(12)**:** 2359-2366.

45. Sirringhaus H, Brown PJ, Friend RH, Nielsen MM, Bechgaard K, Langeveld-Voss BMW, *et al.* Two-dimensional charge transport in self-organized, high-mobility conjugated polymers. *Nature* 1999, **401**(6754)**:** 685-688.

46. Coropceanu V, Cornil J, da Silva DA, Olivier Y, Silbey R, Bredas JL. Charge transport in organic semiconductors. *Chemical Reviews* 2007, **107**(4)**:** 926-952.

47. Freer R, Powell AV. Realising the potential of thermoelectric technology: a Roadmap. *Journal of Materials Chemistry C* 2020, **8**(2)**:** 441-463.

48. Forman C, Muritala IK, Pardemann R, Meyer B. Estimating the global waste heat potential. *Renew Sust Energ Rev* 2016, **57:** 1568-1579.

49. Beretta D, Neophytou N, Hodges JM, Kanatzidis MG, Narducci D, Martin-Gonzalez M, *et al.* Thermoelectrics: From history, a window to the future. *Mat Sci Eng R* 2019, **138:** 210-255.

50. Freer R, Ekren D, Ghosh T, Biswas K, Qiu PF, Wan S, *et al.* Key properties of inorganic thermoelectric materials-tables (version 1). *J Phys-Energy* 2022, **4**(2).

51. Wang SH, Zuo GZ, Kim J, Sirringhaus H. Progress of Conjugated Polymers as Emerging Thermoelectric Materials. *Progress in Polymer Science* 2022, **129**.

52. Zhang Q, Sun Y, Xu W, Zhu D. Organic thermoelectric materials: emerging green energy materials converting heat to electricity directly and efficiently. *Adv Mater* 2014, **26**(40)**:** 6829-6851.

53. Bharti M, Singh A, Samanta S, Aswal DK. Conductive polymers for thermoelectric power generation. *Progress in Materials Science* 2018, **93:** 270-310.

54. Nandihalli N. A short account of thermoelectric film characterization techniques. *Materials Today Physics* 2023**:** 101173.

55. Park T, Park C, Kim B, Shin H, Kim E. Flexible PEDOT electrodes with large thermoelectric power factors to generate electricity by the touch of fingertips. *Energy & Environmental Science* 2013, **6**(3)**:** 788-792.

56. Kim GH, Shao L, Zhang K, Pipe KP. Engineered doping of organic semiconductors for enhanced thermoelectric efficiency. *Nature Materials* 2013, **12**(8)**:** 719-723.

57. Paulsen BD, Tybrandt K, Stavrinidou E, Rivnay J. Organic mixed ionic-electronic conductors. *Nat Mater* 2020, **19**(1)**:** 13-26.

58. White HS, Kittlesen GP, Wrighton MS. Chemical Derivatization of an Array of 3 Gold Microelectrodes with Polypyrrole - Fabrication of a Molecule-Based Transistor. *Journal of the American Chemical Society* 1984, **106**(18)**:** 5375-5377.

59. Sun H, Gerasimov J, Berggren M, Fabiano S. n-Type organic electrochemical transistors: materials and challenges. *Journal of Materials Chemistry C* 2018, **6**(44)**:** 11778-11784.

60. Torricelli F, Adrahtas DZ, Bao Z, Berggren M, Biscarini F, Bonfiglio A, *et al.* Electrolyte-gated transistors for enhanced performance bioelectronics. *Nature Reviews Methods Primers* 2021, **1**(1).

61. Strakosas X, Bongo M, Owens RM. The organic electrochemical transistor for biological applications. *Journal of Applied Polymer Science* 2015, **132**(15)**:** n/a-n/a.

62. Inal S, Rivnay J, Leleux P, Ferro M, Ramuz M, Brendel JC, *et al.* A High Transconductance Accumulation Mode Electrochemical Transistor. *Advanced Materials* 2014, **26**(44)**:** 7450-7455.

63. Ohayon D, Druet V, Inal S. A guide for the characterization of organic electrochemical transistors and channel materials. *Chem Soc Rev* 2023, **52**(3)**:** 1001-1023.

64. Bernards DA, Malliaras GG. Steady-state and transient behavior of organic electrochemical transistors. *Advanced Functional Materials* 2007, **17**(17)**:** 3538-3544.

65. Inal S, Malliaras GG, Rivnay J. Benchmarking organic mixed conductors for transistors. *Nature Communications* 2017, **8**.

66. Tsumura A, Koezuka H, Ando T. Macromolecular Electronic Device - Field-Effect Transistor with a Polythiophene Thin-Film. *Applied Physics Letters* 1986, **49**(18)**:** 1210-1212.

67. Jurchescu OD, Popinciuc M, van Wees BJ, Palstra TTM. Interface-controlled, high-mobility organic transistors. *Advanced Materials* 2007, **19**(5)**:** 688-692.

68. Yao YF, Dong HL, Liu F, Russell TP, Hu WP. Approaching Intra- and Interchain Charge Transport of Conjugated Polymers Facilely by Topochemical Polymerized Single Crystals. *Advanced Materials* 2017, **29**(29).

69. Paterson AF, Singh S, Fallon KJ, Hodsden T, Han Y, Schroeder BC, *et al.* Recent Progress in High-Mobility Organic Transistors: A Reality Check. *Advanced Materials* 2018, **30**(36).

70. Wang Y, Liu Y. Insight into conjugated polymers for organic electrochemical transistors. *Trends in Chemistry* 2023.

71. Kim DH, Lee J, Park JI, Chung JW, Lee WH, Giri G, *et al.* Molecular Weight-Induced Structural Transition of Liquid-Crystalline Polymer Semiconductor for High-Stability Organic Transistor. *Advanced Functional Materials* 2011, **21**(23)**:** 4442-4447.

72. Kline RJ, McGehee MD, Kadnikova EN, Liu JS, Fréchet JMJ. Controlling the field-effect mobility of regioregular polythiophene by changing the molecular weight. *Advanced Materials* 2003, **15**(18)**:** 1519-+.

73. Nahid MM, Matsidik R, Welford A, Gann E, Thomsen L, Sommer M, *et al.* Unconventional Molecular Weight Dependence of Charge Transport in the High Mobility n-type Semiconducting Polymer P(NDI2OD-T2). *Advanced Functional Materials* 2017, **27**(9).

74. Onwubiko A, Yue W, Jellett C, Xiao MF, Chen HY, Ravva MK, *et al.* Fused electron deficient semiconducting polymers for air stable electron transport. *Nature Communications* 2018, **9**.

75. Schroeder BC, Kurosawa T, Fu TR, Chiu YC, Mun J, Wang GJN, *et al.* Taming Charge Transport in Semiconducting Polymers with Branched Alkyl Side Chains. *Advanced Functional Materials* 2017, **27**(34).

76. Kawabata K, Saito M, Takemura N, Osaka I, Takimiya K. Effects of branching position of alkyl side chains on ordering structure and charge transport property in thienothiophenedione- and quinacridone-based semiconducting polymers. *Polymer Journal* 2017, **49**(1)**:** 169-176.

77. Hallani RK, Paulsen BD, Petty AJ, Sheelamanthula R, Moser M, Thorley KJ, *et al.* Regiochemistry-Driven Organic Electrochemical Transistor Performance Enhancement in Ethylene Glycol-Functionalized Polythiophenes. *Journal of the American Chemical Society* 2021, **143**(29)**:** 11007-11018.

78. Yang YZ, Liu ZT, Zhang GX, Zhang XS, Zhang DQ. The Effects of Side Chains on the Charge Mobilities and Functionalities of Semiconducting Conjugated Polymers beyond Solubilities. *Advanced Materials* 2019, **31**(46).

79. Zheng YQ, Yao ZF, Lei T, Dou JH, Yang CY, Zou L, *et al.* Unraveling the Solution-State Supramolecular Structures of Donor-Acceptor Polymers and their Influence on Solid-State Morphology and Charge-Transport Properties. *Advanced Materials* 2017, **29**(42).

80. Wu HY, Yang CY, Li QF, Kolhe NB, Strakosas X, Stoeckel MA, *et al.* Influence of Molecular Weight on the Organic Electrochemical Transistor Performance of Ladder-Type Conjugated Polymers. *Advanced Materials* 2022, **34**(4).

81. Wang SH, Sun HD, Ail U, Vagin M, Persson POÅ, Andreasen JW, *et al.* Thermoelectric Properties of Solution-Processed n-Doped Ladder-Type Conducting Polymers. *Advanced Materials* 2016, **28**(48)**:** 10764-+.

82. Lu Y, Yu ZD, Zhang RZ, Yao ZF, You HY, Jiang L, *et al.* Rigid Coplanar Polymers for Stable n-Type Polymer Thermoelectrics. *Angew Chem-Int Edit* 2019, **58**(33)**:** 11390-11394.

83. Yan XW, Xiong M, Li JT, Zhang S, Ahmad Z, Lu Y, *et al.* Pyrazine-Flanked Diketopyrrolopyrrole (DPP): A New Polymer Building Block for High-Performance n-Type Organic Thermoelectrics. *Journal of the American Chemical Society* 2019, **141**(51)**:** 20215-20221.

84. Griggs S, Marks A, Meli D, Rebetez G, Bardagot O, Paulsen BD, *et al.* The effect of residual palladium on the performance of organic electrochemical transistors. *Nature Communications* 2022, **13**(1).

85. Druet V, Nayak PD, Koklu A, Ohayon D, Hama A, Chen XX, *et al.* Operation Mechanism of n-Type Organic Electronic Metabolite Sensors. *Advanced Electronic Materials* 2022, **8**(10).

86. Lee SW, Lee KY, Song YW, Choi WK, Chang J, Yi H. Direct Electron Transfer of Enzymes in a Biologically Assembled Conductive Nanomesh Enzyme Platform. *Advanced Materials* 2016, **28**(8)**:** 1577-1584.

87. Sun HD, Vagin M, Wang SH, Crispin X, Forchheimer R, Berggren M, *et al.* Complementary Logic Circuits Based on High-Performance n-Type Organic Electrochemical Transistors. *Advanced Materials* 2018, **30**(9).

88. Li XY, Li YL, Sarang K, Lutkenhaus J, Verduzco R. Side-Chain Engineering for High-Performance Conjugated Polymer Batteries. *Advanced Functional Materials* 2021, **31**(14).

89. Liang Y, Chen Z, Jing Y, Rong Y, Facchetti A, Yao Y. Heavily n-dopable π-conjugated redox polymers with ultrafast energy storage capability. *Journal of the American Chemical Society* 2015, **137**(15)**:** 4956-4959.

90. Liang YL, Zhang P, Chen J. Function-oriented design of conjugated carbonyl compound electrodes for high energy lithium batteries. *Chemical Science* 2013, **4**(3)**:** 1330-1337.

91. Jones BA, Facchetti A, Wasielewski MR, Marks TJ. Tuning orbital energetics in arylene diimide semiconductors. Materials design for ambient stability of n-type charge transport. *Journal of the American Chemical Society* 2007, **129**(49)**:** 15259-15278.

92. Zhan XW, Facchetti A, Barlow S, Marks TJ, Ratner MA, Wasielewski MR, *et al.* Rylene and Related Diimides for Organic Electronics. *Advanced Materials* 2011, **23**(2)**:** 268-284.

93. Usta H, Risko C, Wang ZM, Huang H, Deliomeroglu MK, Zhukhovitskiy A, *et al.* Design, Synthesis, and Characterization of Ladder-Type Molecules and Polymers. Air-Stable, Solution-Processable n-Channel and Ambipolar Semiconductors for Thin-Film Transistors via Experiment and Theory. *Journal of the American Chemical Society* 2009, **131**(15)**:** 5586-5608.

94. Griggs S, Marks A, Bristow H, McCulloch I. n-Type organic semiconducting polymers: stability limitations, design considerations and applications. *J Mater Chem C Mater* 2021, **9**(26)**:** 8099-8128.

95. Ke Z, Abtahi A, Hwang J, Chen K, Chaudhary J, Song I, *et al.* Highly Conductive and Solution-Processable n-Doped Transparent Organic Conductor. *J Am Chem Soc* 2023, **145**(6)**:** 3706-3715.

96. Wood PM. The Potential Diagram for Oxygen at Ph-7. *Biochemical Journal* 1988, **253**(1)**:** 287-289.

97. Giovannitti A, Rashid RB, Thiburce Q, Paulsen BD, Cendra C, Thorley K, *et al.* Energetic Control of Redox-Active Polymers toward Safe Organic Bioelectronic Materials. *Advanced Materials* 2020, **32**(16).

98. Jalilov AS, Nilewski LG, Berka V, Zhang CH, Yakovenko AA, Wu G, *et al.* Perylene Diimide as a Precise Graphene-like Superoxide Dismutase Mimetic. *Acs Nano* 2017, **11**(2)**:** 2024-2032.

99. Katz HE, Lovinger AJ, Johnson J, Kloc C, Siegrist T, Li W, *et al.* A soluble and air-stable organic semiconductor with high electron mobility. *Nature* 2000, **404**(6777)**:** 478-481.

100. Shao S, Liu J. Molecular Insights into n-Type Organic Thermoelectrics. *CCS Chemistry* 2021, **3**(10)**:** 2702-2716.

101. Guo XG, Watson MD. Conjugated Polymers from Naphthalene Bisimide. *Organic Letters* 2008, **10**(23)**:** 5333-5336.

102. Sommer M. Conjugated polymers based on naphthalene diimide for organic electronics. *Journal of Materials Chemistry C* 2014, **2**(17)**:** 3088-3098.

103. Nielsen CB, Turbiez M, McCulloch I. Recent Advances in the Development of Semiconducting DPP-Containing Polymers for Transistor Applications. *Advanced Materials* 2013, **25**(13)**:** 1859-1880.

104. Ding L, Wang ZY, Wang JY, Pei J. Organic Semiconducting Materials Based on BDOPV: Structures, Properties, and Applications. *Chinese Journal of Chemistry* 2019, **38**(1)**:** 13-24.

105. Shi K, Zhang FJ, Di CA, Yan TW, Zou Y, Zhou X, *et al.* Toward High Performance n-Type Thermoelectric Materials by Rational Modification of BDPPV Backbones. *Journal of the American Chemical Society* 2015, **137**(22)**:** 6979-6982.

106. Yan H, Chen ZH, Zheng Y, Newman C, Quinn JR, Dotz F, *et al.* A high-mobility electron-transporting polymer for printed transistors. *Nature* 2009, **457**(7230)**:** 679-U671.

107. Shi K, Zhang F, Di CA, Yan TW, Zou Y, Zhou X, *et al.* Toward High Performance n-Type Thermoelectric Materials by Rational Modification of BDPPV Backbones. *J Am Chem Soc* 2015, **137**(22)**:** 6979-6982.

108. Hwang YJ, Ren GQ, Murari NM, Jenekhe SA. n-Type Naphthalene Diimide-Biselenophene Copolymer for All-Polymer Bulk Heterojunction Solar Cells. *Macromolecules* 2012, **45**(22)**:** 9056-9062.

109. Hwang YJ, Murari NM, Jenekhe SA. New n-type polymer semiconductors based on naphthalene diimide and selenophene derivatives for organic field-effect transistors. *Polymer Chemistry* 2013, **4**(11)**:** 3187-3195.

110. Fukutomi Y, Nakano M, Hu JY, Osaka I, Takimiya K. Naphthodithiophenediimide (NDTI): Synthesis, Structure, and Applications. *Journal of the American Chemical Society* 2013, **135**(31)**:** 11445-11448.

111. Nakano M, Osaka I, Takimiya K. Naphthodithiophene Diimide (NDTI)-Based Semiconducting Copolymers: From Ambipolar to Unipolar n-Type Polymers. *Macromolecules* 2015, **48**(3)**:** 576-584.

112. Maria IP, Griggs S, Rashid RB, Paulsen BD, Surgailis J, Thorley K, *et al.* Enhancing the Backbone Coplanarity of n-Type Copolymers for Higher Electron Mobility and Stability in Organic Electrochemical Transistors. *Chemistry of Materials* 2022, **34**(19)**:** 8593-8602.

113. Dai Y-Z, Ai N, Lu Y, Zheng Y-Q, Dou J-H, Shi K, *et al.* Embedding electron-deficient nitrogen atoms in polymer backbone towards high performance n-type polymer field-effect transistors. *Chemical Science* 2016, **7**(9)**:** 5753-5757.

114. Shi YQ, Guo H, Qin MC, Zhao JY, Wang YX, Wang H, *et al.* Thiazole Imide-Based All-Acceptor Homopolymer: Achieving High-Performance Unipolar Electron Transport in Organic Thin-Film Transistors. *Advanced Materials* 2018, **30**(10).

115. Schlitz RA, Brunetti FG, Glaudell AM, Miller PL, Brady MA, Takacs CJ, *et al.* Solubility-Limited Extrinsic n-Type Doping of a High Electron Mobility Polymer for Thermoelectric Applications. *Advanced Materials* 2014, **26**(18)**:** 2825-2830.

116. Liu J, Qiu L, Alessandri R, Qiu X, Portale G, Dong J, *et al.* Enhancing Molecular n-Type Doping of Donor-Acceptor Copolymers by Tailoring Side Chains. *Adv Mater* 2018, **30**(7).

117. Giovannitti A, Maria IP, Hanifi D, Donahue MJ, Bryant D, Barth KJ, *et al.* The Role of the Side Chain on the Performance of N-type Conjugated Polymers in Aqueous Electrolytes. *Chem Mater* 2018, **30**(9)**:** 2945-2953.

118. Szumska AA, Maria IP, Flagg LQ, Savva A, Surgailis J, Paulsen BD, *et al.* Reversible Electrochemical Charging of n-Type Conjugated Polymer Electrodes in Aqueous Electrolytes. *J Am Chem Soc* 2021, **143**(36)**:** 14795-14805.

119. Xu K, Sun HD, Ruoko TP, Wang G, Kroon R, Kolhe NB, *et al.* Ground-state electron transfer in all-polymer donor-acceptor heterojunctions. *Nature Materials* 2020, **19**(7)**:** 738-+.

120. Chen H, Moser M, Wang S, Jellett C, Thorley K, Harrison GT, *et al.* Acene Ring Size Optimization in Fused Lactam Polymers Enabling High n-Type Organic Thermoelectric Performance. *J Am Chem Soc* 2020.

121. Chen X, Marks A, Paulsen BD, Wu R, Rashid RB, Chen H, *et al.* n-Type Rigid Semiconducting Polymers Bearing Oligo(Ethylene Glycol) Side Chains for High-Performance Organic Electrochemical Transistors. *Angew Chem Int Ed Engl* 2021, **60**(17)**:** 9368-9373.

122. Liu J, Shi Y, Dong J, Nugraha MI, Qiu X, Su M, *et al.* Overcoming Coulomb Interaction Improves Free-Charge Generation and Thermoelectric Properties for n-Doped Conjugated Polymers. *ACS Energy Letters* 2019, **4**(7)**:** 1556-1564.

123. Liu J, Ye G, Potgieser HGO, Koopmans M, Sami S, Nugraha MI, *et al.* Amphipathic Side Chain of a Conjugated Polymer Optimizes Dopant Location toward Efficient N-Type Organic Thermoelectrics. *Adv Mater* 2020**:** e2006694.

# Chapter 2

## The effect of aromatic ring size in electron deficient semiconducting polymers for n-type organic thermoelectrics

Disclaimer: The numbering of the headings in this chapter has been adjusted to adhere with the formatting used in this thesis, differing from the originally published manuscript and is the only adjustment made.

## 2.1 Abstract

N-type semiconducting polymers have been recently utilized in thermoelectric devices, however they have typically exhibited low electrical conductivities and poor device stability, in contrast to p-type semiconductors, which have been much higher performing. This is due in particular to the n-type semiconductor's low doping efficiency, and poor charge carrier mobility. Strategies to enhance the thermoelectric performance of n-type materials include optimizing the electron affinity (EA) with respect to the dopant to improve the doping process and increasing the charge carrier mobility through enhanced molecular packing. Here, we report the design, synthesis and characterization of fused electron-deficient n-type copolymers incorporating the electron withdrawing lactone unit along the backbone. The polymers were synthesized using metal-free aldol condensation conditions to explore the effect of enlarging the central phenyl ring to a naphthalene ring, on the electrical conductivity. When n-doped with N-DMBI, electrical conductivities of up to 0.28 S $cm^{-1}$, Seebeck coefficients of -75 μV $K^{-1}$ and maximum Power factors of 0.16 μW $m^{-1}$ $K^{-2}$ were observed from the polymer with the largest electron affinity of -4.68 eV. Extending the aromatic ring reduced the electron affinity, due to reducing the density of electron withdrawing groups and subsequently the electrical conductivity reduced by almost two orders of magnitude.

## Table of content

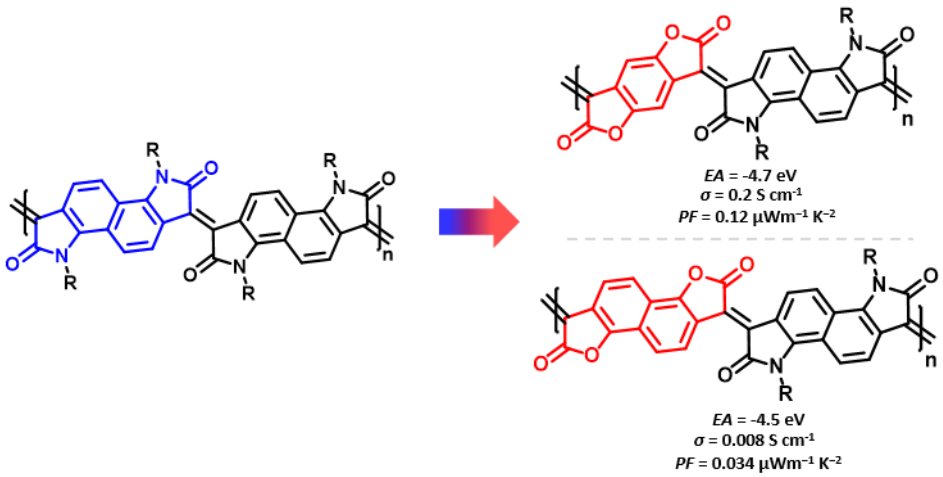

## 2.2 Introduction

Conjugated polymers play an essential role in the development of next-generation organic electronics.[1-3] Recently, they have been heavily exploited in the development of cost-competitive organic thermoelectric devices (OTE) that could be employed to convert waste thermal energy collected from mechanical, chemical, and electrical processes, into electricity[4]. Although developing OTE materials is still a work in progress especially for n-type OTE, the low cost, ease of fabrication, and high degree of flexibility offer π-conjugated polymers a potential advantage over other type of thermoelectric materials such as inorganic alloys (i.e., lead telluride and bismuth chalcogenide).[5] The figure of merit, ZT, expresses the efficiency of heat conversion to electricity by thermoelectric materials, which is determined by electrical conductivity (σ), Seebeck coefficient (α), and thermal conductivity (k), ($ZT = \alpha^2\sigma/k$). However, due to the low thermal conductivity that conjugated polymers possess,[6] their thermoelectric performance is usually evaluated by the power factor (PF) where $PF = S^2\sigma$. Since the power factor is proportional to the electrical conductivity, which is dependent on carrier concentration n ($cm^{-3}$), (maximized upon doping), and carrier mobility μ ($cm^2\ V^{-1}s^{-1}$), a polymer with high electron mobility and an efficient doping process would lead to a boost in thermoelectric performance.

Hole conducting polymers have demonstrated high electrical conductivities of over 1000 S $cm^{-1}$. As a result, their thermoelectric figures of merit (ZT) exhibited high values in the range of 0.2-0.4,[7-11] comparable to the state-of-the-art inorganic (TE) materials. However, the conductivity of n-type electron-conducting polymers have been trailing behind their p-type counterparts, with few examples having achieved conductivities of over 1 S $cm^{-1}$,[12-15] This is predominantly arising from not exhibiting a large enough electron affinity (too shallow LUMO energy level) to facilitate electron transfer from n-dopant. A deep LUMO level is required to achieve an energy offset that allows electron transfer from the HOMO level of the dopant to

the LUMO level of the polymer, thus facilitating the doping mechanism.[16, 17] Additionally, a low LUMO level is beneficial towards preventing the common redox reactions of water and oxygen with the doped polymer radical anion which could quench the doped state and lead to a rapid decay in electrical conductivities and irreversible chemical degradation.[18-20] A consequence of the synthetic schemes for transition metal mediated aromatic coupling polymerization reactions, is the requirement of an electron rich monomer, which is incorporated along the backbone. This hinders the design of very deep LUMO polymers, with large electron affinities, as it dilutes the positive effect on EA of electron deficient co-repeat units. Therefore, it is desirable to introduce new synthetic strategies to couple acceptor-acceptor (A-A) repeat units to afford unipolar n-type semiconducting polymers with large electron affinities and stable ambient operation.[21, 22]

The strategy most adopted to improve the conductivity of semiconducting polymers is electronic doping. To achieve an effective electron doping process, the LUMO energy level of the semiconductor must be deeper than the HOMO energy level of the dopant.[17, 23] This thermodynamic requirement in effect narrows the choice of dopant to extremely electron rich molecules, which often suffer from ambient oxidation, thus presenting an additional problem. To help alleviate this constraint, it is desirable therefore to design polymers with as large electron affinities (deep LUMO energy levels) as possible. The charge carrier mobility of semiconducting polymers has been shown to increase with decreasing energetic disorder,[24] which in turn decreases with increasing backbone rigidity. The conformationally locked molecular design of a series of previously reported electron deficient aldol condensation polymers, can therefore be exploited to facilitate both electron doping and high electron mobility.[17, 20, 25, 26] By selecting the appropriate alkyl side chain size,[27, 28] or by extending the aryl repeat unit size,[29, 30] intermolecular close contacts can be modified to explore the effect on charge carrier mobility and energy levels.

Herein, replacement of the bis-oxindole monomer with a more electron withdrawing bis-lactone, to synthesize an alternating lactam-lactone copolymer was expected to further deepen the polymer LUMO energy level relative to all previously reported lactams, of which the deepest LUMO was (-4.2 eV). Within the lactam-lactone backbone, sterically accessible sites are promoted by the aryl rings, which will promote intermolecular contacts and thus potentially enhance charge hopping between chains, to ultimately improve the thermoelectric performance. (Figure.1).

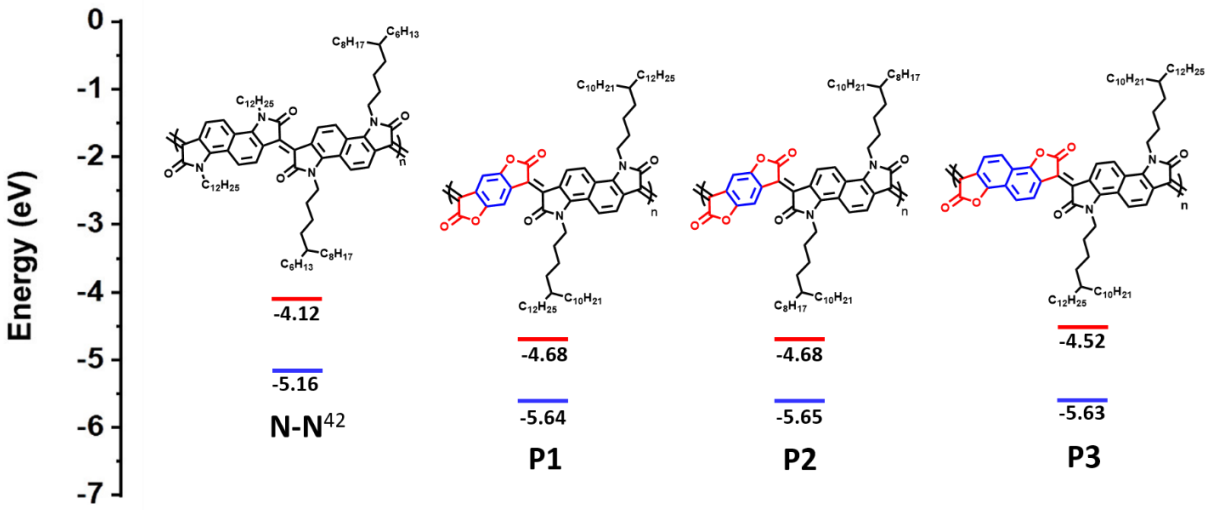


Figure 1. Chemical structures and calculated HOMO/LUMO of previous studied polymer (N-N) and new polymers, illustrating the effect of introducing bis-lactone units. HOMO is measured by photoelectron spectroscopy in air (PESA). LUMO is calculated from $E_{opt.gap}$ and IP.

## 2.3 Results and discussion

### 2.3.1 Polymers design, synthesis, and characterization

**Monomer synthesis:** The synthesis of bis-isatin and bis-lactone monomers were executed as reported in literature,[31-33]As shown in (Figure.2), bis-isatin monomers M1 and M2 were synthesized starting with the Martinet dioxindole condensation of 1,5-diaminonapthalene to form the bis-oxindole intermediate, which was then oxidized to form the bis-isatin (compound 1). The n-alkylation of the bis-isatin compound was then performed using an alkyl bromide

and sodium bicarbonate in dimethylformamide to form monomers M1 and M2 in 11% and 25% yield respectively. The experimental procedures for synthesizing the side chains comprising M1 and M2, R1, and R2, are described in the supporting information (Section 5.1.2). The phenyl-bis-lactone monomer was synthesized starting with the nucleophilic addition of ethyl cyanoacetate to 1,4-benzoquinone followed by a hydrolysis step using water and hydrochloric acid to generate the diacid intermediate, which was then subjected to a dehydration reaction using acetic anhydride to yield 26% of the phenyl-bis-lactone monomer (M3). Finally, naphthalene-bis-lactone monomer was obtained via the addition of 1,1,2-trichloroethyelene to the 1,5-dihydroxynaphthalene using sodium hydroxide to generate compound 4. This was followed by an elimination step using n-BuLi to generate the dialkyne (Compound 5), which was subjected to an oxidative cyclization reaction to provide (M4) in 5% yield. Detailed

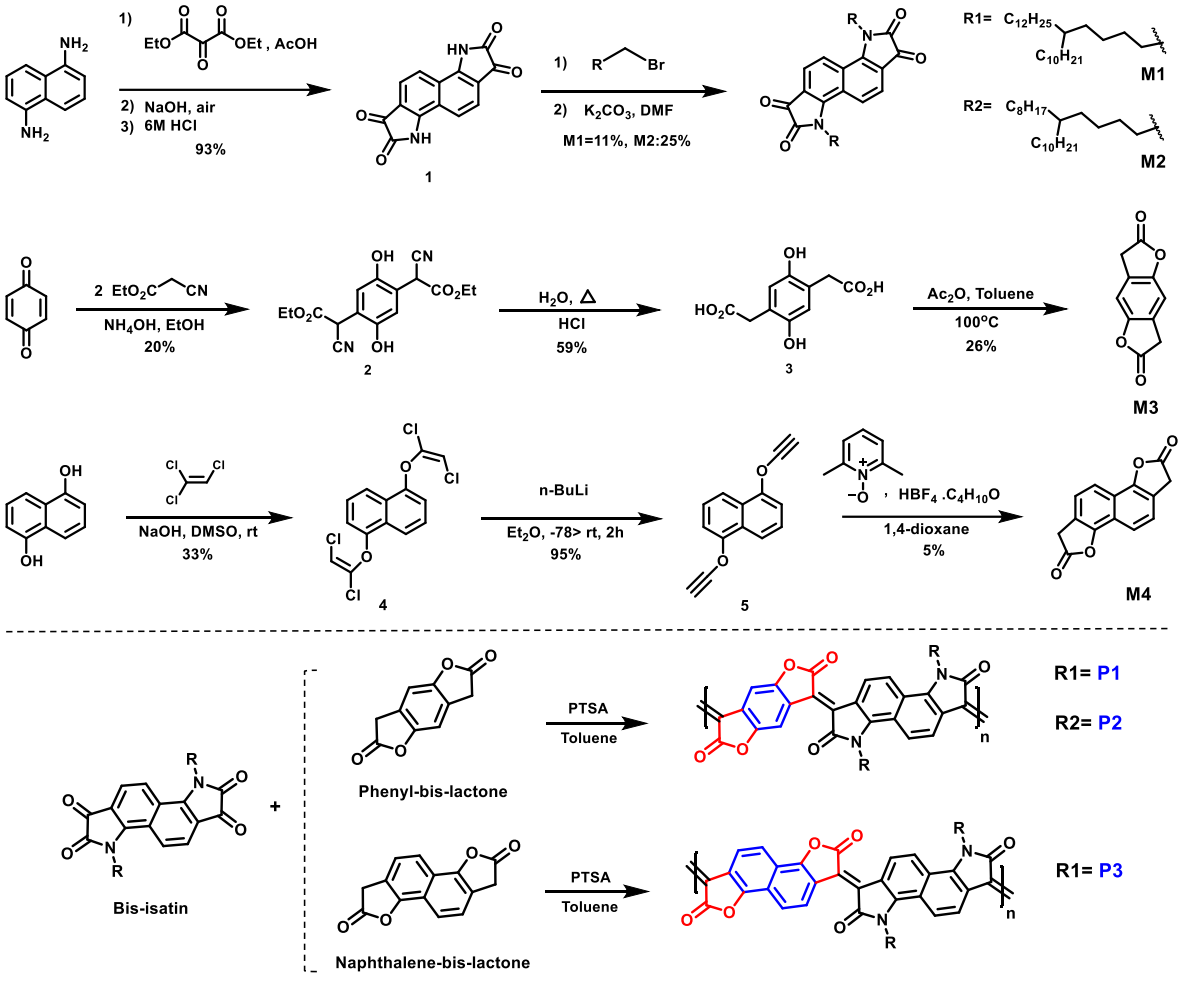


Figure 2. Synthetic approach to monomers (M1, M2, M3, and M4) and polymers (P1, P2, and P3).

synthetic protocols with monomer identifications are reported in the supporting information (Section 5.1.2).

**Polymer design:** The design and synthesis of conjugated polymers with low LUMO energy levels has been extremely challenging.[18] A previously reported aldol condensation polymerization[34] was adapted by replacing the bis-oxindole monomer with bis-lactone, for copolymerization with a bis-isatin monomer to form the extremely electron deficient alternating lactam-lactone copolymers P1, P2, and P3. Unlike transition-metal mediated reactions (i.e. Stille, Suzuki-Miyaura or Kumada coupling) where metal reagents could be highly toxic and require strenuous purification processes, this metal-free polymerization has water as the only by-product.

Optimizing the doping process depends not only on the electron affinity but also the steric accessibility of the dopant to be effectively accommodated within the polymer microstructure. For polymers P1 and P2, the selection of side chains R1 and R2 involves consideration of polymer solubility, as well the facilitation of intermolecular short contacts by locating the branch points away from the backbone.[27] For polymer P3, the phenyl-bis-lactone was replaced with a naphthalene-bis-lactone, anticipating that the enlarged ring size would further promote intermolecular short contacts.[30] Through extending the unsubstituted aryl size, it was also expected that the solubility of the resultant polymer would be potentially compromised, hence a longer side chain (R1) was selected.

**Polymers synthesis and characterization:** Having successfully synthesized the four monomers, the polymerization was carried out using an acid catalyzed, metal free, aldol condensation between the bis-isatin unit and the enolisable bis-lactone. Both monomers were refluxed in a toluene solution in the presence of *p*-toluene sulphonic acid to produce the acceptor-acceptor (A-A) copolymers, P1, P2, and P3 with yields of 86%, 43% and 45%, respectively. Detailed polymerization conditions are reported in the supporting information

(Section 5.1.2). The polymers were subsequently purified by Soxhlet extraction, and their chemical structures were verified using $^{1}$H NMR spectra. Supporting information (Section 5.1.3). P1 and P2 have been extracted as dark blue solid, while P3 exhibited a dark green colour. Polymers dissolve very well in both chloroform and chlorobenzene, and have similar molecular weights ($M_n$) of around 14 kDa, which were evaluated by high-temperature gel permeation chromatography (GPC) at 150 °C using 1,2,4-tricholorobenzene (TCB) as eluent (Table 1).

The thermal properties of the polymers were investigated through thermogravimetric analysis (TGA) and differential scanning calorimetry (DSC). All polymers showed excellent thermal stability with a decomposition temperature of over 350 °C, and no phase transitions in the range from room temperature to 300 °C were observed. Supporting information (Section 5.1.6 and 5.1.7).

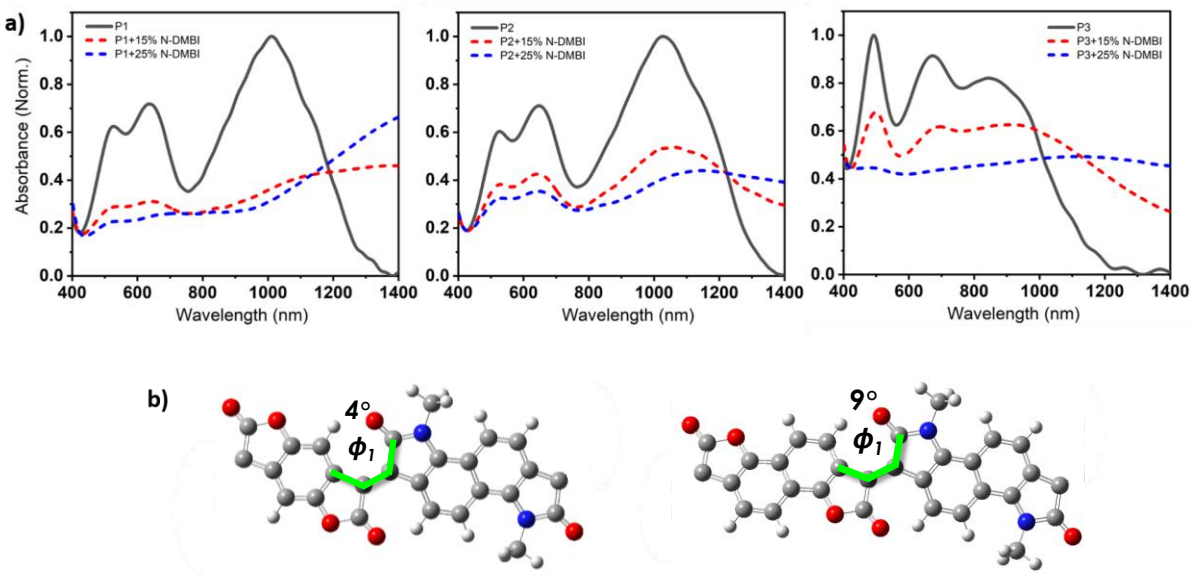


Figure 3. (a) UV-Vis-NIR absorption spectra of the pristine and doped (at 15 and 25 mol% N-DMBI doping ratio) thin films of P1, P2, and P3. (b) DFT-optimized molecular model of the phenyl-bis-lactone and naphthalene-bis-lactone fragments (ωB97XD/6-31G**).

Density functional theory (DFT) calculations show that both P1 and P2 polymers exhibited a dihedral angle between the adjacent lactone and lactam cores of ($\phi$ = 4°), while for P3, the dihedral angle is ($\phi$ = 9°). (Figure.3b), as shown in the supporting information (Section

5.1.11). As can be seen from the DFT modelling, the replacement of the phenyl ring with naphthalene resulted in an increased backbone twist.

A combination of photo electron spectroscopy in air (PESA) and thin-film absorption spectra (UV-vis-NIR) were used to determine the energy levels of the polymers. As shown in (Figure.3a), all pristine polymers exhibit three absorption peaks, two of which are high energy bands in the visible, as well as a broad NIR absorption band. P1 and P2 exhibit similar absorption features, with two absorption peaks in the visible region at 506, 505 nm and 609, 617 nm respectively. Both polymers show a broad NIR with a maximum long-wavelength absorption peaks of 930 and 947 nm respectively. P3, on the other hand featured different absorption characteristics, with two absorption peaks in the visible region of 469 and 647 nm at a shorter wavelength of that of P1 and P2. It also has the shortest wavelength absorption maximum of 820 nm, which could be attributed to backbone twisting that would reduce the pi orbital overlap along the backbone. Upon doping with N-DMBI, the neutral absorption features in the spectrum region at 400-700 nm sharply decrease in intensity, regardless of the polymer. At the same time, the n-doping is accompanied by the rising of new absorption bands at 1100-1200 nm with a tail extending also in the IR region at longer wavelength, which we ascribed to the formation of negative polarons. Supporting information (Section 5.1.4).

The ionization potential (IP) and the electron affinity (EA) of the polymers are summarized in (Table.1). As indicated, P1 and P2 show similar energy levels with ionization potentials (IP) of 5.65 eV and 5.64 eV, respectively, and an extremely large EA of 4.68 eV, one of the largest reported among all semiconducting polymers. The naphthalene derivative (P3) exhibits an ionization potential (IP) of 5.63 eV, which is slightly lower than that of P1 and P2 (5.65 eV). However, the electron affinity (EA) of P3 (4.52 eV) is considerably smaller than that of P1 and P2. This is mainly attributed to the dilution of the density of electron withdrawing lactone units along the conjugated backbone, by increasing the size of the aryl ring.

Additionally, having an increased twist in the backbone of P3 will reduce the pi orbital overlap along the backbone and leads to a widening of the bandgap to 1.13 eV, calculated from the absorption spectra, with deepening of the HOMO and a shallowing of the LUMO, and subsequently larger IP and smaller EA. These results are consistent with the absorption spectrum behavior of P3.

Table 1. Polymer physical and electrical properties.

| Polymer | $M_n/M_w$ [kDa] | PDI | IP[a] [eV] | EA[b] [eV] | λ (thin film/solution)[c] [nm] | $E_{opt.gap}$[d] [eV] | $\mu_e$[e] [$cm^2 V^{-1}s^{-1}$] | $\sigma_{max}$ [S $cm^{-1}$] | Seebeck [μV $K^{-1}$] | $PF_{max}$ [μW $m^{-1} K^{-2}$] |
|---|---|---|---|---|---|---|---|---|---|---|
| **P1** | 14/29 | 2.1 | 5.64 | 4.68 | 930/940 | 0.97 | $1\times10^{-2}$ | 0.20±0.05 | -22±4 | 0.12±0.04 |
| **P2** | 16/27 | 1.7 | 5.65 | 4.68 | 932/962 | 0.97 | $7\times10^{-3}$ | 0.28±0.01 | -21±5 | 0.16±0.02 |
| **P3** | 14/20 | 1.5 | 5.63 | 4.52 | 820/817 | 1.13 | $1\times10^{-3}$ | 0.008±0.001 | -210±14 | 0.034±0.008 |

[a] Measured by photoelectron spectroscopy in air (PESA)
[b] Calculated from $E_{opt.gap}$ and IP.
[c] Thin film and solution absorption onset.
[d] Estimated optical gap calculated using onset of absorption spectra ($E_{opt.gap} = 1240/\lambda_{onset}$)
[e] Mobilities measured using a field-effect transistor with a top-gate bottom contact configuration (see supporting information, section 8).

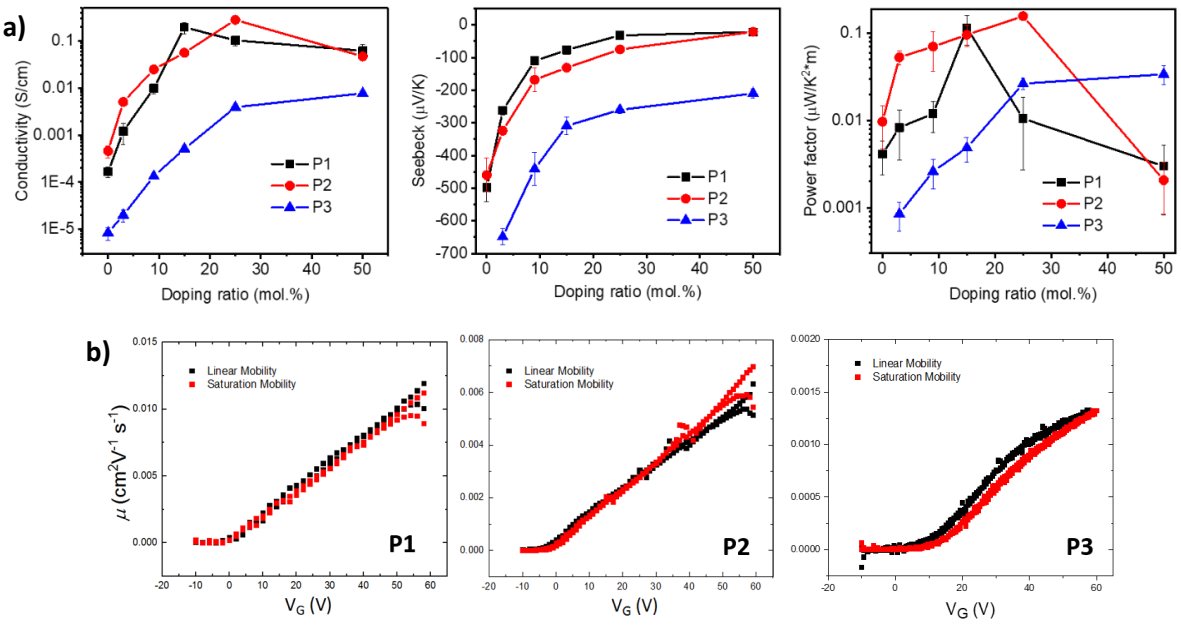


Figure 4. (a) Thermoelectric properties of doped polymers at different doping concentrations including electrical conductivities, Seebeck coefficients and power factors. (b) Transistor properties of pristine P1, P2 and P3.

## 2.3.2 Thermoelectric and Charge Transport Measurements

1,3-Dimethyl-2-phenyl-2,3-dihydro-1*H*-benzoimidazole (DMBI) derivatives have imparted effective electrochemical reductions of various organic transformations,[35-37] presenting an ideal class as n-type dopants. More particularly, N-DMBI, 4-(1,3-dimethyl-2,3-dihydro-1*H*-benzoimidazol-2-yl)-*N*,*N*-dimethylaniline, was chosen to dope all the polymers due to its strong n-doping ability for various n-type semiconductors such as [6,6]-phenyl-$C_{61}$-butyric acid methyl ester, (PCBM),[35] and P(NDIOD-2T)[38]. Furthermore, its shallow HOMO energy level of (- 4.4 eV) offers an effective energy offset with our polymers,[23,16] in that the HOMO level of N-DMBI is closer to vacuum energy than the LUMO levels of our polymers, which is a requirement for electron transfer from the donor (N-DMBI) to the host polymers. The electrical conductivity and Seebeck coefficient were evaluated to quantify the TE properties of the polymers. As demonstrated in (Figure 4), the electrical conductivities dramatically rise with increasing dopant ratio reaching a maximum value when the mass percentage of N-DMBI is 15% for P1, 25% for P2, and 50% for P3. As noted from (Figure.4a), unlike P1 and P2, P3 does not feature an electrical conductivity maximum in the same dopant concentration range. For P3, the electrical conductivity increases about three orders of magnitude from 0 to 25% N-DMBI ratio, but only by a factor of two at dopant concentration of 50%. We attributed this to the aggregation of N-DMBI, which is known to occur at high load.[39] As the dopant concentration increases, the conductivity of P1 and P2 starts to decrease, possibly due to the disruption of the thin film microstructure by a large number of dopants leading to a drop in carrier mobility. The polymers P1, P2, and P3 exhibited maximum conductivities of 0.20±0.05, 0.28±0.01, and 0.008±0.001 S $cm^{-1}$, respectively. These results suggest that dominant factor in conductivity optimization is energy level offset, which drives electron transfer. The Seebeck coefficients of all three polymers are negative, confirming a predominant n-type character.[40]

The Seebeck coefficient of P1 and P2 decreases continuously with increasing the dopant concentration, going from -498±43 μV $K^{-1}$ and -460±52 μV $K^{-1}$ for pristine films to -22±4 μV $K^{-1}$ and-21±5 μV $K^{-1}$ at 50% doping. For P3, the Seebeck coefficient decreases only to -210±14 μV $K^{-1}$ at 50% N-DMBI mass percentage, a value which agrees well with the lower conductivity of P3 as compared to P1 and P2. The maximum power factors obtained were 0.12±0.04, 0.16±0.02, and 0.034±0.008 μW $m^{-1}$ $K^{-2}$ for P1, P2, and P3, respectively. P2 showed a higher conductivity than P1, despite the lower charge carrier mobility, suggesting that the longer alkyl chains of P1 play a role in reducing the doping effectiveness, perhaps due to a less optimal affinity between the dopant and the polymer. However, both P1 and P2 showed

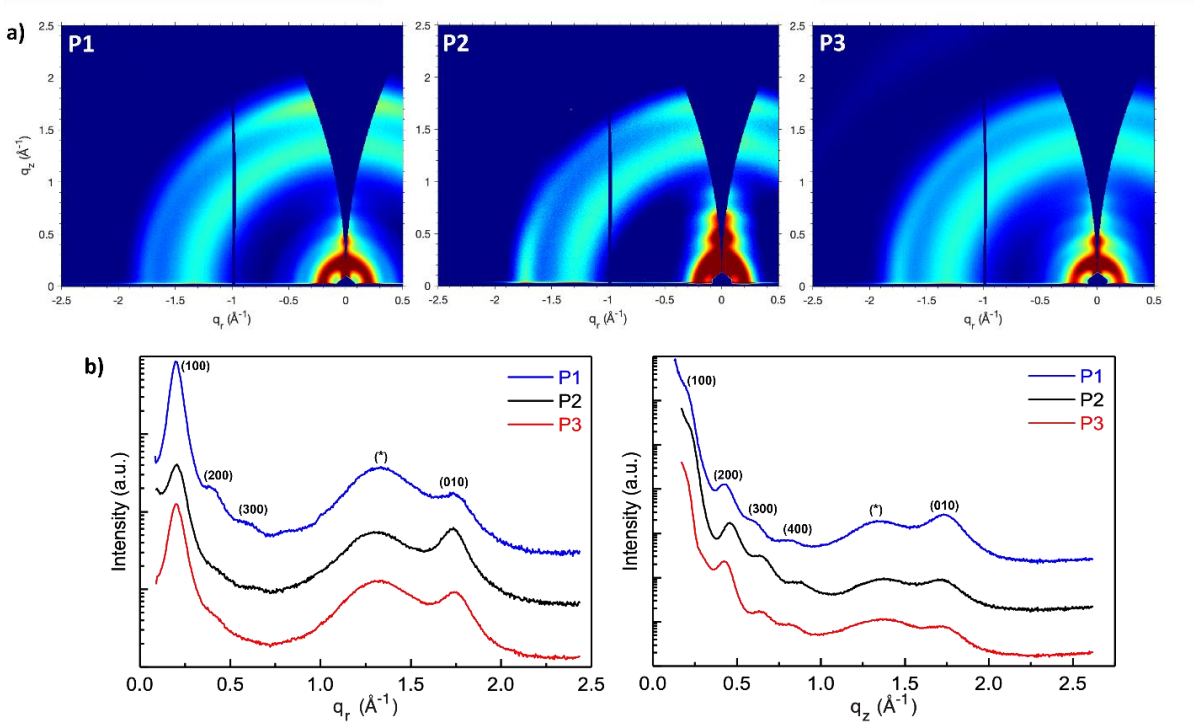


Figure 5 .GIWAXS: Two-dimensional grazing incidence X-ray qr-qz scattering map of (a) P1, (b) P2, and (c) P3. Note the π-stack (010) scattering (q ~ 1.75 Å-1) is strong out of plane for P1, strong both in- and out-of-plane for P2, and completely isotropic for P3. (d) In-plane ($q_r$) and (e) out-of-plane ($q_z$) scattering line cuts from P1, P2, and P3 (offset in intensity for clarity) highlightingthe lamellar (h00), π-stack (010), and isotropic amorphous (*) scattering.

a higher performance than P3, corresponding to the lower electron affinity.

Grazing-incidence wide-angle X-ray scattering (GIWAXS) were performed to evaluate the molecular packing and the morphologies of the polymer films, (Figure 5a-c). The lamellar

stack (100), π-π stack (010) and amorphous scattering d-spacing were calculated based on the fits of respective peaks from the in-plane (Figure 5d) and out-of-plane (Figure 5e) GIWAXS line cuts and listed in Table S1. In general, P1 showed a strong out-of-plane π-scattering with a π–π stacking distances around 3.61 Å while the in-plane π-scattering was relatively weak. The ring-shape scattering pattern observed in the 2D GIWAXS figure represented isotropic amorphous ordering with a characteristic d-spacing of ~4.7 Å. In addition, multiple orders of lamellar (h00) scattering were present both in and out-of-plane. The lamellar stack d-spacing was calculated to be 31.3 Å from the in-plane (100) peak. The anisotropic nature of the π-scattering of the P1 indicate a predominate crystallite population with a face-on orientation while a minority population with edge-on orientation.

Compared with P1, P2 showed stronger in-plane π-scattering, with a π–π stacking distances around 3.63 Å and noticeable out-of-plane π-scattering. Similar to P1, P2 also exhibited as isotropic amorphous scattering ring representing a d-spacing around ~4.8 Å. In terms of lamellar stacking, four orders of out-of-plane lamellar (h00) scattering were present while only one clear in-plane lamellar (100) scattering was observed that. The decreased lamellar d-spacing (30.7 Å), compared with P1, is consistent with the shorter branched alkyl side chain on the naphthalene-bis-isatin unit of P2. Considering the strong in-plane π-stack scattering, noticeable out-of-plane π-stack scattering and multiple out-of-plane lamellar scattering, P2 is speculated to possess a predominant population of edge-on orientated crystallites and a significant minority population of face-on orientated crystallites. The structure of P1 and P2 was nominally similar to that reported for the all phenyl analogue,[41]with pronounced out-of-plane π-stack scattering and an isotropic amorphous scattering ring. However, while increasing the alkyl branch length in the all-phenyl analogue diminished ordering and decreased scattering intensity (with an accompanying diminishment in charge transport), here increasing the alkyl branch length did not significantly decrease ordering or

scattering intensity, but instead induced increased edge-on texture with minimal change in charge transport.

Comparing P3 with P1, the aryl expansion most dramatically affected film texture. The isotropic (ring-like) π-scattering pattern indicated that crystallite orientation was no longer predominately either edge-on or face-on, as with P1 and P2, but instead randomly oriented. This also contrasted with the all bis-oxindole analogue which lacked a fully isotropic amorphous scattering ring.[34]The P3 lamellar scattering was not fully isotropic, indicating more extensive lamellar ordering out-of-plane than in-plane. P3 displayed a similar lamellar d-spacing (31.1 Å) as P1, consistent with their identical side chain architecture. In addition, both the π–π stacking (3.60 Å) and isotropic amorphous scattering (~4.75 Å) d-spacings of P3 were similar to P1. Beyond the isotropic nature of π-scattering, the intensity of P3 π-scattering intensity was also diminished relative to the amorphous scattering both in- and out-of-plane. This was contrasted with π-scattering that was stronger than amorphous scattering in-plane or out-of-plane, for P1 and P2 respectively.

The weaker and isotropic π–π stacking of the aryl ring extended P3 were coincident with decreased electron mobility and electrical conductivity compared with P1 and P2. The moderate differences in field effect mobility and peak conductivity between P1 and P2 mirrors the similarity in P1 and P2 microstructure, with essentially differ only in ratio edge-on and face-on crystallites. The higher P1 OFET mobility may be in part due to the more uniform orientation of crystallites which could be of benefit in the case of two dimensional charge transport. Likewise, the stronger mix of edge-on and face-one orientated crystallites in P2 may have contributed to the improved peak electrical conductivity as charge transport in doped films follows three dimensional percolated pathways.

## 2.4 Conclusion

New conformationally locked polymers were designed and synthesized, incorporating highly electron deficient bis aryl lactone groups, alternating with alkylated bis-aryl lactam co-repeat units along a conjugated backbone. Derivatives, P1, P2, and P3 that have the deepest LUMO level in all reported lactam rigid-rod building blocks. The partial substitution of the lactam groups with more electron deficient lactone groups along the backbone of conformationally locked aldol condensation polymers, results in extremely electron deficient semiconductors. The large electron affinities facilitated electron transfer from the dopant N-DMBI, achieving conductivities of up to almost 0.3 S $cm^{-1}$. The polymer conductivity was observed to decrease with decreasing electron affinity, suggesting the doping density was the dominant factor in optimizing conductivity and subsequently the power factor in thermoelectric devices.

## Acknowledgment

The research reported in this publication was supported by funding from King Abdullah University of Science and Technology Office of Sponsored Research (OSR) under awards no. OSR-2018-CARF/CCF-3079, no. OSR-2015-CRG4-2572 and OSR -4106 CPF2019. We acknowledge EC FP7 Project SC2 (610115), EC H2020 (643791), and EPSRC Projects EP/G037515/1, EP/M005143/1, and EP/L016702/1.

X.D., B.P., and J.R. gratefully acknowledge support from the National Science Foundation Grant No. NSF DMR-1751308. Special thanks to Joseph Strzalka and Qingteng Zhang for beam line assistance. This research used resources of the Advanced Photon Source, a U.S. Department of Energy (DOE) Office of Science User Facility operated for the DOE Office of Science by Argonne National Laboratory under Contract No. DE-AC02-06CH11357.

S.F. acknowledges the Swedish Research Council (2016-03979), ÅForsk (18-313, 19-310), Olle Engkvists Stiftelse (204-0256), and the Advanced Functional Materials Center at Linköping University (2009-00971) for financial support.

## 2.5 References

1. J. Lee, H. F. Chen, T. Batagoda, C. Coburn, P. I. Djurovich, M. E. Thompson and S. R. Forrest, *Nat Mater*, 2016, **15**, 92-98.
2. L. Dou, J. You, Z. Hong, Z. Xu, G. Li, R. A. Street and Y. Yang, *Adv Mater*, 2013, **25**, 6642-6671.
3. H. Sirringhaus, *Adv Mater*, 2014, **26**, 1319-1335.
4. B. Russ, A. Glaudell, J. J. Urban, M. L. Chabinyc and R. A. Segalman, *Nature Reviews Materials*, 2016, **1**.
5. J.-L. Brédas, D. Beljonne, V. Coropceanu and J. Cornil, *Chemical reviews*, 2004, **104**, 4971-5004.
6. M. Bharti, A. Singh, S. Samanta and D. K. Aswal, *Progress in Materials Science*, 2018, **93**, 270-310.
7. O. Bubnova, Z. U. Khan, A. Malti, S. Braun, M. Fahlman, M. Berggren and X. Crispin, *Nature materials*, 2011, **10**, 429-433.
8. G. H. Kim, L. Shao, K. Zhang and K. P. Pipe, *Nat Mater*, 2013, **12**, 719-723.
9. Y. Xia, K. Sun and J. Ouyang, *Adv Mater*, 2012, **24**, 2436-2440.
10. N. Kim, S. Kee, S. H. Lee, B. H. Lee, Y. H. Kahng, Y. R. Jo, B. J. Kim and K. Lee, *Adv Mater*, 2014, **26**, 2268-2272, 2109.
11. S. H. Lee, H. Park, S. Kim, W. Son, I. W. Cheong and J. H. Kim, *Journal of Materials Chemistry A*, 2014, **2**, 7288-7294.

12. C. Y. Yang, W. L. Jin, J. Wang, Y. F. Ding, S. Nong, K. Shi, Y. Lu, Y. Z. Dai, F. D. Zhuang, T. Lei, C. A. Di, D. Zhu, J. Y. Wang and J. Pei, *Adv Mater*, 2018, **30**, e1802850.

13. Y. Wang, M. Nakano, T. Michinobu, Y. Kiyota, T. Mori and K. Takimiya, *Macromolecules*, 2017, **50**, 857-864.

14. X. Yan, M. Xiong, J. T. Li, S. Zhang, Z. Ahmad, Y. Lu, Z. Y. Wang, Z. F. Yao, J. Y. Wang, X. Gu and T. Lei, *J Am Chem Soc*, 2019, **141**, 20215-20221.

15. K. Shi, F. Zhang, C. A. Di, T. W. Yan, Y. Zou, X. Zhou, D. Zhu, J. Y. Wang and J. Pei, *J Am Chem Soc*, 2015, **137**, 6979-6982.

16. D. Huang, H. Yao, Y. Cui, Y. Zou, F. Zhang, C. Wang, H. Shen, W. Jin, J. Zhu and Y. Diao, *Journal of the American Chemical Society*, 2017, **139**, 13013-13023.

17. Y. Lu, J.-Y. Wang and J. Pei, *Chemistry of Materials*, 2019, **31**, 6412-6423.

18. D. De Leeuw, M. Simenon, A. Brown and R. Einerhand, *Synthetic Metals*, 1997, **87**, 53-59.

19. M. L. Tietze, B. D. Rose, M. Schwarze, A. Fischer, S. Runge, J. Blochwitz-Nimoth, B. Lüssem, K. Leo and J.-L. Brédas, *Advanced Functional Materials*, 2016, **26**, 3730-3737.

20. S. Wang, H. Sun, T. Erdmann, G. Wang, D. Fazzi, U. Lappan, Y. Puttisong, Z. Chen, M. Berggren, X. Crispin, A. Kiriy, B. Voit, T. J. Marks, S. Fabiano and A. Facchetti, *Adv Mater*, 2018, **30**, e1801898.

21. Z. Yuan, B. Fu, S. Thomas, S. Zhang, G. DeLuca, R. Chang, L. Lopez, C. Fares, G. Zhang, J.-L. Bredas and E. Reichmanis, *Chemistry of Materials*, 2016, **28**, 6045-6049.

22. D. Di Nuzzo, C. Fontanesi, R. Jones, S. Allard, I. Dumsch, U. Scherf, E. von Hauff, S. Schumacher and E. Da Como, *Nat Commun*, 2015, **6**, 6460.

23. B. D. Naab, S. Guo, S. Olthof, E. G. Evans, P. Wei, G. L. Millhauser, A. Kahn, S. Barlow, S. R. Marder and Z. Bao, *J Am Chem Soc*, 2013, **135**, 15018-15025.

24. D. Venkateshvaran, M. Nikolka, A. Sadhanala, V. Lemaur, M. Zelazny, M. Kepa, M. Hurhangee, A. J. Kronemeijer, V. Pecunia and I. Nasrallah, *Nature*, 2014, **515**, 384-388.

25. S. Wang, H. Sun, U. Ail, M. Vagin, P. O. Persson, J. W. Andreasen, W. Thiel, M. Berggren, X. Crispin, D. Fazzi and S. Fabiano, *Adv Mater*, 2016, **28**, 10764-10771.

26. P. Prins, F. C. Grozema, J. M. Schins, S. Patil, U. Scherf and L. D. Siebbeles, *Phys Rev Lett*, 2006, **96**, 146601.

27. I. Meager, R. S. Ashraf, S. Mollinger, B. C. Schroeder, H. Bronstein, D. Beatrup, M. S. Vezie, T. Kirchartz, A. Salleo, J. Nelson and I. McCulloch, *J Am Chem Soc*, 2013, **135**, 11537-11540.

28. T. Lei, J. H. Dou and J. Pei, *Adv Mater*, 2012, **24**, 6457-6461.

29. H. Chen, M. Hurhangee, M. Nikolka, W. Zhang, M. Kirkus, M. Neophytou, S. J. Cryer, D. Harkin, P. Hayoz, M. Abdi-Jalebi, C. R. McNeill, H. Sirringhaus and I. McCulloch, *Adv Mater*, 2017, **29**.

30. T. H. Thomas, D. J. Harkin, A. J. Gillett, V. Lemaur, M. Nikolka, A. Sadhanala, J. M. Richter, J. Armitage, H. Chen, I. McCulloch, S. M. Menke, Y. Olivier, D. Beljonne and H. Sirringhaus, *Nat Commun*, 2019, **10**, 2614.

31. N. M. Randell, P. C. Boutin and T. L. Kelly, *Journal of Materials Chemistry A*, 2016, **4**, 6940-6945.

32. P. Singla, N. Van Steerteghem, N. Kaur, A. Z. Ashar, P. Kaur, K. Clays, K. S. Narayan and K. Singh, *Journal of Materials Chemistry C*, 2017, **5**, 697-708.

33. Y. Deng, B. Sun, Y. He, J. Quinn, C. Guo and Y. Li, *Chem Commun (Camb)*, 2015, **51**, 13515-13518.

34. A. Onwubiko, W. Yue, C. Jellett, M. Xiao, H. Y. Chen, M. K. Ravva, D. A. Hanifi, A. C. Knall, B. Purushothaman, M. Nikolka, J. C. Flores, A. Salleo, J. L. Bredas, H. Sirringhaus, P. Hayoz and I. McCulloch, *Nat Commun*, 2018, **9**, 416.

35. P. Wei, J. H. Oh, G. Dong and Z. Bao, *Journal of the American Chemical Society*, 2010, **132**, 8852-8853.

36. E. Hasegawa, H. Hirose and K. Sasaki, *Heterocycles*, 2009, **77**, 1147-1161.

37. X.-Q. Zhu, M.-T. Zhang, A. Yu, C.-H. Wang and J.-P. Cheng, *Journal of the American Chemical Society*, 2008, **130**, 2501-2516.

38. R. A. Schlitz, F. G. Brunetti, A. M. Glaudell, P. L. Miller, M. A. Brady, C. J. Takacs, C. J. Hawker and M. L. Chabinyc, *Adv Mater*, 2014, **26**, 2825-2830.

39. D. Kiefer, A. Giovannitti, H. Sun, T. Biskup, A. Hofmann, M. Koopmans, C. Cendra, S. Weber, L. J. Anton Koster, E. Olsson, J. Rivnay, S. Fabiano, I. McCulloch and C. Muller, *ACS Energy Lett*, 2018, **3**, 278-285.

40. G. J. Snyder and E. S. Toberer, in *materials for sustainable energy: a collection of peer-reviewed research and review articles from Nature Publishing Group*, World Scientific, 2011, pp. 101-110.

41. Y. Lu, Z. D. Yu, R. Z. Zhang, Z. F. Yao, H. Y. You, L. Jiang, H. I. Un, B. W. Dong, M. Xiong, J. Y. Wang and J. Pei, *Angew Chem Int Ed Engl*, 2019, **58**, 11390-11394.

42. H.Chen, M.Moser, S.Wang, C.Jellet, K.Thorley, G.Harrison, B. Purushothaman, M.Alsufyani, H.Bristow, A. Wadsworth, S.Fabiano and I.McCulloch, Unpublished manuscript.

# 2.6 Statement of authorship

**Statement of Authorship for joint/multi-authored papers for PGR thesis**

To appear at the end of each thesis chapter submitted as an article/paper

The statement shall describe the candidate's and co-authors' independent research contributions in the thesis publications. For each publication there should exist a complete statement that is to be filled out and signed by the candidate and supervisor **(only required where there isn't already a statement of contribution within the paper itself).**

| | |
|---|---|
| Title of Paper | The effect of aromatic ring size in electron deficient semiconducting polymers for n-type organic thermoelectrics |
| Publication Status | ☑ Published □ Accepted for Publication<br>□Submitted for Publication □Unpublished and unsubmitted work written in a manuscript style |
| Publication Details | Alsufyani, M., Hallani, R. K., Wang, S., Xiao, M., Ji, X., Paulsen, B. D., Xu, K, Bristow, H., Chen, H., Chen, X., Sirringhaus, H., Rivnay, J., Fabiano, S., & McCulloch, I. (2020). The effect of aromatic ring size in electron deficient semiconducting polymers for n-type organic thermoelectrics. Journal of Materials Chemistry C, 8(43), 15150-15157. |

Student Confirmation

| | | | |
|---|---|---|---|
| Student Name: | Maryam Alsufyani | | |
| Contribution to the Paper | M.A carried out the synthetic experiments of the monomers and polymers, performed characterization experiments (GC-MS, NMR, and GPC), thermal (TGA and DSC), electrical and optical characterization of the pristine polymers (Film and solution UV-vis-NIR and PESA), and wrote the manuscript, in advice and consultation with R.H. S.W fabricated the polymers in thermoelectric devices and measured the thermoelectric performance. M.X and H.B fabricated the thin film organic field effect transistor (OFETs) and measured the electron mobilities of the polymers. X.J and B.P carried out (GIWAXS) experiments to provide insight into the polymer's morphology and microstructure with full analysis. K.X measured (UV-vis) absorption spectrums of the doped polymers. H.C Performed computational modelling of the polymers by density functional theory (DFT) calculations. X.C aided in the synthesis work, and the characterization techniques including PESA and UV- vis absorption spectroscopy. All co-authors discussed the paper and revised the manuscript. H.S, J.R, S.F and I.M supervised the work. | | |
| Signature |  | Date | 31/08/2023 |

Supervisor Confirmation

By signing the Statement of Authorship, you are certifying that the candidate made a substantial contribution to the publication, and that the description described above is accurate.

| | | |
|---|---|---|
| Supervisor name and title: Professor Iain McCulloch FRS | | |
| Supervisor comments | | |
|  | Date | 01/09/2023 |

This completed form should be included in the thesis, at the end of the relevant chapter.

# Chapter 3

# Lactone Backbone Density in Rigid Electron-Deficient Semiconducting Polymers Enabling High n-type Organic Thermoelectric Performance

Disclaimer: The numbering of the headings in this chapter has been adjusted, including the addition of some headings been added to adhere with the formatting used in this thesis, differing from the originally published manuscript and is the only adjustment made.

## 3.1 Abstract

Three lactone-based rigid semiconducting polymers were designed to overcome major limitations in the development of n-type organic thermoelectrics, namely electrical conductivity and air stability. Experimental and theoretical investigations demonstrated that increasing the lactone group density by increasing the benzene content from 0% benzene (P-0), to 50% (P-50), and 75% (P-75) resulted in progressively larger electron affinities (up to 4.37 eV), suggesting a more favorable doping process, when employing (N-DMBI) as the dopant. Larger polaron delocalization was also evident, due to the more planarized conformation, which is proposed to lead to a lower hopping energy barrier. As a consequence, the electrical conductivity increased by three orders of magnitude, to achieve values of up to 12 S $cm^{-1}$and Power factors of 13.2 μW $m^{-1}$ $K^{-2}$ were thereby enabled. These findings present new insights into material design guidelines for the future development of air stable n-type organic thermoelectrics.

## Table of content

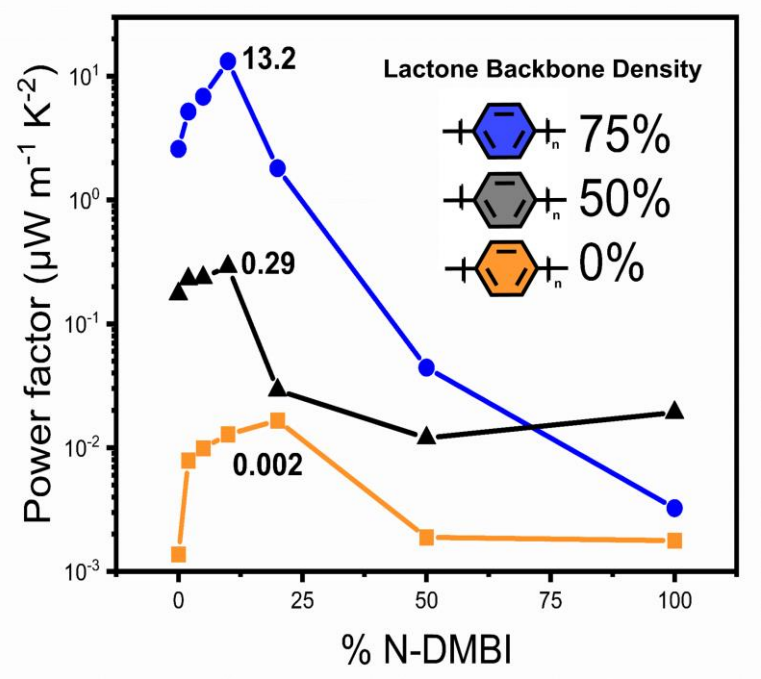

## 3.2 Introduction

Energy harvesting with conjugated polymers (CP) is most obviously exemplified in organic photovoltaics (OPVs), to enable high throughput production of flexible solar energy converters for clean energy generation.[1] Recently, conjugated polymers (CP) have also supported the development of emerging energy conversion technologies such as thermoelectric devices (TE), which offer direct conversion of heat into electric power without mechanical moving parts, making them compact and quiet compared with conventional heat engines.[2],[3] In contrast with the widely studied inorganic alloys, organic polymers have significant attraction as thermoelectric materials due to their low thermal conductivity (κ), necessary for efficient energy conversion as defined by the thermoelectric figure-of-merit $ZT = \alpha^2\sigma/\kappa$, where α is the Seebeck coefficient, σ is the electrical conductivity and T is the absolute temperature.[3a, 4]Moreover, the incorporation of solution-processable, flexible, and non-toxic conjugated polymers offer thermoelectric devices with great potential for the next generation of low-cost wearable heating/cooling devices, and near-room-temperature energy generation.[3a] Such features are impractical for toxic, rigid, and high temperature functioning inorganic materials.[5] Nonetheless, achieving high Seebeck coefficients (α) and electrical conductivities (σ) remains a challenge for organic thermoelectrics (OTEs), leading to lower than average thermoelectric (TE) performance. The development of higher performing organic thermoelectric (OTE) materials is thus essential to encourage their widespread utility.

While several p-type polymer thermoelectrics (OTE) are leading the field with electrical conductivities of >1000 S $cm^{-1}$ and power factors ($PF = \alpha^2\sigma$) of >100 μW $m^{-1}$ $K^{-2}$,[6] the highest performing n-type materials trail behind these values, mainly due to lack of air instability.[7] As such, the quest for high performing n-type polymers becomes key for further development of the organic thermoelectric (OTE) field. Since the Seebeck coefficients (α) of p- and n-type polymeric materials are comparable, approaching values of |40–200| μV $K^{-1}$ at

their maximum power factors (PFs),[8]optimizing the electrical conductivity (σ) has been the focus of many studies towards improving the thermoelectric performance of n-type polymers.[7d, 9]Currently, naphthalenetetracarboxylic diimide (NDI) based polymers, specifically N2200, are the most widely investigated n-type polymers for organic thermoelectrics, yet exhibit electrical conductivity (σ) of only $8\times10^{-3}$ S $cm^{-1}$ and power factor (PF) of 0.6 $\mu Wm^{-1}K^{-2}$. [9c] This is firstly ascribable to interchain charge localization observed in N2200 and related donor–acceptor (D-A) polymers,[9b, 10] which arises from large torsional angles between the donor and acceptor units, combined with the inefficient n-doping of the donor unit, due to its poor electron accepting ability.[7a, 7e, 11]Theoretical and experimental investigations reveal that the HOMO and LUMO orbital coefficients of (D-A) polymers are localized on the donor and acceptor moieties respectively, and the negative polaron of the n-doped polymer is localized only on the acceptor unit.[9e, 11a, 12] These indications suggest that the inactive n-doping of the donor unit together with the respective orbital energies of the donor and acceptor units have a significant impact in charge localization reported for N2200 and several other (D-A) polymers, ultimately limiting their carrier mobility and conductivity.[9b] Inducing charge delocalization along the polymer backbone has been the focus of a myriad of studies by i) boosting a more planarized structures[9e, 13]and ii) reducing the donor character of the traditional (D-A) polymers.[7e, 14] The ladder-type polymer, polybenzimidazo-benzophenanthroline (BBL) provides a good example to highlight the significance of a planarized rigid backbone in overcoming this limitation, reaching electrical conductivity (σ) up to 3 orders of magnitude larger, and power factor (PF) of 1 order of magnitude higher than N2200, which suggests a higher polaron mobility.[9e] Furthermore, a recent study demonstrated that enhancing backbone planarity together with minimizing (D−A) character help overcome the columbic interaction between polymer and dopant, reducing the number of free charges and subsequently the doping efficiency.[15]

Secondly, the modest performance of N2200 is also ascribed to the poor miscibility between the host polymer and employed dopant.[16] Such extrinsic limitation has been resolved by a number of related studies, such as increasing the side chains polarity by utilizing ethylene glycol oligomeric derivatives, which results in an improved dopant dispersion in the polymer matrix, as compared to the traditional alkyl side chains, leading to several fold enhancement in electrical conductivities (σ) and subsequent thermoelectric performance.[9d, 17]

We hypothesized that molecular engineering of conjugated polymers exhibiting rigid backbone with all acceptor (A-A) properties and polar side chains, will be beneficial in achieving high performing n-type organic thermoelectric devices. These rigid polymers exhibit excellent thermal stability, imperative for thermoelectric applications.[18] Enhanced dopant/polymer mixing imparted by the use of glycol-based side chains is expected, which crucially affects the doping process, and subsequently the thermoelectric performance. All electron deficient backbone polymers will also exhibit high electron affinity due to the electron withdrawing accepting functional groups, thus enabling a thermodynamically favorable n-doping mechanism that is also essential for facile n-doping in the presence of oxygen and water and thus for achievement of air-stable n-organic thermoelectrics.[19]

Few electron deficient rigid polymers have been reported with thermoelectric performance reaching power factor (PF) milestones of the order of $10^{0-}10^{1}$ $\mu Wm^{-1}K^{-2}$.[7c, 9e, 13] Nonetheless, considering that in most organic thermoelectric studies, the electrical conductivity (σ) is the main parameter to improve, values above 10 S $cm^{-1}$ have been scarcely reported for n-type conjugated polymers.[7c, 7d, 9a] We believe that this is due to the insufficient studies giving structural design guidelines to optimize device performance.[13-14, 17a]

We demonstrate judicious molecular design of electron deficient fused lactone-based polymers to optimize thermoelectric performance. A series of three co-polymers containing

benzene and naphthalene building blocks were synthesized, exhibiting a rigidified structure. The backbone conformation has been planarised by the double bonds imparted by a simple aldol condensation of enolic bis-lactone and electrophilic bis-lactam electron-withdrawing units. We sought to use a mixture of alkylated and glycolated solubilizing components to balance self assembly, aggregation and dopant compatibility, ultimately affording the co-polymers P-0, P-50, and P-75. Polymer structures are illustrated in Figure 1.

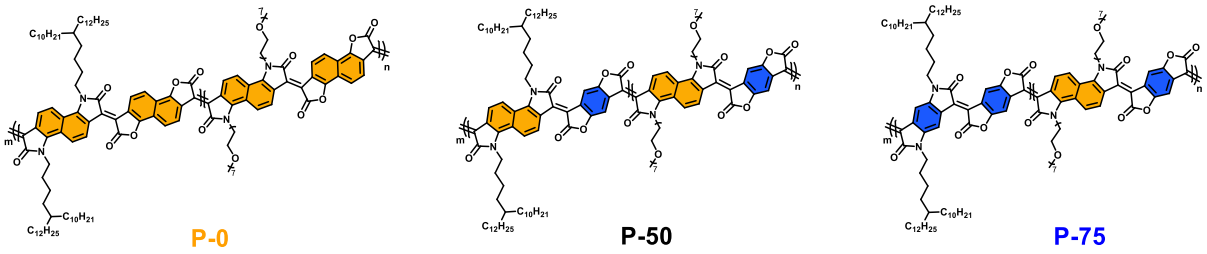


**Figure 1.** Chemical structures of the lactone based-rigid polymers investigated herein.

We explore the effect of aromatic size core on controlling the electron deficiency and the overall organization of the polymers, which impacts the thermoelectric performance. Upon optimized doping conditions, P-75 with the highest number of benzene core, and therefore the highest lactone density, displays the largest electrical conductivity (σ) of 12 S $cm^{-1}$ and power factor (PF) up to 13.2 μW$m^{-1}K^{-2}$. The conductivity of P-75 is significantly higher than that of other doped (A-A) and (D-A polymers),[7a-c, 7e, 13a] and one of the few reported n-type polymers displaying an electrical conductivity value over 10 S $cm^{-1}$.[7c, 7d, 9a, 20] Its power factor is also among the highest reported for solution processable n-type thermoelectric polymers. Our work demonstrates the critical role of aromatic ring size optimization in successful n-doping of the attractive all-acceptor rigid conjugated polymers and provide future material design guidelines for the advancement of n-type organic thermoelectrics.

## 3.3 Results and discussion

### 3.3.1 Polymer synthesis

All monomers were synthesized according to literature procedures.[21] Firstly, benzene-bis-isatin (M1) is prepared by oxidizing cyclohexanedione in ethanol, followed by amination and aromatization in the same reaction vessel. The corresponding diamine undergoes acylation, followed by ester hydrolysis. Swern oxidation of the intermediate dialcohol produces a diglyoxamide, prior to a Pummerer cyclisation. Oxidation of the resulting tricyclic intermediate yields benzene- bis-isatin (M1) in 25% yield. Second, synthesis of the naphthalene-bis-isatin monomers (M2) and (M3) followed a Martinet dioxindole condensation approach, by reacting 1,5-diaminonapthalene with diethyl ketomalonate form the bis-oxindole intermediate, which was then oxidized to form the bis-isatin. The subsequent n-alkylation/n-glycolation has afforded (M2) and (M3) in 20% yield. Preparation of benzo-difuran monomer begins with a nucleophilic addition of 1,4-benzoquinone by ethyl cyanoacetate, followed by a hydrolysis to generate the diacid intermediate, which is subsequently dehydrated with acetic anhydride to yield 30% of the benzo-difuran monomer (M4). Lastly, naphtha-difuran monomer was obtained via the addition of 1,1,2-trichloroethyelene to the 1,5-dihydroxynaphthalene to generate dichlorovinyl-oxynaphthalene intermediate. Following that, an elimination step with n-BuLi has afforded the dialkyne, which was subjected to an oxidative cyclization procedure to provide (M5) in 10% yield.

Polymers P-0, P-50 and P-75 were synthesized using the previously reported metal-free polymerization[21a] where an acid catalyst is employed to drive the aldol condensation between the enolic and electrophilic carbonyl units of bis-lactone and bis-isatin building blocks. This metal-free approach offers numerous advantages over transition-metal mediated reactions (such as Stille, Suzuki-Miyaura, or Kumada coupling), in which metal reagents can be costly

and highly toxic. Furthermore, having water as the only byproduct provides aldol condensation with no arduous purification steps that accompanies the use of metals such as palladium. Ultimately, P-0, P-50, and P-75 were obtained with number-average molecular weights (Mn) of 10 kDa, 10.7 kDa, and 18 kDa. Detailed polymerization conditions are reported in the supporting information (Section 5.2.2). Unfortunately, the synthesis of the P100 extension of this series was synthetically unattainable via the Martinet dioxindole condensation route. This route requires the synthesis of a glycolated benzo-bis-isatin co-monomer, which, under our conditions, was not isolable.

### 3.3.2 Polymers characterization

The thermal properties of P-0, P-50, and P-75 can be found in Figure.S18. All polymers showed excellent thermal stability with a decomposition temperature of over 350 °C, as determined by thermogravimetric analysis (TGA) and no phase transitions in the range from room temperature to 300 °C were observed by differential scanning calorimetry (DSC) for P-0, and P-50. Conversely, P-75 exhibits endothermic and exothermic peaks at 142°C and 120°C, with a slightly increased peak intensity. The same peaks were observed in the second cycle for P-75 polymer. The thermal transition behavior suggests a more ordered structure as the benzene content increase from P-0 to P-75. Note that the observed peaks in P-50 are more likely due to artefact from water.

The ionization potential (IP), the electron affinity (EA) and optical gap (Eg) of the polymers were determined by a variety of spectroscopic techniques including photo electron spectroscopy in air (PESA), thin-film absorption spectra (UV-Vis-NIR), ultraviolet photoelectron spectroscopy (UPS), and low energy inverse photoelectron spectroscopy (LE-IPES). The corresponding data are listed in Table 1. P-75 showed the largest ionization potential (IP) and electron affinity (EA) of 5.30 and 4.37 eV, respectively, one of the largest

reported electron affinities among glycolated n-type semiconducting polymers, which is attributed to the high density of the electron-withdrawing carbonyl groups. As the lactone content is reduced by reducing the benzene core to 50% in P-50, the ionization potential (IP) and electron affinity (EA) slightly decreased to 5.29 and 4.30 eV. The all naphthalene derivative P-0 has considerably exhibited the smallest ionization potential (IP) and electron affinity (EA) of 5.21 and 4.09 eV. This is chiefly attributed to the effective dilution of the electron withdrawing group density (C=O) along the conjugated backbone, by increasing the size of the aryl ring and consequently rendering the benzene free backbone (P-0) less electron deficient compared with its lactone- benzene-containing counterparts P-50 and P-75. Additionally, introducing more benzene content has been shown to reduce the backbone twisting (discussed later in the theoretical modelling section) and increase the pi orbital overlap along the backbone which leads to a narrowing of the bandgap to 0.93 eV for P-75. The optical band gap widens with reducing benzene content in P-50 and P-0 to reach 0.99 and 1.12 eV, respectively. Moreover, these lactone-based polymers exhibited lower LUMO levels than analogous previously reported lactam fused polymers,[13b] suggesting greater electron-withdrawing properties of the lactone functional group, when compared with lactam groups, thus higher electron affinities are achieved.

**Table 2.** Polymers physical and electrical properties.

| Polymer | Mn/Mw [kDa] | PDI | IP[a] [eV] | EA[a] [eV] | Eg[a] [eV] | IP[b] [eV] | EA[b] [eV] | Eg[b] [eV] | λmax,film[c] [nm] | IP[d] [eV] | EA[d] [eV] | Eg[d] [eV] |
|---|---|---|---|---|---|---|---|---|---|---|---|---|
| P-0 | 10/14 | 1.4 | 5.69 | 3.44 | 2.25 | 5.55 | 4 | 1.55 | 823 | 5.21 | 4.09 | 1.12 |
| P-50 | 10.7/14 | 1.3 | 5.72 | 3.61 | 2.11 | 5.55 | 4.2 | 1.35 | 973 | 5.29 | 4.30 | 0.99 |
| P-75 | 18/33 | 1.8 | 5.77 | 3.68 | 2.09 | 5.55 | 4.3 | 1.25 | 998 | 5.30 | 4.37 | 0.93 |

[a] Calculated by Density Functional Theory (DFT) simulations. [b] IP is measured by ultraviolet photoelectron spectroscopy (UPS) and EA by low energy inverse photoelectron spectroscopy (LE-IPES). [c] Thin films were spin-cast on glass substrates from chloroform solution; λ is the peak of the first low energy absorption band of the polymers. [d] Estimated optical gap calculated using onset of absorption spectra ($E_{opt.gap}$ =1240/$\lambda_{onset}$), IP is measured by photo electron spectroscopy in air (PESA) and EA is calculated from $E_{opt.gap}$ and IP.

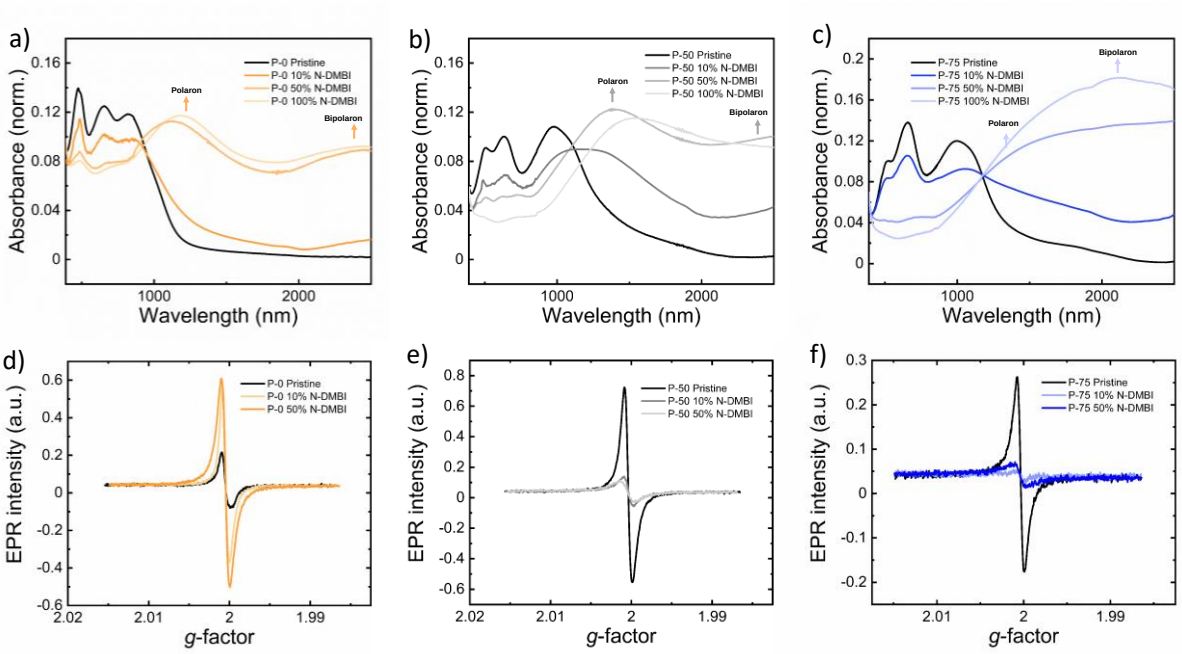


**Figure 2.** UV−vis−NIR thin film absorption spectra of the pristine and doped a) P-0, b) P-50, and c) P-75. EPR signals of the pristine and the doped d) P-0, e) P-50, and f) P-75.

The doping behavior of the three polymers were studied by UV−vis−NIR absorption spectroscopy and electron paramagnetic resonance (EPR) spectroscopy. The corresponding absorption spectra can be found in Figure 2a-c. In the pristine state, all polymers exhibit three absorption peaks. Two absorption bands with maximum absorption wavelength ($\lambda_{max}$) at (467 and 652 nm for P-0), (497 and 631 nm for P-50) and (516 and 658 nm for P-75). The onset absorption wavelength for P-0, P-50, and P-75 are 1107, 1252, and 1333 nm, respectively. P-0 exhibits a shorter onset absorption wavelength than P-50 and P-75. This is consistent with its wider optical band gap, resulting from the reduced pi orbital overlap upon backbone twisting. The dopant N-DMBI, 4-(1,3-dimethyl-2,3-dihydro-1*H*-benzoimidazol-2-yl)-*N*,*N*-dimethylaniline, was selected to solution-dope all the polymers due to its reported strong n-doping ability for various n-type semiconductors,[7c, 9c, 22] high chemical stability, and good solution processability.[22b]

Moreover, its shallow SOMO energy level of (- 2.8 eV) offer an effective energy offset with the polymers in this study, which is necessary for electron transfer from the donor (N-

DMBI) to the host polymers.[23] As shown in Figure 2a-c, upon doping the three polymers with N-DMBI, the neutral absorption features in the spectrum region at 400-700 nm sharply decrease in intensity. The n-doping is concurrently accompanied by the rising of a new absorption band at 1100-1200 nm, which we attributed to polarons, and one in the IR region at wavelength > 1500 nm, which we ascribed to bipolarons. Furthermore, 50% and 100% doping of P-75 is accompanied with full quenching of the pristine polymer peaks and a more pronounced appearance of bipolaron peaks, which could be the cause for the decreased charge carrier mobility and therefore the conductivity at 100% doping ratio, as will be discussed later.

To shed light on the doping process, the pristine and doped polymers at various doping level were evaluated by electron paramagnetic resonance (EPR) spectroscopy. Bipolarons are EPR silent, whereas polarons are unpaired electrons that are EPR active. Interestingly, as demonstrated in Figure 2 d-f, all pristine polymers showed EPR signals, suggesting the existence of an intrinsic charge density in the pristine (undoped) polymers. While the origin of this intrinsic charge density remains elusive, we note that it has already been observed for similar lactone polymers and tentatively ascribed to diradicals.[13a] The spin density is relatively weak for pristine P-0, and it enhances upon doping, indicating the generation of polaronic species as shown in Figure 2d. In contrast to P-0, P-50 and P-75 displayed a different spin behavior, with a relatively strong spin density of the undoped polymers that considerably decreases upon doping. We tentatively attribute this observation to the formation of EPR-silent bipolarons.

### 3.3.3 Microstructure

The polymers were investigated by grazing-incidence wide-angle X-ray scattering (GIWAXS) to gain insight into their thin film. The two-dimensional scattering patterns and in- and -out-of-plane line cuts are illustrated in Figure 3. All three polymers showed nominally similar scattering patterns in line with the previously reported analogues, though with diminished

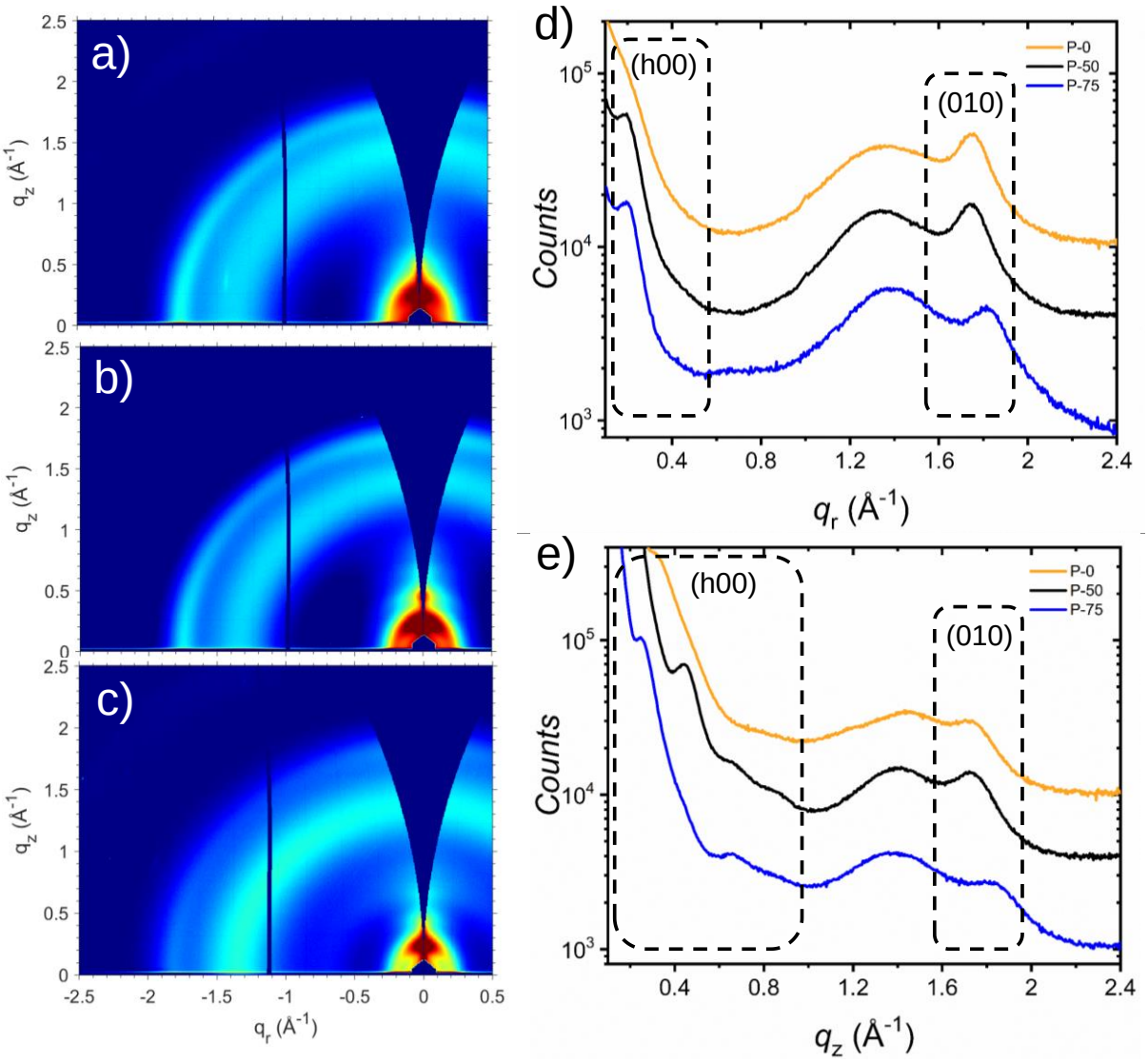


**Figure 3.** GIWAXS Patterns: Two-dimensional grazing incidence X-ray scattering map of (a) P-0, (b) P-50, and (c) P-75. GIWAXS Linecuts. (d) In-plane (qr) and (e) out-of-plane (qz) scattering line cuts from P-0, P-50, and P-75 (offset in intensity for clarity) highlighting the lamellar (h00) and π-stack (010) scattering.

degrees of lamellar scattering.[13a, 14a] As shown in 2D GIWAXS, all three polymers show a strong isotropic amorphous scattering ring centered near 1.4 Å-1, with lamellar stack (h00) and π-π stack (010) scattering present both in- and out-of-plane. The π-π stack (010) scattering transitioned from mostly isotropic in P-0 to a mix of largely in- and out-of-plane for P-75, with P-50 presenting an intermediate case.

This shows that the reduction of the naphthalene rings in the backbone drives the otherwise randomly aligned crystallites into a preference for edge- or face-on texture, which is correlated with the improved thermoelectric performance. As seen in Figure. 3 a-c, the lamellar

(h00) scattering was not well resolved against the scattering background, indicating a relatively diminished population of scatterers, which increases the uncertainty in calculated d-spacings and crystallite coherence lengths (Lc), see Table S1. This is especially true in the case of P-0 which shows only weak scattering shoulders and no evidence of higher ordered scattering peaks/shoulders. In the case of P-50 and P-75, the lamellar stacking appeared tighter out-of-plane than in-plane, and in-plane coherence lengths were roughly equivalent. In general, the π-π stack (010) scattering was better resolved. P-0 showed the largest π-π stack coherence lengths in- and out-of-plane, however, the thermoelectric performance did not correlate with simple coherence length. The π-π stack d-spacings of P-0 and P-50 were very similar (~3.6 Å) both in- and out-of-plane. P-75 however showed a significantly tighter π-π stack d-spacings 3.45 and 3.41 Å in- and out-of-plane, respectively. The P-75 π-π stack d-spacing was tighter than previous analogues as well,[13a, 14a] and correlated with improved thermoelectric performance. Further GIWAXS investigation on the polymer microstructure after doping is detailed in Section 5.2.9.

To investigate the effect of doping on the polymer's surface morphology, atomic force microscopy (AFM) was carried out, Figure S21. All pristine polymers form smooth thin films with roughnesses below 1 nm. Interestingly, after 10% doping with N-DMBI, the polymers thin films display uniform morphologies. Unlike PCBM and N2200 with high crystallinity,[9c, 22b] N-DMBI doped thin films of P-0, P-50 and P-75 present negligible particles and aggregates on the top of the surface. The low crystallinity of the three polymers indicate greater dopant dispersion in polymer films, resulting in a more efficient doping process. Higher content of N-DMBI leads to segregation at the surface of the three polymers, which congruent with the decreased thermoelectric performance at high doping concentrations.

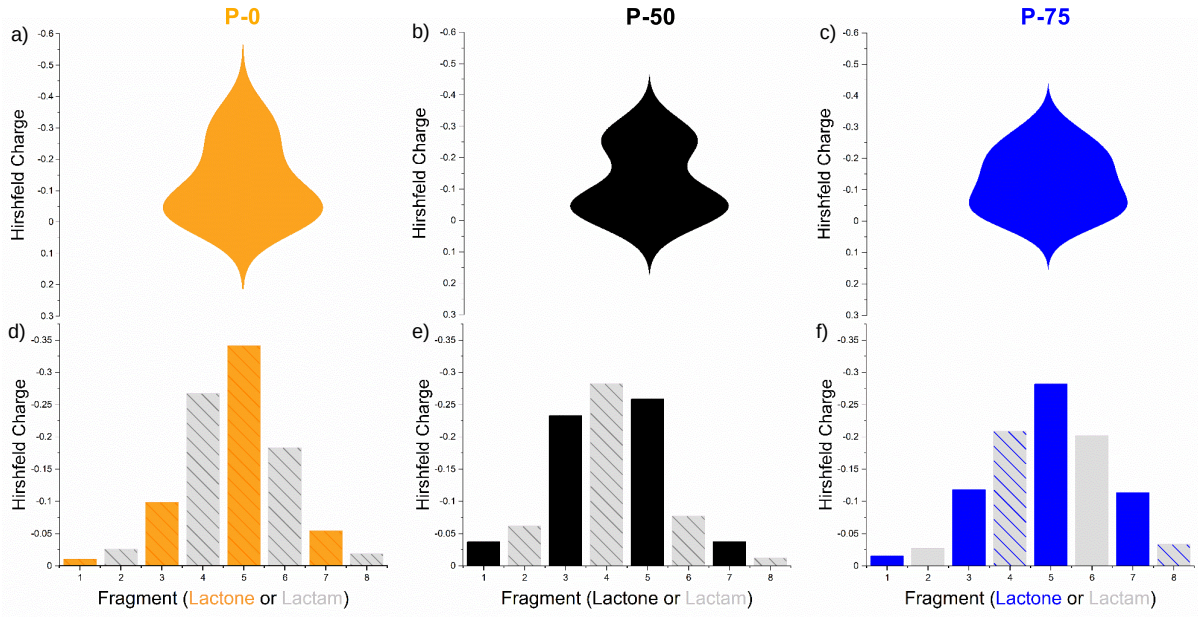


**Figure 4.** The illustrative symmetric violin plots smoothed by Kernel density a) P-0, b) P-50, and c) P-75 of the corresponding Hirschfeld charge distribution d) P-0, e) P-50, and f) P-75 in reduced polymers based on a fragment analysis of the polymer chain. Lactam groups shown in gray, Lactone groups shown in other colors. Napthalene-containing units are diagonally shaded, whereas the benzene rings are not.

### 3.3.4 Theoretical Modeling

To examine the effect of lactone maximization on the conformation of the backbone, oligomers of P-0, P-50, and P-75 were modeled by density functional theory (DFT) simulations. The long solubilizing alkyl and glycol chains were reduced to methyl groups to simplify the simulations. Firstly, the double bond connection appears to significantly reduce the twist angle between the building blocks, with torsional potential energy surfaces showing an energetic minimum at 160°, suggesting a conformationally locked backbone of the three polymers, Figure.S25. P-0, P-50, and P-75 exhibit dihedral angle average of ±20.1°, ±18.5°, and ±14.9°, respectively. The observed reduction in dihedral angle from P-0 to P-75 establishes an indication that increasing the lactone unit through benzene maximization has an influence on reducing the torsional angle between the building blocks and thus backbone planarization. This in turn ought to anticipate P-75 with stronger orbital overlap, extended polaron delocalization and hence an improved charge carrier transport.

We are particularly interested in investigating the negative polaron distribution, given its crucial impact on charge mobility and thereby electrical conductivity. Charge distribution analysis was performed on the density functional theory calculations using Hirshfeld charges, which has previously used to model polaron species of polymers.[24] In short, the Hirshfeld analysis partitions the electron density to allocate a partial charge to each atom. These charges are summed for the atoms making up the different lactone or lactam repeat fragments, such that the spread of charge in the radical anion can be visualised along the polymer chain, and the contibutions of the different functional groups and naphthalene/benzene rings to charge stabilisation can be observed. Figure.4 d), e) and f) illustrates the negative polaron destribution on the alternating lactone and lactam units, where (orange, black and blue bars represent lactone unit, and gray bars represent lactam unit). Additionally the napthalene-containing units are diagonally shaded, whereas the benzene rings are not. Figure.4 d) shows that negative polarons in P-75 were distributed to a greater extent when compared to P-50 and P-0, where the negative charges reside on three fragments (3-4-5) for P-50 and only two fragments (4-5) for P-0. To show a clear comparison of the charge distribution across the polymers, Hirshfeld charges of each polymer were also demonstrated in mirrored distribution curves, also called Violin plots. As seen in Figure.4 a), b) and c), the negative polarons in P-75 appear to be more evenly distributed along the fragments, with a more uniform topology than those shown in P-50 and P-0. The charge distribution within the polymer has shown to have a substantial effect on intermolecular charge transport. [9e] whereby the increased spread of charge provides a larger surface area for charge hopping within the polymer chains, which leads to increasing the interchain carrier mobility and consequently electrical conductivity.[25] The above analysis thus suggest P-75 with a more delocalized nature of the negative polarons, which was attributed to imposing more benzene moieties to the backbone, and subsequently a higher concentration of

carbonyl groups. The planarized backbone and polaron delocalization of P-75 suggest a highly efficient charge transport.

Lastly, the energy levels of the three polymers were computed with respect to the vacuum level. The calculated ionization potential (IP) values for P-0, P-50, and P-75 were 5.69 eV, 5.72 eV, and 5.77 eV, thus reflecting the same trend in the experimentally recorded data. A good fit was also observed between the experimental and simulated trends obtained for the polymer electron affinity (EA), with EA of P-75 being the largest (3.68 eV), the middle for P-50 (3.61 eV) and the smallest for P-0. (3.44 eV).

The maximum electrical conductivity values of pristine and doped polymers are plotted in Figure 5 a-b as a function of temperature. Figure 5 shows that charge transport is thermal activated in these polymers. The Arrhenius-type temperature activation energies ($E_a$) of pristine P-0, P-50, and P-75 are 232, 141, and 114 meV, and drop to 174, 78, and 60 meV, respectively, after doping at 10 mol% of N-DMBI. Upon doping, the decrease in activation energy is ascribed to the filling of trap states near the conduction levels due to the increased number of charge carriers generated by N-DMBI.[26] A doping level of 10 mol% has been selected because it matches the highest conductivity observed for P-75, as a higher percentage of dopant would lead to perturbation of the polymer morphology due to dopant aggregation.[27] These results suggest the trend of the hopping barrier in the pristine and doped films follows: P-75 < P-50 < P-0. The large difference in the hopping activation energy implies that as the benzene-lactone unit is maximized in P-75, the number of free charges increases, due to the enhanced backbone planarization and electron-deficiency, which in turn allow i) easier dissociation of the columbic interaction between the dopant and polymer, hence corresponds to enhanced carrier density.[15]

and ii) better charge transport.[9e] where both parameters have a substantial role in improving the electrical conductivity the subsequent thermoelectric performance.

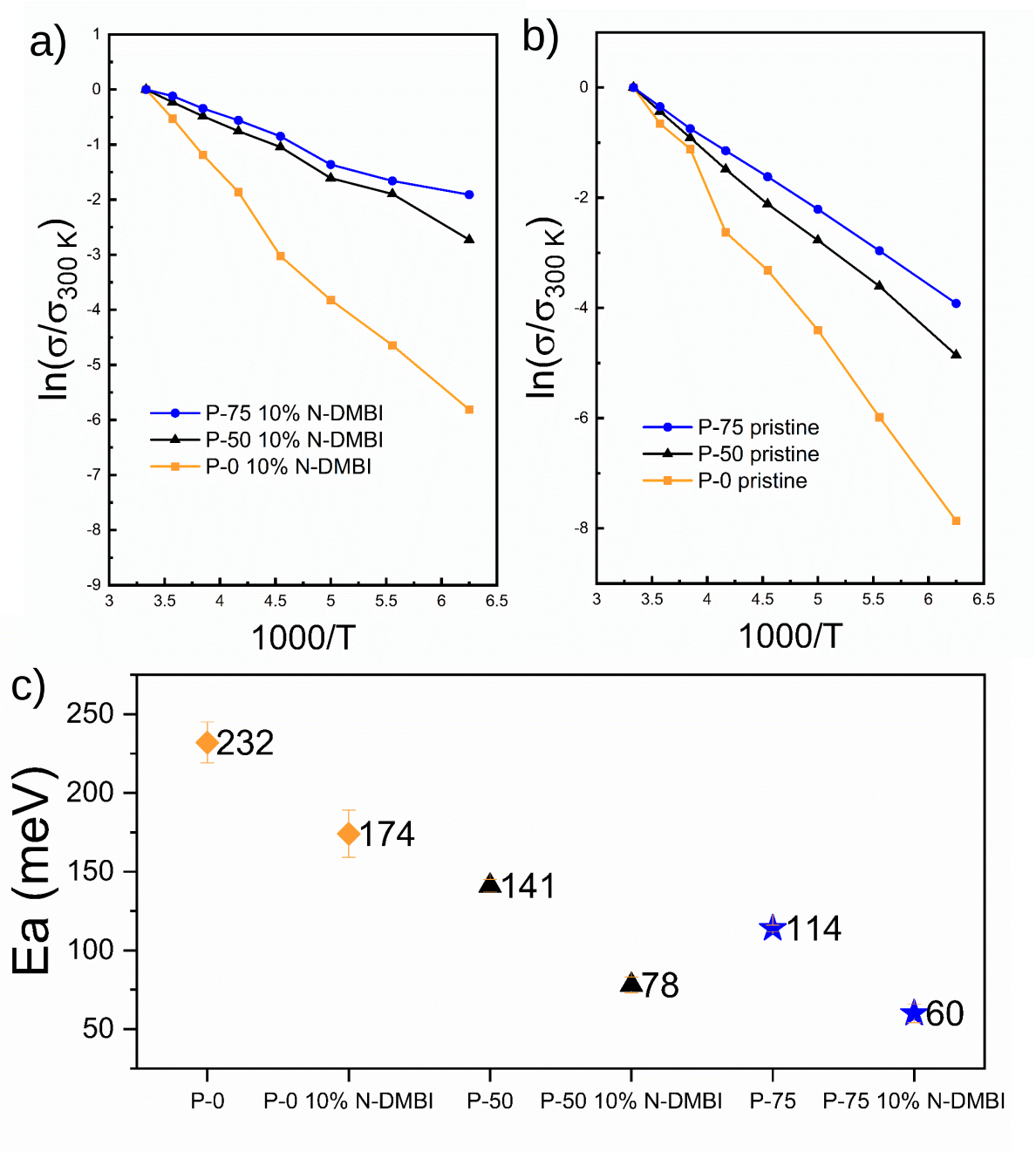


**Figure 5.** The Arrhenius plot of the temperature dependent electrical conductivity of a) pristine and b) doped polymers, measured in 4-probes configuration. C) the extracted activation energy displaying the trend of decreasing the hopping barrier from P-0 to P-75.

### 3.3.5 Thermoelectric properties

To evaluate the thermoelectric properties, the electrical conductivity and Seebeck coefficient of doped P-0, P-50, and P-75 were investigated as a function of the dopant molar concentration. As shown in Figure 6, all three polymers exhibit an intrinsic electrical conductivity. In the case of P-0, this intrinsic electrical conductivity is $3.19\times10^{-5}$ S cm$^{-1}$ and increases to 0.05 S cm$^{-1}$ for P-50, reaching the considerably high value of 0.5 S cm$^{-1}$ for P-75. The recorded intrinsic conductivities correlate well with the EPR signals of the pristine polymers, corroborating the existence of a free charge density in the pristine polymers. Upon doping with N-DMBI, the electrical conductivities dramatically rise, reaching a maximum value when the percentage of N-DMBI is 10 mol% for P-50 and P-75. At higher doping concentrations, the conductivity of P-50 and P-75 starts to decrease, possibly due to the disruption of the thin film microstructure after introducing a large number of dopants, leading to a drop in carrier mobility. P-0, on the other hand, does not feature an electrical conductivity maximum in the same dopant concentration range. For P-0, the electrical conductivity increases about three orders of magnitude from 0 to 20% N-DMBI ratio, but only by a factor of two at dopant concentration between 20-100%. This is ascribed to the aggregation of N-DMBI, which is known to occur at high loading concentrations.[28] The polymers P-0, P-50, and P-75 reached maximum

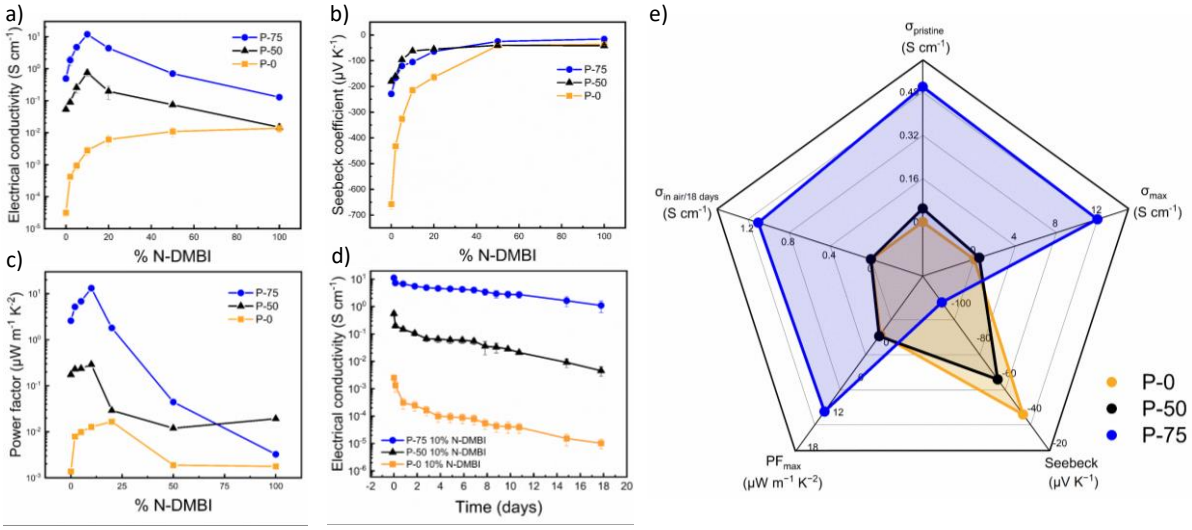


**Figure 6.** (a) Electrical conductivities, (b) Seebeck coefficients, and (c) power factors recorded for P-0, P-50, and P-75 at different doping ratios. D) Conductivity stability of the doped polymer thin films in air. e) Radar chart illustrating the trend of thermoelectric performance of the three polymers.

conductivities of 0.012, 0.76, and 12 S $cm^{-1}$, respectively. To the best of our knowledge, P-75 is one of the few reported n-type polymers displaying an electrical conductivity value over 10 S $cm^{-1}$. [7c, 7d, 9a] These results suggest that dominant factor in conductivity optimization is energy level offset, arising from increasing the density of electron withdrawing groups along the backbone, which drives electron transfer. P-50 demonstrates an electrical conductivity four times higher than its alkylated analogue (P1), which we previously reported[14a] highlighting the effect of polar side chain on enhancing the polymer/dopant miscibility, which has proven to be beneficial for enhancing the electrical conductivity. The Seebeck coefficient values of all three polymers are negative, indicating a predominant n-type character.[29] As shown in Figure 6 b), the Seebeck coefficients of P-0, P-50, and P-75 decreases monotonously with increasing dopant concentration, due to the opposite correlation between Seebeck coefficients and charge carrier concentration. At 10 mol% DMBI, P-75 displays a Seebeck coefficient of -105 μV $K^{-1}$, while P-0 and P-50 have Seebeck coefficients of -213 and -61 μV $K^{-1}$, respectively. Finally, a combination of the electrical conductivity (σ) and Seebeck coefficient (α) yielded a maximum power factor (PF = $\alpha^2\sigma$) as high as 13.2 μW $m^{-1}$ $K^{-2}$ for P-75, which is among the highest recorded for solution-processed n-type OTE materials. In contrast, the maximum power factor of P-50 and P-0 were only 0.29 and 0.002 μW $m^{-1}$ $K^{-2}$, respectively.

The air instability of n-type thermoelectric polymers has an imperative role in limiting their widespread applications, mainly caused by the quenching of the radical anions by $H_2O$ and $O_2$ in ambient air.[30] The deep LUMO energy levels recorded with our polymers helps to effectively suppress this quenching process. Figure 6d shows the stability of doped polymer thin films in air (thicknesses of P-0, P-50 and P-75 were 30 nm, 19 nm and 41 nm respectively), where the electrical conductivity was monitored over 18 days. While the electrical conductivities of P-50 and P-0 drops two orders of magnitude to values of $4\times10^{-3}$ S $cm^{-1}$ and

$1\times10^{-5}$ S $cm^{-1}$, respectively, P-75 showed only one order of magnitude loss and remained at 1.2 S $cm^{-1}$.

## 3.4 Conclusion

In summary, three new lactone-based rigid semiconducting polymers were synthesized with different densities of electron withdrawing functionality along the backbone, for n-type thermoelectric application. Aldol condensation has provided the polymers with simple metal-free approach that does not require complex purification processes, and was also beneficial towards imposing rigidity through double bond linkage between the polymer building blocks. TGA analysis indicated excellent thermal stability of the three polymers. All polymers exhibit deep LUMO energy levels, determined both experimentally and computationally, attributed to the high density of electron-deficient lactone unit along the backbone, reaching measured electron affinities as high as 4.37 eV. Both absorption spectra and EPR signals have confirmed the successful doping of the polymers with N-DMBI. DFT theoretical modelling indicates that all polymers exhibit a locked confirmation and suggests that increasing the lactone-benzene ring density on the backbone leads to enhanced planarization and polaron delocalization, which in turn is proposed to be beneficial for electron transport and lower hopping activation barriers, necessary for high electrical conductivities. Finally, the effect of lactone group density maximisation has resulted in high electrical conductivity of 12 S $cm^{-1}$, one of the few reported n-type polymer with such high conductivities, and subsequent high power factor of 13.2 μW $m^{-1}$ $K^{-2}$, which is among the highest reported n-type thermoelectrics. The enhanced electron affinity accompanied with lactone maximization is suggested as the dominant factor in optimizing the thermoelectric performance with considerable stability in ambient conditions. The findings of this study highlight that replacing the lactam groups with the stronger electron withdrawing lactone group is an effective design strategy to optimize the thermoelectric

performance, and offer new insights into material design guidelines for the future development of air stable n-type organic thermoelectrics.

## Acknowledgements

We acknowledge financial support from KAUST, including Office of Sponsored Research (OSR) awards no. OSR-2018-CRG/CCF-3079, OSR-2019-CRG8-4086 and OSR-2018-CRG7-3749. We acknowledge funding from ERC Synergy Grant SC2 (610115), the European Union's Horizon 2020 research and innovation programme under grant agreement n°952911, project BOOSTER and grant agreement n°862474, project RoLA-FLEX, as well as EPSRC Project EP/T026219/1B.D.P. and J.R. gratefully acknowledge support from the National Science Foundation grant no. NSF DMR-1751308. This research used resources of the Advanced Photon Source (beamline 8-ID-E), a U.S. Department of Energy (DOE) Office of Science User Facility operated for the DOE Office of Science by Argonne National Laboratory under Contract No. DE-AC02-06CH11357. The work at Linköping University was financially supported by the Knut and Alice Wallenberg foundation, the Swedish Research Council (2020-03243), Olle Engkvists Stiftelse (204-0256), the EC for the ITN projects HORATES (GA-955837), and the Swedish Government Strategic Research Area in Materials Science on Functional Materials at Linköping University (Faculty Grant SFO-Mat-LiU 2009-00971).

**Keywords:** • Chemical doping • Metal-free polymerization • Organic thermoelectrics • Rigid semiconducting polymers • Synthetic methods

## 3.5 References

[1] K. A. Mazzio, C. K. Luscombe, *Chem. Soc. Rev.* **2014**, *44*, 78-90.

[2] S. LeBlanc, *Sustainable Materials and Technologies* **2014**, *1*, 26-35.

[3] a) B. Russ, A. Glaudell, J. J. Urban, M. L. Chabinyc, R. A. Segalman, *Nature Reviews Materials* **2016**, *1*; b) M. Massetti, F. Jiao, A. J. Ferguson, D. Zhao, K. Wijeratne, A. Würger, J. L. Blackburn, X. Crispin, S. Fabiano, *Chemical Reviews* **2021**.

[4] M. Goel, M. Thelakkat, *Macromolecules* **2020**, *53*, 3632-3642.

[5] C. J. Yao, H. L. Zhang, Q. Zhang, *Polymers (Basel)* **2019**, *11*.

[6] a) O. Bubnova, Z. U. Khan, A. Malti, S. Braun, M. Fahlman, M. Berggren, X. Crispin, *Nature materials* **2011**, *10*, 429-433; b) G.-H. Kim, L. Shao, K. Zhang, K. P. Pipe, *Nature materials* **2013**, *12*, 719-723; c) Y. Xia, K. Sun, J. Ouyang, *Advanced materials* **2012**, *24*, 2436-2440; d) S. H. Lee, H. Park, S. Kim, W. Son, I. W. Cheong, J. H. Kim, *Journal of Materials Chemistry A* **2014**, *2*, 7288-7294.

[7] a) Y. Wang, M. Nakano, T. Michinobu, Y. Kiyota, T. Mori, K. Takimiya, *Macromolecules* **2017**, *50*, 857-864; b) X. Yan, M. Xiong, J. T. Li, S. Zhang, Z. Ahmad, Y. Lu, Z. Y. Wang, Z. F. Yao, J. Y. Wang, X. Gu, T. Lei, *J Am Chem Soc* **2019**, *141*, 20215-20221; c) K. Shi, F. Zhang, C. A. Di, T. W. Yan, Y. Zou, X. Zhou, D. Zhu, J. Y. Wang, J. Pei, *J Am Chem Soc* **2015**, *137*, 6979-6982; d) Y. Wang, K. Takimiya, *Adv Mater* **2020**, *32*, e) 2002060; eC. Dong, S. Deng, B. Meng, J. Liu, L. Wang, *Angew Chem Int Ed Engl* **2021**, *60*, 16184-16190.

[8] a) R. Yue, J. Xu, *Synthetic metals* **2012**, *162*, 912-917; b) D. Kiefer, R. Kroon, A. I. Hofmann, H. Sun, X. Liu, A. Giovannitti, D. Stegerer, A. Cano, J. Hynynen, L. Yu, *Nature materials* **2019**, *18*, 149-155; c) H. Li, M. E. DeCoster, R. M. Ireland, J. Song, P. E. Hopkins, H. E. Katz, *Journal of the American Chemical Society* **2017**, *139*, 11149-11157; d) C.-K. Mai, R. A. Schlitz, G. M. Su, D. Spitzer, X. Wang, S. L. Fronk, D. G. Cahill, M. L. Chabinyc, G. C. Bazan, *Journal of the American Chemical Society* **2014**, *136*, 13478-13481; e) W. Shi, T. Zhao, J. Xi, D. Wang, Z. Shuai, *Journal of the American Chemical Society* **2015**, *137*, 12929-12938; f) S. N. Patel, A. M. Glaudell, K.

A. Peterson, E. M. Thomas, K. A. O'Hara, E. Lim, M. L. Chabinyc, *Science advances* **2017**, *3*, e1700434.

[9] a) Y. Lu, Z. D. Yu, Y. Liu, Y. F. Ding, C. Y. Yang, Z. F. Yao, Z. Y. Wang, H. Y. You, X. F. Cheng, B. Tang, J. Y. Wang, J. Pei, *J Am Chem Soc* **2020**, *142*, 15340-15348; b) B. D. Naab, X. Gu, T. Kurosawa, J. W. F. To, A. Salleo, Z. Bao, *Advanced Electronic Materials* **2016**, *2*; c) R. A. Schlitz, F. G. Brunetti, A. M. Glaudell, P. L. Miller, M. A. Brady, C. J. Takacs, C. J. Hawker, M. L. Chabinyc, *Adv Mater* **2014**, *26*, 2825-2830; d) Y.-h. Shin, H. Komber, D. Caiola, M. Cassinelli, H. Sun, D. Stegerer, M. Schreiter, K. Horatz, F. Lissel, X. Jiao, C. R. McNeill, S. Cimò, C. Bertarelli, S. Fabiano, M. Caironi, M. Sommer, *Macromolecules* **2020**, *53*, 5158-5168; e) S. Wang, H. Sun, U. Ail, M. Vagin, P. O. Persson, J. W. Andreasen, W. Thiel, M. Berggren, X. Crispin, D. Fazzi, S. Fabiano, *Adv Mater* **2016**, *28*, 10764-10771; f) C. Y. Yang, W. L. Jin, J. Wang, Y. F. Ding, S. Nong, K. Shi, Y. Lu, Y. Z. Dai, F. D. Zhuang, T. Lei, C. A. Di, D. Zhu, J. Y. Wang, J. Pei, *Adv Mater* **2018**, *30*, e1802850; g) K. Yang, X. Zhang, A. Harbuzaru, L. Wang, Y. Wang, C. Koh, H. Guo, Y. Shi, J. Chen, H. Sun, K. Feng, M. C. Ruiz Delgado, H. Y. Woo, R. P. Ortiz, X. Guo, *J Am Chem Soc* **2020**, *142*, 4329-4340; h) X. Zhao, D. Madan, Y. Cheng, J. Zhou, H. Li, S. M. Thon, A. E. Bragg, M. E. DeCoster, P. E. Hopkins, H. E. Katz, *Adv Mater* **2017**, *29*; i) Y. Lu, J.-Y. Wang, J. Pei, *Chemistry of Materials* **2019**, *31*, 6412-6423.

[10] a) D. Fazzi, M. Caironi, C. Castiglioni, *Journal of the American Chemical Society* **2011**, *133*, 19056-19059; b) G.-J. A. Wetzelaer, M. Kuik, Y. Olivier, V. Lemaur, J. Cornil, S. Fabiano, M. A. Loi, P. W. Blom, *Physical Review B* **2012**, *86*, 165203; c) L. Zhang, B. D. Rose, Y. Liu, M. M. Nahid, E. Gann, J. Ly, W. Zhao, S. J. Rosa, T. P. Russell, A. Facchetti, *Chemistry of Materials* **2016**, *28*, 8580-8590; d) B. J. Eckstein, F. S.

Melkonyan, E. F. Manley, S. Fabiano, A. R. Mouat, L. X. Chen, A. Facchetti, T. J. Marks, *Journal of the American Chemical Society* **2017**, *139*, 14356-14359.

[11] a) S. Wang, H. Sun, T. Erdmann, G. Wang, D. Fazzi, U. Lappan, Y. Puttisong, Z. Chen, M. Berggren, X. Crispin, A. Kiriy, B. Voit, T. J. Marks, S. Fabiano, A. Facchetti, *Adv Mater* **2018**, *30*, e1801898; b) H. Jia, T. Lei, *Journal of Materials Chemistry C* **2019**, *7*, 12809-12821.

[12] S. Wang, D. Fazzi, Y. Puttisong, M. J. Jafari, Z. Chen, T. Ederth, J. W. Andreasen, W. M. Chen, A. Facchetti, S. Fabiano, *Chemistry of Materials* **2019**, *31*, 3395-3406.

[13] a) Y. Lu, Z. D. Yu, R. Z. Zhang, Z. F. Yao, H. Y. You, L. Jiang, H. I. Un, B. W. Dong, M. Xiong, J. Y. Wang, J. Pei, *Angew Chem Int Ed Engl* **2019**, *58*, 11390-11394; b) H. Chen, M. Moser, S. Wang, C. Jellett, K. Thorley, G. T. Harrison, X. Jiao, M. Xiao, B. Purushothaman, M. Alsufyani, H. Bristow, S. De Wolf, N. Gasparini, A. Wadsworth, C. R. McNeill, H. Sirringhaus, S. Fabiano, I. McCulloch, *J Am Chem Soc* **2020**.

[14] a) M. Alsufyani, R. K. Hallani, S. Wang, M. Xiao, X. Ji, B. D. Paulsen, K. Xu, H. Bristow, H. Chen, X. Chen, H. Sirringhaus, J. Rivnay, S. Fabiano, I. McCulloch, *Journal of Materials Chemistry C* **2020**, *8*, 15150-15157; b) K. Huang, G. Huang, X. Wang, H. Lu, G. Zhang, L. Qiu, *ACS Appl Mater Interfaces* **2020**, *12*, 17790-17798; c) D. Qu, T. Qi, H. Huang, *Journal of Energy Chemistry* **2021**, *59*, 364-387; d) Z. Yuan, B. Fu, S. Thomas, S. Zhang, G. DeLuca, R. Chang, L. Lopez, C. Fares, G. Zhang, J.-L. Bredas, E. Reichmanis, *Chemistry of Materials* **2016**, *28*, 6045-6049.

[15] J. Liu, Y. Shi, J. Dong, M. I. Nugraha, X. Qiu, M. Su, R. C. Chiechi, D. Baran, G. Portale, X. Guo, L. J. A. Koster, *ACS Energy Letters* **2019**, *4*, 1556-1564.

[16] J. Liu, L. Qiu, R. Alessandri, X. Qiu, G. Portale, J. Dong, W. Talsma, G. Ye, A. A. Sengrian, P. C. T. Souza, M. A. Loi, R. C. Chiechi, S. J. Marrink, J. C. Hummelen, L. J. A. Koster, *Adv Mater* **2018**, *30*.

[17] a) J. Liu, G. Ye, H. G. O. Potgieser, M. Koopmans, S. Sami, M. I. Nugraha, D. R. Villalva, H. Sun, J. Dong, X. Yang, X. Qiu, C. Yao, G. Portale, S. Fabiano, T. D. Anthopoulos, D. Baran, R. W. A. Havenith, R. C. Chiechi, L. J. A. Koster, *Adv Mater* **2020**, e2006694; b) D. Kiefer, A. Giovannitti, H. Sun, T. Biskup, A. Hofmann, M. Koopmans, C. Cendra, S. Weber, L. J. Anton Koster, E. Olsson, J. Rivnay, S. Fabiano, I. McCulloch, C. Muller, *ACS Energy Lett* **2018**, *3*, 278-285.

[18] A. Babel, S. A. Jenekhe, *Journal of the American Chemical Society* **2003**, *125*, 13656-13657.

[19] a) Y. Qiao, Y. Guo, C. Yu, F. Zhang, W. Xu, Y. Liu, D. Zhu, *Journal of the American Chemical Society* **2012**, *134*, 4084-4087; b) F. Hinkel, J. Freudenberg, U. H. Bunz, *Angewandte Chemie International Edition* **2016**, *55*, 9830-9832; cJ. Hioe, D. Šakić, V. Vrček, H. Zipse, *Org. Biomol. Chem.* **2015**, *13*, 157-169.

[20] C.-Y. Yang, M.-A. Stoeckel, T.-P. Ruoko, H.-Y. Wu, X. Liu, N. B. Kolhe, Z. Wu, Y. Puttisong, C. Musumeci, M. Massetti, *Nature communications* **2021**, *12*, 1-8.

[21] a) A. Onwubiko, W. Yue, C. Jellett, M. Xiao, H. Y. Chen, M. K. Ravva, D. A. Hanifi, A. C. Knall, B. Purushothaman, M. Nikolka, J. C. Flores, A. Salleo, J. L. Bredas, H. Sirringhaus, P. Hayoz, I. McCulloch, *Nat Commun* **2018**, *9*, 416; b) P. Singla, N. Van Steerteghem, N. Kaur, A. Z. Ashar, P. Kaur, K. Clays, K. S. Narayan, K. Singh, *Journal of Materials Chemistry C* **2017**, *5*, 697-708; c) N. M. Randell, P. C. Boutin, T. L. Kelly, *Journal of Materials Chemistry A* **2016**, *4*, 6940-6945; d) X. Chen, A. Marks, B. D. Paulsen, R. Wu, R. B. Rashid, H. Chen, M. Alsufyani, J. Rivnay, I. McCulloch, *Angew Chem Int Ed Engl* **2020**; e) Y. Deng, B. Sun, Y. He, J. Quinn, C. Guo, Y. Li, *Chem Commun (Camb)* **2015**, *51*, 13515-13518.

[22] a) P. Wei, T. Menke, B. D. Naab, K. Leo, M. Riede, Z. Bao, *Journal of the American Chemical Society* **2012**, *134*, 3999-4002; b) P. Wei, J. H. Oh, G. Dong, Z. Bao, *Journal of the American Chemical Society* **2010**, *132*, 8852-8853.

[23] S. Riera-Galindo, A. Orbelli Biroli, A. Forni, Y. Puttisong, F. Tessore, M. Pizzotti, E. Pavlopoulou, E. Solano, S. Wang, G. Wang, *ACS applied materials & interfaces* **2019**, *11*, 37981-37990.

[24] A. Giovannitti, R. B. Rashid, Q. Thiburce, B. D. Paulsen, C. Cendra, K. Thorley, D. Moia, J. T. Mefford, D. Hanifi, D. Weiyuan, *Advanced Materials* **2020**, *32*, 1908047.

[25] M. Moser, A. Savva, K. Thorley, B. D. Paulsen, T. C. Hidalgo, D. Ohayon, H. Chen, A. Giovannitti, A. Marks, N. Gasparini, A. Wadsworth, J. Rivnay, S. Inal, I. McCulloch, *Angew Chem Int Ed Engl* **2021**, *60*, 7777-7785.

[26] S. Olthof, S. Mehraeen, S. K. Mohapatra, S. Barlow, V. Coropceanu, J.-L. Brédas, S. R. Marder, A. Kahn, *Physical review letters* **2012**, *109*, 176601.

[27] I. E. Jacobs, E. W. Aasen, J. L. Oliveira, T. N. Fonseca, J. D. Roehling, J. Li, G. Zhang, M. P. Augustine, M. Mascal, A. J. Moulé, *Journal of Materials Chemistry C* **2016**, *4*, 3454-3466.

[28] D. Kiefer, A. Giovannitti, H. Sun, T. Biskup, A. Hofmann, M. Koopmans, C. Cendra, S. Weber, L. J. Anton Koster, E. Olsson, *ACS energy letters* **2018**, *3*, 278-285.

[29] V. Dusastre, *Materials for sustainable energy: a collection of peer-reviewed research and review articles from Nature Publishing Group*, World Scientific, **2010**.

[30] D. De Leeuw, M. Simenon, A. Brown, R. Einerhand, *Synthetic Metals* **1997**, *87*, 53-5

# 3.6 Statement of authorship

## Statement of Authorship for joint/multi-authored papers for PGR thesis

To appear at the end of each thesis chapter submitted as an article/paper

The statement shall describe the candidate's and co-authors' independent research contributions in the thesis publications. For each publication there should exist a complete statement that is to be filled out and signed by the candidate and supervisor **(only required where there isn't already a statement of contribution within the paper itself).**

| | |
|---|---|
| Title of Paper | Lactone Backbone Density in Rigid Electron-Deficient Semiconducting Polymers Enabling High n-type Organic Thermoelectric Performance |
| Publication Status | ☑ Published □ Accepted for Publication<br>□Submitted for Publication □Unpublished and unsubmitted work written in a manuscript style |
| Publication Details | Alsufyani, M., Stoeckel, M. A., Chen, X., Thorley, K., Hallani, R. K., Puttisong, Y., Ji, X., Meli, D., Paulsen, B., Strzalka, J., Regeta, K., Combe, C., Chen, H., Tian, J., Rivnay, J., Fabiano, S., & McCulloch, I. (2022). Lactone Backbone Density in Rigid Electron-Deficient Semiconducting Polymers Enabling High n-type Organic Thermoelectric Performance. Angewandte Chemie, 134(7), e202113078. |

Student Confirmation

| | | | |
|---|---|---|---|
| Student Name: | Maryam Alsufyani | | |
| Contribution to the Paper | M.A carried out the synthetic experiments of the monomers and polymers, performed characterization experiments (GPC and NMR), thermal (TGA and DSC), electrical and optical characterization of the pristine polymers (Film and solution UV-Vis-NIR and PESA), and wrote the manuscript. M-A.S fabricated the polymers in thermoelectric devices and measured the thermoelectric performance and stability; performed (UV-Vis-NIR) of the doped polymers, EPR and AFM and fabricated the thin film OFET transistor. K.T Performed computational modelling of the polymers by density functional theory (DFT) calculations. X.C synthesized the glycolated monomer (M3). X.J and B.P carried out (GIWAXS) experiments to provide insight into the polymer's morphology and microstructure with full analysis. K.R and C.C performed Ultraviolet photoelectron spectroscopy (UPS) and low energy inverse photoelectron spectroscopy (LE-IPES) experiments. H.C aided in performing HR-MS experiments and provided valuable advices in the project. All co-authors discussed the paper and revised the manuscript. J.R, S.F and I.M supervised the work. | | |
| Signature |  | Date | 31/08/2023 |

Supervisor Confirmation

By signing the Statement of Authorship, you are certifying that the candidate made a substantial contribution to the publication, and that the description described above is accurate.

| | | |
|---|---|---|
| Supervisor name and title: Professor Iain McCulloch FRS | | |
| Supervisor comments | | |
|  | Date | 01/09/2023 |

This completed form should be included in the thesis, at the end of the relevant chapter.

# Chapter 4

## The effect of organic semiconductor electron affinity on the operando generation of superoxide radical anions in organic electrochemical transistors

Disclaimer: The numbering of the headings in this chapter has been adjusted to adhere with the formatting used in this thesis, differing from the originally submitted manuscript and is the only adjustment made.

## 4.1 Abstract

A key challenge in the development of N-type conjugated polymers (CPs) for high performance electrochemical transistors, is their stable performance in ambient. When operating in aqueous electrolyte, potential reactions of the electrochemically injected electrons with air and water could hinder their persistence, leading to a reduction in charge transport. Here, we evaluate the impact of one of the reactions of electrons with molecular oxygen, namely the formation of superoxide radical anions, on organic electrochemical transistors (OECTs) performance. Employing time resolved spectroelectrochemistry and electron paramagnetic spectroscopy with three analogous polymers having varying electron affinities (EA), we find that an EA below the thermodynamic threshold for superoxide formation significantly improves electron transport and lifetime in air. We report a polymer with a sufficiently large EA and subsequent thermodynamically unfavorable superoxide formation, which was used as the semiconducting layer in an OECT, in its neutral and N-DMBI doped form, resulting in an excellent and air-stable OECT performance. Our results show a general design methodology to avoid detrimental parasitic reactions under ambient conditions, and the benefits that arise in electrical performance.

## 4.2 Introduction

The coupled fields of electronics and biology, bioelectronics, holds enormous potential for the development of novel biomedical devices for chemical/biological sensing, and medical diagnostics.[3] Soft, solution-processable, and redox-active conjugated polymers (CP) have recently been employed to construct low-power bioelectronic devices which are biocompatible with the human body. [3] These polymers, are typically comprised of a conjugated backbone with hydrophilic side chains, giving rise to mixed ionic-electronic transport. They are commonly used in the development of organic electrochemical transistors (OECTs),[3,5] where electrolyte ions can permeate the polymer film throughout its entire volume, doping the polymer. The degree of ion permeation and doping can be modulated by a gate voltage ($V_G$) (input), tuning the electrical conductivity of the polymer film, allowing modulation of the drain current ($I_D$) (output) at low-gate voltage, thus rendering OECTs efficient switches and powerful amplifiers. This feature makes OECTs a promising technology for flexible and ultra-sensitive bioelectronic interfaces, such as memory/neuromorphic brain implants[6, 7, 8] skin-conformable biosensors,[9, 10, 11]and *in vivo* electrophysiological recorders.[12, 13, 14, 15]

Both p-type (hole-transporting) and n-type (electron transporting) OECT devices have been demonstrated employing polymers with electron rich, and electron deficient conjugated backbones, respectively. So far, p-type materials such as PEDOT:PSS, [16, 17, 18] and p(g2T-TT),[16, 19] have delivered higher mobility OECT devices compared to their n-type analogues. Nevertheless, n-type OECTs are fundamentally required for i) direct-electron-transfer-based biological sensors, [20, 21, 22] ii) complementary logic circuits,[23, 24] and iii) cathodes for lithium/sodium ion batteries.[25, 26, 27] The origin of the disparity between n- and p-type OECT semiconductors may, in part, arise from the air instability found in the current n-type conjugated polymers with shallow LUMO levels (3.8 - 4.0 eV). It has been shown[28] that such instabilities can arise from the susceptibility of the doped species to react with atmospheric

water and/or oxygen. Semiconductors with deep LUMO energy levels, capable of exhibiting low energy electron polarons, are required to avoid such processes. In the context of aqueous-gated OECTs in an ambient atmosphere, electrochemically n-doped polymers can undergo two main degradation pathways. Firstly, they can react with molecular oxygen, leading to the formation of a primary reactive oxygen species, the superoxide radical anion ($O_2^{\bullet-}$), through a monovalent reduction of $O_2$ by singly charged anionic species with reduction potential of $E^0_{O_2/O_2^{\bullet-}} = -0.33 V_{SHE}$ (-4.11 eV vs. vacuum), see equation (1).[29, 30, 31] Secondly the reduction of water to form hydrogen ($H_2$) can occur with reduction potential of $E^0_{H_2O/H_2} = -0.41 V_{SHE}$ (-4.05 eV vs. vacuum).[28] Currently, the LUMO levels of most reported n-type semiconducting polymers range do not exceed -4.0 eV. Oxygen reduction is therefore thermodynamically possible, which involves a one-electron transfer from the n-doped polymer to molecular oxygen (eq.1), leading to the formation of superoxide and, as a result, oxidizing the polymer negative polaron back to its neutral state. This oxidation process hinders the polaron persistence, leading to a reduction in charge transport, and, ultimately, OECT performance. Moreover, once this first step of oxygen reduction reaction (ORR) is initiated in neutral aqueous electrolyte, further spontaneous reduction of superoxide can occur (eq 2-4)[30], to hydrogen peroxide ($H_2O_2$), with potentially detrimental effect on OECT operation. While the preference for $H_2O_2$ vs $H_2O$ terminal products varies depending on various factors such as ORR overpotential, active material and electrolyte pH, the role of active material functional groups in directing the pathway is still unclear.[32, 33, 34, 35, 36]

$$O_2 + e^- \rightleftharpoons O_2^{\bullet-} \quad (1)$$

$$O_2^{\bullet-} + 2H^+ + e^- \rightleftharpoons H_2O_2 \quad (2)$$

$$H_2O_2 + H^+ + e^- \rightleftharpoons OH^\bullet + H_2O \quad (3)$$

$$OH^\bullet + H^+ + e^- \rightleftharpoons H_2O \quad (4)$$

To address this issue, we report the effect of n-type semiconducting polymers EA on the generation of superoxide radical anions and its latent product, and demonstrate that it is possible to eliminate superoxide reactive radical anion formation through molecular design optimization. An n-type polymer with LUMO level of –4.30 eV was synthesized which, when employed in OECT device, was able to deliver a state-of-the-art performance with transconductances, $g_{m,}$ of 5.5 and 12.50 S $cm^{-1}$ and products of charge-carrier mobility and volumetric capacitance, $\mu C^{*}$, of 14.8 and 33.44 F $cm^{-1}V^{-1}s^{-1}$ , achieved for the intrinsic and N-DMBI doped polymer, respectively. These results suggest that the elimination of superoxide formation is an important step toward high performing n-type OECTs.

## 4.3 Results and discussion

A series of electron-deficient conjugated polymers comprising an electron-withdrawing lactone functional group, P-0, P-50, and P-75, were designed and synthesized [37] as shown in Fig. 1a. The polymers exhibit a span of LUMO levels from -4.00, -4.10, to -4.30 eV, with electron conductivities reaching 12 S $cm^{-1}$ for P-75, an order of magnitude higher than most reported (D-A) [38, 39, 40, 41, 42, 43]and (A-A) [44, 45, 46, 47] n-type polymers. This high conductivity was attributed to maximizing the lactone repeat unit backbone density to enable as deep a LUMO as possible, as well as backbone rigidity and coplanarity, enabled by the linking double bonds formed as a result of the aldol condensation.[37, 45, 48]. The energy levels of the three polymers was measured using a number of experimental and theoretical techniques showing a consistent trend where the EA increases with increasing ratio of phenyl units from P-0 to P-75 (Supplementary Table. 1).

Additionally, we carried out cyclic voltammetry (CV). EAs were estimated based on the reduction onset potentials ($E_{red}$) relative to ferrocene/ferrocenium (Fc/Fc+) redox couple,

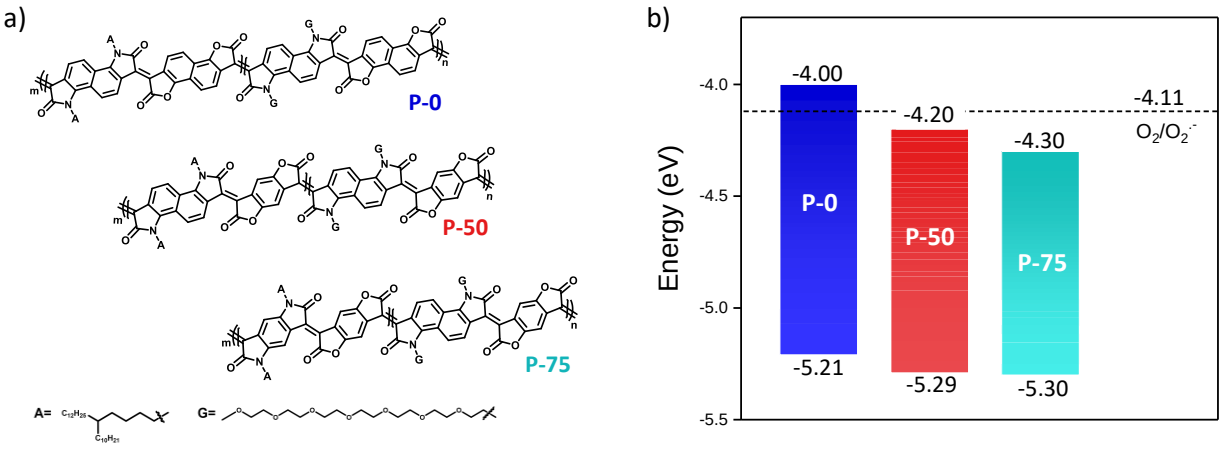


Fig. 1. a) The chemical structures of polymers investigated herein and b) their energy levels in relation to the energy level required for superoxide formation.

and found to be 4.51, 4.84, 5.03 eV for P-0, P-50, and P-75, respectively (Supplementary Figs. 1). The electrochemically obtained EA are larger than those obtained by the aforementioned methods, but they exhibit the same relative trends. Notably, the high EA of P-75 (5.03 eV) is a characteristic previously only demonstrated in the newly reported n-type polymers PBFDO,[49] and PBDF,[50]which exhibit exceptionally high conductivities. Low energy inverse photoelectron spectroscopy (LE-IPES) measures thin film electron affinity directly, while "optical EA" has an inherent overestimation and inaccuracy, as it does not take the exciton binding energy into account, while inaccuracies arise from extrapolation of the spectral maximum.[51, 52, 53, 54, 55 55] Herein, we present EA measured by LE-IPES. The electrochemical potential for the first reduction of molecular oxygen has been determined to be –0.33 V vs SHE at pH =7, with EA of -4.11 eV vs. vacuum [30 33, 56] and is illustrated in Fig. 1b. This implies that in order to ensure that this process is not thermodynamically favorable, the electron affinity of the polymer must be greater than this value.

### 4.3.1 Time Resolved Spectroelectrochemistry

To better understand the stability of the polymer series, we first resolved the spectra of negative polarons using spectroelectrochemistry (SEC) in 0.1M aqueous NaCl solution. For

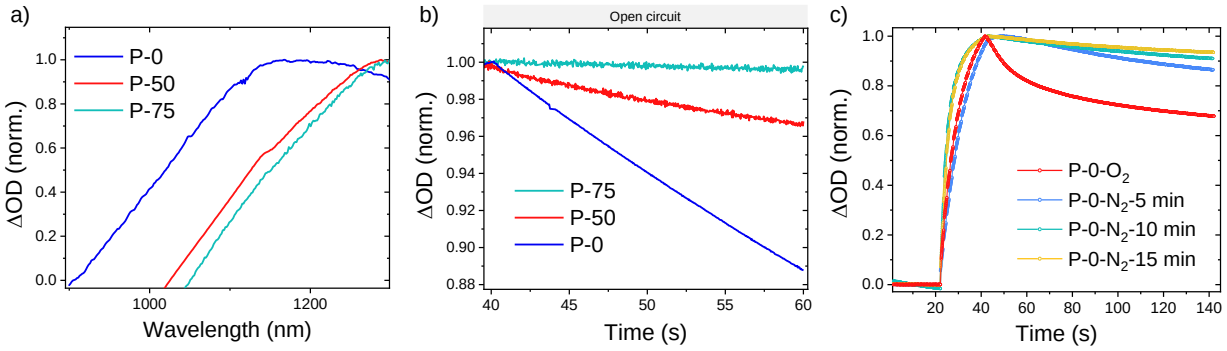


Fig. 2. a) Normalized spectroelectrochemical difference spectra of negative polarons in (P-0)-(P-75). b) The normalised decay kinetics of negative polarons in (P-0)-(P-75) at open circuit at -0.8V. c) Step-potential decay kinetics for negative polarons in air and after 5, 10, and 20 minutes of introducing nitrogen.

each polymer, a spectrum composed of a ground state bleach and an absorption in the near IR was observed to grow monotonically with decreasing bias (Figs. 2a and Supplementary Figs. 2a-c). This absorption is typically attributed to polaron states, [37] with a red-shifted absorption consistent with shifting EA of the polymer series. The stability of the series was investigated using time resolved spectroelectrochemistry. Here, a negative step in potential (-0.8 V) was applied to inject electrons into the conjugated backbone of the polymer. The potential was held for 20 s in order to approach a quasi-steady state, then switched to open circuit potential to investigate the inherent reactivity of injected charge in the absence of applied bias. To resolve kinetics, a wavelength dominated by the polaron absorption (1100, 1200, and 1300 nm) was chosen to compare the stability of polarons at open circuit, and all were found to be identical, indicating a single species monitored. (Supplementary Figs. 2a-c). At open circuit, the inherent activity of polarons in the species could be monitored by the rate of the decay of the optical signal. All polaron species are remarkably long lived, with at least 90% of the original signal persisting for 20s. A clear trend in longevity is observed, correlating with EA energies. P-0 signals decay by around 15% over the course of 20 s, while P-75 signals do not noticeably decay within this timeframe, as illustrated in Fig. 2b.

To investigate the nature of the degradation process in P-0, the least stable polymer, longer timescale step potential/potential decay measurements were performed in air and nitrogen degassed electrolyte. The kinetics of the decay of the polaron signal in P-0 is significantly retarded in the absence of oxygen upon introducing nitrogen, as shown in Fig. 2c, implicating oxygen in the mechanism of the degradation reaction. Overall, the trend in lifetime of negative polarons observed in the three polymers in air are consistent with the trend in EA. To further explore the generality of this observation, a range of state-of-art n-type OECT polymers were also evaluated. All polymers had an EA of less than 4.3 eV and all showed a decay of the negative polaron absorption in air. Supplementary Table.3 and Supplementary Figs. 3-7 provide additional details.

### 4.3.2 In-Situ Superoxide Detection by EPR spectroscopy

Solution-state continuous-wave Electron Paramagnetic Resonance (EPR) spectroscopy was used to verify the formation of superoxide radicals ($O_2^{\bullet-}$) through electron transfer from photoinduced negative polarons on the polymers to molecular oxygen. Since the reactive superoxide radicals are too short-lived for direct EPR detection, a spin trap was employed, which reacts with $O_2^{\bullet-}$ to form a relatively long-lived paramagnetic adduct that can be detected on the timescale of an EPR experiment. [57, 58] We used 5,5-dimethylpyrroline N-oxide (DMPO), which reacts with $O_2^{\bullet-}$ to form a DMPO-$OO^{\bullet-}$ adduct with an EPR spectrum characterized by a distinctive and well-defined spectral pattern determined by hyperfine couplings between the electron spin and the nitrogen and the β-hydrogen nuclei (Fig 3a).[58] Fig. 3b shows a representative dataset of EPR spectra recorded as a function of time before and during illumination for the P-0 polymer. The EPR spectra of all three polymers in the dark and after

ca. 30 minutes of illumination are shown in Fig. 3c (see Supplementary Figs. 8 and 10 for the full time-dependent measurements).

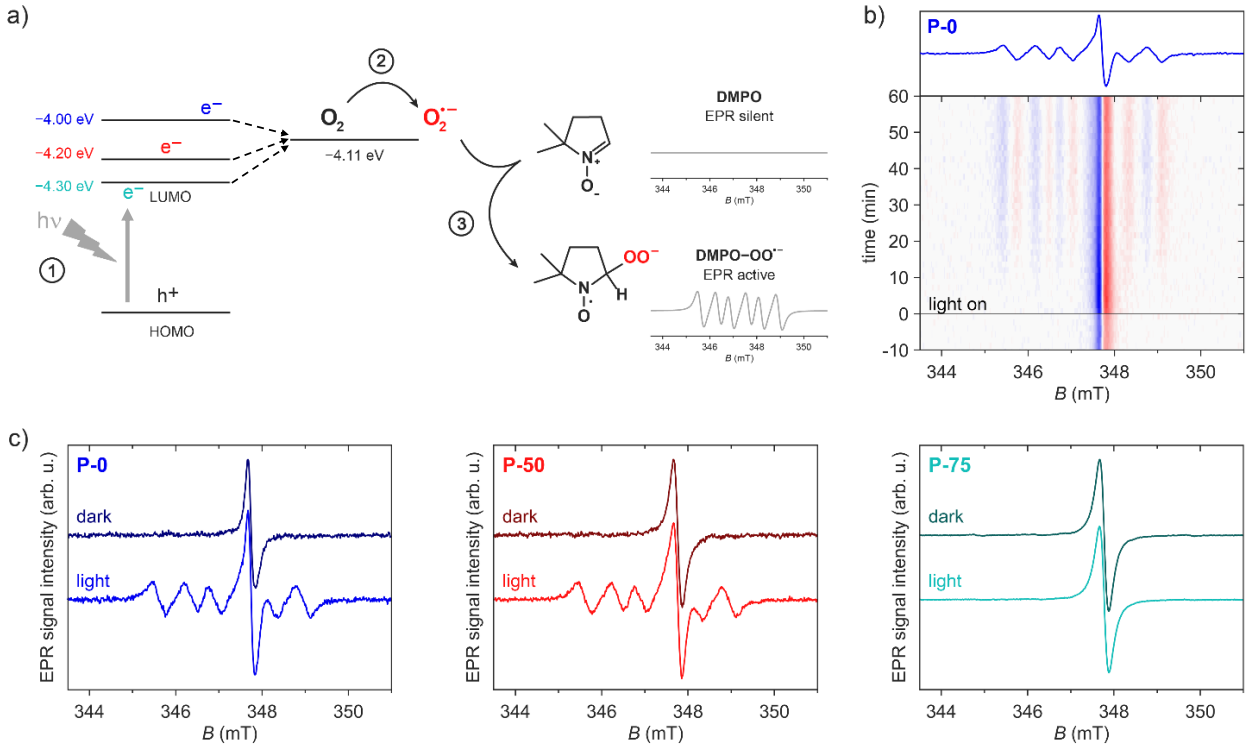


Fig. 3. a) Schematic illustration of superoxide generation after photoinduced polaron formation in the polymer, and formation of the EPR-active DMPO-OO$^{\bullet-}$ adduct. b) Representative EPR spectra measured as a function of time in the dark and under white-light illumination for P-0/CB//DMPO in air, the spectrum displayed on the top was obtained as an average of spectra recorded between 45 and 60 minutes after switching the light on. c) EPR spectra of P-0, P-50 and P-75 polymers recorded in the dark and under white-light illumination (see Supplementary Fig. S8 for details).

All three polymers exhibit a relatively strong EPR signal in the dark due to intrinsic paramagnetic centers, in agreement with previous EPR measurements on pristine polymer films.[37] Upon illumination of the P-0 and P-50 polymer solutions, an additional EPR signal is observed (Fig. 3c). This six-line EPR signal is well reproduced by simulations with a *g*-value of 2.0059, a $^{14}$N hyperfine coupling of 1.294 mT and a proton hyperfine coupling of 0.752 mT .(Supplementary Fig. 8), which are in agreement with reported values for the DMPO-superoxide adduct in solvents of similar polarity.[59] In contrast to the P-0 and P-50 polymers, no additional EPR signals were observed upon illumination of the P-75 polymer. The EPR

measurements demonstrate the formation of a DMPO-superoxide adduct and therefore superoxide generation following photoinduced polaron generation for the P-0 and P-50 polymers, whereas no superoxide radicals are generated for the P-75 polymer.

The double integral of an EPR signal is proportional to the number of spins contributing to it, allowing for the quantification of superoxide generated during illumination of P-0 and P-50 polymers in the presence of DMPO. For an accurate quantification, the experimental data was simulated as a sum of two contributions, and the double integral was determined for each contribution at each time point. (Supplementary Fig. 9c). For both P-0 and P-50, the concentration of DMPO-superoxide adduct increases with time. After 45 minutes illumination, the relative spin concentration of DMPO-$OO^{\bullet-}$ compared to the spin concentration of the polymer in the dark reached a factor of about 3.5 for P-0 and a factor of 2.2 for P-50. This correlates with time-resolved spectroelectrochemistry results showing a more significant oxygen-induced decay for P-0, with the smallest EA.

### 4.3.3 In-Situ Electrochemical Resonant Raman Spectroscopy

To evaluate the relative polymer stabilities and their degradation chemistry after an electrochemical reduction, *in situ* electrochemical resonant Raman spectroscopy (ERRS) was performed on thin films in 0.1 M NaCl aqueous electrolyte.[60, 61] This allows examination of the nature of electrochemical interactions and the specific chemistry of polymer degradation. The Raman peak assignment of the three polymers was assisted by DFT simulations and published literature,[62, 63, 64] (Supplementary Fig. S12), this allows the examination of changes to individual vibrational modes in order to pinpoint the functional groups where polymer degradation occur.[65] Here, we applied a high stress bias of -0.8 V for 10 minutes followed by 30 seconds of +0.2 V reverse voltage and use *in situ* Raman probe to measure the changes to

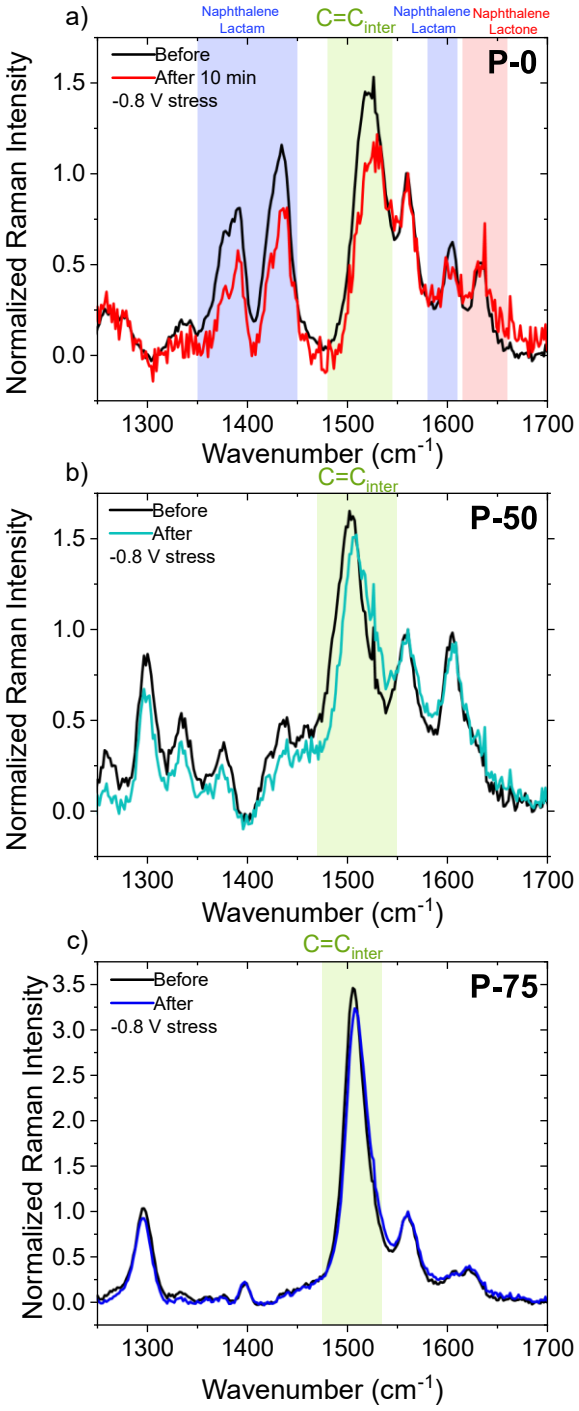


Fig. 4. *In situ* electrochemical Resonant Raman (ERRS) probe at 633 nm excitation in 0.1 M NaCl electrolyte under no bias of degradation after 10 minutes reductive stress for a) P-0, b) P-50 and c) P-75.

the vibrational modes before and after stress as shown in Fig 4. P-0 shows a poor reversibility of the Raman modes after -0.8 V bias stress (Fig. 4a). The overall Raman signal is greatly reduced (decrease in the maximum peak intensity to the order of $10^3$ counts compared to $10^4$ before stress). The relative peak intensity also shows a reduction in intensity of the 1518 $cm^{-1}$ peak, attributed to the C=C inter-ring vibration. Additionally, the Raman modes at 1392 and 1434 $cm^{-1}$ assigned to the naphthalene rings of the naphthalene lactam units show a 30% reduction from the initial relative peak intensity. However, the naphthalene lactone peak at 1632 $cm^{-1}$ returns to the initial peak intensity after high stress. This indicates the changes to the P-0 after stress are primarily centered on the naphthalene lactam units. Fig. 4b shows that the post stress Raman spectrum of P-50 is much less degraded, there are some changes in relative peak intensity, with a reduction of the C=C inter-ring peak and the lower wavenumber peaks from the aromatic modes of both the naphthalene and phenyl units. However, the degree of degradation in P-50 is much smaller than in P-0. Finally, Fig. 4c shows

the almost complete recovery for P-75, with a very minor relative peak intensity change to the C=C inter-ring but overall, there is a strong reversibility of all the Raman peaks indicating stable reversible redox behavior.

### 4.3.4 Organic electrochemical transistors

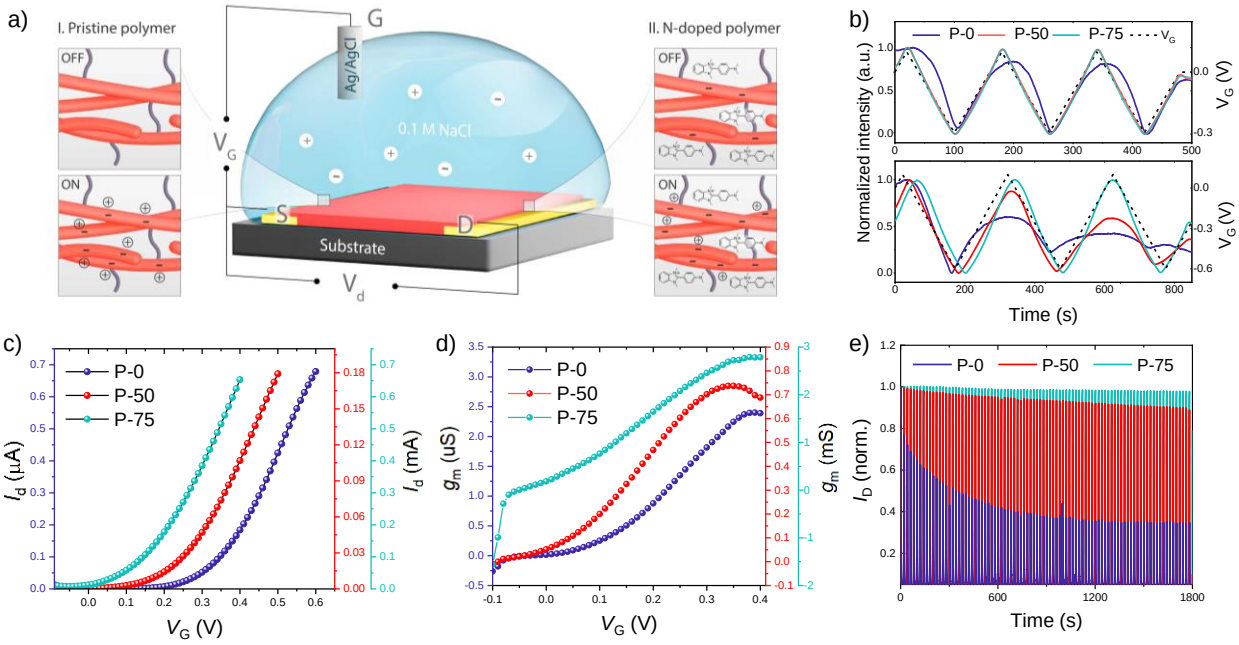


Fig. 5. a) An illustration of OECT device in pristine and molecular n-doped polymers. b) Probing absorption spectrum over three cycles of each polymer under low (top) and high (bottom) reductive stress. Representative c) transfer d) transconductance curves recorded for single channel of P-0, P-50, and P-75. e) Operational stability of OECTs under sequential square wave gate voltage for P-0, P-50, and P-75 transistors at ($V_G$ = 0.4 V, $V_D$ = 0.4 V, cycle length = 20 s)

We next evaluated the performance of the three polymers as active layer in OECT devices. Their electrochemical redox stability in a 0.1 M NaCl aqueous electrolyte was first evaluated using spectroelectrochemistry. All three polymers exhibit a gradual decrease in neutral absorption with increasing reduction potential, accompanied by a new absorption band (1100-1300 nm) assigned to polarons. (Supplementary Fig. 13a). The absorption spectrum was probed over three CV cycles under low and high reductive stress. Under –0.3 V, shown in Fig 5b, P-0 exhibited irreversible redox behavior, with the intensity of the absorption maximum decreasing

after each cycle, while P-50 and P-75 displayed stable redox behavior. This is evidence that P-0 displays poor electrochemical reversibility even at low reductive stress, indicating poor long-term devicestability. The redox stability of P-50 starts to decrease at a higher voltage (0.6 V), where P-75 sustains its reversible redox behavior up -0.6V. This irreversibility/reversibility is well aligned with the polymers' negative polaron decay behavior in time resolved spectroelectrochemistry and superoxide formation. Further details including SEC absorption color-maps and CV cycle analysis are presented in Supplementary Figs. 13b-15.

OECT devices were fabricated employing P-0 , P-50 and P-75 as the active channel layer with an aqueous 0.1 M NaCl electrolyte with an Ag/AgCl gate electrode, as demonstrated in Fig. 5a,. OECT figure of merits, namely, transconductance ($g_m$), and the product of charge-carrier mobility and volumetric capacitance ($\mu C^*$) were measured and calculated. The output characteristics recorded for each polymer can be found in (Supplementary Fig. 16), while characteristic transfer and transconductance curves are reported in Figs. 5c and d. Devices of P-0 displayed a moderate threshold voltage ($V_{th}$) (0.18 V) and low electron mobility, ($\mu_e$) ( ($3.12\times10^{-5}$ $cm^2$ $V^{-1}$ $s^{-1}$). In comparison, P-50 displayed a slightly lower $V_{th}$ (0.12 V) and significantly enhanced $\mu_e$ ($9.45\times10^{-3}$ $cm^2$ $V^{-1}$ $s^{-1}$). OECT devices of P-75 displayed a significantly lower $V_{th}$ (-0.02 V) and further enhanced $\mu_e$ (0.15 $cm^2$ $V^{-1}$ $s^{-1}$). The transconductance curves of the three polymers at varying gate voltage ($V_G$) are displayed in Fig. 5d. Both $g_m$ and $\mu C^*$ trends closely followed the mobility $\mu_e$ trends, with P-75 exhibiting the highest $g_m$ and $\mu C^*$ of 5.5 S $cm^{-1}$ and 14.76 F $cm^{-1}V^{-1}s^{-1}$, respectively. The corresponding OECT results are summarized in Table. 1. The transient response details can be found in Supplementary Fig. 18.

Stability measurements were conducted under sequential square wave gate voltage for 30 minutes in ambient conditions. As shown in Fig. 5e, P-0 showed the lowest stability, losing 65% of initial $I_d$, whereas P-50 showed improved stability, retaining 89% of initial current, and

P-75 demonstrated the highest stability, retaining 98% of initial current. Moreover, P-75, demonstrated OECT devices with state-of-the-art figures of merit, with $g_m$ of 12.5 S $cm^{-1}$ and $\mu C^*$ of 33.44 F $cm^{-1}V^{-1}s^{-1}$, when doped with ultra-low N-DMBI concentration (0.1 wt.%). The corresponding OECT characteristics, GIWAXS and EPR analysis of N-DMBI doped P-75 can be found in Extended Data Fig. 1, and Supplementary Figs. 19-22. A summary of OECT results can be found in Table.1

Table 3. Polymer OECT performance of three 'as casted' polymers and the best performing OECT devices of N- DMBI doped P-75 polymer

| ***Polymer*** | $V_{th}$ ***[V]*** | $g_m$ $[uS]^{[a]}$ | $g_{m,\,max,\,norm.}$ $(S\ cm^{-1})^{[b]}$ | $\mu_{sat,\,OECT}$ $(cm^2\ V^{-1}\ s^{-1})^{[c]}$ | $C^*$ $(F\ cm^{-3})^{[d]}$ | $\mu C^*$ $(F\ cm^{-1}\ V^{-1}\ s^{-1})^{[e]}$ |
|---|---|---|---|---|---|---|
| P-0 | 0.18 ± 0.01 | 2.8 | (9.44 ± 1.47) $x10^{-4}$ | $3.12x10^{-5}$± 5.3 $x10^{-6}$ | 93.4 ± 16.3 | 2.90 $x10^{-3}$ ±5.00 $x10^{-4}$ |
| P-50 | 0.12 ± 0.02 | 730 | 0.35 ± 0.051 | (9.45 ±1.42) $x10^{-3}$ | 97.7 ± 10.9 | 0.92 ± 0.14 |
| P-75 | -0.02 ± 0.02 | 2800 | 5.5 ± 1.57 | 0.15 ± 0.04 | 98.4 ± 2.76 | 14.76 ± 0.04 |

[a] Peak transconductance extracted from the transfer curve at saturation regime. [b] Extracted from the slope of OECT transfer curves and normalized by channel thickness and aspect ratio. [c] Saturation mobility extracted from the slope of $I_D$ vs. $V_G$. [d] Volumetric capacitance measured with electrochemical impedance spectroscopy (See Supplementary Figs. 17.). [e] The product of the saturation mobility and the volumetric capacitance. The reported uncertainties of the three "as casted" polymers are based on data from six devices (n = 6).

## 4.4 Conclusions

We present evidence to demonstrate that semiconducting polymers with an electron affinity less than the threshold for molecular superoxide formation, exhibit reduced ambient electrochemical stability and subsequently, when operated in OECT devices, exhibit reduced OECT performance. Time resolved spectroelectrochemistry experiments conducted in an electrochemical environment revealed that P-75 polymer with the largest EA, exhibited no decay in air, and an absence of superoxide formation, whereas the P-50 and P-0 polymers with smaller EA values showed a noticeable decay in air attributed to degradation arising from superoxide formation and its subsequent reactive species in water, for P-0 and P-50, but not P-

75. The results were further supported by EPR spin trapping experiments, which demonstrated the absence of superoxide formation from photoinduced polarons of P-75 and its presence in P-50 and P-0, with increased generation of superoxide arising from the P-0 polymer, with the smallest EA. These observations have been shown to correlate with the polymers electrochemical behavior, which indicated an increasing trend in redox reversibility from P-0 to P-75, as well as in-situ electrochemical resonant Raman spectroscopy, which showed an increasing trend in resilience in chemical degradation from P-0 to P-75 as evidenced by full structural recovery after electrochemical charging/discharging. The subsequent performance of OECT devices correlated directly with these trends in polymer reversibility, with P-75, demonstrating excellent performance, achieving a $g_m$ of 5.5 S $cm^{-1}$ and $\mu C^*$ of 14.8 F $cm^{-1}$ $V^{-1}$ $s^{-1}$, while also maintaining a stable device operation. Doping P-75 with N-DMBI enabled further improvement in n-type OECT performance with high $g_m$ and $\mu C^*$ of 12.50 S $cm^{-1}$ and 14.8 and 33.44 F $cm^{-1}$ $V^{-1}$ $s^{-1}$, at relatively low doping levels, arising from an improved electron mobility and charge carrier concentration. These results establish a precedent for the importance of superoxide-free device operation, facilitated by conjugated polymers with large electron affinities to improve the stability and performance of n-type organic electrochemical transistors. This progress is a significant step towards practical applications that demand avoidance of such parasitic side reactions.

## Acknowledgment

The authors acknowledge financial support from KAUST Office of Sponsored Research CRG10, by EU Horizon2020 grant agreement n°952911, BOOSTER, grant agreement n°862474, RoLA-FLEX, and grant agreement n°101007084 CITYSOLAR, as well as EPSRC Projects EP/T026219/1, EP/W017091/1, and EP/L011972/1. C.E.T. would like to acknowledge support from the Royal Society through grant URF\R1\201071. 

Accepted Manuscript (AAM) version arising from this submission. K.S. and J.-S.K. would like to acknowledge the UK EPSRC for funding through both the ATIP Programme Grant (EP/T028513/10) and the Plastic Electronics Centre for Doctoral Training (EP/L016702/1), and the Imperial College High Performance Computing Service for DFT calculations.

## 4.5 References

1. Zhao W, Ding J, Zou Y, Di CA, Zhu D. Chemical doping of organic semiconductors for thermoelectric applications. *Chem Soc Rev* 2020, **49**(20)**:** 7210-7228.

2. Lu Y, Yu ZD, Liu Y, Ding YF, Yang CY, Yao ZF, *et al.* The Critical Role of Dopant Cations in Electrical Conductivity and Thermoelectric Performance of n-Doped Polymers. *J Am Chem Soc* 2020, **142**(36)**:** 15340-15348.

3. Rivnay J, Inal S, Salleo A, Owens RM, Berggren M, Malliaras GG. Organic electrochemical transistors. *Nature Reviews Materials* 2018, **3**(2).

4. Alsufyani M, Stoeckel MA, Chen X, Thorley K, Hallani RK, Puttisong Y, *et al.* Lactone Backbone Density in Rigid Electron-Deficient Semiconducting Polymers Enabling High n-type Organic Thermoelectric Performance. *Angew Chem Int Ed Engl* 2021.

5. Torricelli F, Adrahtas DZ, Bao Z, Berggren M, Biscarini F, Bonfiglio A, *et al.* Electrolyte-gated transistors for enhanced performance bioelectronics. *Nature Reviews Methods Primers* 2021, **1**(1)**:** 1-24.

6. Lee W, Kim D, Matsuhisa N, Nagase M, Sekino M, Malliaras GG, *et al.* Transparent, conformable, active multielectrode array using organic electrochemical transistors. *Proceedings of the National Academy of Sciences* 2017, **114**(40)**:** 10554-10559.

7. Dimov IB, Moser M, Malliaras GG, McCulloch I. Semiconducting polymers for neural applications. *Chemical Reviews* 2022, **122**(4)**:** 4356-4396.

8. van De Burgt Y, Melianas A, Keene ST, Malliaras G, Salleo A. Organic electronics for neuromorphic computing. *Nature Electronics* 2018, **1**(7)**:** 386-397.

9. Liu Y, Liu J, Chen S, Lei T, Kim Y, Niu S, *et al.* Soft and elastic hydrogel-based microelectronics for localized low-voltage neuromodulation. *Nature biomedical engineering* 2019, **3**(1)**:** 58-68.

10. Wang S, Xu J, Wang W, Wang G-JN, Rastak R, Molina-Lopez F, *et al.* Skin electronics from scalable fabrication of an intrinsically stretchable transistor array. *Nature* 2018, **555**(7694)**:** 83-88.

11. Ma Z, Kong D, Pan L, Bao Z. Skin-inspired electronics: Emerging semiconductor devices and systems. *Journal of Semiconductors* 2020, **41**(4)**:** 041601.

12. Khodagholy D, Doublet T, Gurfinkel M, Quilichini P, Ismailova E, Leleux P, *et al.* Highly conformable conducting polymer electrodes for in vivo recordings. *Advanced Materials* 2011, **23**(36)**:** H268-H272.

13. Khodagholy D, Doublet T, Quilichini P, Gurfinkel M, Leleux P, Ghestem A, *et al.* In vivo recordings of brain activity using organic transistors. *Nature communications* 2013, **4**(1)**:** 1-7.

14. Strakosas X, Donahue MJ, Hama A, Braendlein M, Huerta M, Simon DT, *et al.* Biostack: Nontoxic Metabolite Detection from Live Tissue. *Advanced Science* 2022, **9**(2)**:** 2101711.

15. Leleux P, Rivnay J, Lonjaret T, Badier JM, Bénar C, Hervé T, *et al.* Organic electrochemical transistors for clinical applications. *Advanced Healthcare Materials* 2015, **4**(1)**:** 142-147.

16. Inal S, Malliaras GG, Rivnay J. Benchmarking organic mixed conductors for transistors. *Nature communications* 2017, **8**(1)**:** 1-7.

17. Rivnay J, Leleux P, Sessolo M, Khodagholy D, Hervé T, Fiocchi M, *et al.* Organic electrochemical transistors with maximum transconductance at zero gate bias. *Advanced Materials* 2013, **25**(48)**:** 7010-7014.

18. Savagian LR, Österholm AM, Ponder Jr JF, Barth KJ, Rivnay J, Reynolds JR. Balancing charge storage and mobility in an Oligo (Ether) functionalized dioxythiophene copolymer for organic-and aqueous-based electrochemical devices and transistors. *Advanced Materials* 2018, **30**(50)**:** 1804647.

19. Giovannitti A, Sbircea D-T, Inal S, Nielsen CB, Bandiello E, Hanifi DA, *et al.* Controlling the mode of operation of organic transistors through side-chain engineering. *Proceedings of the National Academy of Sciences* 2016, **113**(43)**:** 12017-12022.

20. Druet V, Nayak PD, Koklu A, Ohayon D, Hama A, Chen X, *et al.* Operation Mechanism of n-Type Organic Electronic Metabolite Sensors. *Advanced Electronic Materials* 2022, **8**(10)**:** 2200065.

21. Lee SW, Lee KY, Song YW, Choi WK, Chang J, Yi H. Direct electron transfer of enzymes in a biologically assembled conductive nanomesh enzyme platform. *Advanced Materials* 2016, **28**(8)**:** 1577-1584.

22. Liu Y, Wang M, Zhao F, Xu Z, Dong S. The direct electron transfer of glucose oxidase and glucose biosensor based on carbon nanotubes/chitosan matrix. *Biosensors and Bioelectronics* 2005, **21**(6)**:** 984-988.

23. Sun H, Vagin M, Wang S, Crispin X, Forchheimer R, Berggren M, *et al.* Complementary logic circuits based on high-performance n-type organic electrochemical transistors. *Advanced Materials* 2018, **30**(9)**:** 1704916.

24. Wu HY, Yang CY, Li Q, Kolhe NB, Strakosas X, Stoeckel MA, *et al.* Influence of Molecular Weight on the Organic Electrochemical Transistor Performance of Ladder-Type Conjugated Polymers. *Advanced Materials* 2022, **34**(4)**:** 2106235.

25. Li X, Li Y, Sarang K, Lutkenhaus J, Verduzco R. Side-Chain Engineering for High-Performance Conjugated Polymer Batteries. *Advanced Functional Materials* 2021, **31**(14)**:** 2009263.

26. Liang Y, Chen Z, Jing Y, Rong Y, Facchetti A, Yao Y. Heavily n-dopable π-conjugated redox polymers with ultrafast energy storage capability. *Journal of the American Chemical Society* 2015, **137**(15)**:** 4956-4959.

27. Liang Y, Zhang P, Chen J. Function-oriented design of conjugated carbonyl compound electrodes for high energy lithium batteries. *Chemical Science* 2013, **4**(3)**:** 1330-1337.

28. De Leeuw D, Simenon M, Brown A, Einerhand R. Stability of n-type doped conducting polymers and consequences for polymeric microelectronic devices. *Synthetic Metals* 1997, **87**(1)**:** 53-59.

29. Vasudevan D, Wendt H. Electroreduction of oxygen in aprotic media. *Journal of Electroanalytical Chemistry* 1995, **392**(1-2)**:** 69-74.

30. Wood PM. The potential diagram for oxygen at pH 7. *Biochemical Journal* 1988, **253**(1)**:** 287.

31. Zhuo JM, Zhao LH, Png RQ, Wong LY, Chia PJ, Tang JC, *et al.* Direct Spectroscopic Evidence for a Photodoping Mechanism in Polythiophene and Poly (bithiophene-alt-thienothiophene) Organic Semiconductor Thin Films Involving Oxygen and Sorbed Moisture. *Advanced materials* 2009, **21**(46)**:** 4747-4752.

32. Giovannitti A, Rashid RB, Thiburce Q, Paulsen BD, Cendra C, Thorley K, *et al.* Energetic Control of Redox-Active Polymers toward Safe Organic Bioelectronic Materials. *Adv Mater* 2020, **32**(16)**:** e1908047.

33. Vagin M, Gueskine V, Mitraka E, Wang S, Singh A, Zozoulenko I, *et al.* Negatively-Doped Conducting Polymers for Oxygen Reduction Reaction. *Advanced Energy Materials* 2020, **11**(3).

34. Druet V, Nayak PD, Koklu A, Ohayon D, Hama A, Chen X, *et al.* Operation Mechanism of n-Type Organic Electronic Metabolite Sensors. *Advanced Electronic Materials* 2022, **8**(10).

35. Durán ADLF, Liang AY-L, Denti I, Yu H, Pearce D, Marks A, *et al.* Origins of hydrogen peroxide selectivity during oxygen reduction on organic mixed ionic-electronic conducting polymers. 2022.

36. Jalilov AS, Nilewski LG, Berka V, Zhang C, Yakovenko AA, Wu G, *et al.* Perylene Diimide as a Precise Graphene-like Superoxide Dismutase Mimetic. *ACS Nano* 2017, **11**(2)**:** 2024-2032.

37. Alsufyani M, Stoeckel MA, Chen X, Thorley K, Hallani RK, Puttisong Y, *et al.* Lactone Backbone Density in Rigid Electron-Deficient Semiconducting Polymers Enabling High n-type Organic Thermoelectric Performance. *Angewandte Chemie* 2022, **134**(7)**:** e202113078.

38. Yan X, Xiong M, Li J-T, Zhang S, Ahmad Z, Lu Y, *et al.* Pyrazine-flanked diketopyrrolopyrrole (DPP): a new polymer building block for high-performance n-type organic thermoelectrics. *Journal of the American Chemical Society* 2019, **141**(51)**:** 20215-20221.

39. Shi K, Zhang F, Di C-A, Yan T-W, Zou Y, Zhou X, *et al.* Toward high performance n-type thermoelectric materials by rational modification of BDPPV backbones. *Journal of the American Chemical Society* 2015, **137**(22)**:** 6979-6982.

40. Wang S, Sun H, Erdmann T, Wang G, Fazzi D, Lappan U, *et al.* A chemically doped naphthalenediimide-bithiazole polymer for n-type organic thermoelectrics. *Advanced Materials* 2018, **30**(31)**:** 1801898.

41. Wang Y, Takimiya K. Naphthodithiophenediimide–Bithiopheneimide Copolymers for High-Performance n-Type Organic Thermoelectrics: Significant Impact of Backbone Orientation on Conductivity and Thermoelectric Performance. *Advanced Materials* 2020, **32**(30)**:** 2002060.

42. Liu J, Qiu L, Alessandri R, Qiu X, Portale G, Dong J, *et al.* Enhancing Molecular n-Type Doping of Donor–Acceptor Copolymers by Tailoring Side Chains. *Advanced Materials* 2018, **30**(7)**:** 1704630.

43. Liu J, Ye G, Potgieser HG, Koopmans M, Sami S, Nugraha MI, *et al.* Amphipathic Side Chain of a Conjugated Polymer Optimizes Dopant Location toward Efficient N-Type Organic Thermoelectrics. *Advanced Materials* 2021, **33**(4)**:** 2006694.

44. Wang S, Sun H, Ail U, Vagin M, Persson P. Å.; Andreasen JW; Thiel W.; Berggren M.; Crispin X.; Fazzi D.; Fabiano S. *Thermoelectric Properties of Solution-Processed n-Doped Ladder-Type Conducting Polymers Adv Mater* 2016, **28:** 10764-10771.

45. Alsufyani M, Hallani RK, Wang S, Xiao M, Ji X, Paulsen BD, *et al.* The effect of aromatic ring size in electron deficient semiconducting polymers for n-type organic thermoelectrics. *Journal of Materials Chemistry C* 2020, **8**(43)**:** 15150-15157.

46. Lu Y, Yu ZD, Zhang RZ, Yao ZF, You HY, Jiang L, *et al.* Rigid coplanar polymers for stable n-type polymer thermoelectrics. *Angewandte Chemie* 2019, **131**(33)**:** 11512-11516.

47. Dong C, Deng S, Meng B, Liu J, Wang L. A Distannylated Monomer of a Strong Electron-Accepting Organoboron Building Block: Enabling Acceptor–Acceptor-Type Conjugated Polymers for n-Type Thermoelectric Applications. *Angewandte Chemie* 2021, **133**(29)**:** 16320-16326.

48. Onwubiko A, Yue W, Jellett C, Xiao M, Chen H-Y, Ravva MK, *et al.* Fused electron deficient semiconducting polymers for air stable electron transport. *Nature communications* 2018, **9**(1)**:** 1-9.

49. Tang H, Liang Y, Liu C, Hu Z, Deng Y, Guo H, *et al.* A solution-processed n-type conducting polymer with ultrahigh conductivity. *Nature* 2022, **611**(7935)**:** 271-277.

50. Ke Z, Abtahi A, Hwang J, Chen K, Chaudhary J, Song I, *et al.* Highly Conductive and Solution-Processable n-Doped Transparent Organic Conductor. *J Am Chem Soc* 2023, **145**(6)**:** 3706-3715.

51. Bertrandie J, Han J, De Castro CSP, Yengel E, Gorenflot J, Anthopoulos T, *et al.* The Energy Level Conundrum of Organic Semiconductors in Solar Cells. *Adv Mater* 2022, **34**(35)**:** e2202575.

52. Zhou X, Zhang J, Bai G, Wang C, He W, Sun X, *et al.* A novel energy level detector for molecular semiconductors. *Physical Chemistry Chemical Physics* 2022, **24**(5)**:** 2717-2728.

53. Yoshida H. Low-energy inverse photoemission study on the electron affinities of fullerene derivatives for organic photovoltaic cells. *The Journal of Physical Chemistry C* 2014, **118**(42)**:** 24377-24382.

54. Cardona CM, Li W, Kaifer AE, Stockdale D, Bazan GC. Electrochemical considerations for determining absolute frontier orbital energy levels of conjugated polymers for solar cell applications. Wiley Online Library; 2011.

55. Bertrandie J, Han J, De Castro CS, Yengel E, Gorenflot J, Anthopoulos T, *et al.* The energy level conundrum of organic semiconductors in solar cells. *Advanced Materials* 2022, **34**(35)**:** 2202575.

56. Trasatti S. The absolute electrode potential: an explanatory note (Recommendations 1986). *Pure and Applied Chemistry* 1986, **58**(7)**:** 955-966.

57. Villamena F. Chapter 5-EPR spin trapping. *Reactive Species Detection in Biology, edited by: Villamena, FA, Elsevier, Boston, USA* 2017**:** 163-202.

58. Buettner GR. Spin Trapping: ESR parameters of spin adducts 1474 1528V. *Free radical biology and medicine* 1987, **3**(4)**:** 259-303.

59. Harbour JR, Hair ML. Detection of superoxide ions in nonaqueous media. Generation by photolysis of pigment dispersions. *The Journal of Physical Chemistry* 1978, **82**(12)**:** 1397-1399.

60. Nightingale J, Wade J, Moia D, Nelson J, Kim J-S. Impact of molecular order on polaron formation in conjugated polymers. *The Journal of Physical Chemistry C* 2018, **122**(51)**:** 29129-29140.

61. Luke J, Speller EM, Wadsworth A, Wyatt MF, Dimitrov S, Lee HK, *et al.* Twist and degrade—impact of molecular structure on the photostability of nonfullerene acceptors and their photovoltaic blends. *Advanced Energy Materials* 2019, **9**(15)**:** 1803755.

62. Preuss M, Bechstedt F. Vibrational spectra of ammonia, benzene, and benzene adsorbed on Si (001) by first principles calculations with periodic boundary conditions. *Physical Review B* 2006, **73**(15)**:** 155413.

63. Hewett KB, Shen M, Brummel CL, Philips LA. High resolution infrared spectroscopy of pyrazine and naphthalene in a molecular beam. *The Journal of chemical physics* 1994, **100**(6)**:** 4077-4086.

64. Razzell-Hollis J, Wade J, Tsoi WC, Soon Y, Durrant J, Kim J-S. Photochemical stability of high efficiency PTB7: PC 70 BM solar cell blends. *Journal of Materials Chemistry A* 2014, **2**(47)**:** 20189-20195.

65. Wood S, Wade J, Shahid M, Collado-Fregoso E, Bradley DD, Durrant JR, *et al*. Natures of optical absorption transitions and excitation energy dependent photostability of diketopyrrolopyrrole (DPP)-based photovoltaic copolymers. *Energy & Environmental Science* 2015, **8**(11)**:** 3222-3232.

# 4.6 Extended Data

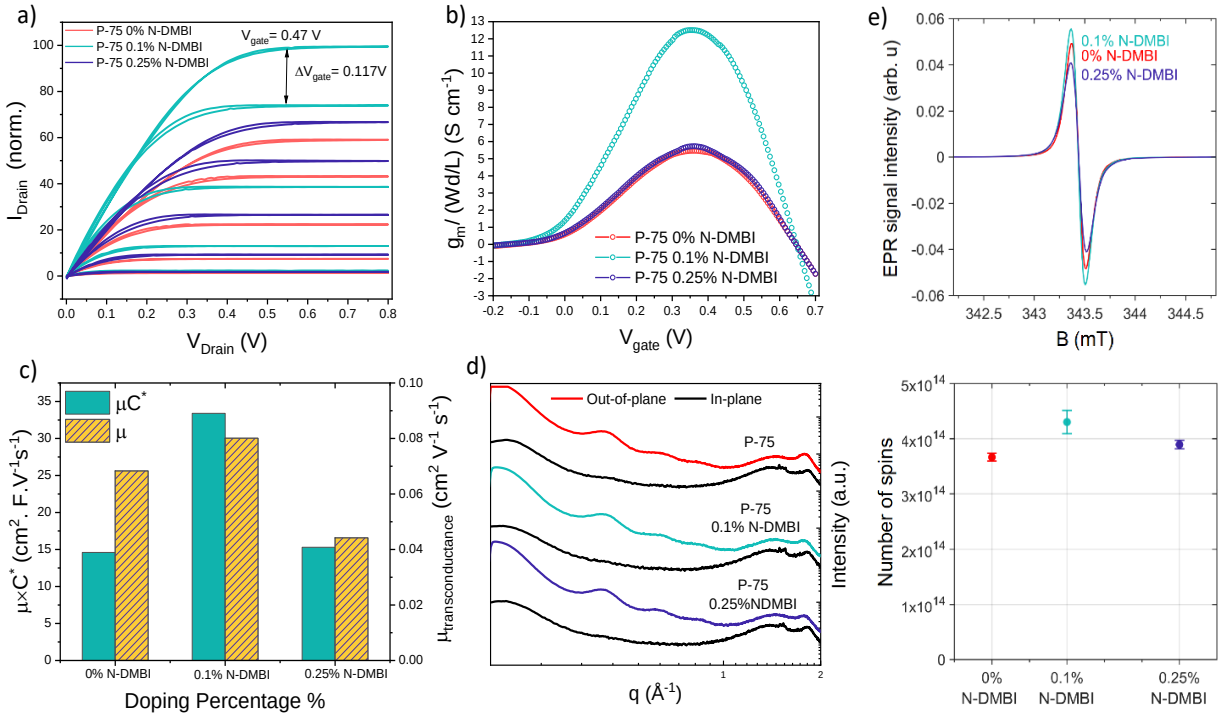


Extended Data Fig. 1. P-75, was doped with N-DMBI, [1] a widely used n-dopant, in solution, and NaCl electrolyte gated OECT were tested over a range of dopant concentrations (0, 0.1, and 0.25 wt.%).) **a)-b)** Normalized output and transconductance curves obtained for the three dopant concentrations . Data for transfer curves was collected at $V_D$=0.7 V and output curves were obtained for different gate voltages starting from $V_{gate}$= 0 and increasing in 0.117V steps up to $V_G$= 0.47 V. (P-75-0.1% N-DMBI) displayed the best performing device with an extremely low threshold voltage of -0.025 V, an enhanced volumetric capacitance of 418 F $cm^{-3}$, a $g_{m,\,norm}$ of 12.5 S $cm^{-1}$ and $\mu C^*$ of 33.44 F $cm^{-1}V^{-1}s^{-1}$. OECT results of the highest performing devices are summarized in Table.1. ***c)*** The effect of varying the dopant concentration on electron mobility and $\mu C^*$. ***d)*** Grazing incidence wide angle X-ray scattering (GIWAXS) is used to investigate the impact of N-DMBI on P-75 microstructure and morphology. As shown in Figure. 5d and Supplementary Fig. 22, P-75 with 0, 0.1 and 0.25 wt.% NDMBI, show an isotropic amorphous scattering ring centered near 1.5 $Å^{-1}$. At 0.1% doping , significant differences were observed on i) the film texture, as it transitions from face-on orientation to a preference for edge- and face-on orientation, ii) π-π coherence length (Lc) (extracted from FWHM of (010) peak), which expanded from 35.79 to 41.27 Å, both observations are aligned with the improved OECT performance at 0.1% doping level. Lamellar and π-π distances showed negligible changes, indicating an undisturbed polymer microstructure despite NDMBI's large size and π-system, contrary to the substantial disturbance in the polymer ordering that has been noted in heavily doped polymers[2]. **e)** EPR spectra recorded for undoped and doped P-75 polymer and detected number of spins as a function of doping concentration. Doping with N-DMBI at low concentrations (0.1 wt.%) increased the EPR signal, confirming an increase in charge density, as confirmed by spin quantification. However, at higher doping concentration (0.25 wt.%), the EPR signal decreased in amplitude. The presence of 0.1 wt.% dopant represents a threshold level for decreasing polaron concentration due to bipolaron formation through polaron-polaron interactions, and matches a previous report on P-75 films with high dopant concentrations.[4] Both GIWAXS and EPR results suggest that ultra-low doping concentrations do not disturb film microstructure, resulting in improved OECT performance. Further details can be found in Supplementary Figs. 19-22.

Extended Data Table 1. OECT performance of molecularly n-doped P-75 polymer

| **Doping level** | $V_T\ [V]$ | $g_m\ [mS]$ [a] | $\frac{g_m}{Wd/L}$ $[\mathrm{S\ cm^{-1}}]$ [b] | $\mu$ $[\frac{cm^2}{Vs}]$ [c] | $\mu_{transient}$ $[\frac{cm^2}{Vs}]$ [d] | $C^*$ $[Fcm^{-3}]$ [e] | $\mu_{transient} * C^*$ $[Fcm^{-1}V^{-1}s^{-1}]$ [f] | $\mu * C^*$ $[Fcm^{-1}V^{-1}s^{-1}]$ [g] |
|---|---|---|---|---|---|---|---|---|
| P-75 (0%NDMBI) | $-0.014$ | 0.21 | 5.46 | 0.058 | 5.36 x $10^{-4}$ | 250 | 0.13 | 14.55 |
| P-75 (0.1%NDMBI) | $-0.025$ | 0.3 | 12.50 | 0.08 | 0.0031 | 418 | 1.28 | 33.44 |
| P-75 (0.25%NDMBI) | $-0.012$ | 0.29 | 5.73 | 0.044 | 0.0025 | 346 | 0.88 | 15.31 |

[a] Peak transconductance extracted from the transfer curve at saturation regime. [b] Peak transconductance extracted from the transfer curve at saturation regime and normalized by channel thickness and aspect ratio. [c] Saturation mobility obtained from the peak transconductance.[d] Mobility obtained from transient method. [e] Volumetric capacitance measured with electrochemical impedance spectroscopy (See Supplementary Fig. 21). [f] The product of the transient mobility and the volumetric capacitance.[g] The product of the saturation mobility and the volumetric capacitance.

# 4.6 Statement of authorship

**Statement of Authorship for joint/multi-authored papers for PGR thesis**

To appear at the end of each thesis chapter submitted as an article/paper

The statement shall describe the candidate's and co-authors' independent research contributions in the thesis publications. For each publication there should exist a complete statement that is to be filled out and signed by the candidate and supervisor **(only required where there isn't already a statement of contribution within the paper itself).**

| | |
|---|---|
| Title of Paper | The effect of organic semiconductor electron affinity on the operando generation of superoxide radical anions in organic electrochemical transistors |
| Publication Status | □ Published □ Accepted for Publication<br>✓Submitted for Publication □Unpublished and unsubmitted work written in a manuscript style |
| Publication Details | Alsufyani, M., Benjamin, M., Tait, C.E., Myers, W.K., Shahi, M., Stewart, k., Zhao ,X., Rashid, M., Meli, D., Wu, R., Paulsen, B.D., Thorley, K., Lin, Y., Combe. C., Kniebe-Evans, C., Inal, S., Ritchie, G., Kim, J-S., Rivnay , J., Paterson, A., Durrant, J.R., & McCulloch, I. (2022). The effect of organic semiconductor electron affinity on the operando generation of superoxide radical anions in organic electrochemical transistors. Nature Chemistry, Submitted, 2023. |

Student Confirmation

| | | | |
|---|---|---|---|
| Student Name: | Maryam Alsufyani | | |
| Contribution to the Paper | M.A carried out time resolved spectroelectrochemistry, in-Situ Superoxide Detection by EPR spectroscopy, cyclic voltammetry, Electron Paramagnetic Spectroscopy of N-DMBI doped P-75 film, analyzed and interpreted the data, and wrote the manuscript. B.M trained and aided M.A for time resolved spectroelectrochemistry experiments. C.T and W.M, trained and aided M.A for in-Situ Superoxide Detection by EPR spectroscopy experiments. C.T plotted and interpreted the superoxide detection data and performed EPR simulations. M.S fabricated OECT devices of n-dope polymers. K.S, performed In situ electrochemical resonant Raman spectroscopy (ERRS). K.T performed DFT calculations. X.Z performed OECT operational stability and transient response of pristine polymers. R.R, D.M, fabricated OECT devices of pristine polymers, R.W, performed spectroelectrochemical reversibility of the pristine polymers. B.P aided in interpreting the OECT section. K.J, J.R, A.P, J.D supervised the work done by their group members. I.M supervised the entire work, and made significant contributions to writing, reviewing and refining the manuscript. | | |
| Signature |  | Date | 31/08/2023 |

Supervisor Confirmation

By signing the Statement of Authorship, you are certifying that the candidate made a substantial contribution to the publication, and that the description described above is accurate.

| | | |
|---|---|---|
| Supervisor name and title: Professor Iain McCulloch FRS | | |
| Supervisor comments | | |
|  | Date | 01/09/2023 |

This completed form should be included in the thesis, at the end of the relevant chapter.

# Chapter 5

## Experimental procedures

Disclaimer: The numbering of the headings in the supplementary information has been adjusted to align with the formatting used in this thesis, differing from the originally published or submitted files, and is the only adjustment applied to the original files.

# 5.1 Supplementary information for chapter 2

## 5.1.1 General procedures and experimental details

All chemical reagents and starting materials were purchased from commercial sources and used without further purification. Reactions were carried out on a standard Schlenk line technique under a nitrogen atmosphere using solvents and reagents as commercially supplied.

$^{1}$H NMR and $^{13}$C NMR spectra were recorded with Bruker 500 MHz AVANCE III NMR spectrometer equipped with CryoProbe (BrukerBioSpin,Rheinstetten, Germany). Residual proton peaks are 7.26 ppm for $CDCl_3$ and 2.52 ppm for DMSO-$d_6$. High-resolution Mass Spectra (HRMS) were recorded on a Bruker HRMS MICROTOF II spectrometer. Gas Chromatography-Mass Spectrometry (GC-MS) measurements were carried out on Angilent 7890B GC system with Agilent 5977A MSD, and Agilent 7693 auto sampler. The polymer molecular weights (number-average $M_n$ and weight-average $M_w$) and polydispersity were measured using an Agilent Technologies PL-GPC 220 High Temperature gel permeation chromatography in 1,2,4-trichlorobenezene (TCB) as the mobile phase at 150 °C. Absorption spectra were recorded on Varian Cary 5000 spectrophotometer by preparing polymer solutions in chlorobenzene and spin-coated polymer films onto pre-treated glass substrates. Photo Electron Spectroscopy in Air (PESA) measurements were recorded with a Riken Keiki AC-2 PESA spectrometer with a power setting of 5 nW and a power number of 0.3. Samples for PESA were prepared on glass substrates by spin-coating. Thermal gravimetric analyses (TGA) were performed under a $N_2$ atmosphere using TA Instruments Trios V4.3.1.39215, at a heating rate of 10 °C min$^{-1}$. Differential scanning calorimetry (DSC) analyses were performed on a METTLER TOLEDO Instrument DSC822 calorimeter with a heating rate of 10 °C min$^{-1}$, two heating-cooling cycles from RT to- 300 °C under nitrogen atmosphere.

Density functional theory (DFT) calculations were performed on tetramers of the three polymers. In each case, the long solubilizing alkyl chains were replaced by shorter methyl

groups in order to simplify the simulations. All calculations were performed employing the Gaussian-09 software. All geometries were optimized at the ωB97XD/6-31G** level of theory without any constraints.

## 5.1.2 Synthetic routes of the compounds

The synthetic procedures for the preparation of (4-Bromobutyl)tricosane (R1), (4-Bromobutyl)nonadecane (R2)[1], Bisisatin, *N,N'*-bis(5-decylheptadecyl), bisisatin (M1), *N,N'*-bis(5-octylpentadecyl)bisisatin(M2)[2], benzo[1,2-*b*-4,5-*b'*]difuran-2,6-(3*H*,7*H*)-dione (M3)[3] and naphtho-[1,2-*b:*5,6-*b'*]difuran-2,7(3*H*, 8*H*)-dione (M4)[4] were inspired and modified from published literatures. Starting materials 2-decyl-1-tetradecanol, and 2-Octyl-1-dodecanol, were purchased from Sigma-Aldrich. Other reagents were purchased from Sigma-Aldrich, Alfa Aesar, and Fisher Scientific.

**Synthesis of the Alkyl chains**

**Synthesis of (4-Bromobutyl)tricosane (R1) :**

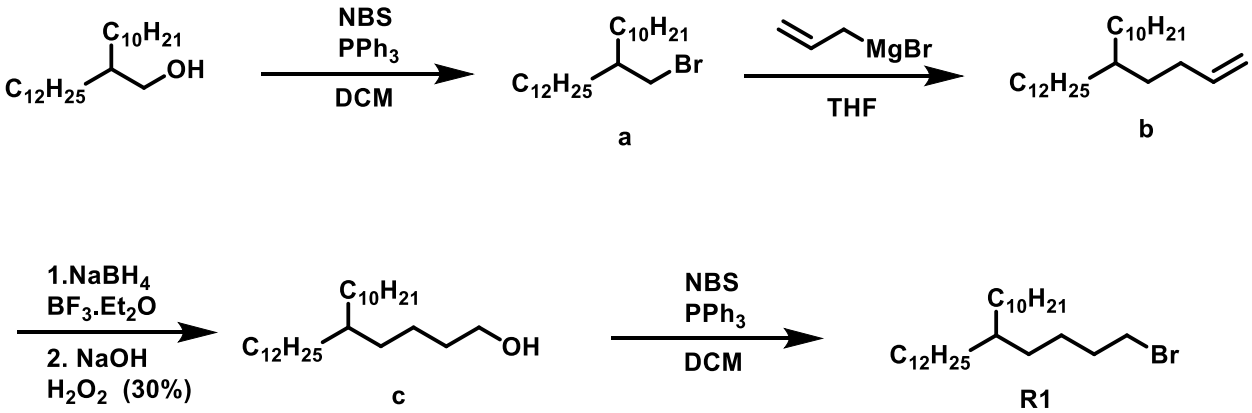


**Synthesis of (a):** NBS (25 g, 140 mmol) was added slowly in portions to a solution of 2-decyl-1-tetradecanol (42 g, 120 mmol) and triphenylphosphine (34 g, 130 mmol) in DCM (250 mL) at 0 °C. The resulting mixture was stirred overnight to give a brown solution. The solvent was removed under vacuum. The solids were extracted with petroleum spirit (3 × 50 mL), to give

a yellow oil which was purified by column chromatography (silica gel, petroleum spirit), to afford as a colorless oil (44.5 g, 89% yield). $^{1}$H NMR (500 MHz, Chloroform-*d*) δ 3.47 (d, *J* = 4.8 Hz, 2H), 1.61 (heptet, *J* = 6.1 Hz, 1H), 1.47 – 1.10 (m, 41H), 0.91 (t, J = 6.6 Hz, 6H). $^{13}$C NMR (125 MHz, Chloroform-*d*) δ 39.60, 39.50, 32.56, 31.91, 29.78, 29.68, 29.67, 29.65, 29.63, 29.59, 29.36, 29.34, 26.55, 22.68, 14.09. GC-MS (m/z): [M+–Br] calc. ($C_{24}H_{48}$): 336.38, 337.38, 338.38. found: 336.4, 337.4, 338.4.

**Synthesis of (b):** 2-decyl-1-tetradecyl bromide (22 g, 53 mmol) was dissolved in anhydrous THF (110 mL), the resulting solution was bubbled with nitrogen for 30 min. Allylmagnesium bromide (40 mL of a 2.0 M solution in THF, 79 mmol) was added and the resulting solution heated at reflux for 48 hrs. The reaction was quenched with water (55 mL) and sulfuric acid (110 mL of 10 wt%) and extracted with Et2O (3 × 100 mL), washed with brine (3 ×100 mL), and dried over $MgSO_4$. The solvent was removed under vacuum. The crude product was purified by column chromatography (silica gel, petroleum spirit), to afford a colorless oil (19 g, 93% yield). GC-MS (m/z): [M+] calc. ($C_{27}H_{54}$): 378.42, 379.43, 380.43. found: 378.4, 379.4, 380.4.

**Synthesis of (c):** 11-(but-3-enyl)tricosane (19 g, 50 mmol) was added to anhydrous diglyme (47 mL) to this solution $NaBH_4$ (2 g, 60 mmol) was added and stirred at RT for 30 min. To the resulting mixture $BF_3.OEt_2$ (4.4 mL, 35 mmol) was added dropwise and stirred for 2 hrs. 3M NaOH (20 mL) and water (5 mL) were added slowly and the mixture was stirred for another 2 hrs at 40 °C. Followed by dropwise addition of $H_2O_2$ (20 mL). The resulting mixture was stirred at RT overnight and poured to water (60 mL). The organic solvent was extracted with $Et_2O$ (3 × 40 mL), washed with saturated $NaHCO_3$ (3 × 60 mL) and brine (3 × 60 mL), then dried over $MgSO_4$. The solvent was removed under vacuum. The crude product was purified by column chromatography (silica gel, petroleum spirit: ethyl acetate (4:1)), to afford as a colorless oil

(16.8 g, 85% yield). GC-MS (m/z): [M+–H] calc. ($C_{27}H_{56}O$): 396.43, 397.44, 398.44. found: 395.4, 397.3, 398.4.

**Synthesis of Alkyl1:** NBS (16 g, 40 mmol) was added slowly in portions to a solution of 5-decy-1-heptadecanol (10.5 g, 59.2 mmol) and TriphenylPhosphine (14 g, 54 mmol) in DCM (100mL) at 0 °C. The resulting mixture was stirred overnight to give a brown solution. The solvent was removed under vacuum. The dark purple solids were extracted with petroleum spirit (3 × 80 mL), to give a yellow oil which was purified by column chromatography (silica gel, petroleum spirit), to afford as a colorless oil (16 g, 88% yield). $^{1}$H NMR (500 MHz, Chloroform-*d*) δ 3.43 (t, *J* = 6.9 Hz, 2H), 1.86 (pentet, *J* = 7.0 Hz, 2H), 1.46 – 1.38 (m, 3H), 1.27 (m, *J* = 18.7 Hz, 44H), 0.91 (t, *J* = 6.9 Hz, 6H). $^{13}$C NMR (125 MHz, Chloroform-*d*) δ 37.26, 33.98, 33.56, 33.30, 32.75, 31.98, 30.17, 29.76, 29.43, 26.68, 25.32, 22.75, 14.17. GC-MS (m/z): [M+] calc. ($C_{27}H_{55}Br$): 458.35, 460.35, 459.35. found: 458.4, 459.4, 460.4.

**Synthesis of (4-Bromobutyl)nonadecane (R2):**

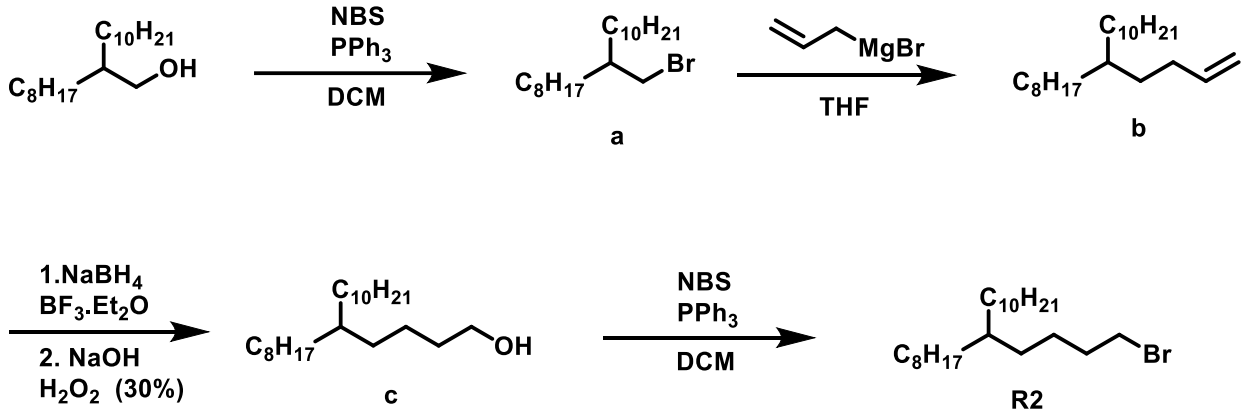


**Synthesis of (a):** NBS (72 g, 410 mmol) was added slowly in portions to a solution 2-Octyl-1-dodecanol (81.68 g, 274 mmol) and TriphenylPhosphine (97 g, 262.29 mmol) in DCM (600 mL) at 0 °C. The resulting mixture was stirred overnight to give a brown solution. The solvent was removed under vacuum. The solids were extracted with petroleum spirit (3 × 50 mL), to give a yellow oil which was purified by column chromatography (silica gel, petroleum

spirit), to afford as a colorless oil (93 g, 94% yield). $^{1}$H NMR (500 MHz, Chloroform-*d*) δ 3.45 (d, *J* = 4.8 Hz, 2H), 1.67 – 1.55 (m, 1H), 1.39 – 1.20 (m, 32H), 0.88 (t, *J* = 6.8 Hz, 6H). $^{13}$C NMR (125 MHz, Chloroform-*d*) δ 39.89, 39.65, 32.71, 32.07, 32.05, 29.94, 29.79, 29.78, 29.75, 29.71, 29.50, 29.46, 26.71, 22.85, 22.83, 14.27. GC-MS (m/z): [M+–Br] calc. ($C_{20}H_{40}$): 280.31, 281.32, 282.32. found:, 280.3, 281.4 282.4.

**Synthesis of (b):** 2-Octyl-1-dodecyl bromide (22 g, 61 mmol) was dissolved in anhydrous THF (130 mL), the resulting solution was bubbled with nitrogen for 30 min. Allylmagnesium bromide (46 mL of a 2.0 M solution in THF, 91 mmol) was added and the resulting solution heated at reflux for 48 hrs. The reaction was quenched with water (73 mL) and sulfuric acid (146 mL of 10 wt%) and extracted with $Et_2O$ (3 × 100 mL), washed with brine (3 × 100 mL), and dried over $MgSO_4$. The solvent was removed under vacuum. The crude product was purified by column chromatography (silica gel, petroleum spirit), to afford as a colorless oil (19 g, 97% yield). GC-MS (m/z): [M+] calc. ($C_{23}H_{46}$): 322.36, 323.36, 324.37. found: 322.4, 323.4, 324.4.

**Synthesis of (c):** 9-(but-3-enyl) nonadecane (25 g, 77 mmol) was added to anhydrous diglyme (75 mL). to this solution $NaBH_4$ (3 g, 77 mmol) was added and stirred at RT for 30 min. to the resulting mixture $BF_3.OEt_2$ (7 mL, 54 mmol) was added dropwise and stirred for 2 hrs. 3M NaOH (30 mL) and water (8 mL) were added slowly and the mixture was stirred for another 2 hrs at 40 °C. Followed by dropwise addition of $H_2O_2$ (30 mL). The resulting mixture was stirred at RT overnight. The organic solvent was extracted with $Et_2O$ (3 × 100 mL), washed with saturated $NaHCO_3$ (3 × 100 mL) and brine (3 × 100 mL), then dried over $MgSO_4$. The solvent was removed under vacuum. The crude product was purified by column chromatography (silica gel, petroleum spirit: ethyl acetate (4:1)), to afford as a colorless oil (19.7 g, 71% yield). GC-MS (m/z): [M+–H] calc. ($C_{23}H_{48}O$): 340.37, 341.37, 342.38. found: 340.2, 341.3 342.4.

**Synthesis of Alkyl2:** NBS (18 g, 100 mmol) was added slowly in portions to a solution of 5-octyl-1-pentadecanol (19 g, 56 mmol) and TriphenylPhosphine (22 g, 83 mmol) in DCM (125 mL) at 0 °C. The resulting mixture was stirred overnight to give a brown solution. The solvent was removed under vacuum. The solids were extracted with petroleum spirit (3 × 50 mL), to give a yellow oil which was purified by column chromatography (silica gel, petroleum spirit), to afford as a colorless oil (19.9 g, 88% yield). $^{1}$H NMR (500 MHz, Chloroform-*d*) δ 3.43 (t, *J* = 6.9 Hz, 2H), 1.86 (pentet, *J* = 7.0 Hz, 2H), 1.42 (m, *J* = 7.6 Hz, 2H), 1.37 – 1.15 (m, 36H), 0.91 (t, *J* = 6.9 Hz, 6H). $^{13}$C NMR (125 MHz, Chloroform-*d*) δ 37.26, 33.99, 33.30, 32.75, 31.97, 30.17, 29.76, 29.42, 26.68, 25.32, 22.74, 14.17. GC-MS (m/z): [M+] calc. ($C_{23}H_{47}Br$): 402.29, 404.28, 403.29. found: 402.2, 403.4, 404.4.

**Monomer Synthesis**

**Synthesis of N-alkylated bisisatin core monomers (Monomer1 & 2):**

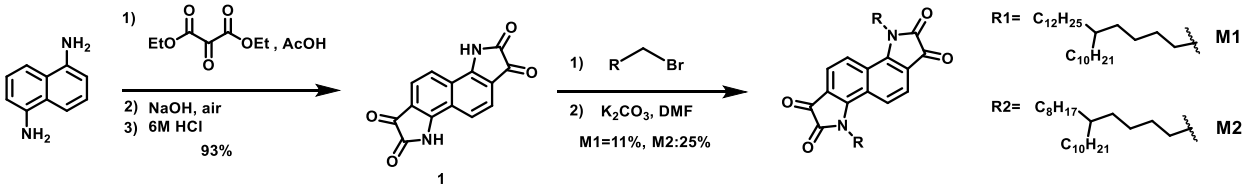


**Synthesis of Bisisatin (1):**

1,5-Diaminonaphthalene (4 g, 25 mmol) was dissolved in (41 mL) glacial acetic acid and heated to reflux. To the resulting dark purple solution was added dropwise, diethylketomalonate (32 mL, 205 mmol) in glacial acetic acid (46 mL). The resulting mixture was heated to 150 °C overnight. The solvent was removed under vacuum and 1M NaOH was added to the resulting dark brick red solids until complete dissolution to a final pH of (11-12). The resulting red brown solution was heated at 150 °C overnight with sparging air into the solution. The resulting mixture was poured onto ice and 6M HCl was added until pH=0 to give a purple precipitate, which was filtered and washed with water to give dark red-purple solids

(6 g, 93% yield) and carried out without further purification.). $^{1}$H NMR (500 MHz, DMSO-*d6*) δ 11.77 (s, 1H), 7.78 (d, *J* = 8.4 Hz, 1H), 7.59 (d, *J* = 8.4 Hz, 1H). $^{13}$C NMR (125 MHz, DMSO-*d6*) δ 183.85, 152.36, 124.50, 120.51, 117.60, 115.75.

**Synthesis of N,N'-bis(5-decylheptadecyl)bisisatin (M1):**

To a mixture of crude (3 g,11 mmol) and dry $K_2CO_3$ (8 g, 55 mmol) in anhydrous DMF (65 mL), was added 5-decy-1-heptadecyl bromide (21.7 g, 47.3 mmol). The resulting mixture was stirred at 70 °C for 4 hours. The reaction mixture was poured over $H_2O$ and acidified with 1M HCl to pH of 7. The aqueous layer was extracted with DCM, washed with $H_2O$, brine and dried over $MgSO_4$. The solvent was removed under vacuum. The crude viscous dark purple oil was purified by column chromatography (silica gel, DCM:petroleum spirit (7:3)), followed by precipitation in MeOH and filtered to afford the product as dark blue solid (1.2 g, 11% yield). $^{1}$H NMR (500 MHz, Chloroform-*d*) δ 7.97 (d, *J* = 8.7 Hz, 1H), 7.70 (d, *J* = 8.7 Hz, 1H), 4.25 (t, *J* = 7.6 Hz, 2H), 1.82 (p, *J* = 7.7 Hz, 2H), 1.59 (s, 3H), 1.49 – 1.39 (m, 2H), 1.36 – 1.10 (m, 48H), 0.90 (t, *J* = 6.8 Hz, 7H). $^{13}$C NMR (125 MHz, Chloroform-*d*) δ 182.81, 158.99, 152.21, 127.28, 119.63, 116.19, 43.56, 37.30, 33.29, 31.95, 30.15, 29.74, 29.40, 26.66, 23.93, 22.72, 14.17. HRMS (m/z): (M·+) calc. ($C_{68}H_{114}N_2O_4$): 1022.87786. found: 1023.88593.

**Synthesis of N,N'-bis(5-octylpentadecyl)bisisatin (M2):**

To a mixture of crude (3 g, 11 mmol) and dry $K_2CO_3$ (8 g, 55 mmol) in anhydrous DMF (65 mL), was added 5-octyl-1-pentadecyl bromide (20 g, 49.5mmol). The resulting mixture was stirred at 70 °C for 4 hours. The reaction mixture was poured over $H_2O$ and acidified with 1M HCl to pH of 7. The aqueous layer was extracted with DCM, washed with $H_2O$, brine and dried over $MgSO_4$. The solvent was removed under vacuum. The crude viscous dark purple oil was purified by column chromatography (silica gel, DCM: Petroleum spirit (7:3)), followed by precipitation in MeOH and filtered to afford the product as dark blue solids (2.5 g, 25% yield).

$^{1}$H NMR (500 MHz, Chloroform-*d*) δ 7.97 (d, *J* = 8.7 Hz, 1H), 7.70 (d, *J* = 8.6 Hz, 1H), 4.30 – 4.19 (m, 2H), 1.82 (p, *J* = 7.8 Hz, 2H), 1.59 (s, 4H), 1.49 – 1.39 (m, 2H), 1.37 – 1.06 (m, 39H), 0.90 (t, *J* = 6.6 Hz, 6H). $^{13}$C NMR (125 MHz, Chloroform-*d*) δ 182.81, 158.99, 152.21, 127.28, 120.27, 119.63, 116.20, 43.56, 37.29, 33.48, 33.29, 31.94, 30.15, 29.79, 29.74, 29.70, 29.68, 29.39, 26.66, 23.93, 22.72, 14.17. HRMS (m/z): (M·+) calc. ($C_{68}H_{114}N_2O_4$): 910.75266. found: 911.75935.

**Synthesis of benzo[1,2-b-4,5-b']difuran-2,6-(3H,7H)-dione (M3):**

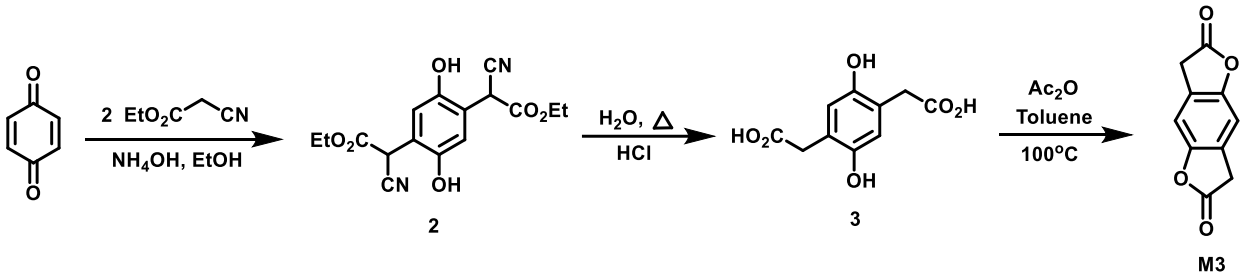


**Synthesis of (2):**

To a three-neck round-bottom flask equipped with two dropping funnels was added ethyl cyanoacetate (4.21 g, 4 ml, 37.25 mmol) in ethanol (15 ml). to the solution, concentrated ammonium hydroxide (3.17 g, 3.5 ml, 90.62 mmol) was added.in one dropping funnel was added ammonium hydroxide (11.28 g, 12.5 ml, 322 mmol) in water (20 ml) was added. Meanwhile, to a solution of ethyl cyanoacetate (6.4 g, 6 ml, 56 mmol) in ethanol (50 ml) was added p-benzoquinone (5 g, 46 mmol), the resulting solution was stirred at 40 °C for 30 min and transferred while hot to the other dropping funnel. The solutions in both dropping funnels were delivered to the flask at the same time with uniform rate. all the ammonium hydroxide solution should be added by the time 90% of the p-benzoquinone solution has been added. After completion of the addition, the resulting solution was stirred at RT for 1 hour. The

precipitates formed were filtered under vacuum and washed with ethanol and dried to get Compound 2 (3.01g, 20%yield) as an ashy purple solid.

**Synthesis of (3):**

To a residue of 1 (3 g, 9 mmol) was added concentrated HCl (0.027 g, 23 ml, 0.76 mmol) and water (18 mL) and the resulting solution was refluxed at 110 °C overnight. Water (15 ml) and celite (1.5 g) were added to the hot reaction mixture and stirred for 5 min, after which it is rapidly filtered with suction and the filtrate was taken and cooled. White creamy crystals have been collected upon filtration 3 (1.42 g, 59% yield).

**Synthesis of (M3):**

To a residue of 2 (1.4 g, 6.2 mmol) in anhydrous toluene (75 mL), acetic anhydride (16.4 g, 15 ml, 195.96 mmol). The resulting mixture was stirred at 100 °C overnight. The solvent was removed under vacuum, to the resulting solids was added chloroform and filtered, the filtrate was recrystallized in toluene to give the pure final product as beige crystals (0.1g, 26% yield). $^{1}$H NMR (500 MHz, DMSO-*d6*) δ 7.25 (s, 1H), 3.96 (s, 2H). $^{13}$C NMR (125 MHz, DMSO-*d6*) δ 174.85, 150.57, 124.42, 107.81, 33.78. HRMS (m/z): $[M+H]^+$ calc. ($C_{10}H_7O_4$): 191.0339. found: 191.0272.

**Synthesis of naphtho-[1,2-b:5,6-b']difuran-2,7(3H, 8H)-dione (M4):**

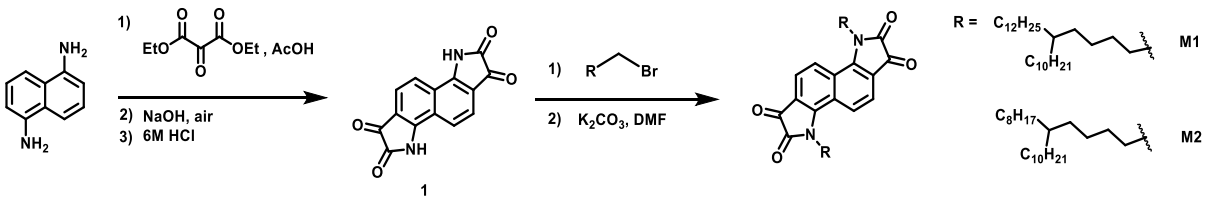


**Synthesis of (4):**

1,5-dihydroxynaphtelene (4.2 g, 26 mmol) was dissolved in DMSO (105 ml), to which grinded pellets of NaOH was added (2.3 g, 56.9 mmol) and the resulting mixture was stirred at RT for

2 h, then 1,1,2-trichloroethylene (7 ml, 78 mmol) was slowly added. The resulting mixture was stirred at RT overnight. Water was slowly added (100 mL). The two phases were separated, and the aqueous layer was extracted with DCM, washed with brine and dried over $MgSO_4$ and the solvent was removed under vacuum. The crude product was purified by column chromatography (silica gel, petroleum spirit), to afford 4 as a colorless solid (3 g, 33% yield). $^1$H NMR (500 MHz, Chloroform-*d*) δ 8.07 (d, *J* = 8.5 Hz, 1H), 7.53 (t, *J* = 8.1 Hz, 1H), 7.16 (d, *J* = 7.6 Hz, 1H), 6.10 (d, *J* = 1.2 Hz, 1H), $^{13}$C-NMR (125 MHz, Chloroform-*d*) δ 149.94, 140.53, 127.32, 126.40, 119.01, 111.98, 105.32.

**Synthesis of (5):**

Compound 4 (3 g, 8.57 mmol) was dissolved in $Et_2O$ (60 ml). the mixture was cooled to -78 °C to which 2.5 M solution of n-BuLi in hexane (28 mL, 68.5 mmol) was slowly added and stirred at -78 °C for 1 hour and subsequently warmed to -40 °C and stirred for 2 hours at the same temperature. Water was slowly added (60 mL). The two phases were separated and the aqueous layer was extracted with hexane, washed with saturated $NH_4Cl$, then brine and dried over $MgSO_4$ and the solvent was removed under vacuum to afford 5 as pale brown solids which was directly used for the next step without further purification due to its instability

**Synthesis of (M4):**

In 1,4 dioxane (22 mL), was added tetrafluoroboric acid diethyl ether complex (0.23 ml, 1.7 mmol) and 2,6-Dimethylpyridine *N*-oxide (2 ml, 17 mmol). Afterwards, Compound 5 (1.78 g, 8.5 mmol) was added and the resulting mixture was stirred at 80 °C overnight. The solvent was removed under vacuum, then methanol was added to form a precipitate, which was collected by filtration. The solids were dissolved in hot toluene the undissolved solids were filtered off. The filtrate was taken and the solvent was removed under vacuum. The resulting solids were dissolved in acetone, the undissolved solids were collected by filtration to afford the final pure

product as pale brown solids (10 mg, 5% Yield). $^{1}$H NMR (500 MHz, DMSO-*d6*) δ 7.75 (d, *J* = 8.3 Hz, 1H), 7.63 (d, *J* = 8.4 Hz, 1H), 4.15 (s, 2H). $^{13}$C NMR (125 MHz, DMSO-*d6*) δ 174.95, 149.98, 123.65, 120.29, 119.41, 116.39, 34.27.

**Polymer Synthesis:**

The synthetic procedure for the polymers were tailored from literature[5].

**Synthesis of P1:**

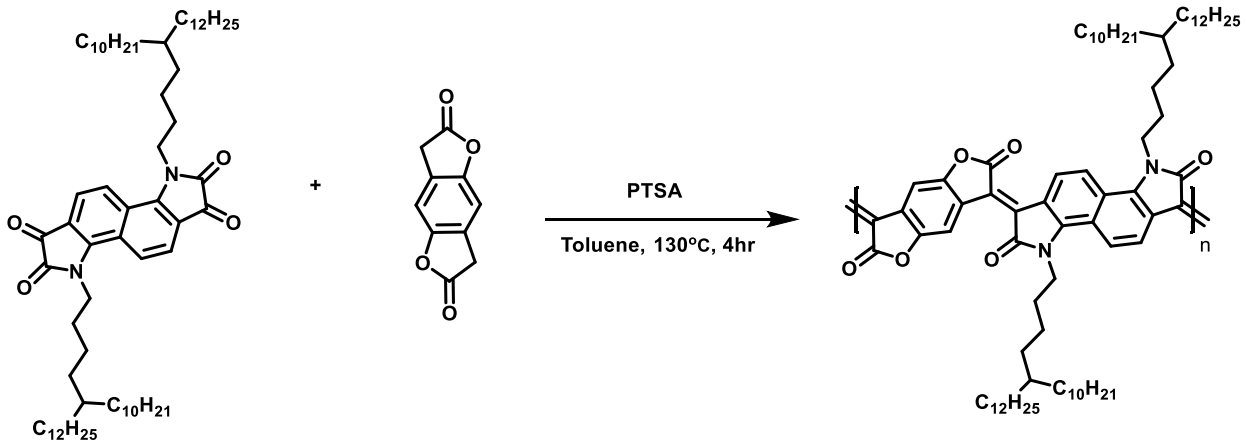


A microwave vial was charged with *N,N'*-bis(5-decylheptadecyl)bisisatin (109 mg, 0.106 mmol), benzo[1,2-*b*-4,5-*b'*]difuran-2,6-(3*H*,7*H*)-dione (20.27 mg, 0.106 mmol), p-toluene sulfonic acid monohydrate (6 mg, 0.0315 mmol ). Anhydrous toluene (1.5 mL) was injected. The resulting solution was purged with N2 for 30 min and the reaction was heated to 130 °C for 4 hours. The reaction mixture changed color from dark purple to dark blue over the polymerization period. The crude polymer was precipitated in methanol and purified by Soxhlet extraction with methanol, acetone, hexane and finally chloroform. The chloroform fraction was collected and the solvent was removed under vacuum. Afterwards, the polymer precipitated into methanol, filtered and dried. Yield: 110 mg, 86 % dark blue solid. GPC (1,2,4-

trichlorobenzene, 150 °C): Mn 14 kDa, Mw 29 kDa. $^{1}$H NMR (500 MHz, Chloroform-*d*) δ 7.72-8.89 ppm (d), 3.55 ppm (t), 1.92 ppm (t), 0.67-1.75 ppm (broad).

**Synthesis of P2:**

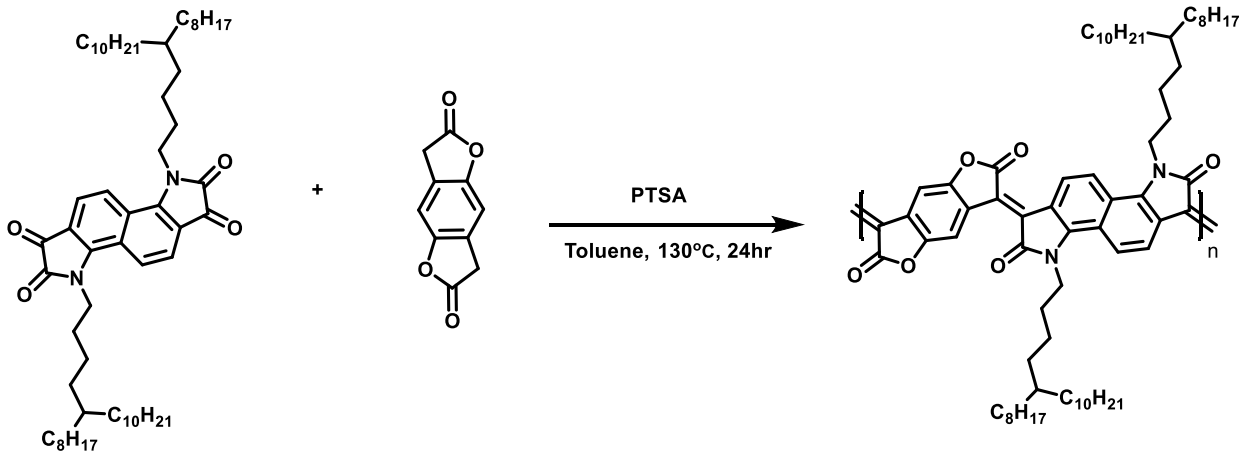


A microwave vial was charged with *N,N'*-bis(5-octylpentadecyl)bisisatin (115 mg, 0.126 mmol), benzo[1,2-*b*-4,5-*b'*]difuran-2,6-(3*H*,7*H*)-dione (23.99 mg, 0.126 mmol), p-toluene sulfonic acid monohydrate (6 mg, 0.0315 mmol ). Anhydrous toluene (1.5 mL) was injected. The resulting solution was purged with N2 for 30 min and the reaction was heated to 130 °C for 24 hours. The reaction mixture changed color from dark purple to dark blue over the polymerization period. The crude polymer was precipitated in methanol and purified by Soxhlet extraction with methanol, acetone, hexane and finally chloroform. The chloroform fraction was collected and the solvent was removed under vacuum. Afterwards, the polymer precipitated into methanol, filtered and dried. Yield: 59 mg, 43 % dark blue solid. GPC (1,2,4-trichlorobenzene, 80 °C): Mn 16 kDa, Mw 27 kDa.$^{1}$H NMR (500 MHz, Chloroform-*d*) δ 3.63 ppm (t), 1.89 ppm (t), 0.72-1.82 ppm (broad).

**Synthesis of P3:**

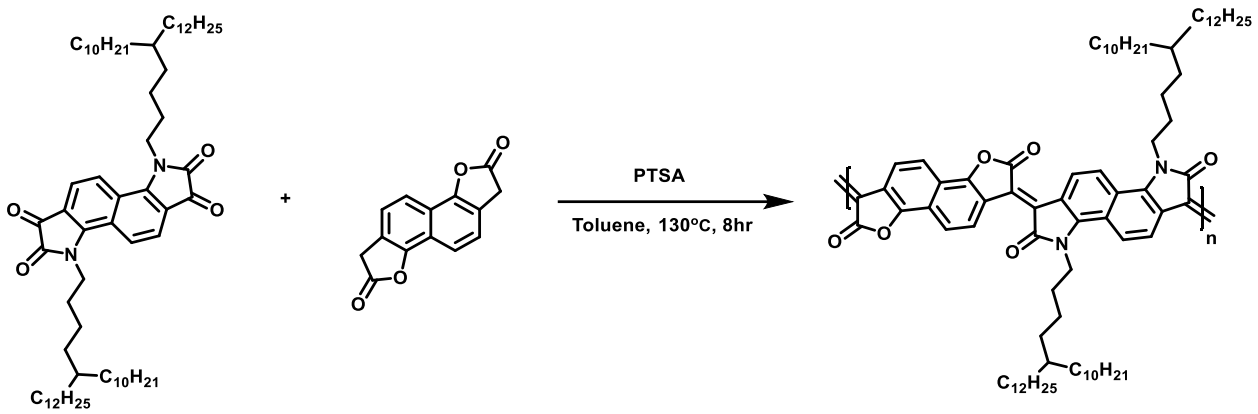


A microwave vial was charged with *N,N'*-bis(5-decylheptadecyl)bisisatin (85.23 mg, 0.083 mmol), naphtho-[1,2-*b*:5,6-*b*']difuran-2,7(3*H*, 8*H*)-dione (19.99 mg, 0.083 mmol), p-toluene sulfonic acid monohydrate (6 mg, 0.0315 mmol ). Anhydrous toluene (1.5 mL) was injected. The resulting solution was purged with N2 for 30 min and the reaction was heated to 130 °C for 8 hours. The reaction mixture changed color from dark purple to dark green over the polymerization period. The crude polymer was precipitated in methanol and purified by Soxhlet extraction with methanol, acetone, hexane and finally chloroform. The chloroform fraction was collected and the solvent was removed under vacuum. Afterwards, the polymer precipitated into methanol, filtered and dried. Yield: 46.85 mg, 45 % dark green solid. GPC (1,2,4-trichlorobenzene, 80 °C): Mn 14 kDa, Mw 20 kDa. $^{1}$H NMR (500 MHz, Chloroform-*d*) δ 7.73-7.90 ppm (d), 3.55 ppm (t), 1.92 ppm (t), 0.67-1.75 ppm (broad).

## 5.1.3 NMR measurements for the monomers and polymers

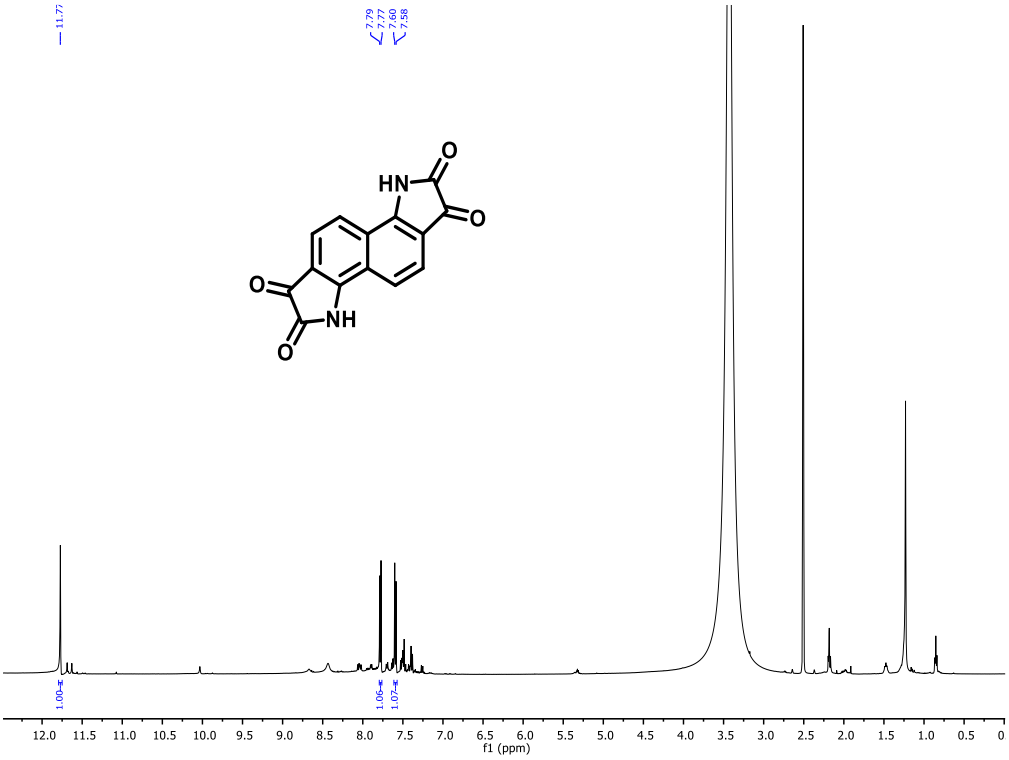


Figure 1. $^{1}$H NMR spectrum of compound 1

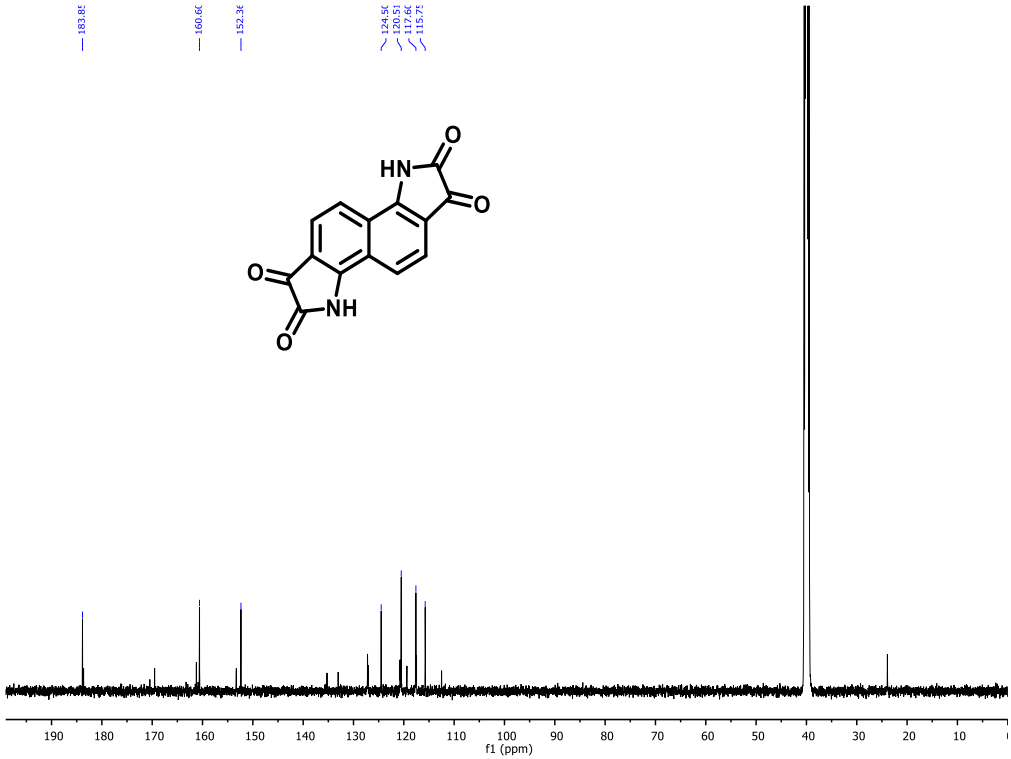


Figure 2. $^{13}$C NMR spectrum of compound 1

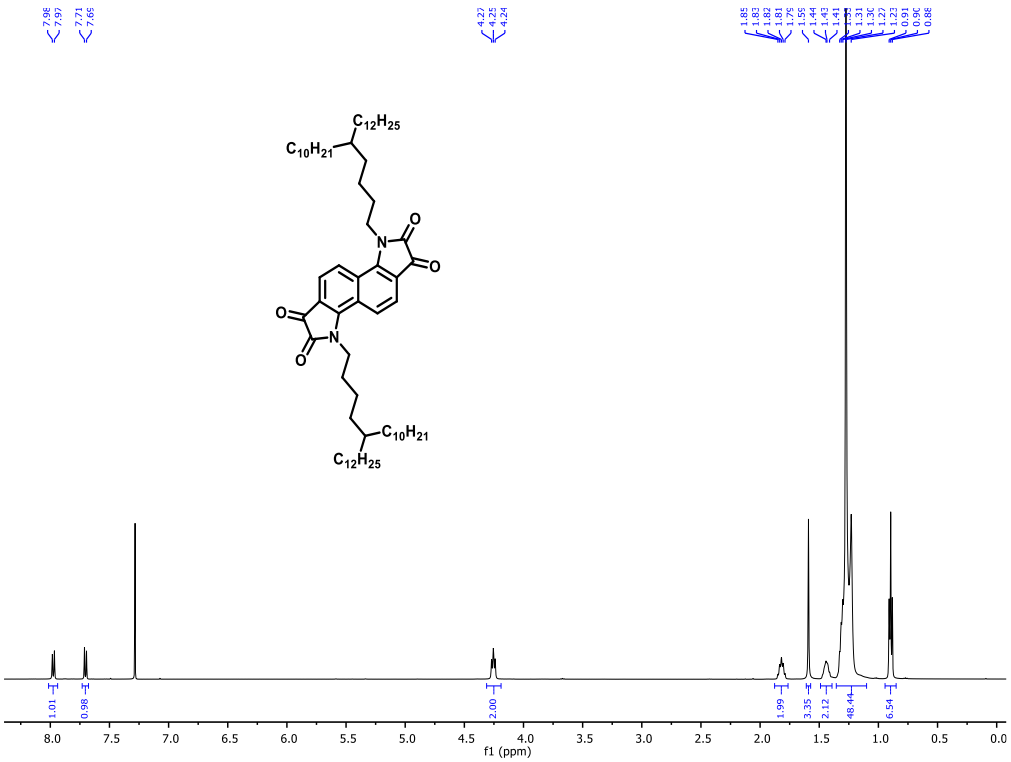


Figure 3. $^{1}$H NMR spectrum of compound M1

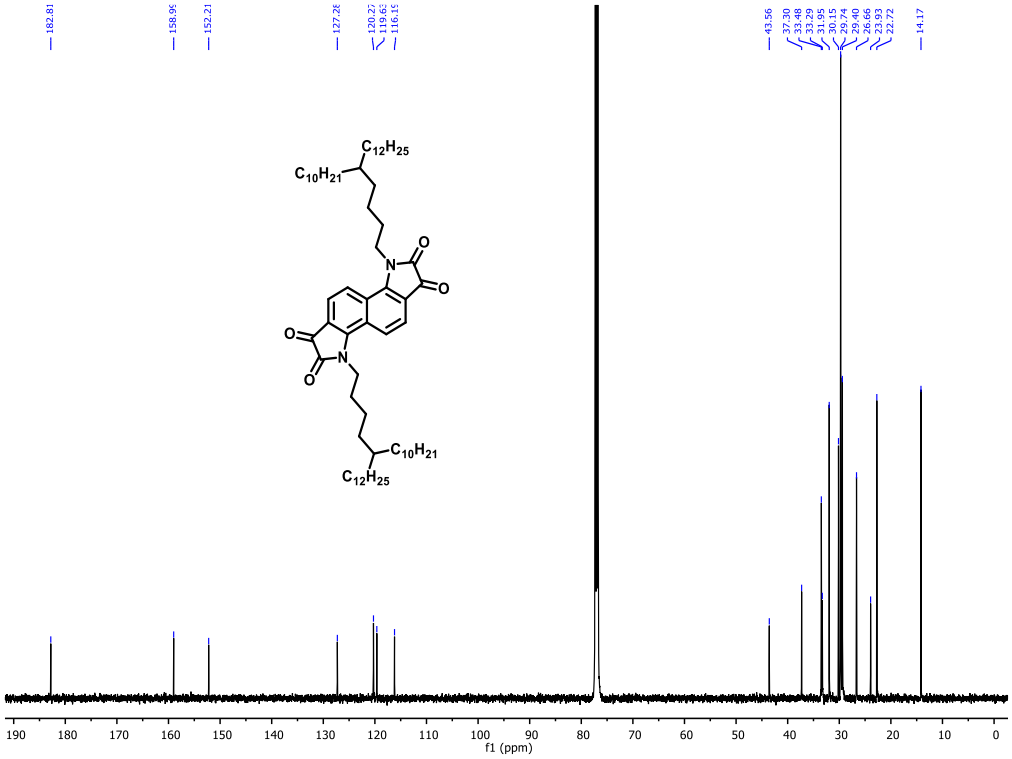


Figure 4. $^{13}$C NMR spectrum of compound M1

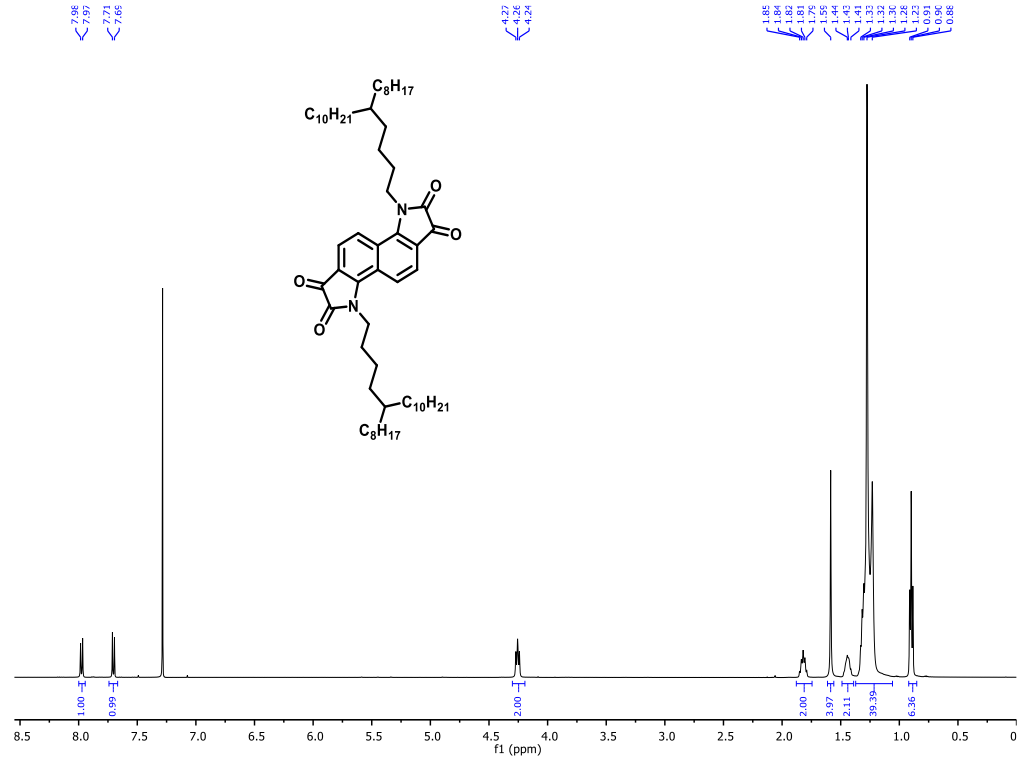


Figure 5. $^{1}$H NMR spectrum of compound M2

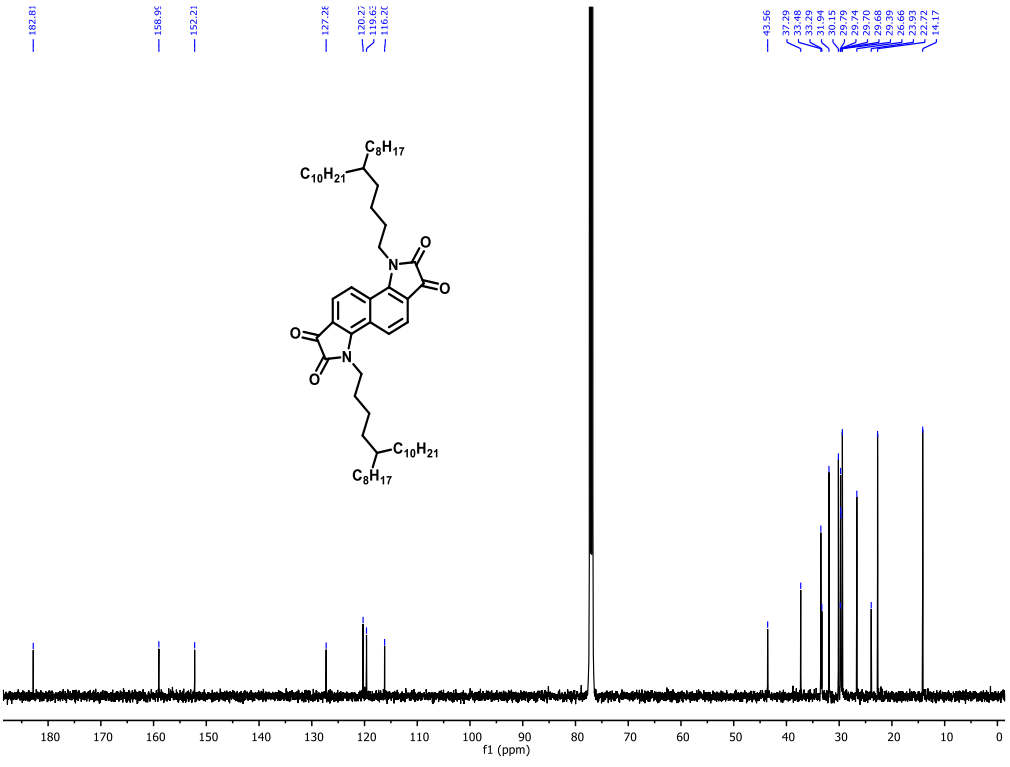


Figure 6. $^{13}$C NMR spectrum of compound M2

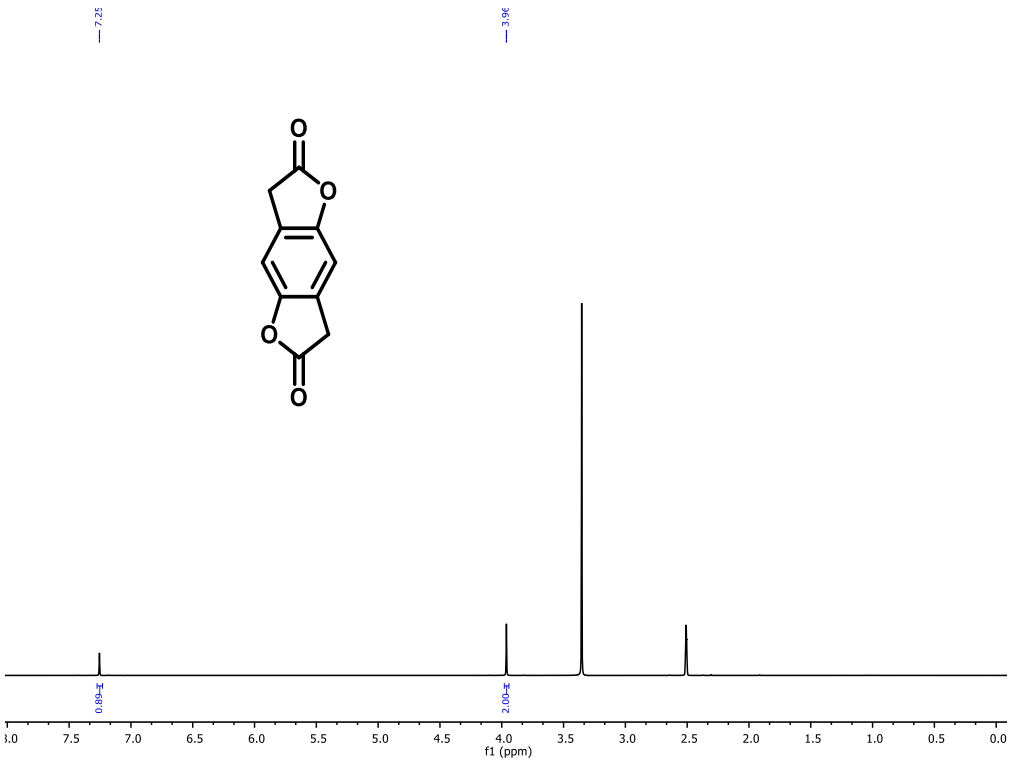


Figure 7. $^{1}$H NMR spectrum of compound M3

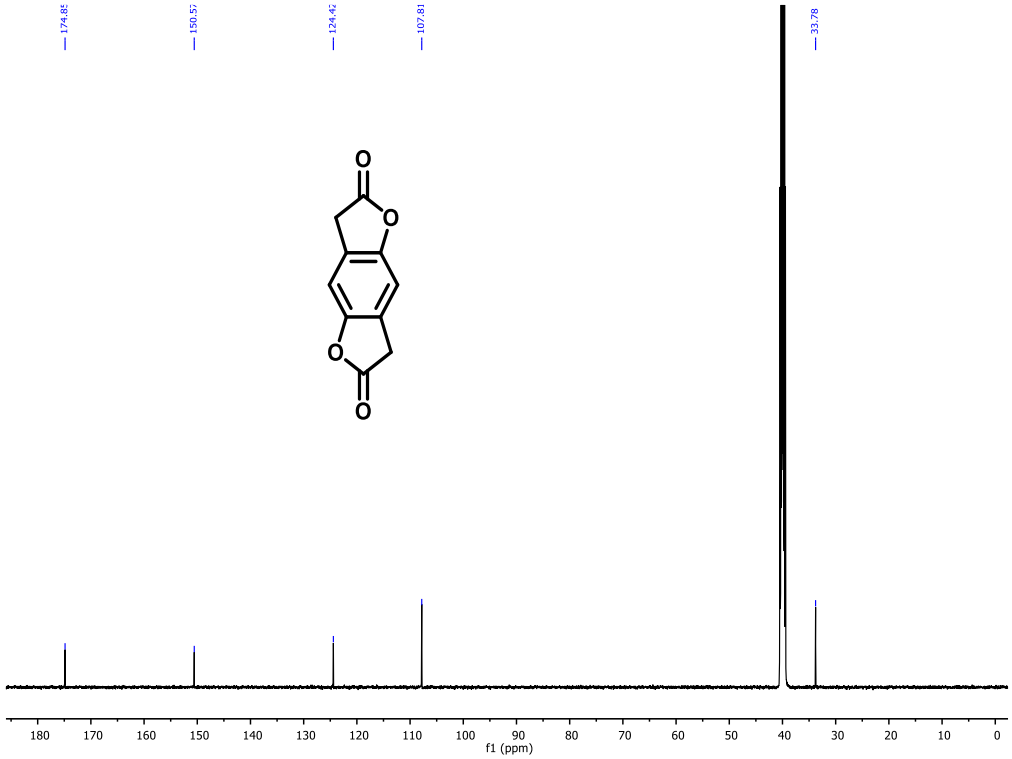


Figure 8. $^{13}$C NMR spectrum of compound M3


Figure 9. $^{1}$H NMR spectrum of compound M4

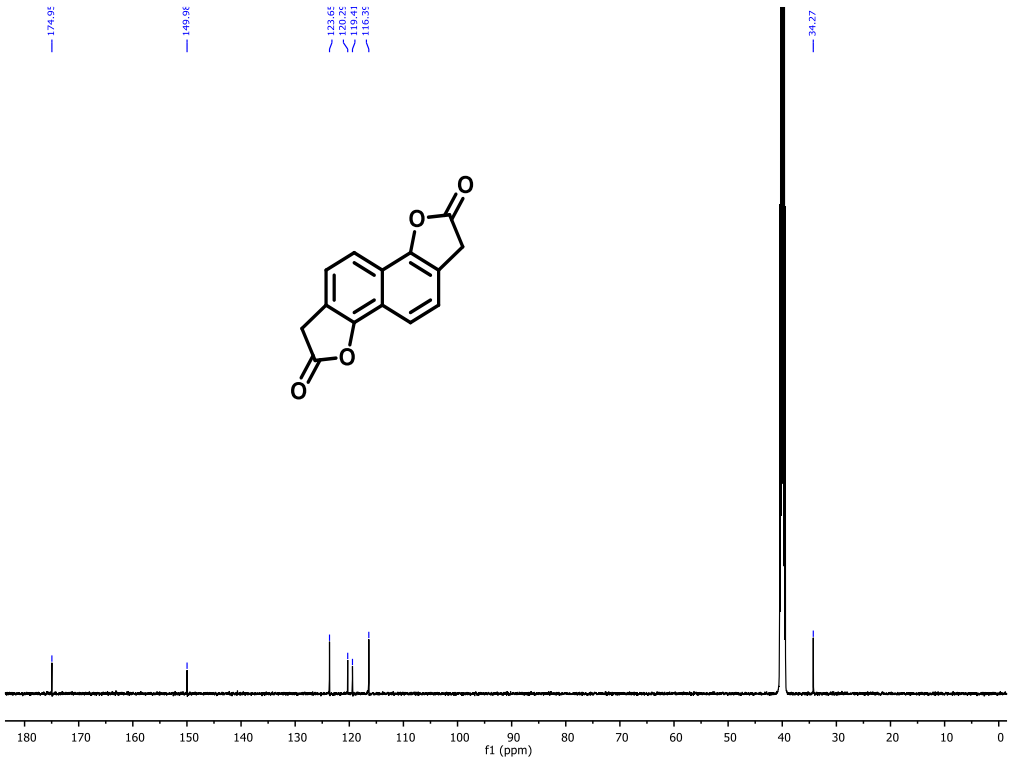


Figure 10. $^{13}$C NMR spectrum of compound M4

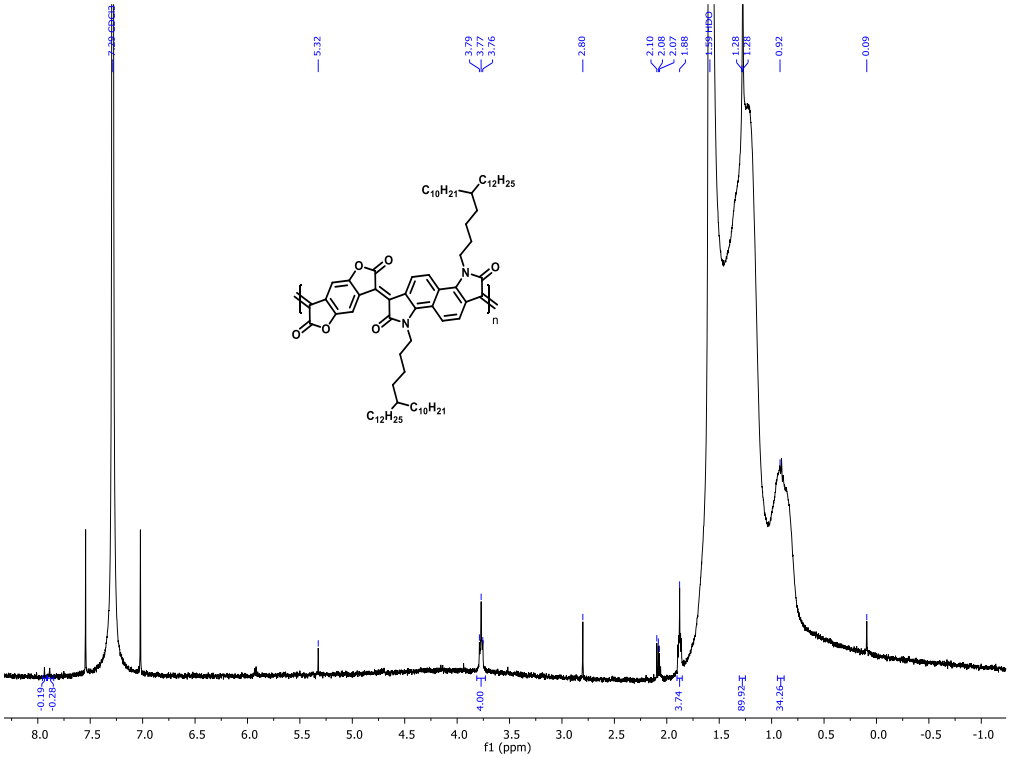


Figure 11. $^{1}$H NMR spectrum of polymer P1

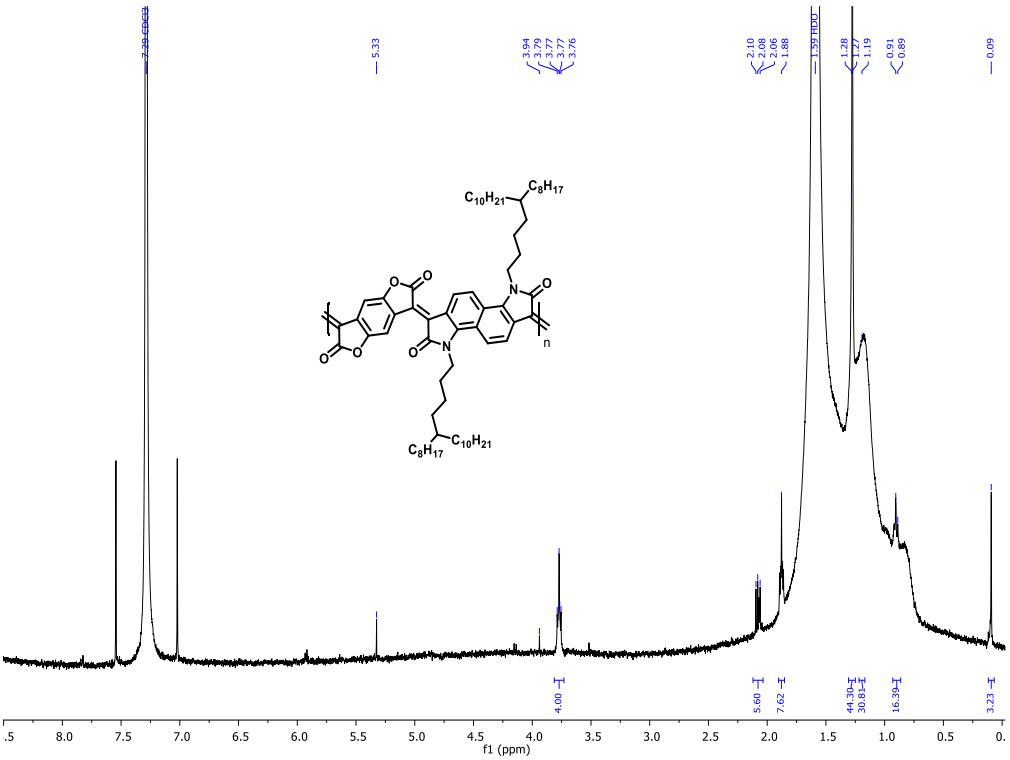


Figure 12. $^{1}$H NMR spectrum of polymer P2

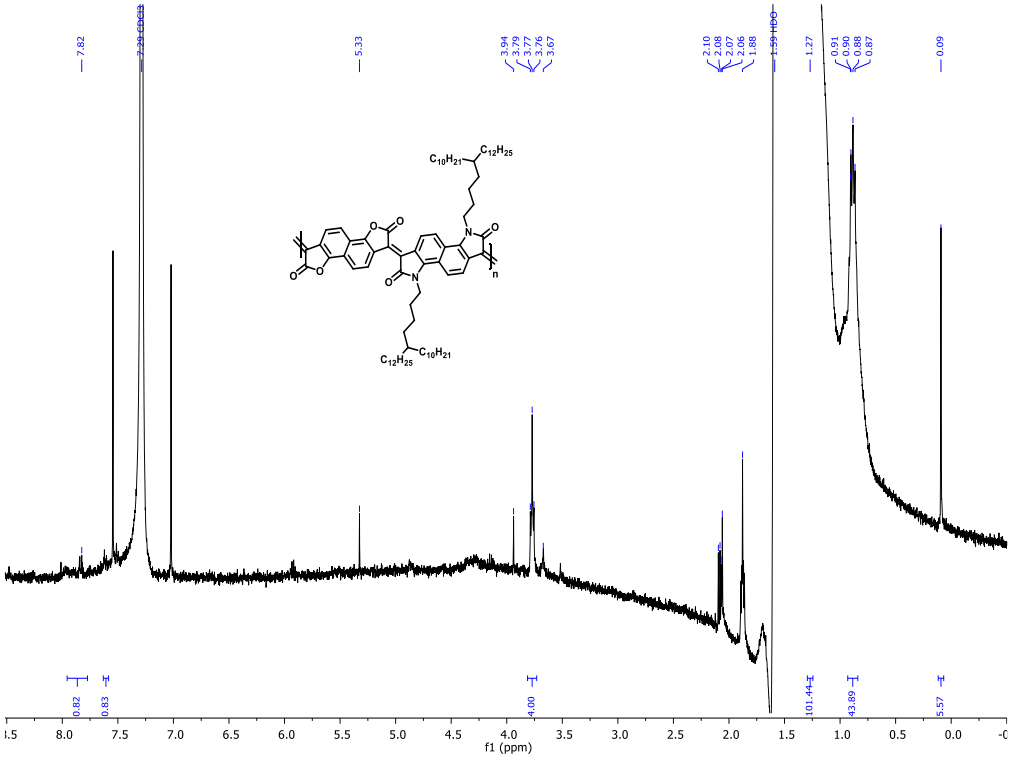


Figure 13. $^{1}$H NMR spectrum of polymer P3

## 5.1.4 UV-vis absorbance spectroscopy

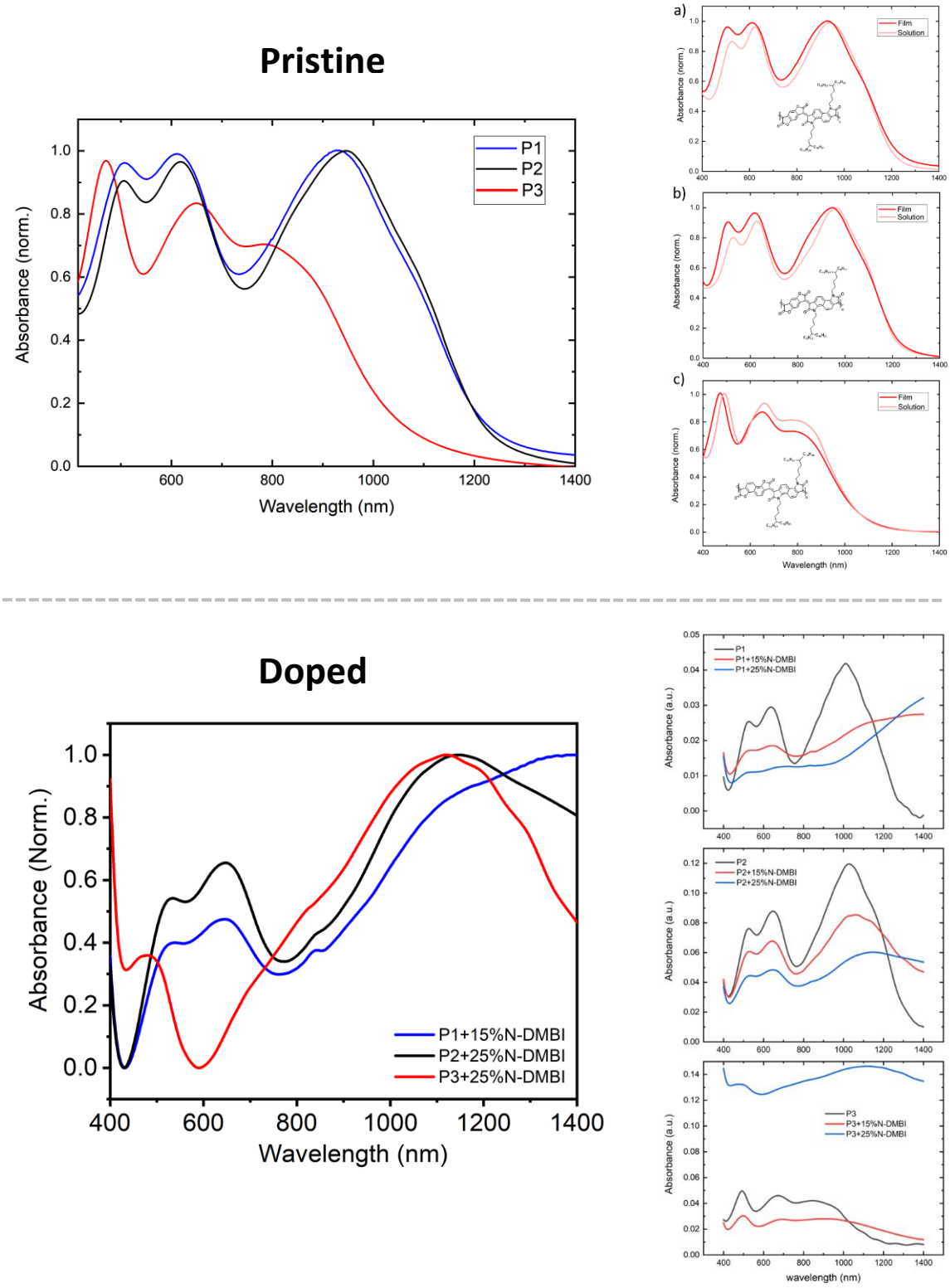


Figure 14. Thin films and solution UV-vis absorbance of pristine and doped polymers

## 5.1.5 Gel permeation chromatography (GPC) measurements

**P1**

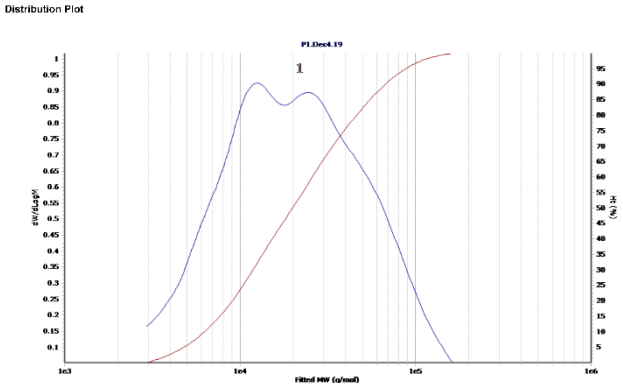


**Molecular Weight Averages**

| Peak | Mp | Mn | Mw | Mz | Mz+1 | Mv | PD |
|---|---|---|---|---|---|---|---|
| Peak 1 | 25637 | 13961 | 29476 | 54561 | 79004 | 50877 | 2.111 |

**P2**

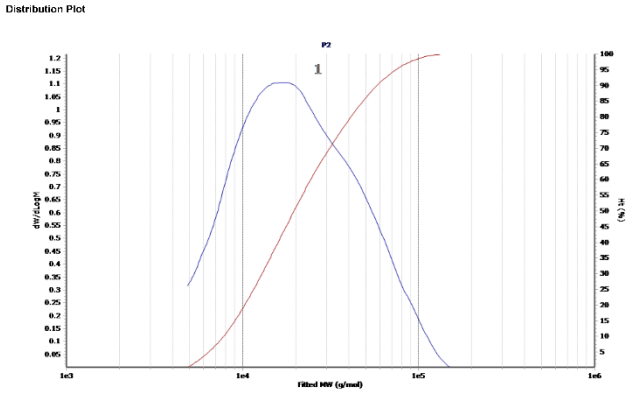


**Molecular Weight Averages**

| Peak | Mp | Mn | Mw | Mz | Mz+1 | Mv | PD |
|---|---|---|---|---|---|---|---|
| Peak 1 | 18792 | 15902 | 27209 | 45116 | 63857 | 42357 | 1.711 |

**P3**

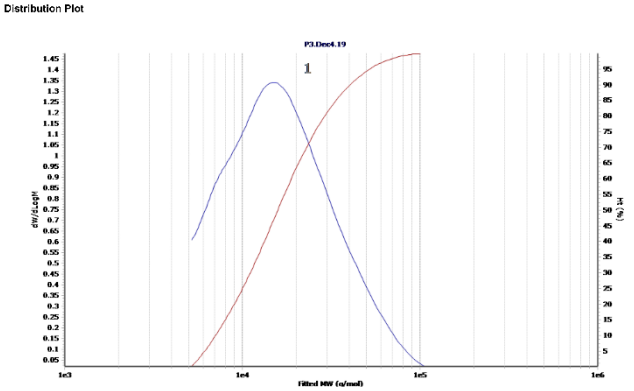


**Molecular Weight Averages**

| Peak | Mp | Mn | Mw | Mz | Mz+1 | Mv | PD |
|---|---|---|---|---|---|---|---|
| Peak 1 | 15589 | 13591 | 20463 | 31542 | 44830 | 29704 | 1.506 |

## 5.1.6 Thermal gravimetric analysis (TGA)

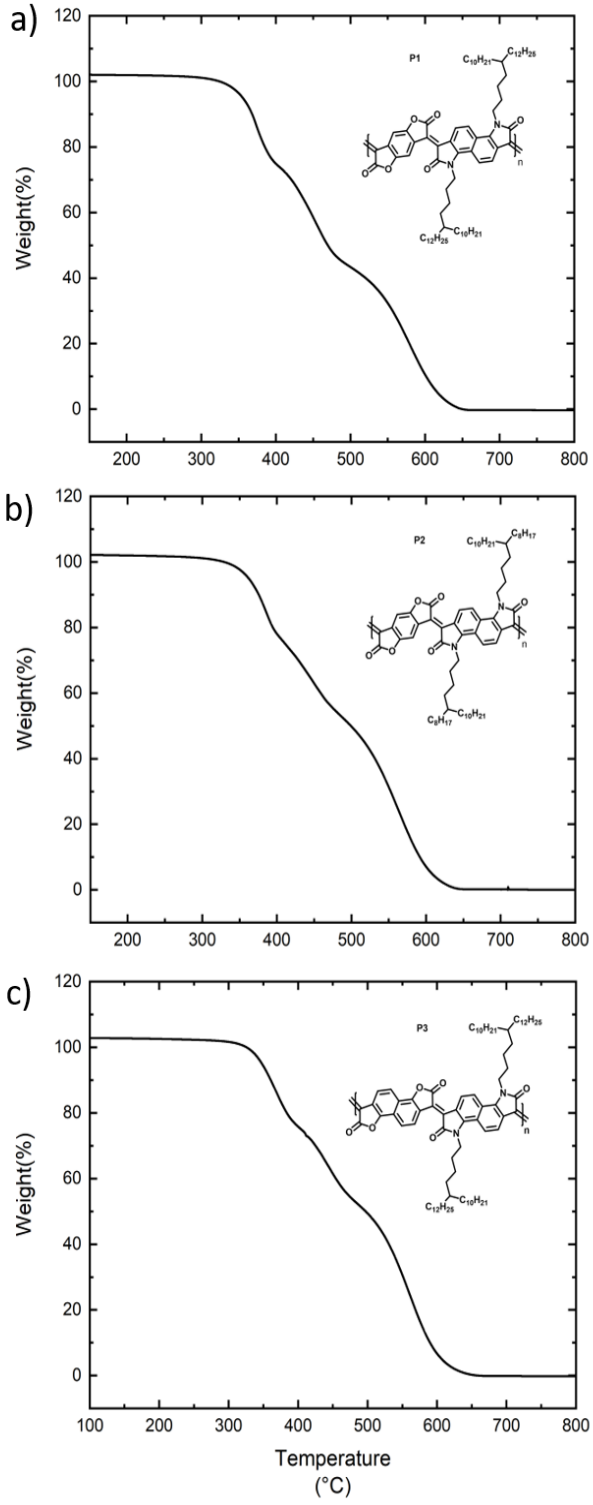


Figure 15. TGA curves of a) P1, b) P2 and c) P3

### 5.1.7 Differential scanning calorimeter (DSC)

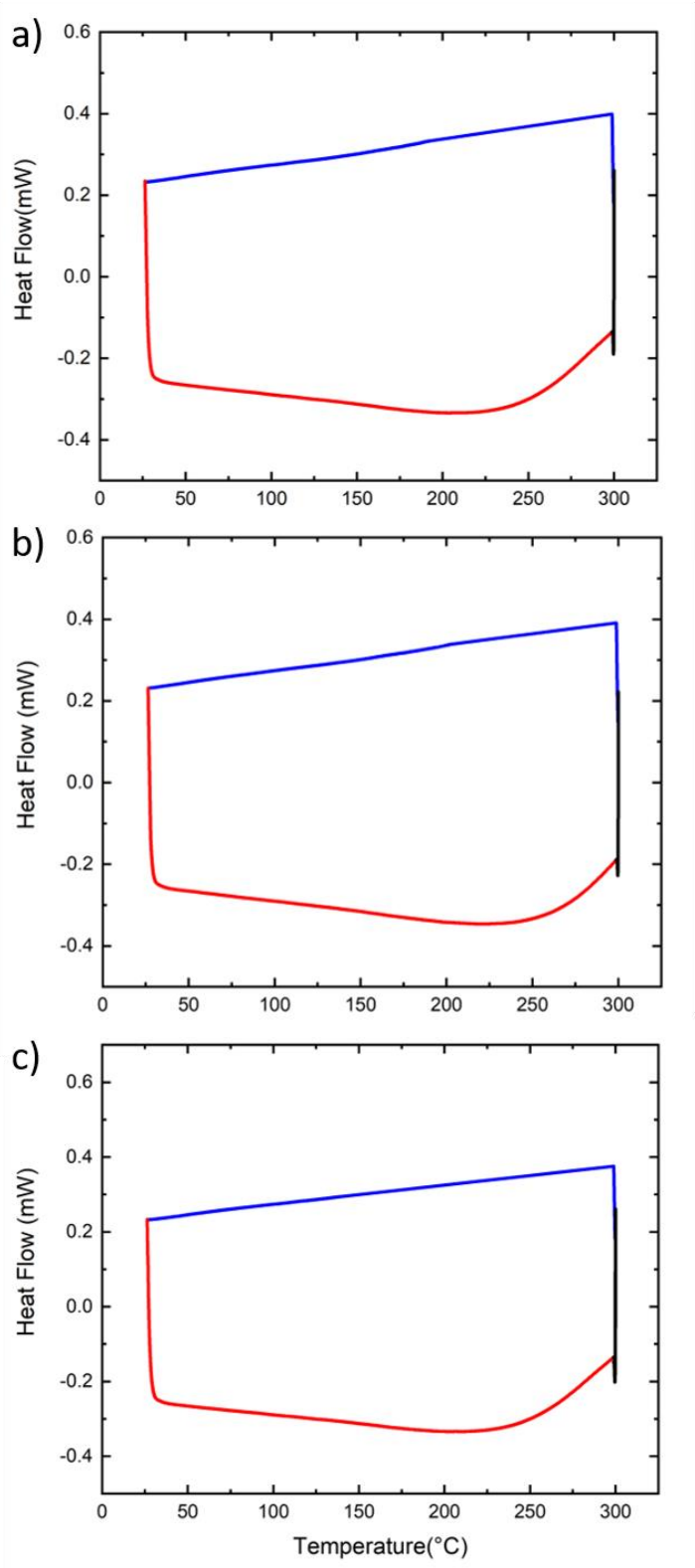


Figure 16. DSC measurements of a) P1, b) P2 and c) P3

## 5.1.8 Organic field effect transistor (OFET) measurements

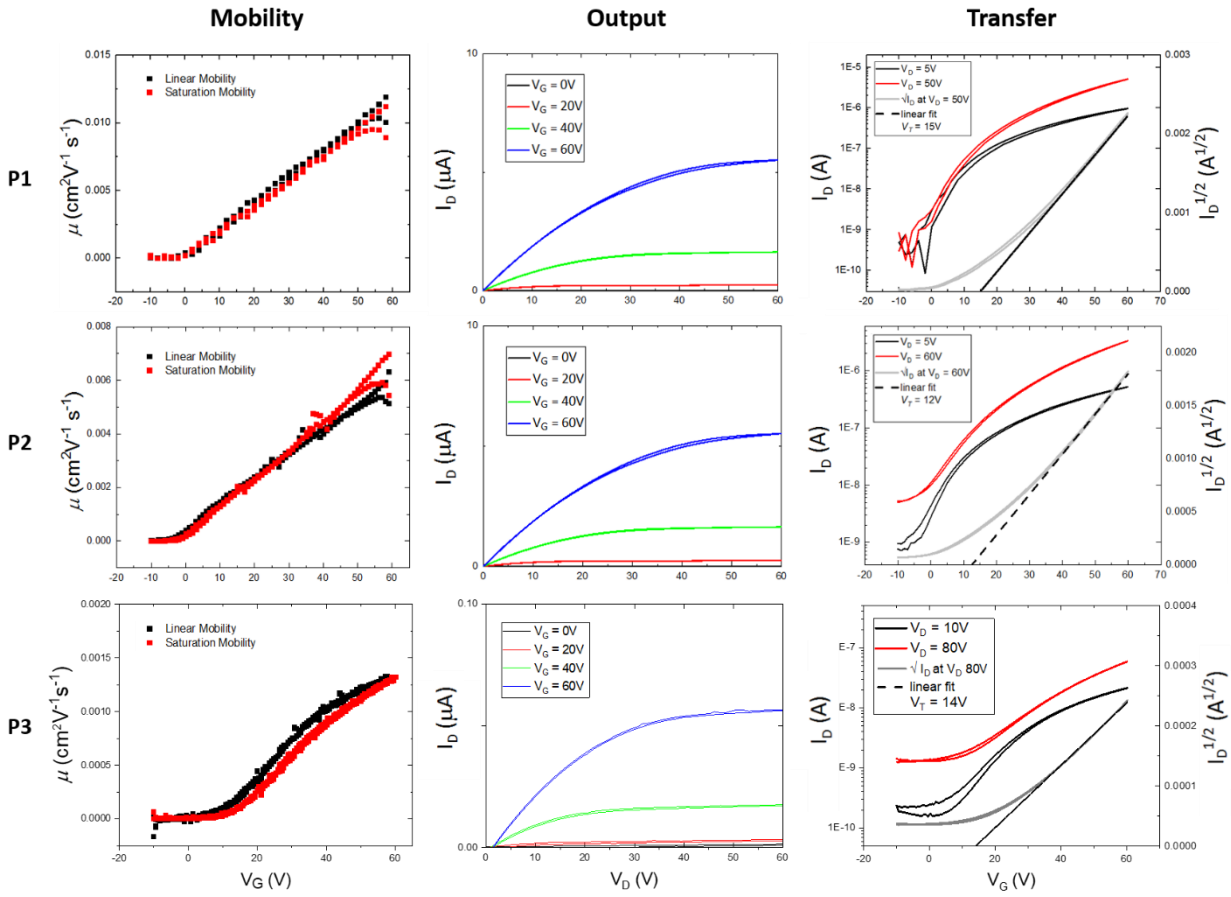


Figure 17. Transistor properties of the polymers.

Photolithographyically defined interdigitated gold electrodes are used in this work, the thickness of which is 20 nm, and with a channel length of 20 um and a channel width of 1 mm, respectively. 30 nm semiconductor layer is spin-coated on top of cleaned electrodes, which is annealed at 200 degrees for half an hour to achieve optimal microstructure. After the annealing process, 500 nm PMMA layer is spin-coated on top of the semiconductor layer and annealed at 90 degrees for 20 minutes. Then for the final step, 30 nm aluminum is evaporated around the channel region on top of the PMMA layer to form the gate electrode and encapsulate the devices.

### 5.1.9 Thermoelectric measurements

All films were deposited inside a nitrogen-filled glovebox. Glass substrates were cleansed in water, acetone and isopropanol. P1, P2, and P3 solutions (all at 5 mg/ml) were obtained by dissolving the polymers in o-dichlorobenzene, and stirring at 100 °C for at least 10 h to ensure dissolution. The pristine films were obtained by spin-coating the warm solutions (70 °C) onto the substrates at 1000 rpm for 30 s. Afterwards, the films were thermally annealed at 110 °C on a hot template for 30 min, followed by cooling down to room temperature. For solution doping, polymer solutions in o-dichlorobenzene (5 mg/mL) and corresponding N-DMBI solution in o-dichlorobenzene (same molar concentration as the corresponding polymer) were firstly mixed in volume ratios, stirring at 70 °C for at least 1h. Then, the aforementioned warm solutions were spin-casted onto the glass substrates (1000 rpm, 30 s). Afterwards, the films were heated at 110 °C for 30 min and cooled down to ambient temperature. Electrical conductivity and Seebeck were both measured inside the nitrogen-filled glovebox using a Keithley 4200-SCS. For all measurements, prior to polymer layers deposition, 25 nm Au electrodes with a 5 nm Ti adhesion layer were firstly deposited on top of glass substrates. The electrodes dimensions for conductivity and Seebeck measurements were L/W = 30 μm/1000 μm and L/W = 0.5 mm/15 mm, respectively. Two Peltier elements were used to achieve a temperature gradient (ΔT) across the samples, and the thermovoltage (ΔV) was tested between two electrodes. The Seebeck was determined from the slope of ΔV measured at six different ΔT values.

### 5.1.9 2D-Grazing Incidence Wide Angle X-ray Scattering (GIWAXS)

2-D GIWAXS was carried out at the Advanced Photon Source at Argonne National Laboratory on beam line 8-ID-E at room temperature under vacuum with 10.92 keV ($\lambda$ = 1.135 Å) synchrotron radiation with a 0.14° incident angle and measured with a Pilatus 1M hybrid pixel array detector during 10 second exposures. GIWAXS samples were spin coated on Si wafer (University Wafer) substrates (~20 mm x 20 mm) from chloroform solutions (5 mg polymer/ml chloroform). Data analysis was carried out with GIXSGUI Matlab toolbox[6].

Table S4.GIWAXS scattering peak centers and d-spacing.

| | | P1 | P2 | P3 |
|---|---|---|---|---|
| In-plane (100) | q ($Å^{-1}$) | 0.201 | 0.205 | 0.202 |
| | d (Å) | 31.3 | 30.7 | 31.1 |
| In-plane (010) | q ($Å^{-1}$) | 1.740 | 1.733 | 1.746 |
| | d (Å) | 3.61 | 3.63 | 3.60 |
| Out-of-plane (010) | q ($Å^{-1}$) | 1.736 | 1.722 | 1.741 |
| | d (Å) | 3.62 | 3.65 | 3.61 |

## 5.1.10 Density functional theory (DFT)

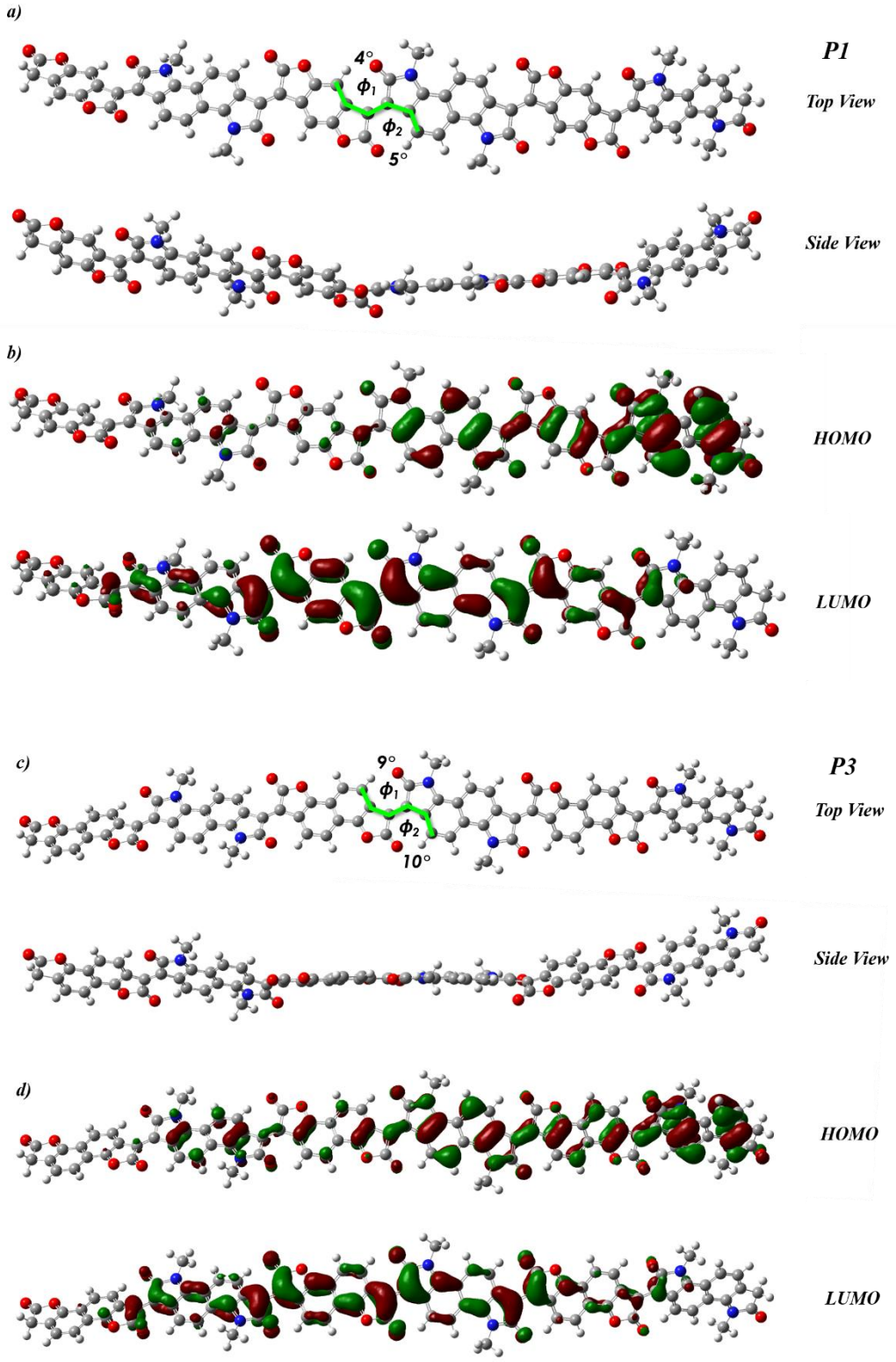


Figure 18. DFT-optimized geometries and molecular frontier orbitals of the trimer of (a) and (b) P1 and P2, (c) and (d) P3.

### 5.1.11 References


1. B. Fu, J. Baltazar, A. R. Sankar, P.-H. Chu, S. Zhang, D. M. Collard and E. Reichmanis, *Advanced Functional Materials*, 2014, **24**, 3734-3744.
2. N. M. Randell, P. C. Boutin and T. L. Kelly, *Journal of Materials Chemistry A*, 2016, **4**, 6940-6945.
3. P. Singla, N. Van Steerteghem, N. Kaur, A. Z. Ashar, P. Kaur, K. Clays, K. S. Narayan and K. Singh, *Journal of Materials Chemistry C*, 2017, **5**, 697-708.
4. Y. Deng, B. Sun, Y. He, J. Quinn, C. Guo and Y. Li, *Chem Commun (Camb)*, 2015, **51**, 13515-13518.
5. A. Onwubiko, W. Yue, C. Jellett, M. Xiao, H. Y. Chen, M. K. Ravva, D. A. Hanifi, A. C. Knall, B. Purushothaman, M. Nikolka, J. C. Flores, A. Salleo, J. L. Bredas, H. Sirringhaus, P. Hayoz and I. McCulloch, *Nat Commun*, 2018, **9**, 416.
6. Z. Jiang, *Journal of Applied Crystallography*, 2015, **48**, 917-926.


## 5.2 Supplementary information for chapter 3

### 5.2.1 General procedures and experimental details

All chemical reagents and starting materials were purchased from commercial sources and used without further purification. Reactions were carried out on a standard Schlenk line technique under a nitrogen atmosphere using solvents and reagents as commercially supplied.

$^{1}$H NMR and $^{13}$C NMR spectra were recorded with Bruker 500 MHz AVANCE III NMR spectrometer equipped with CryoProbe (BrukerBioSpin,Rheinstetten, Germany). Residual proton peaks are 7.26 ppm for $CDCl_3$ and 2.52 ppm for DMSO-$d_6$. High-resolution Mass Spectra (HRMS) were recorded on a Bruker HRMS MICROTOF II spectrometer. The

polymer molecular weights (number-average $M_n$ and weight-average $M_w$) and polydispersity were measured using an Agilent Technologies PL-GPC 220 High Temperature gel permeation chromatography in Chloroform ($CHCl_3$) as the mobile phase at 40 °C. Absorption spectra were recorded on Varian Cary 5000 spectrophotometer by preparing polymer solutions in chloroform and spin-coated polymer films onto pre-treated glass substrates. Photo Electron Spectroscopy in Air (PESA) measurements were recorded with a Riken Keiki AC-2 PESA spectrometer with a power setting of 5 nW and a power number of 0.3. Samples for PESA were prepared on glass substrates by spin-coating. Thermal gravimetric analyses (TGA) were performed under a $N_2$ atmosphere using TA Instruments Trios V4.3.1.39215, at a heating rate of 10 °C $min^{-1}$. Differential scanning calorimetry (DSC) analyses were performed on a METTLER TOLEDO Instrument DSC822 calorimeter with a heating rate of °C $min^{-1}$, two heating-cooling cycles from RT to 300 °C under nitrogen atmosphere.

Ultraviolet photoelectron spectroscopy (UPS) and low energy inverse photoelectron spectroscopy (LE-IPES) measurements were conducted in a single UHV multi-probe chamber (ScientaOmicron) operating at $10^{-10}$ mbar. UPS was conducted with a Helium discharge lamp (focus) He(1) 21.22 eV and a hemispherical electron analyzer Sphera II with a multiple channelton detector. LE-IPES measurements were conducted in isochromatic bremsstrahlung mode using a home built set up consisting of a mono-energetic (0.25 eV-0.5 eV) incident electron source (STAIB) directed normal to the sample biased at -20 V, emitted photons were collected using an assembly of internal and external focusing lens (Thorlabs) through an optical band pass filter (280 nm) and detected with a photo multiplier tube (PMT) (Hammatsu). All other light in the chamber was excluded. Calibration was achieved with reference to an evaporated Au film fermi level for UPS. The calibration of LE-IPES was performed in accordance with literature with reference to the 0 eV kinetic energy point E0 assigned to the centre of a Gaussian fitted to the turn on drain current with linearly increased beam energy.

The spectra onset are then referenced to the Evac position at E0 + hυ (4.43 eV). Samples were prepared by spincoating from dilute solutions in chloroform (5 mg/mL) on evaporated Au substrates. Processing and fitting of the data was achieved using Origin, removing a small 2% He(1) β 23.09 eV satellite from the UPS and arbitrary intensity normalization for ease of comparison with fitting.

Electron paramagnetic resonance (EPR) measurement were recorded by using a Bruker Elexsys E500 spectrometer operating at 9.8 GHz (X-band). EPR spectra were recorded on quartz substrates sealed in nitrogen atmosphere, in dark at room temperature. Atomic force microscopy (AFM) was performed with a Dimension 3100 system from Veeco, operating in tapping mode. UV-vis-NIR spectra of doped thin-films were recorded with a Lambda 900 from Perkin Elmer, with a resolution of 2 nm on calcium fluoride windows placed in air-tight sample holder sealed in nitrogen environment.

## 5.2.2 Synthetic details

The synthetic procedures for the side chain preparation of (4-Bromobutyl)tricosane (R1)[1], 5-decylheptadecan-1-amine (R2)[7], and 22-iodo2,5,8,11,14,17,20-heptaoxadocosane (R3)[8], were inspired from literature. Starting materials 2-decyl-1-tetradecanol, was purchased from Sigma-Aldrich. Other reagents were purchased from Sigma-Aldrich, Alfa Aesar, and Fisher Scientific.

Synthesis of 3,8-dihydroindolo[7,6-*g*]indole-1,2,6,7-tetraone (Bisisatin),[2] 1,5-bis(5-decylheptadecyl)-1,5-dihydropyrrolo[2,3-*f*]indole-2,3,6,7-tetraone (M1),[5] *N*,*N*'-bis(5-decylheptadecyl)bis-isatin (M2),[2] 3,8-Di-(2,5,8,11,14,17,20-heptaoxadocosan-22-yl)-3,8-dihydroindolo[7,6-*g*]indole1,2,6,7-tetraone (M3),[2] benzo[1,2-*b*-4,5-*b'*]difuran-2,6-(3*H*,7*H*)-dione (M4)[3], and naphtho-[1,2-*b:*5,6-*b'*]difuran-2,7(3*H*, 8*H*)-dione (M5)[4] were inspired and modified from published literatures.

## Monomer Synthesis

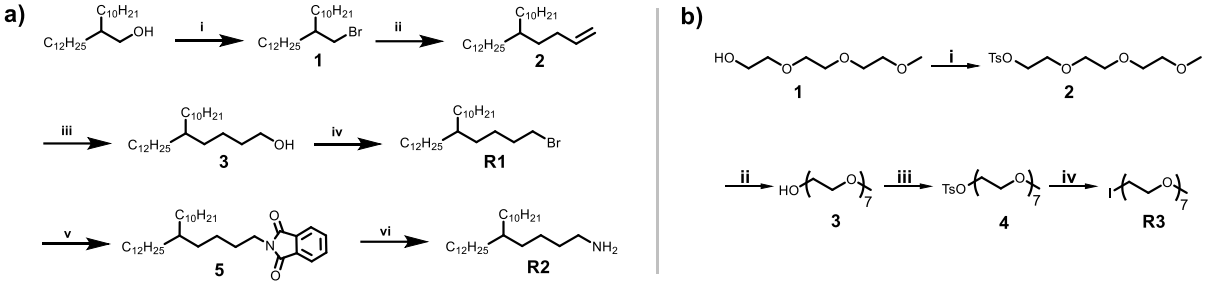


**Figure S1.** Synthesis of the different side chains used in the synthesis. a) alkyl chain and b) glycol chain synthesis procedure. a) i) NBS,$PPh_3$,DCM, 0 °C-r.t ; ii) Allylmagnisuum bromide, THF, 170 °C; iii) $NaBH_4$, $BF_3.Et_2O$, NaOH, $H_2O_2$.; iv) NBS,$PPh_3$,DCM, 0 °C-r.t; v) phthalimide potassium salt, DMF, 90 °C; vi) $NH_2NH_2$, MeOH, 90 °C; b) i) TsCl (4-Toluene sulfonyl chloride), KOH, THF, water, r.t, ii) Tetra(ethylene glycol), NaH, DMF, r.t., iii) $(CH_3)_3N{\cdot}HCl$, TsCl, $Et_3N$, DCM, r.t; iv) NaI, acetone, 60 °C.

## Synthesis of 1,5-bis(5-decylheptadecyl)-1,5-dihydropyrrolo[2,3-*f*]indole-2,3,6,7-tetraone (M1):

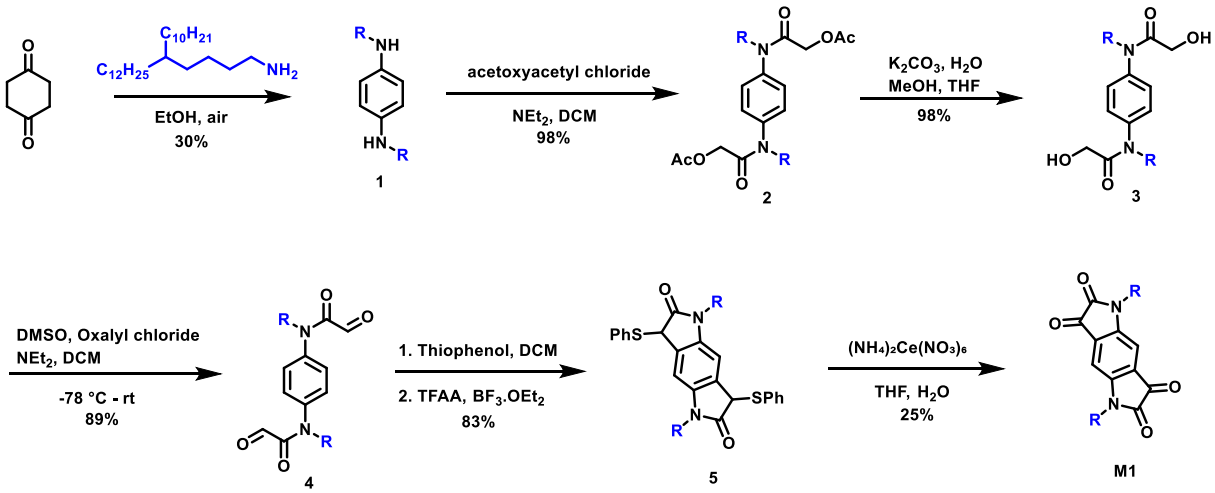

**Synthesis of N,N'-bis(2-decyltetradecyl)benzene-1,4-diamine (1):**

1,4-Cyclohexanedione (7.5 g, 67 mmol) was dissolved in 300 mL ethanol and 2-decyltetradecan-1-amine (53 g, 134 mmol) added to the solution. Air was bubbled through the solution for 2 hours and the solvent was removed under reduced pressure. The red residue was purified on basified silica gel (3% EtOAc in PE) to furnish the title compound (41 g, 71 %) as brown oil. $^{1}$H NMR (400 MHz, $CDCl_3$) δ 6.48 (s, 4H), 2.97 (t, *J* = 7.1 Hz, 5H), 1.54 – 1.43 (m, 5H), 1.27 – 1.09 (m, 139H), 0.80 – 0.76 (m, 7H). $^{13}$C NMR (100 MHz, Chloroform-*d*) δ 136, 118.5, 43.9, 38.4, 32, 33.3, 37.4, 28.8, 27.4, 29.9, 29.6, 29.3, 31.9, 22.7, 14.1.

**Synthesis of benzene-1,4-diylbis{[(2-decyltetradecyl)imino]-2-oxoethane-2,1diydiacetate (2):**

Triethylamine (7.04 mL, 50.8 mmol) was added to *N,N'*-bis(2-decyltetradecyl)benzene-1,4diamine (20 g, 23.1 mmol) dissolved in anhydrous DCM (260 mL) at 0 °C. Acetoxyacetyl chloride (5.46 mL, 50.8 mmol) was injected drop wise into the flask before the reaction was warmed to room temperature and stirred for 16 hours. The reaction was quenched with $NaHCO_3$. The phases were separated and the aqueous phase extracted with EtOAc. The combined organic phase was washed with brine dried over $MgSO_4$, the solvent removed under pressure to give pale yellow solid, (24 g, 98 %). $^{1}$H NMR (400 MHz, $CDCl_3$) δ 3.62 (t, *J* = 7.8 Hz, 4H), 2.06 (s, 7H), 1.44 (dd, *J* = 10.5, 5.1 Hz, 5H), 1.30 – 1.04 (m, 154H), 0.79 (s, 5H). $^{13}$C NMR (100 MHz, Chloroform-*d*) δ 135, 131.6, 170.2, 169.6, 62.8, 42.4, 38.4, 27.7, 33.3, 37.4, 24.8, 27.4, 29.9, 29.6, 29.3, 31.9, 22.7, 20.0, 14.1.

**Synthesis of *N,N'*-benzene-1,4-diylbis[N-(2-decyltetradecyl)-2-hydroxyacetamide] (3):**

Benzene-1,4-diylbis{[(2-decyltetradecyl)imino]-2-oxoethane-2,1-diyl} diacetate (3.60 g, 28.1 mmol) in THF (1666 mL) and MeOH/water mixture (1500 ml, 167 mL). The reaction mixture was stirred in the presence of excess $K_2CO_3$ (38.8 g, 281 mmol) at room temperature for 4 hours and the salts were filtered off. The mixture was concentrated under reduced pressure and water and ethyl acetate added to the residue. The phases were separated and the aqueous phase is extracted with ethyl acetate. The combined organic phases were washed with brine dried over $MgSO_4$ and the solvent removed in the rotary evaporator to furnish compound (3) as light yellow oil. (24 g, 87%). $^1$H NMR (400 MHz, $CDCl_3$) δ 7.19 (s, 5H), 4.05 (q, *J* = 7.2 Hz, 4H), 3.69 (d, *J* = 5.4 Hz, 7H), 1.48 – 1.40 (m, 5H), 1.29 – 1.05 (m, 159H), 0.83 – 0.73 (m, 20H). $^{13}$C NMR (100 MHz, Chloroform-*d*) δ 135, 131.6,169.6, 61, 42.7, 38.4, 27.7, 33.3, 37.4, 24.8, 27.4, 29.9, 29.6, 29.3, 31.9, 22.7, 20.0, 14.1.

**Synthesis of *N,N'*-(1,4-phenylene)bis(N-(2-decyltetradecyl)-2-oxoacetamide) (4):**

Under argon atmosphere, oxalyl chloride (7.4 mL, 89 mmol) was diluted with DCM (100 ml) and cooled to -78 °C. A solution of DMSO (7 mL) in DCM (104 mL) was added to the reaction flask. The reaction flask was stirred for 20 minutes before a solution of *N,N'*-benzene1,4-diylbis[N-(2-decyltetradecyl)-2-hydroxyacetamide] (36 g, 37.1 mmol) in 170 mL DCM was injected drop wise into the flask. After 2 hours, trimethylamine (51.4 mL, 371 mmol) was added slowly at -78 °C. The reaction was then stirred at the same temperature for 4 hours before it was warmed to room temperature slowly. The reaction was quenched with saturated $NaHCO_3$ solution and the phases separated. The aqueous phase was extracted with DCM and the

combined phases washed with brine, dried over $MgSO_4$ and the solvent removed under vacuum to yield brown oil. (36 g, 99%). Which was used immediately.

**Synthesis of 1,5-bis(2-decyltetradecyl)-3,7-bis(phenylthio)-5,7-dihydropyrrolo[2,3*f*]indole-2,6(1*H*,3*H*)-dione (5):**

Crude *N,N'*-(1,4-phenylene)bis(N-(2-decyltetradecyl)-2-oxoacetamide) (18 g, 18.4 mmol) was diluted with DCM (90 mL) before thiophenol (3.76 mL, 36.8 mml) was added to flask. The reaction mixture was then stirred for 16 hours at room temperature. Following this, TFAA (23 mL, 166 mmol) was added slowly to the reaction and stirred for 1 hour 30 minutes, after which, $BF_3 \cdot Et_2O$ (11.6 mL, 92 mmol) was added to the flask cautiously. Following further stirring for 3 hours, the reaction was cooled to 0 °C before it was quenched with $NaHCO_3$. The aqueous phase was extracted with DCM and the organic phases combined and washed with brine and dried over $MgSO_4$. The solvent was removed under reduced pressure to furnish red /brown residue as the crude product, which was used without further purification. Yield (18 g, 83%).

**Synthesis of 1,5-bis(2-decyltetradecyl)-1,5-dihydropyrrolo[2,3-*f*]indole-2,3,6,7-tetraone (M1):**

Ceric ammonium nitrate (158 g, 289 mmol) was added to the solution of 1,5-bis(2decyltetradecyl)-3,7-bis(phenylthio)-5,7-dihydropyrrolo[2,3-*f*]indole-2,6(1*H*,3*H*)-dione (42 g, 36.1 mmol) dissolved in a 6:1 ratio of THF/water (750 mL) mixture. Following 30 minutes stirring at room temperature the reaction mixture takes a deep purple coloration. After 3 hours stirring the reaction mixture was reduced under vacuum. The crude residue was purified by column chromatography on Biotage Isolera at a gradient of 3-10 % ethyl acetate in

petroleum spirit to furnish the titled compound, yield: 5 g, 15 %. $^{1}H$ and $^{13}C$ NMR are in section 3. . HRMS (m/z): (M·+) calc. ($C_{64}H_{112}N_2O_4$): 972.8622100940. Found: 972.86201

**Synthesis of N-alkylated bisisatin core monomers (M2 & M3):**

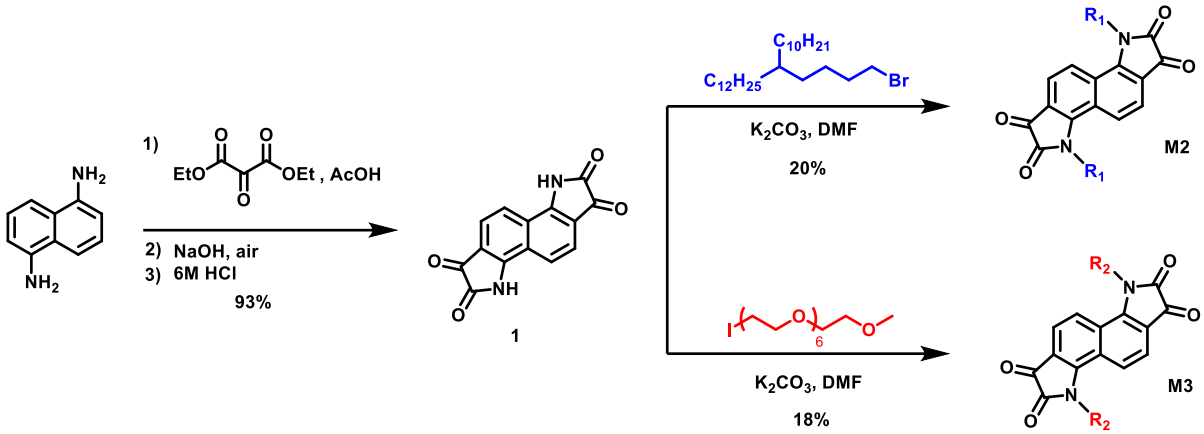


**Synthesis of 3,8-dihydroindolo[7,6-*g*]indole-1,2,6,7-tetraone (Bisisatin) (1) :**

1,5-Diaminonaphthalene (4 g, 25 mmol) was dissolved in (41 mL) glacial acetic acid and heated to reflux. To the resulting dark purple solution was added dropwise, diethylketomalonate (32 mL, 205 mmol) in glacial acetic acid (46 mL). The resulting mixture was heated to 150 °C overnight. The solvent was removed under vacuum and 1M NaOH was added to the resulting dark brick red solids until complete dissolution to a final pH of (11-12). The resulting red brown solution was heated at 150 °C overnight with sparging air into the solution. The resulting mixture was poured onto ice and 6M HCl was added until pH=0 to give a purple precipitate, which was filtered and washed with water to give dark red-purple solids (6 g, 93% yield) and carried out without further purification. $^{1}H$ NMR (500 MHz, DMSO-*d6*) δ 11.77 (s, 1H), 7.78 (d, *J* = 8.4 Hz, 1H), 7.59 (d, *J* = 8.4 Hz, 1H). $^{13}C$ NMR (125 MHz, DMSO-*d6*) δ 183.85, 152.36, 124.50, 120.51, 117.60, 115.75.

**Synthesis of *N,N*'-bis(5-decylheptadecyl)bisisatin (M2) :**

To a mixture of crude (3 g,11 mmol) and dry $K_2CO_3$ (8 g, 55 mmol) in anhydrous DMF (65 mL), was added 5-decy-1-heptadecyl bromide (21.7 g, 47.3 mmol). The resulting mixture was stirred at 70 °C for 4 hours. The reaction mixture was poured over $H_2O$ and acidified with 1M HCl to pH of 7. The aqueous layer was extracted with DCM, washed with $H_2O$, brine and dried over $MgSO_4$. The solvent was removed under vacuum. The crude viscous dark purple oil was purified by column chromatography (silica gel, DCM:petroleum spirit (7:3)), followed by precipitation in MeOH and filtered to afford the product as dark blue solids (2.3 g, 20% yield). $^1$H NMR (500 MHz, Chloroform-*d*) δ 7.97 (d, *J* = 8.7 Hz, 1H), 7.70 (d, *J* = 8.7 Hz, 1H), 4.25 (t, *J* = 7.6 Hz, 2H), 1.82 (pentet, *J* = 7.7 Hz, 2H), 1.59 (s, 3H), 1.49 – 1.39 (m, 2H), 1.36 – 1.10 (m, 48H), 0.90 (t, *J* = 6.8 Hz, 7H). $^{13}$C NMR (125 MHz, Chloroform-*d*) δ 182.81, 158.99, 152.21, 127.28, 119.63, 116.19, 43.56, 37.30, 33.29, 31.95, 30.15, 29.74, 29.40, 26.66, 23.93, 22.72, 14.17. HRMS (m/z): (M·+) calc. ($C_{68}H_{114}N_2O_4$): 1022.87786. found: 1023.88593.

$d_{(010)}$

**Synthesis of 3,8-Di-(2,5,8,11,14,17,20-heptaoxadocosan-22-yl)-3,8-dihydroindolo[7,6-*g*]indole1,2,6,7-tetraone (M3):**

To a suspension of bisisatin (1.65 g, 6.2 mmol) in anhydrous DMF (20 mL) was added freshly dried $K_2CO_3$ (4.30 g, 31.0 mmol). The mixture was heated to 70 °C. After 1 h, 22-iodo-2,5,8,11,14,17,20-heptaoxadocosane (11.20 g, 24.8 mmol) was added in one portion. The reaction mixture was stirred at 70 $^o$C for 6 hrs. The reaction mixture was cooled down to room temperature and poured over water and acidified with 1 M HCl to pH of 7. The aqueous layer was extracted with DCM, washed with water, brine and dried over $MgSO_4$. The solvent was removed under vacuum. The crude product was purified by column chromatography (silica gel,

DCM: Methanol = 25:1), followed by precipitation in hexane and filtered to afford the product as a blue sticky solid (1.02 g, 18%). $^{1}$H NMR (400 MHz, Chloroform-*d*) δ (ppm) 8.31 (d, *J* = 8.7 Hz, 2H), 7.69 (d, *J* = 8.6 Hz, 2H), 4.47 (t, *J* = 5.6 Hz, 4H), 3.92 (t, *J* = 5.6 Hz, 4H), 3.71 – 3.52 (m, 48H), 3.40 (s, 6H). $^{13}$C NMR (100 MHz, Chloroform-*d*) δ (ppm) 182.63, 159.93, 152.34, 127.41, 120.62, 119.94, 116.71, 71.90, 70.72, 70.64-70.26 (br), 68.59, 59.03, 43.74. HRMS (m/z): (M·+) calc. ($C_{44}H_{66}N_2O_{18}$): 910.43107. found: 911.43876.

**Synthesis of benzo[1,2-*b*-4,5-*b'*]difuran-2,6-(3*H*,7*H*)-dione (M4):**

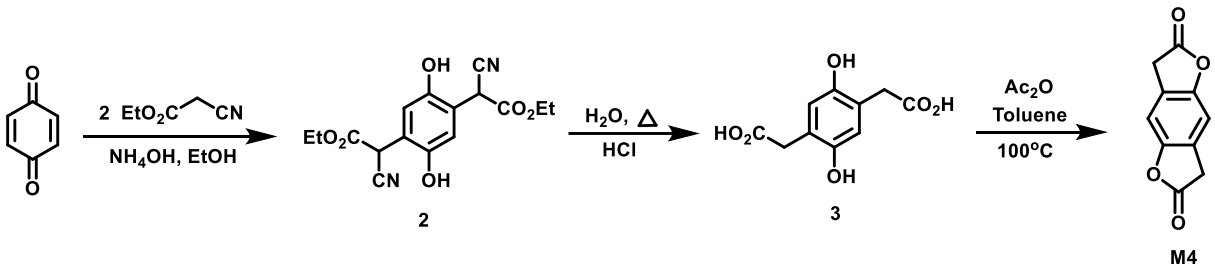


**Synthesis of (2):**

To a three-neck round-bottom flask equipped with two dropping funnels was added ethyl cyanoacetate (4.21 g, 4 ml, 37.25 mmol) in ethanol (15 ml). to the solution, concentrated ammonium hydroxide (3.17 g, 3.5 ml, 90.62 mmol) was added.in one dropping funnel was added ammonium hydroxide (11.28 g, 12.5 ml, 322 mmol) in water (20 ml) was added. Meanwhile, to a solution of ethyl cyanoacetate (6.4 g, 6 ml, 56 mmol) in ethanol (50 ml) was added p-benzoquinone (5 g, 46 mmol), the resulting solution was stirred at 40 °C for 30 min and transferred while hot to the other dropping funnel. The solutions in both dropping funnels were delivered to the flask at the same time with uniform rate. all the ammonium hydroxide solution should be added by the time 90% of the p-benzoquinone solution has been added.

After completion of the addition, the resuting solution was stirred at RT for 1 hour. The precipitates formed were filtered under vacuum and washed with ethanol and dried to get Compound 2 (3.01 g, 20% yield) as ashy purple solid.

**Synthesis of (3):**

To a residue of 1 (3 g, 9 mmol) was added concentrated HCl (0.027 g, 23 ml, 0.76 mmol) and water (18 mL) and the resulting solution was refluxed at 110 ℃ overnight. Water (15 ml) and celite (1.5 g) were added to the hot reaction mixture and stirred for 5 min, after which it is rapidly filtered with suction and the filtrate was taken and cooled. White creamy crystals have been collected upon filtration 3 (1.42 g, 59% yield).

**Synthesis of (M4):**

To a residue of 2 (1.4 g, 6.2 mmol) in anhydrous toluene (75 mL), acetic anhydride (16.4 g, 15 ml, 195.96 mmol). The resulting mixture was stirred at 100 ℃ overnight. The solvent was removed under vacuum, to the resulting solids was added chloroform and filtered, the filtrate was recrystallized in toluene to give the pure final product as beige crystals (0.1g, 26% yield). $^{1}$H NMR (500 MHz, DMSO-*d6*) δ 7.25 (s, 1H), 3.96 (s, 2H). $^{13}$C NMR (125 MHz, DMSO-*d6*) δ 174.85, 150.57, 124.42, 107.81, 33.78. HRMS (m/z): $[M+H]^+$ calc. ($C_{10}H_7O_4$): 191.0339. found: 191.0272.

**Synthesis of naphtho-[1,2-*b*:5,6-*b*']difuran-2,7(3*H*, 8*H*)-dione (M5):**

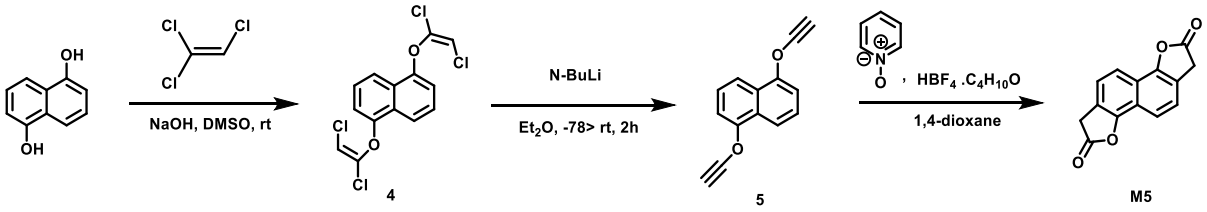


**Synthesis of (4):**

1,5-dihydroxynaphtelene (4.2 g, 26 mmol) was dissolved in DMSO (105 ml), to which grinded pellets of NaOH was added (2.3 g, 56.9 mmol) and the resulting mixture was stirred at RT for 2 h, then 1,1,2-trichloroethylene (7 ml, 78 mmol) was slowly added. The resulting mixture was stirred at RT overnight. Water was slowly added (100 mL). The two phases were separated and the aqueous layer was extracted with DCM, washed with brine and dried over $MgSO_4$ and the solvent was removed under vacuum. The crude product was purified by column chromatography (silica gel, petroleum spirit)), to afford 4 as a colorless solid (3 g, 33% yield). $^1$H NMR (500 MHz, Chloroform-*d*) δ 8.07 (d, *J* = 8.5 Hz, 1H), 7.53 (t, *J* = 8.1 Hz, 1H), 7.16 (d, *J* = 7.6 Hz, 1H), 6.10 (d, *J* = 1.2 Hz, 1H), $^{13}$C NMR (125 MHz, Chloroform-*d*) δ 149.94, 140.53, 127.32, 126.40, 119.01, 111.98, 105.32.

**Synthesis of (5):**

Compound 4 (3 g, 8.57 mmol) was dissolved in $Et_2O$ (60 ml). the mixture was cooled to -78 °C to which 2.5 M solution of n-BuLi in hexane (28 mL, 68.5 mmol) was slowly added and stirred at -78 °C for 1 hour and subsequently warmed to -40 °C and stirred for 2 hours at the same temperature. Water was slowly added (60 mL). The two phases were separated and the aqueous layer was extracted with hexane, washed with saturated $NH_4Cl$, then brine and dried over $MgSO_4$ and the solvent was removed under vacuum to afford 5 as pale brown solids which was directly used for the next step without further purification due to its instability

**Synthesis of (M5):**

In 1,4 dioxane (22 mL), was added tetrafluoroboric acid diethyl ether complex (0.23 ml, 1.7 mmol) and 2,6-Dimethylpyridine *N*-oxide (2 ml, 17 mmol). Afterwards, Compound 5 (1.78 g, 8.5 mmol) was added and the resulting mixture was stirred at 80 °C overnight. The solvent was removed under vacuum, then methanol was added to form a precipitate, which was collected by filtration. The solids were dissolved in hot toluene the undissolved solids were filtered off. The filtrate was taken and the solvent was removed under vacuum. The resulting solids were dissolved in acetone, the undissolved solids were collected by filtration to afford the final pure product as pale brown solids (10 mg, 5% Yield). $^{1}$H NMR (500 MHz, DMSO-*d6*) δ 7.75 (d, *J* = 8.3 Hz, 1H), 7.63 (d, *J* = 8.4 Hz, 1H), 4.15 (s, 2H). $^{13}$C NMR (125 MHz, DMSO-d6) δ 174.95, 149.98, 123.65, 120.29, 119.41, 116.39, 34.27.

**Polymer Synthesis**

The synthetic procedure for the polymers were tailored from literature.[5]

**Synthesis of P-0:**

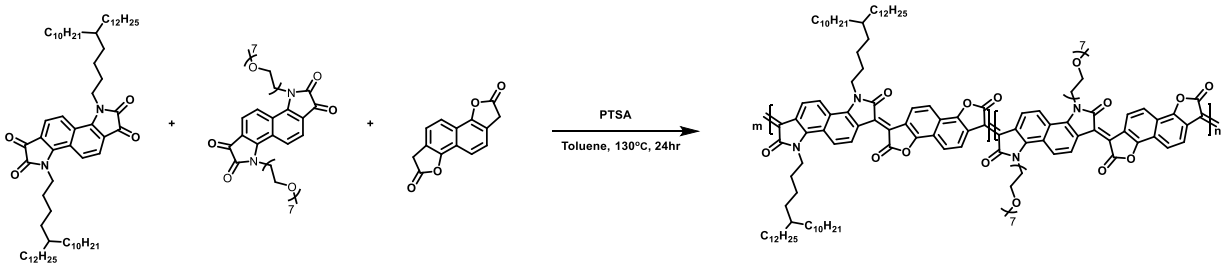


A microwave vial was charged with M5 (13.34 mg, 0.055 mmol), M2 (28.42 mg, 0.027 mmol), M3 (25.29 mg, 0.027 mmol) and p-toluene sulfonic acid monohydrate (6 mg, 0.0315 mmol). Anhydrous toluene (1.5 mL) was injected. The resulting solution was purged with $N_2$ for 30

min and the reaction was heated to 130 °C for 24 hours. The reaction mixture changed color from dark purple to dark green over the polymerization period. The crude polymer was precipitated in methanol and purified by Soxhlet extraction with methanol, acetone, hexane and finally chloroform. The chloroform fraction was collected and the solvent was removed under vacuum. Afterwards, the polymer precipitated into methanol, filtered and dried. Yield: 28.5 mg, 45 % dark green solid. GPC (Chloroform, 40 °C): Mn 10 kDa, Mw 14kDa. $^{1}$H NMR (400 MHz, Chloroform-*d*) δ 7.72-8.89 ppm (d), 3.55 ppm (t), 1.92 ppm (t), 0.67-1.75 ppm (broad).

**Synthesis of P-50:**

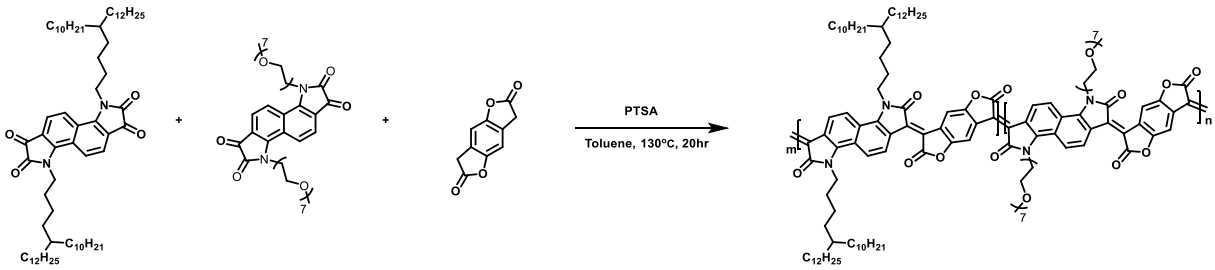


A microwave vial was charged with M4 (29.7 mg, 0.156 mmol), M2 (80 mg, 0.078 mmol), M3 (71.7 mg, 0.078 mmol) and p-toluene sulfonic acid monohydrate (6 mg, 0.0468 mmol). Anhydrous toluene (1.5 mL) was injected. The resulting solution was purged with $N_2$ for 30 min and the reaction was heated to 130 °C for 20 hours. The reaction mixture changed color from dark purple to dark green over the polymerization period. The crude polymer was precipitated in methanol and purified by Soxhlet extraction with methanol, acetone, hexane and finally chloroform. The chloroform fraction was collected and the solvent was removed under vacuum. Afterwards, the polymer precipitated into methanol, filtered and dried. Yield:

77 mg, 40 % dark blue solid. GPC (Chloroform, 40 °C): Mn 10.7 kDa, Mw 14 kDa. $^1$H NMR (400 MHz, Chloroform-*d*) δ 7.72-8.89 ppm (d), 3.55 ppm (t), 1.92 ppm (t), 0.67-1.75 ppm (broad).

**Synthesis of P-75:**

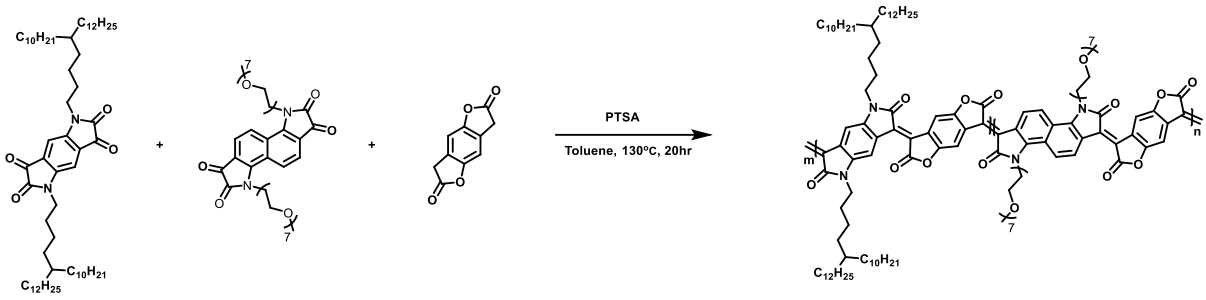


A microwave vial was charged with M4 (37.1 mg, 0.195 mmol), M1 (95 mg, 0.0976 mmol), M3 (88.8 mg, 0.0975 mmol) and p-toluene sulfonic acid monohydrate (6 mg, 0.0585 mmol). Anhydrous toluene (1.5 mL) was injected. The resulting solution was purged with $N_2$ for 30 min and the reaction was heated to 130 °C for 20 hours. The reaction mixture changed color from dark purple to dark blue over the polymerization period. The crude polymer was precipitated in methanol and purified by Soxhlet extraction with methanol, acetone, hexane and finally chloroform. The chloroform fraction was collected and the solvent was removed under vacuum. Afterwards, the polymer precipitated into methanol, filtered and dried. Yield: 85 mg, 45 % dark blue solid. GPC (Chloroform, 40 °C): Mn 18 kDa, Mw 33 kDa. $^1$H NMR (400 MHz, Chloroform-*d*) δ 7.72-8.89 ppm (d), 3.55 ppm (t), 1.92 ppm (t), 0.67-1.75 ppm (broad).

## 5.2.3 NMR spectra for monomers and polymers

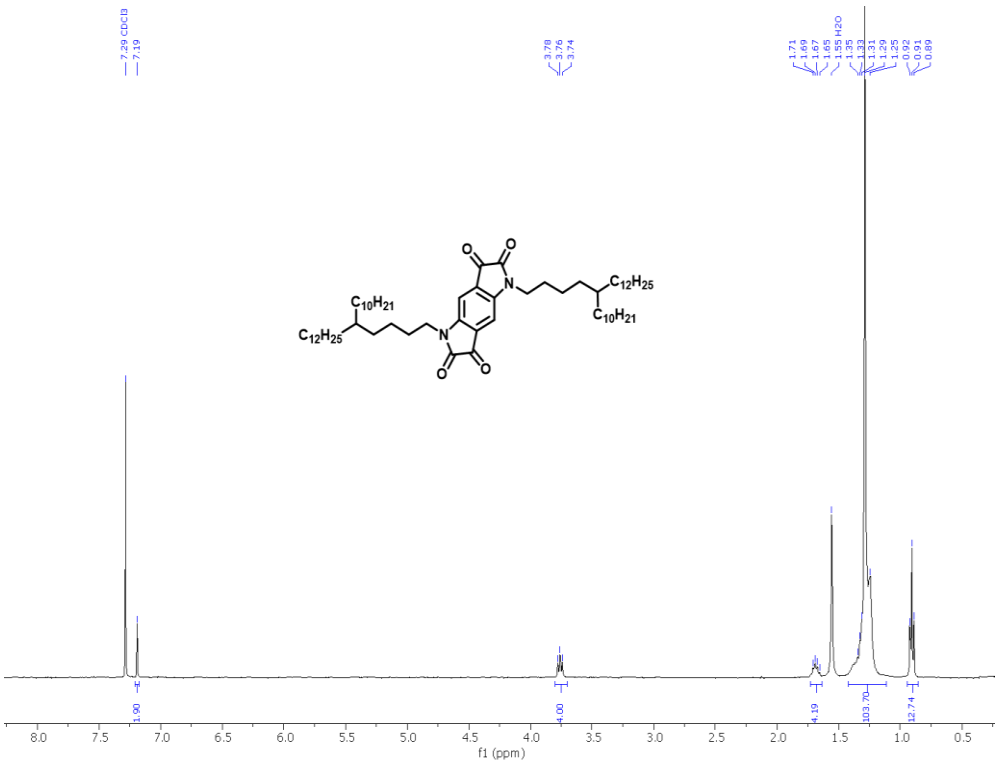


**Figure S2.** $^{1}$H NMR spectrum of M1

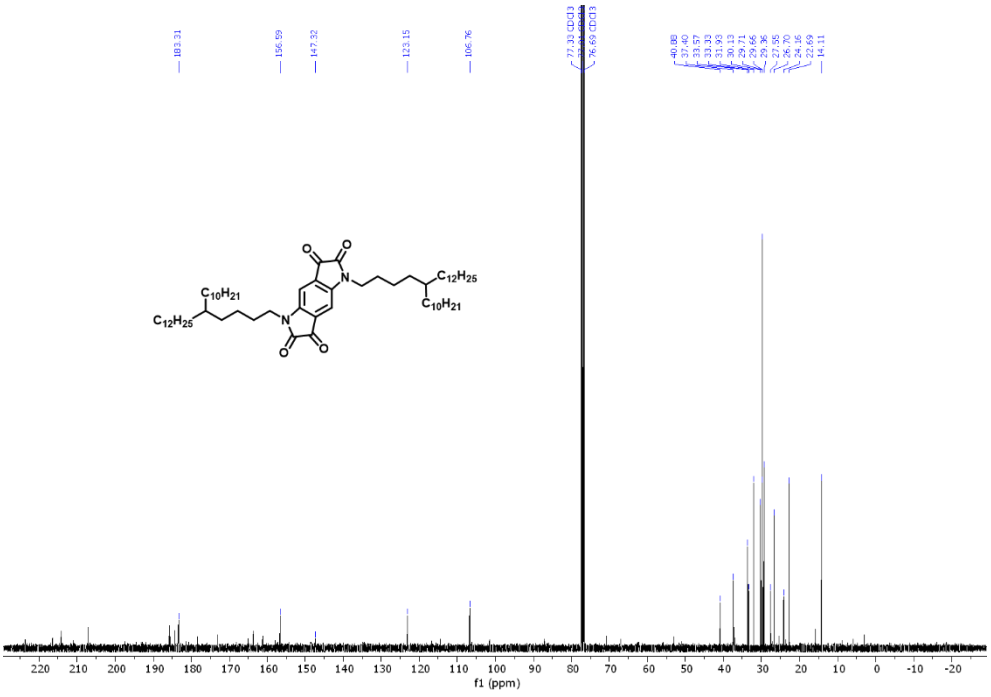


**Figure S3.** $^{13}$C NMR spectrum of M1

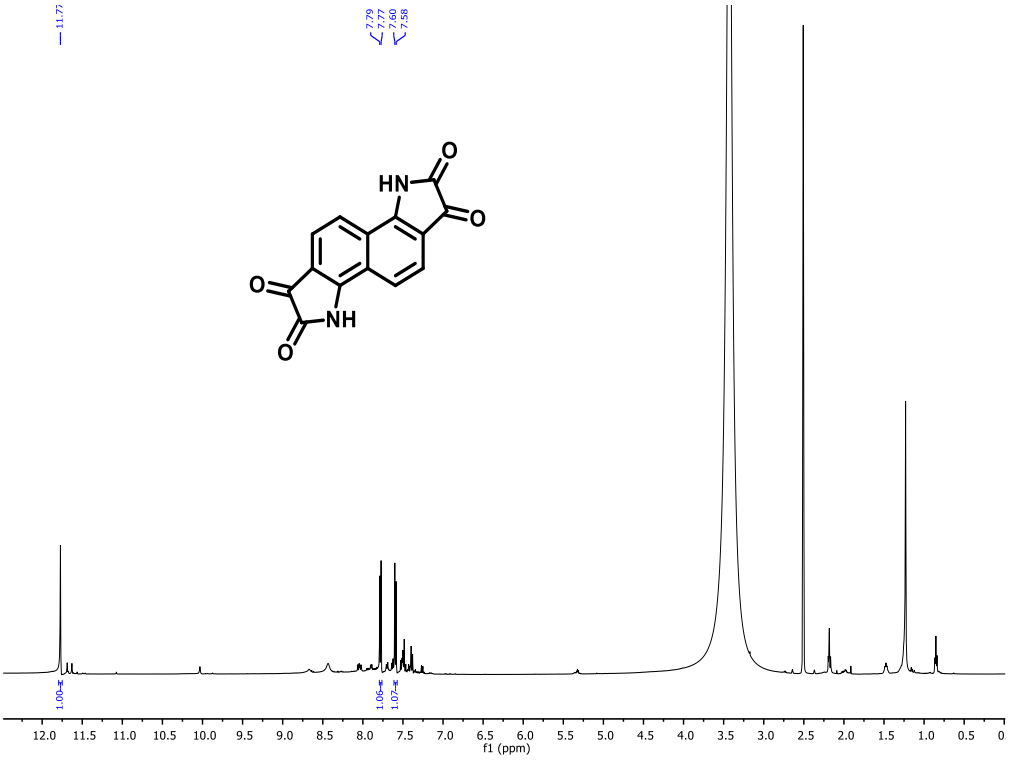


**Figure S4.** $^{1}$H NMR spectrum of bisisatin

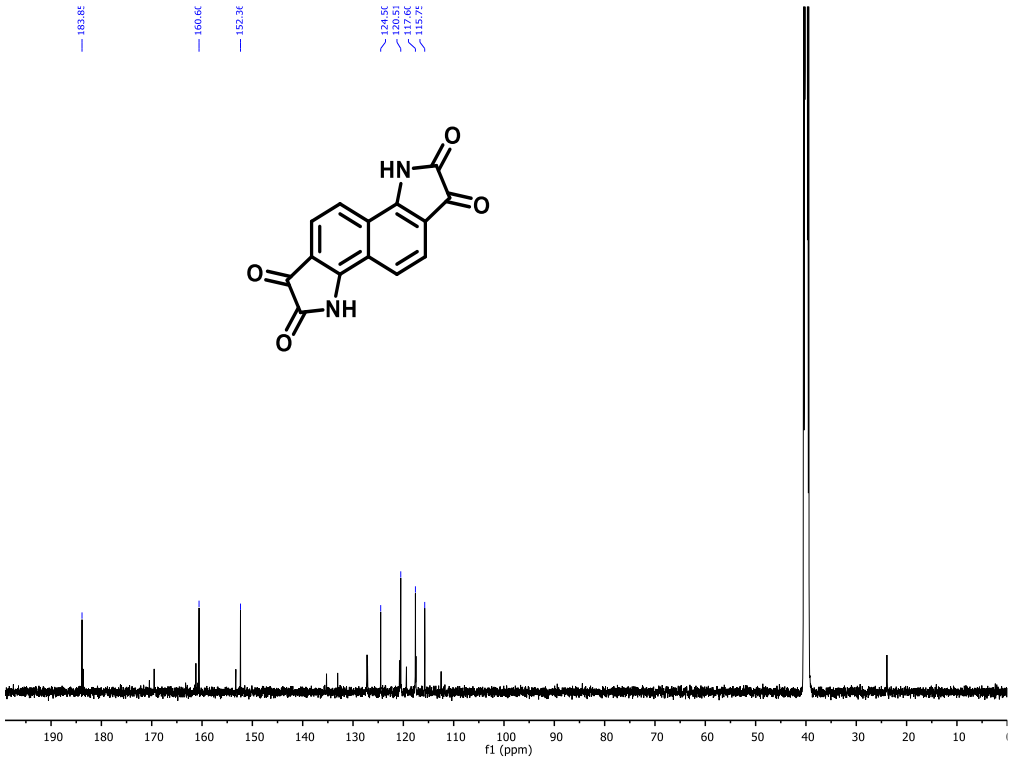


**Figure S5.** $^{13}$C NMR spectrum of Bisisatin

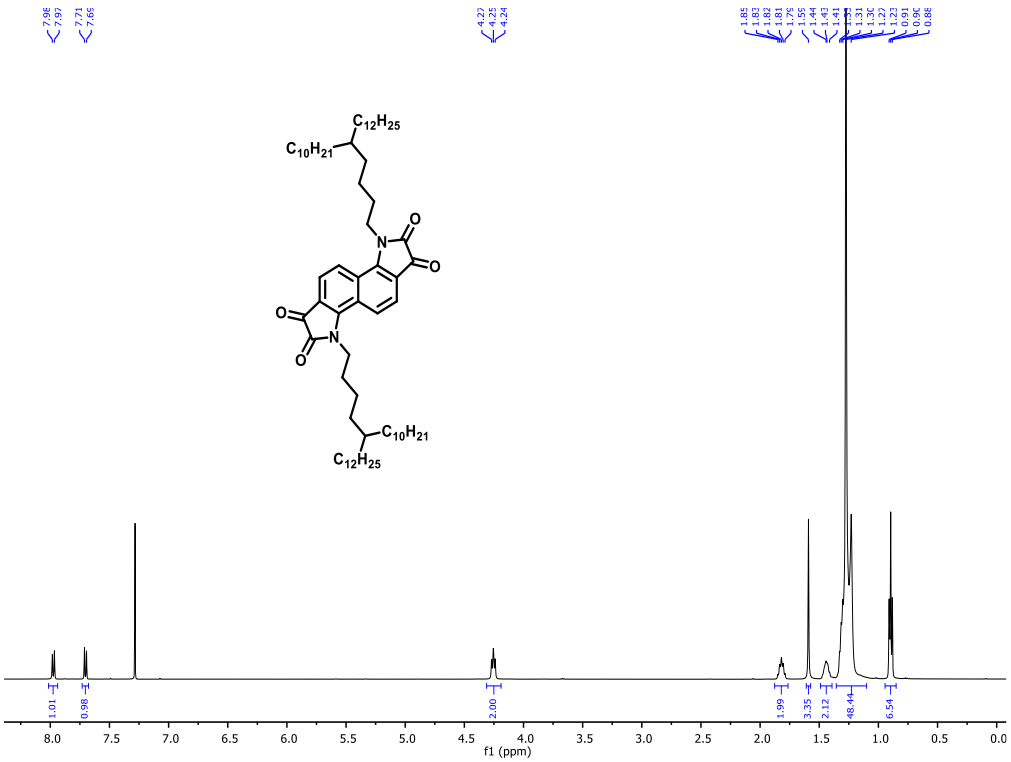


**Figure S6.** $^{1}$H NMR spectrum of compound M2

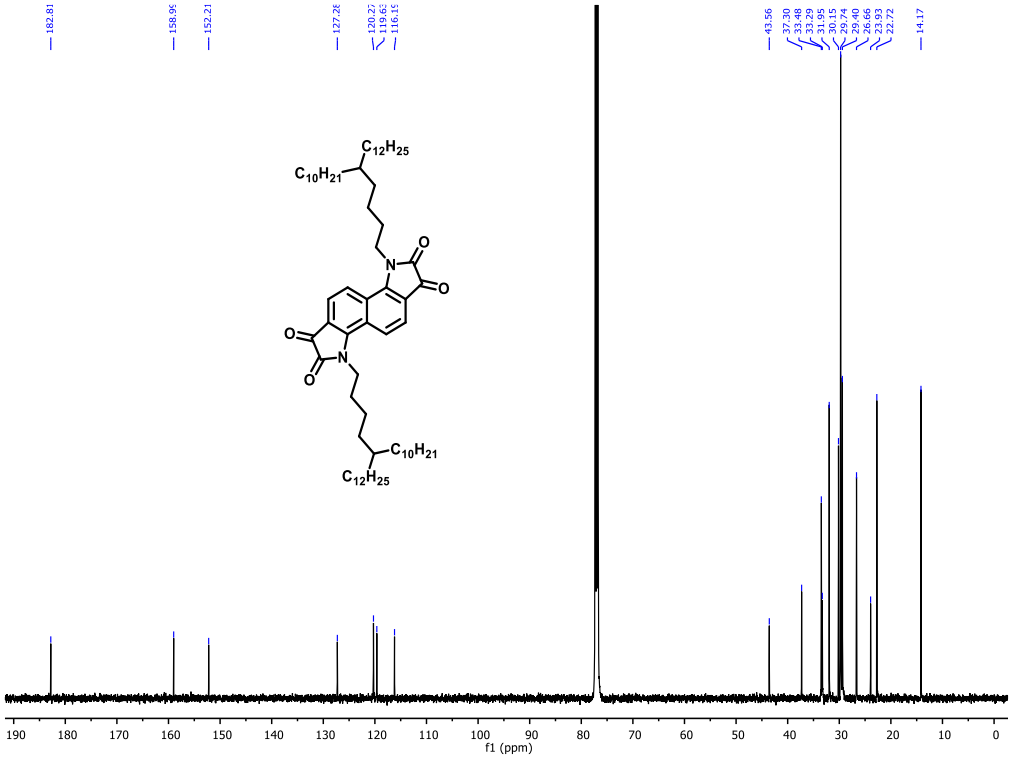


**Figure S7.** $^{13}$C NMR spectrum of compound M2

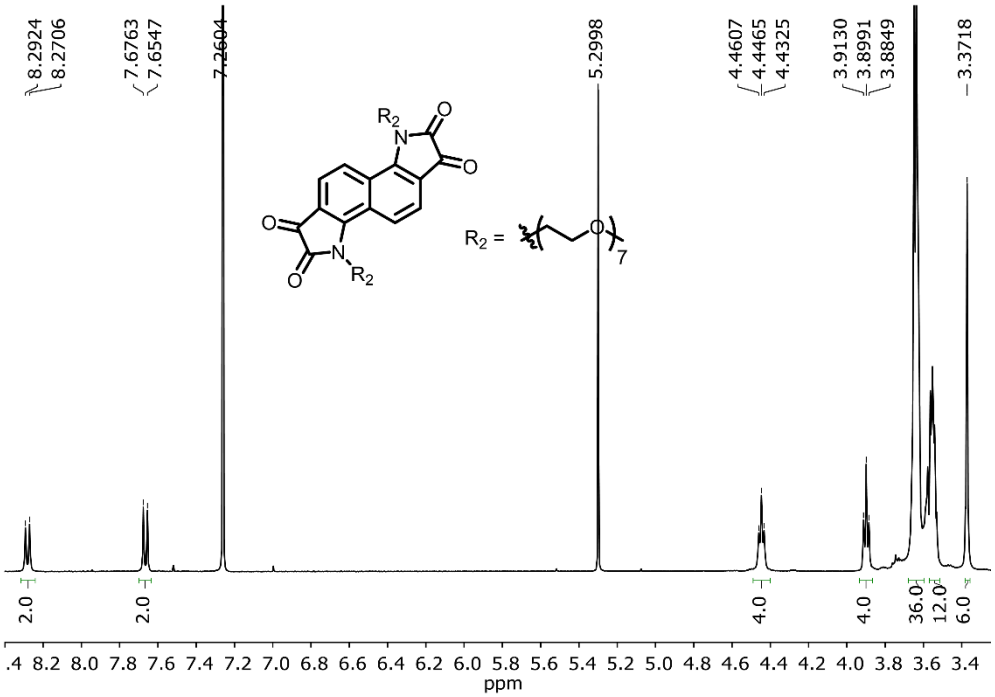


**Figure S8.** [1]H NMR spectrum of compound M3

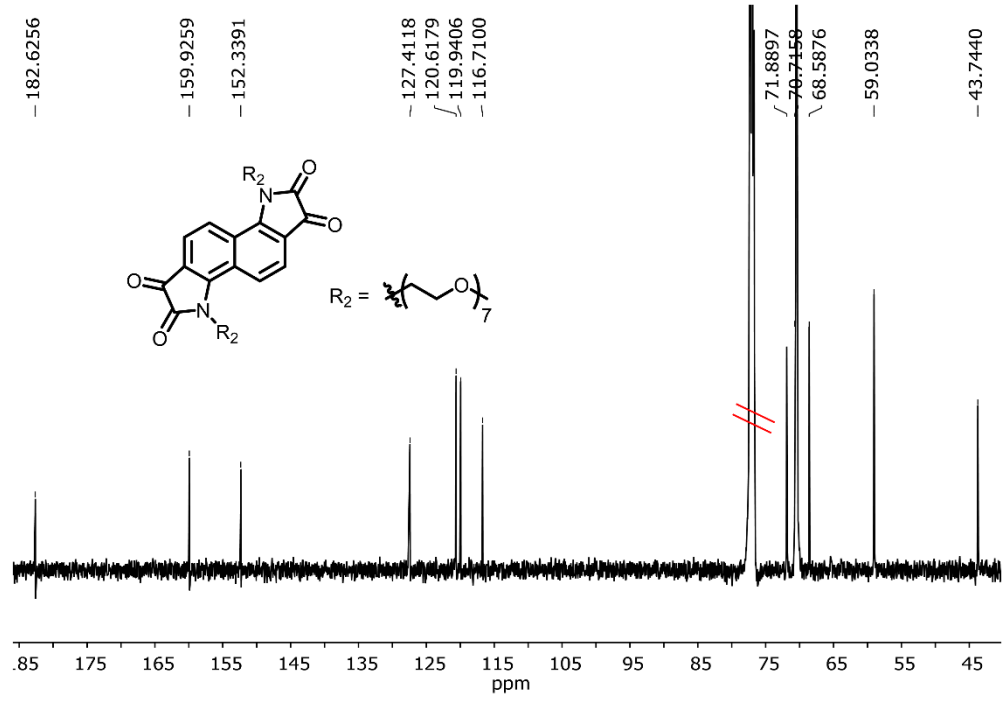


**Figure S9.**[13]C NMR spectrum of compound M3

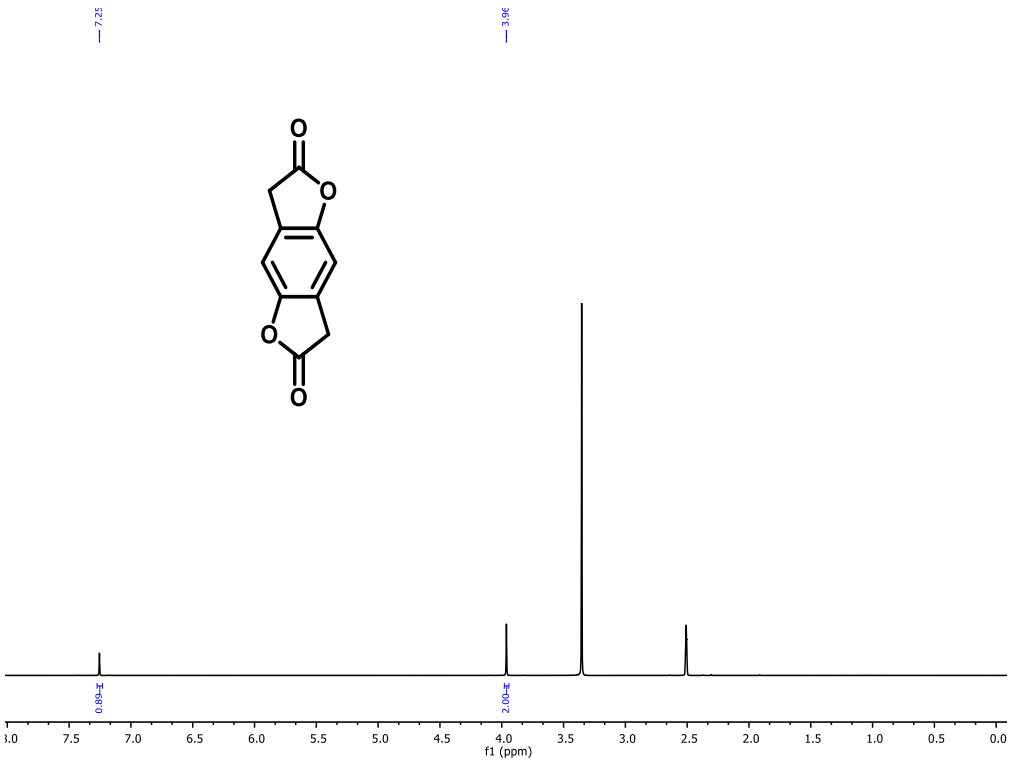


**Figure S10.** $^{1}$H NMR spectrum of compound M4

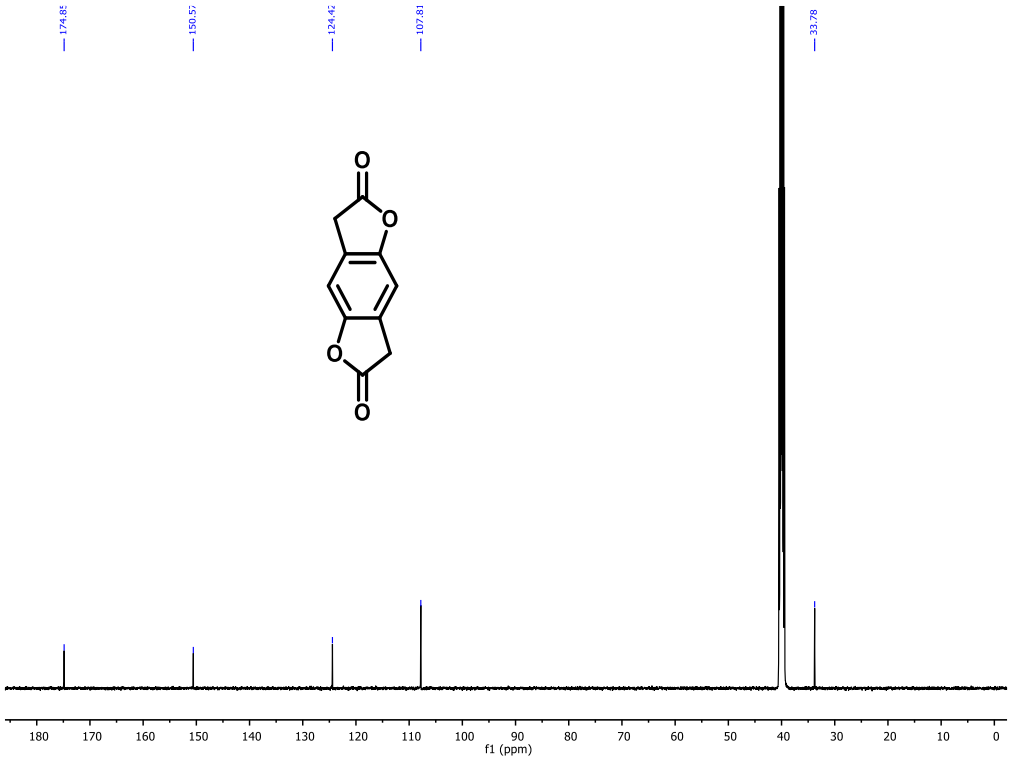


**Figure S11.** $^{13}$C NMR spectrum of compound M4


**Figure S12.** $^{1}$H NMR spectrum of compound M5

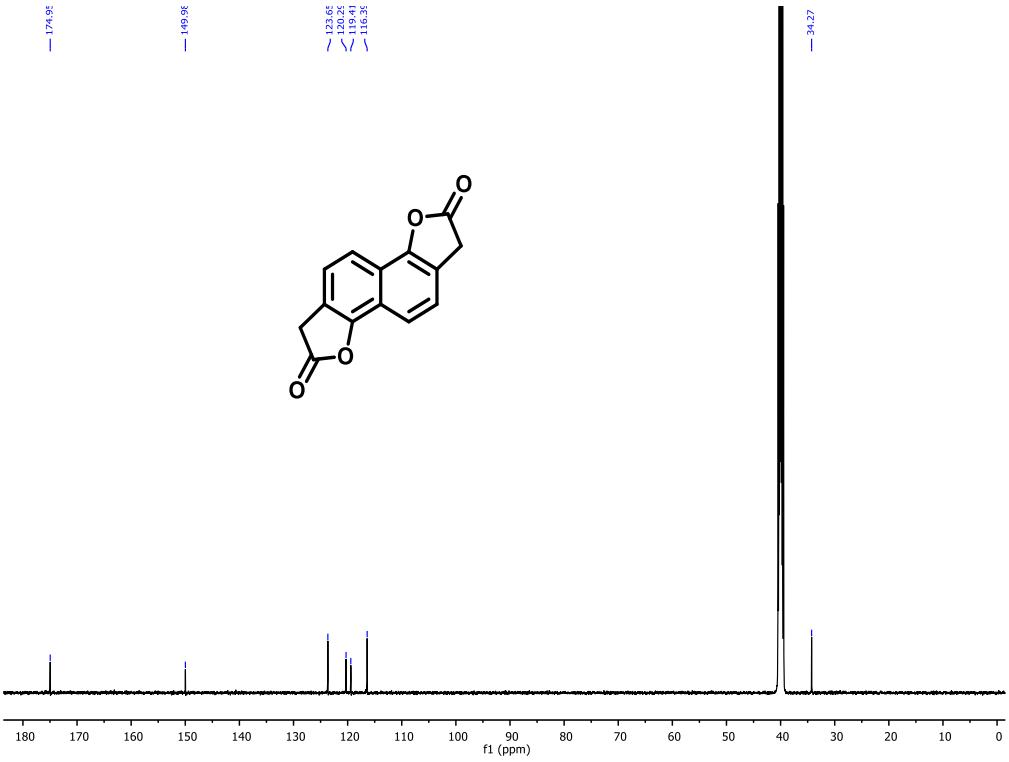


**Figure S13.** $^{13}$C NMR spectrum of compound M5

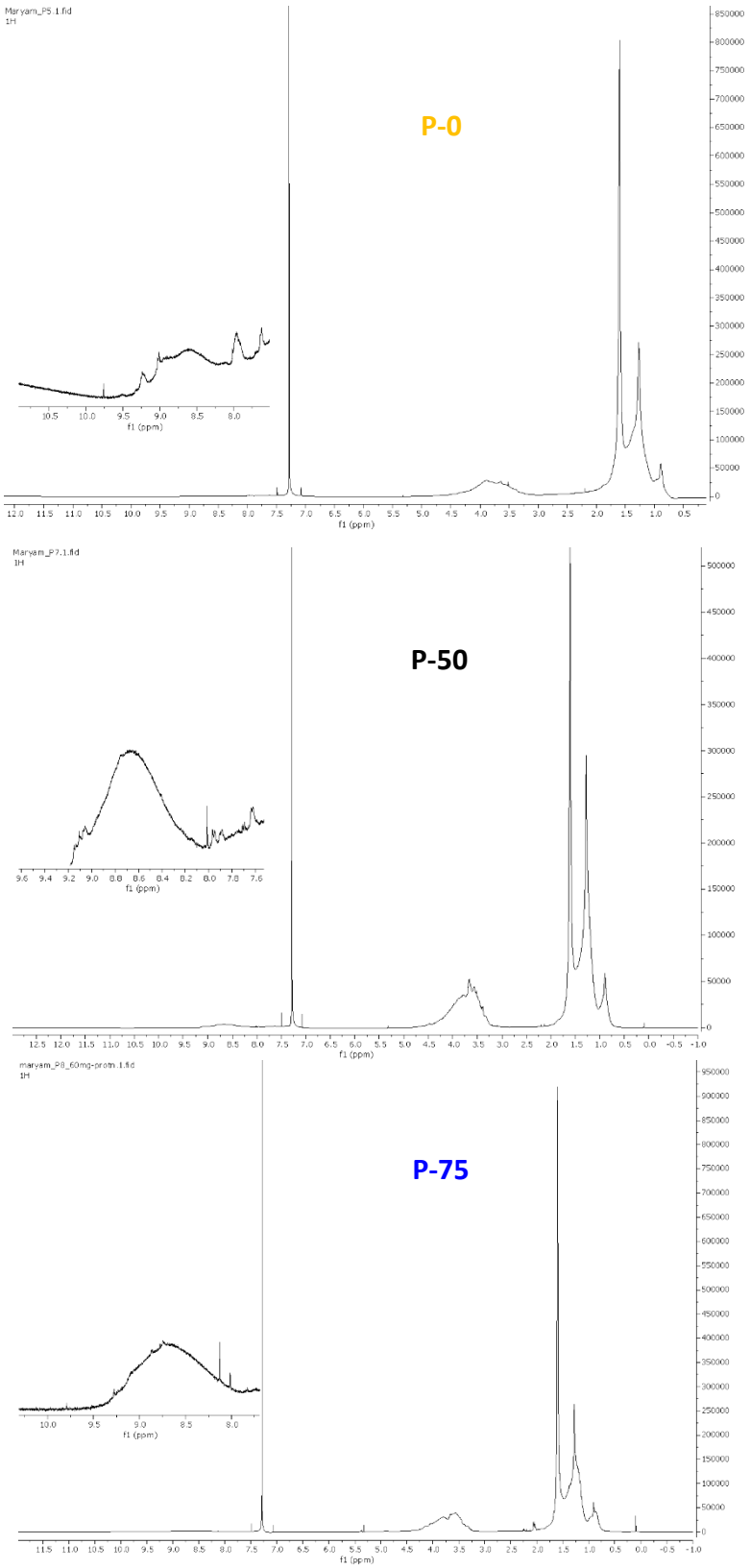


**Figure S14.** [1] H NMR of the corresponding polymers.

## 5.2.4 Gel permeation chromatography (GPC) measurements

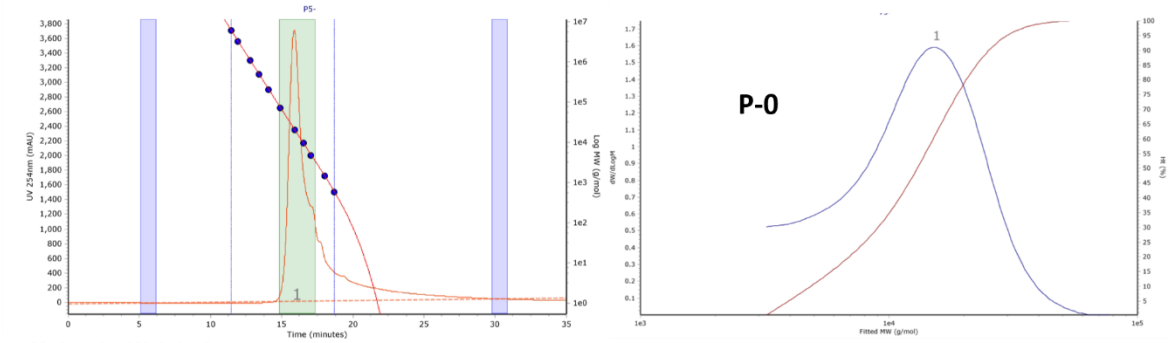


**Molecular Weight Averages**

| Peak | Mp (g/mol) | Mn (g/mol) | Mw (g/mol) | Mz (g/mol) | Mz+1 (g/mol) | Mv (g/mol) | PD |
|---|---|---|---|---|---|---|---|
| Peak 1 | 15239 | 9987 | 14345 | 19143 | 23887 | 18451 | 1.436 |

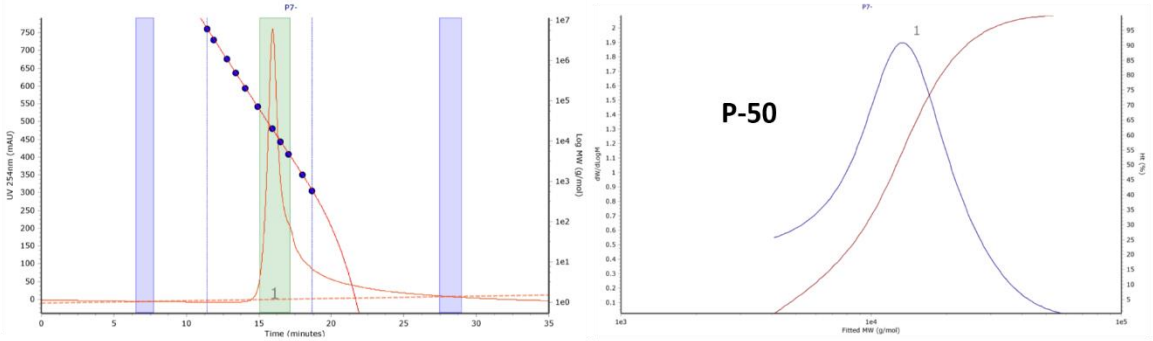


**Molecular Weight Averages**

| Peak | Mp (g/mol) | Mn (g/mol) | Mw (g/mol) | Mz (g/mol) | Mz+1 (g/mol) | Mv (g/mol) | PD |
|---|---|---|---|---|---|---|---|
| Peak 1 | 13314 | 10787 | 14143 | 18383 | 23372 | 17701 | 1.311 |

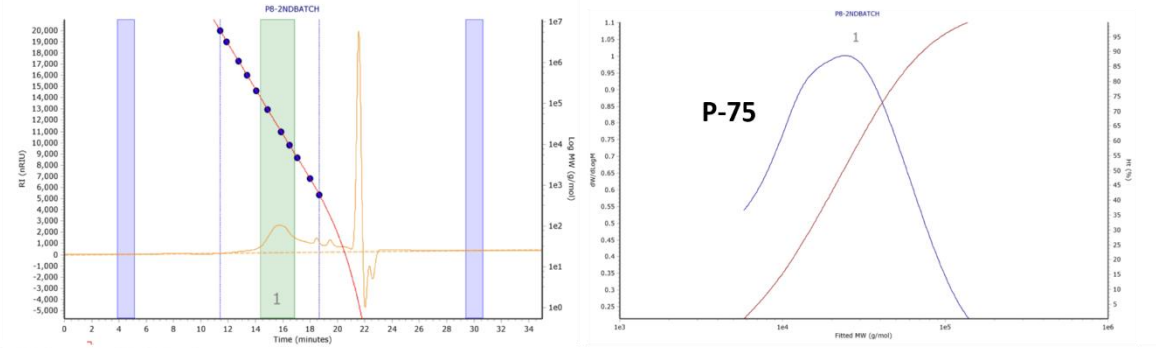


**Molecular Weight Averages**

| Peak | Mp (g/mol) | Mn (g/mol) | Mw (g/mol) | Mz (g/mol) | Mz+1 (g/mol) | Mv (g/mol) | PD |
|---|---|---|---|---|---|---|---|
| Peak 1 | 24646 | 18259 | 32939 | 55640 | 77413 | 52295 | 1.804 |

**Figure S15.** Gel Permeation chromatography plots of the polymers.

## 5.2.5 UV-vis absorbance spectroscopy

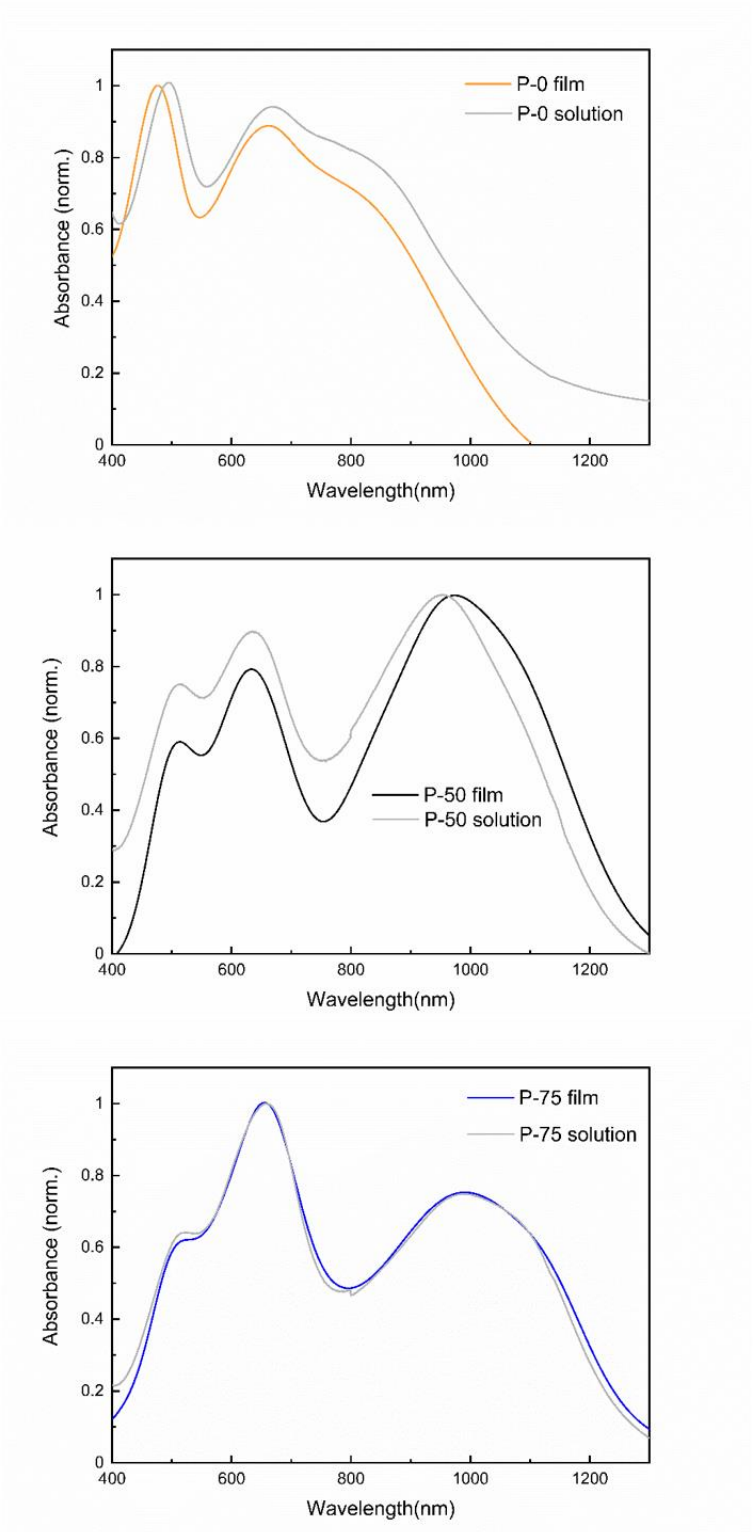


**Figure S16.** Absorption spectra of film and solution pristine polymers.

## 5.2.6 Ultraviolet photoelectron spectroscopy (UPS) and low energy inverse photoelectron spectroscopy (LE-IPES) measurements

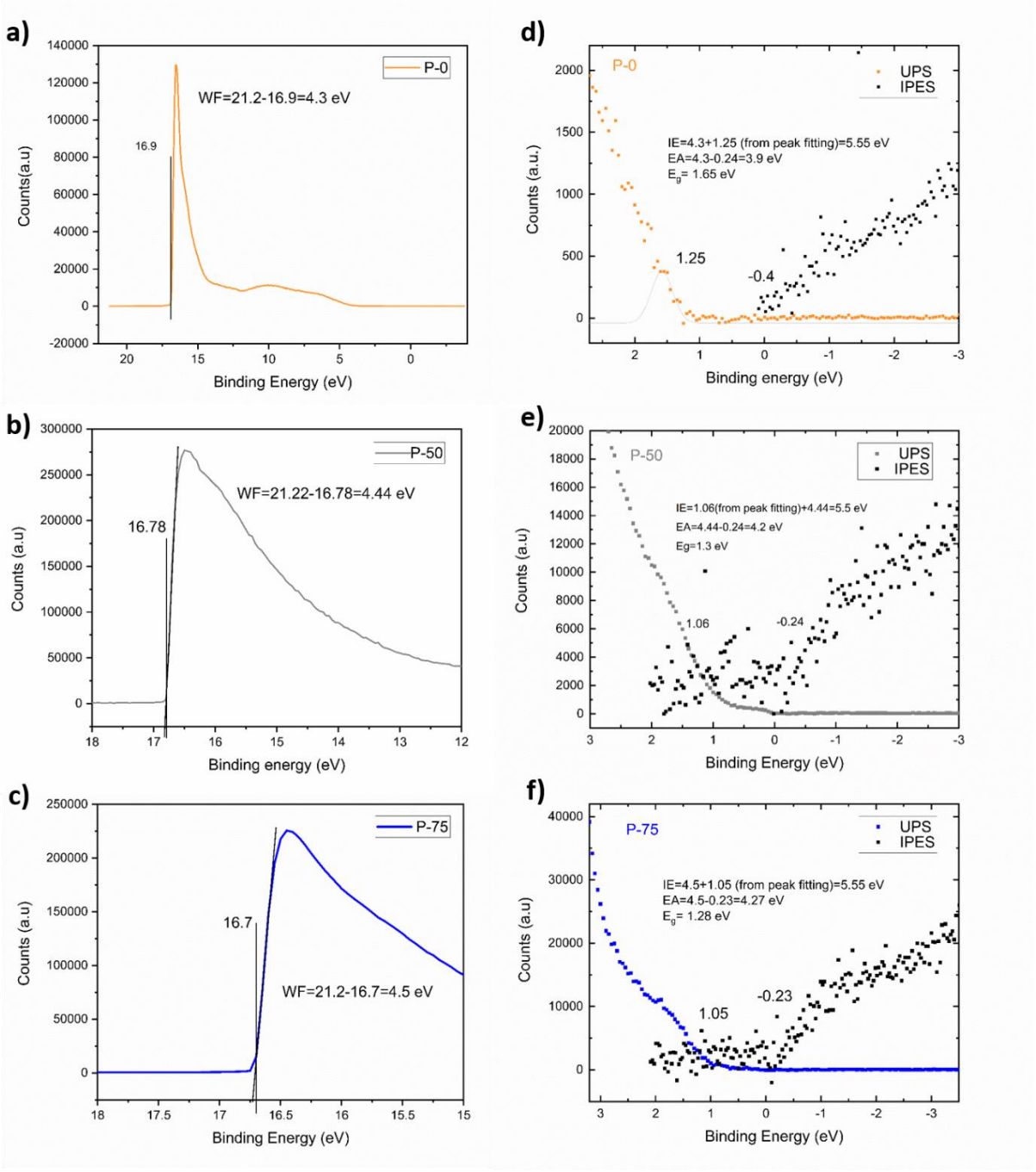


**Figure S17.** UPS and LE-IPES measurements of thin 10-20 nm spin-coated pristine films of P-0, P-50, and P-75. a) UPS Secondary electron cutoff (SECO) determining the work functions. b) Unified plot of the UPS (left hand side) HOMO region spectra and LE-IPES (right hand side) from which the relative positions of the HOMO and LUMO to the $E_f$ position and to $E_{vac}$ are shown providing IP and EA.

## 5.2.7 Thermal gravimetric analysis (TGA) and Differential scanning calorimeter (DSC)

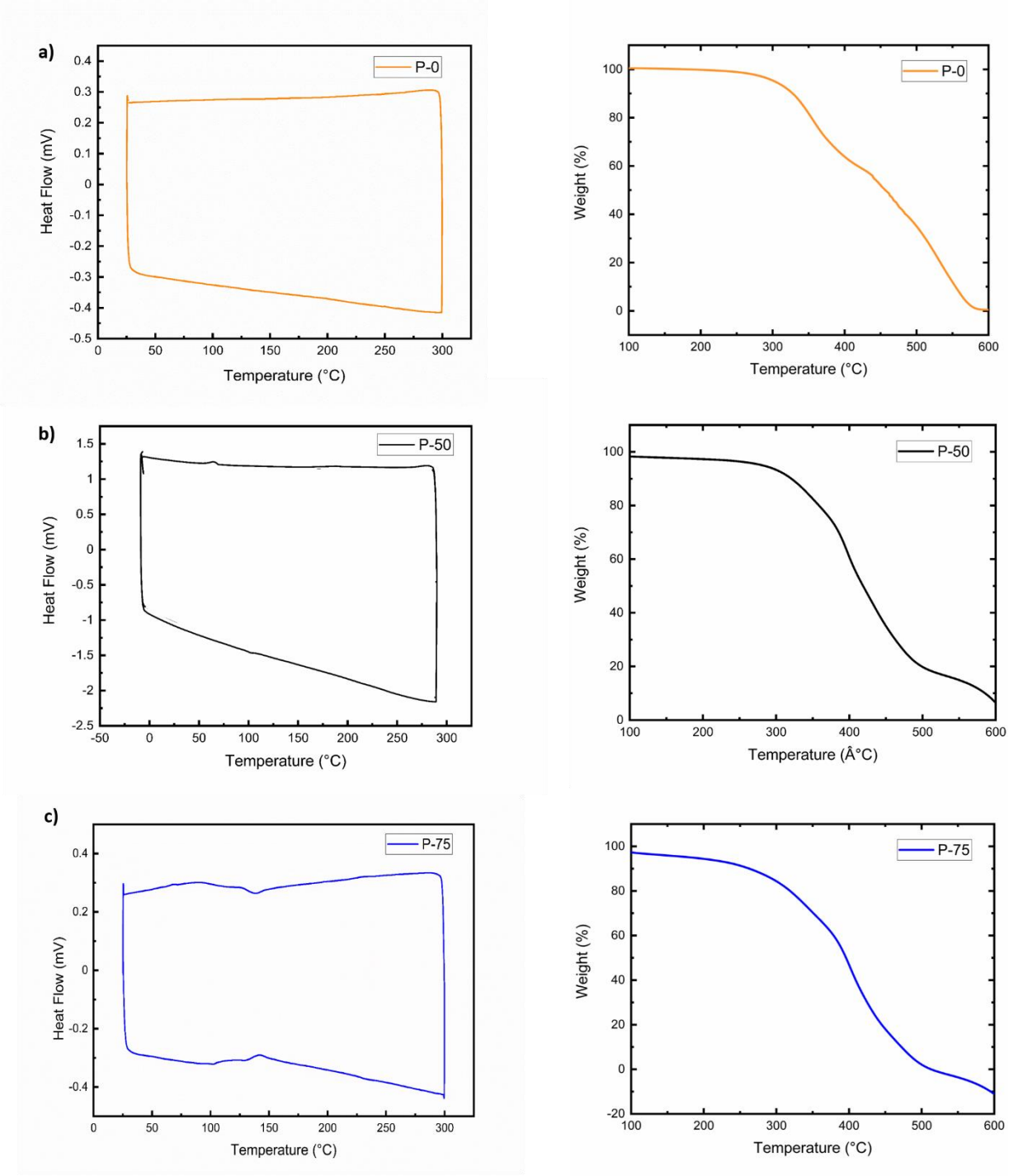


**Figure S18.** DSC and TGA measurements of a) P-0, b) P-50, and c) P-75

### 5.2.8 Thermoelectric measurements

Thin-films were prepared in a nitrogen-filled glovebox from 5 mg/mL of polymers solutions (stirring and heating at 50 ℃ to ensure complete solubilization) in chloroform, with the corresponding amount of N-DMBI to obtain the targeted ratio. 100 µL of solution were spin-coated (1000 rpm, 500 rpm/s, 30 sec) on substrates patterned with electrodes, then annealed at 110 ˚C for 30 min. The substrates were designed as following: 5 nm of chromium and 45 nm of gold were thermally evaporated on clean glass substrates (sonicated acetone, water then isopropanol for 10 min) through a shadow mask, forming electrodes with a channel length/width of 30 µm/0.1 cm, 300 µm/0.3 cm and 500 µm/1.5 cm for 2-probes electrical, 4-probes electrical and Seebeck coefficient characterization, respectively. Electrical characterizations (conductivity and Seebeck coefficient) were performed in a glovebox filled with nitrogen interfaced with a Keithley 4200-SCS. Seebeck coefficients were recorded by using a double Peltier setup calibrated to deliver a difference of temperature between 0.6 K and 3.6 K (0.6 K steps). Temperature-dependent conductivity measurements were performed under vacuum with a SHT-H-4-LF Cryogenic Probe Station from Janis, operating with liquid.

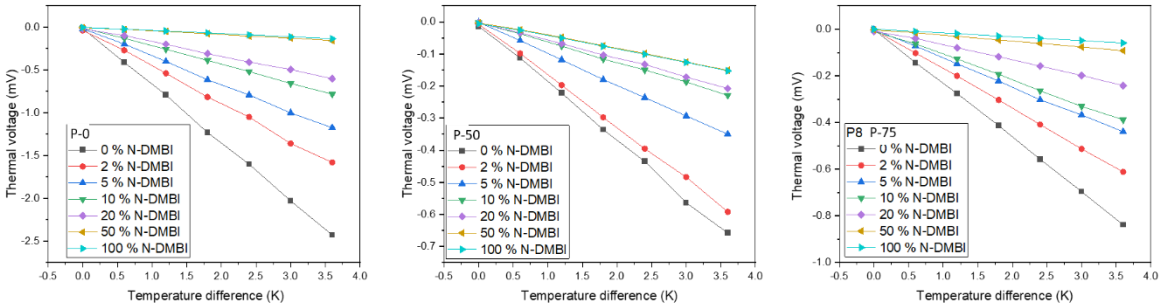


**Figure S20.** Temperature difference dependent thermal voltage of a) P-0, b) P-50 and c) P-75. The Seebeck coefficients were determined by introducing a temperature difference across the samples and measuring the thermovoltage

## 5.2.9 Grazing Incidence Wide Angle X-ray Scattering (GIWAXS)

2-D GIWAXS was carried out at the Advanced Photon Source at Argonne National Laboratory on beam line 8-ID-E at room temperature under vacuum with 10.92 keV ($\lambda$ = 1.135 Å) synchrotron radiation with a 0.14° incident angle and measured with a Pilatus 1M hybrid pixel array detector during 10 second exposures. GIWAXS samples were spin coated on Si wafer (University Wafer) substrates (~20 mm x 20 mm) from chloroform solutions (5 mg polymer/ml chloroform). Data analysis was carried out with GIXSGUI Matlab toolbox.[8]

**Table S5.** GIWAXS Parameters. Calculated in- and out-of-plane d-spacings and crystallite coherence lengths of pristine polymers

| **In-plane** | **$d_{h00}$ (Å)** | **$L_{c,h00}$ (Å)** | **$d_{0l0}$ (Å)** | **$L_{c,0l0}$ (Å)** |
|---|---|---|---|---|
| **P-0** | -- | -- | 3.58 | 37.8 |
| **P-50** | 32.1 | 56.5 | 3.59 | 35.3 |
| **P-75** | 31.7 | 61.2 | 3.45 | 29.5 |
| **Out-of-plane** | **$d_{h00}$ (Å)** | **$L_{c,h00}$ (Å)** | **$d_{0l0}$ (Å)** | **$L_{c,0l0}$ (Å)** |
| **P-0** | ~38 | -- | 3.60 | 45.6 |
| **P-50** | 28.1 | -- | 3.61 | 31.9 |
| **P-75** | 24.2 | -- | 3.41 | 33.1 |

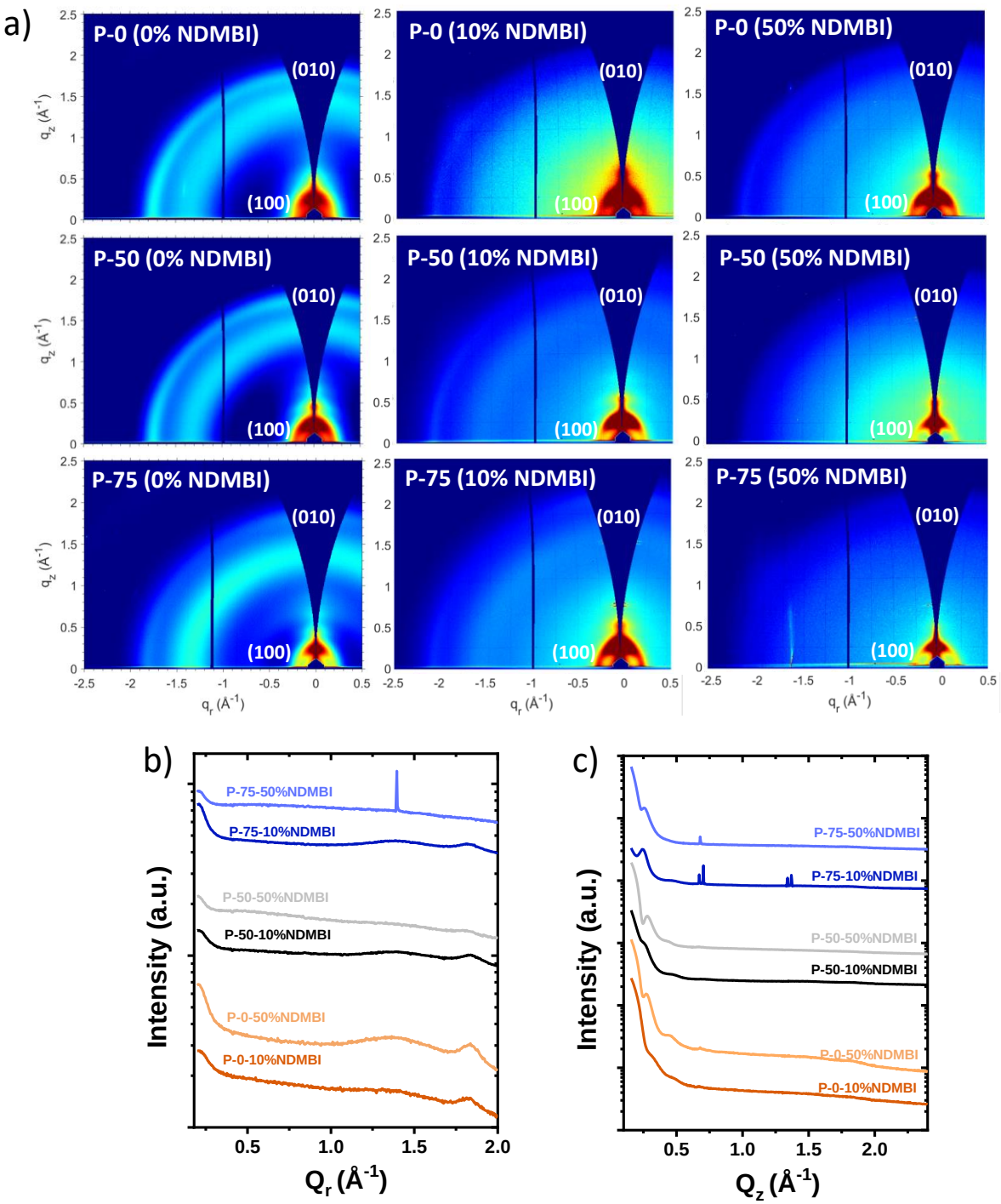


**Figure S21.** a) GIWAXS Patterns: Two-dimensional grazing incidence X-ray scattering maps of the undoped and doped polymers. GIWAXS line cuts of the undoped and doped polymers in the b) in-plane and c) out-of-plane.

**Table S6.** GIWAXS Parameters. Calculated in- and out-of-plane d-spacings and crystallite coherence lengths of undoped and doped polymers

| Polymer (% dopant) | $d_{(100)}$ (Å) | $L_{C\,(100)}$ (Å) | $d_{(010)}$ (Å) | $L_{C\,(010)}$ (Å) |
|---|---|---|---|---|
| P-0 (0% NDMBI) | 38 | - | 3.58 | 37.8 |
| P-0 (10% NDMBI) | 19.7 | 74.1 | 3.44 | 45.6 |
| P-0 (50% NDMBI) | 22.8 | 77.4 | 3.42 | 39.6 |
| P-50 (0% NDMBI) | 28.1 | 56.6 | 3.59 | 35.3 |
| P-50 (10% NDMBI) | 24.1 | 71.7 | 3.41 | 32.8 |
| P-50 (50% NDMBI) | 22.4 | 73.4 | 3.46 | 39.2 |
| P-75 (0% NDMBI) | 24.2 | 61.2 | 3.45 | 29.5 |
| P-75 (10% NDMBI) | 25.4 | 96.6 | 3.44 | 33.2 |
| P-75 (50% NDMBI) | 24.4 | 73.7 | - | - |

We investigated the doped polymer films using grazing-incidence wide-angle X-ray scattering (GIWAXS) to gain insight into the impact of doping on the polymer microstructre and the latter's effect on the thermoelectric performance. Here's two dopant concentrations were explored, the one at the peak performance, 10% N-DMBI and the one at heavy dopant load where the performance started to decline, 50%. From 2D GIWAXS patterns in Figure S21 a, doping seems to have a significant effect on the polymer's microstructre across the three polymers. That is appearant in the strong isotropic amorphous scattering ring centered near 1.4 $A^{-1}$, lamellar (100) and π–π stack (010) scattering, the intensities of which have diminshined, indicating a good polymer-dopant admixing, in correlation with AFM resutls. From GIWAXS line cuts in Figure S21 b and c, lamellar and π–π d-spacing, as well as relevant coherence lengths were obtained. As displayed in Table S6, In P-0, doping with 10% and 50% N-DMBI has significantly decreased the lamellar stacking distances from 38 to 19.7, and 22.8,

respectively, in agreement with the obsereved electrical conductivity. π–π stacking showed a similar effect, with decreasing π–π d-spacing and increasing the π–π stack coherence lengths. The lamellar stack d-spacing in P-50 remained relatively unaffected by doping. In contrast, doping resulted in smaller π–π stack distances, which was consistent with observed trends in electrical conductivity; coherence lengths remained unchanged. In contrast to P-0 and P-50, Doping had a negligible effect on the overall microstructure of P-75, indicating an undisturbed polymer microstructure despite NDMBI's large size and π-system. The substantial increase in lamellar stacking coherence lengths observed in 10% doped P-75 and the reduced π–π stacking distances in undoped P-75 appear to be the underlying factors contributing to the enhanced electrical conductivity of P-75. Overall, the GIWAXS of doped P-75 results show no negative effects on the polymer's microstructural order, giving rise to higher thermoelectric performance.

## 5.2.10 Atomic force microscopy (AFM)

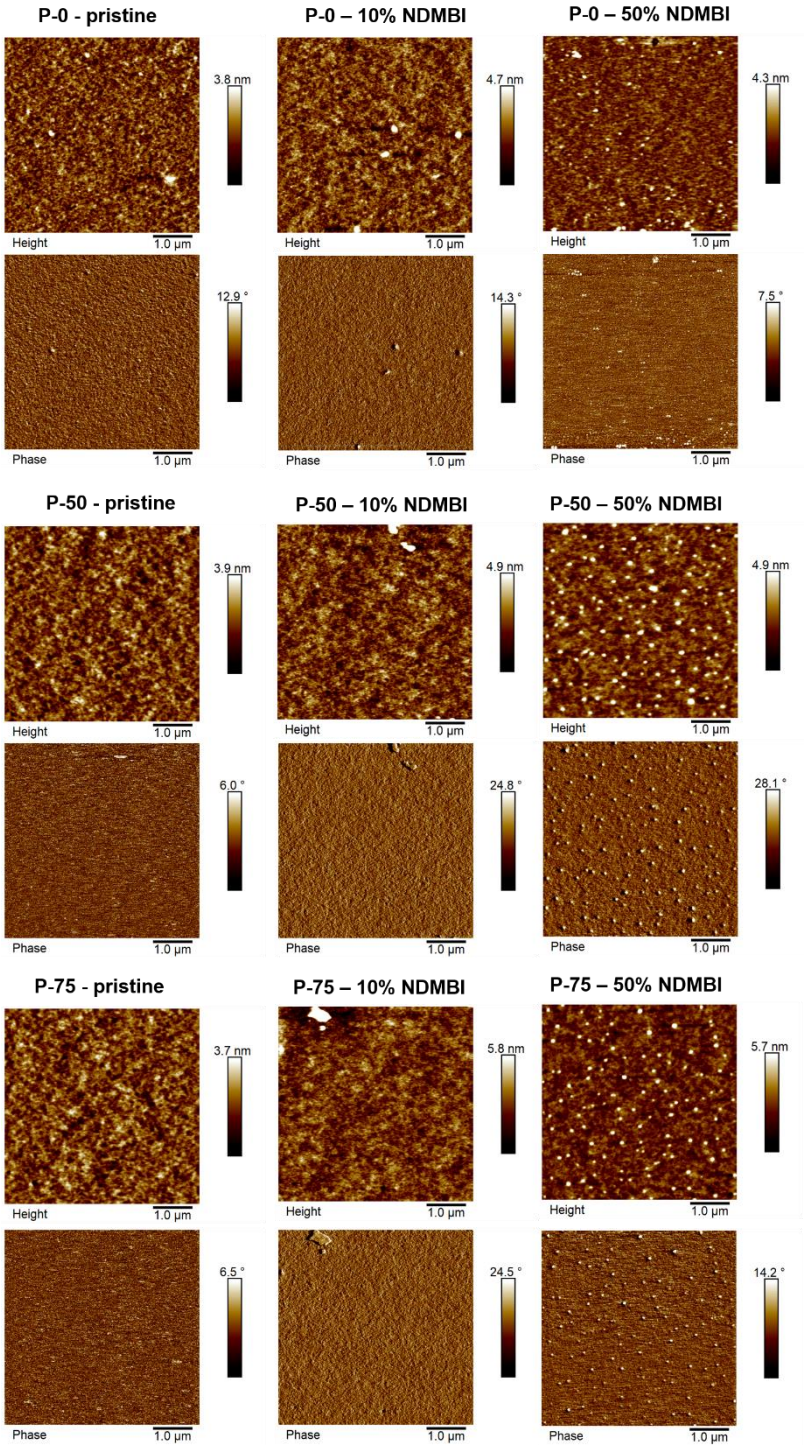


**Figure S22.** AFM height images a) P-0, b) P-50), and c) P-75 and their corresponding phase images (d, e, and f) of the polymer thin film after doping (10% N-DMBI). The root-mean-square (rms) surface roughness is provided in the height images. The scale size is 1.0 um and the images are 5 µm x 5 µm

## 5.2.11 Theoretical modelling

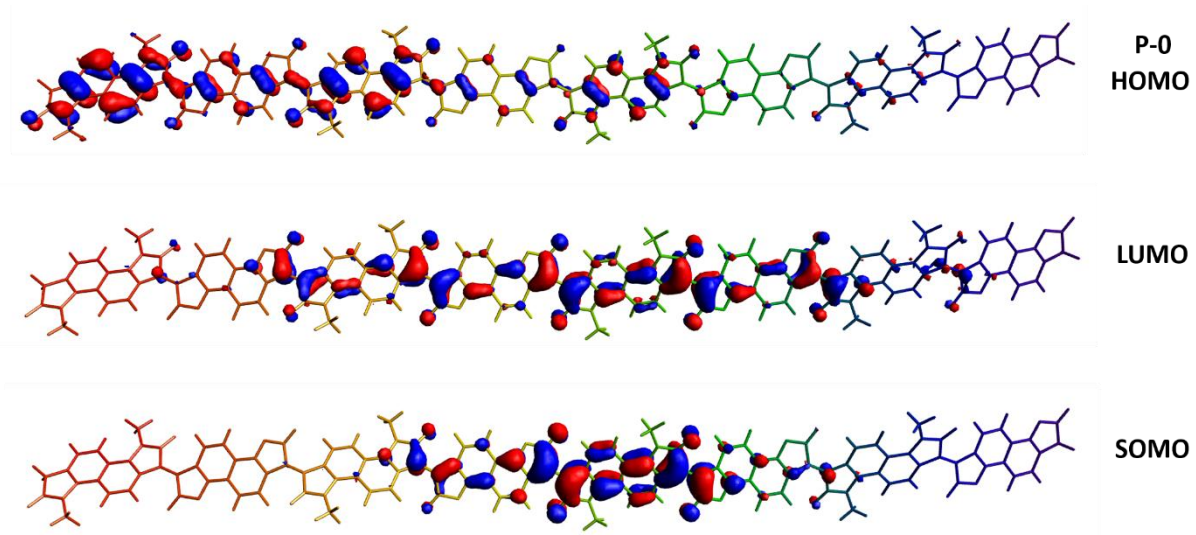


**Figure S23.** HOMO and LUMO of the neutral P-0. SOMO of the anionic P-0

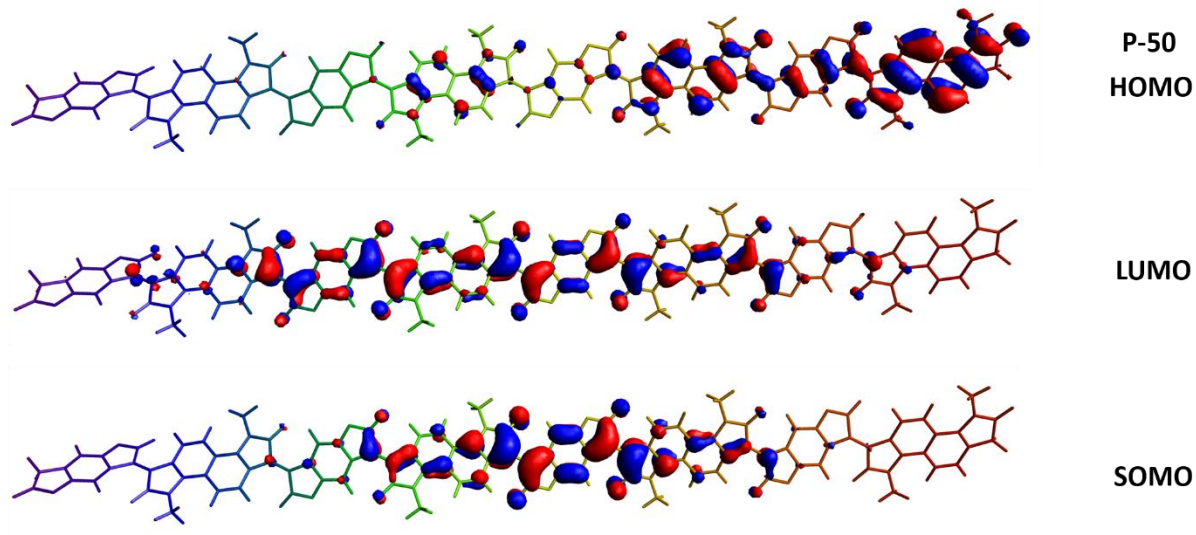


**Figure S24.** HOMO and LUMO of the neutral P-50. SOMO of the anionic P-50

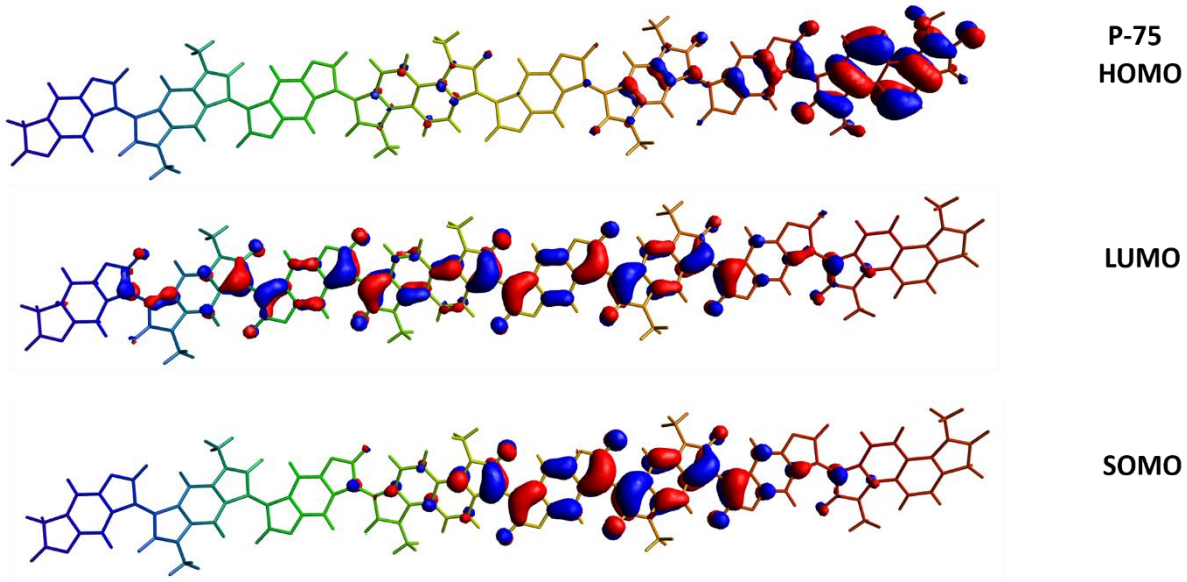


**Figure S26.** HOMO and LUMO of the neutral P-75. SOMO of the anionic P-75

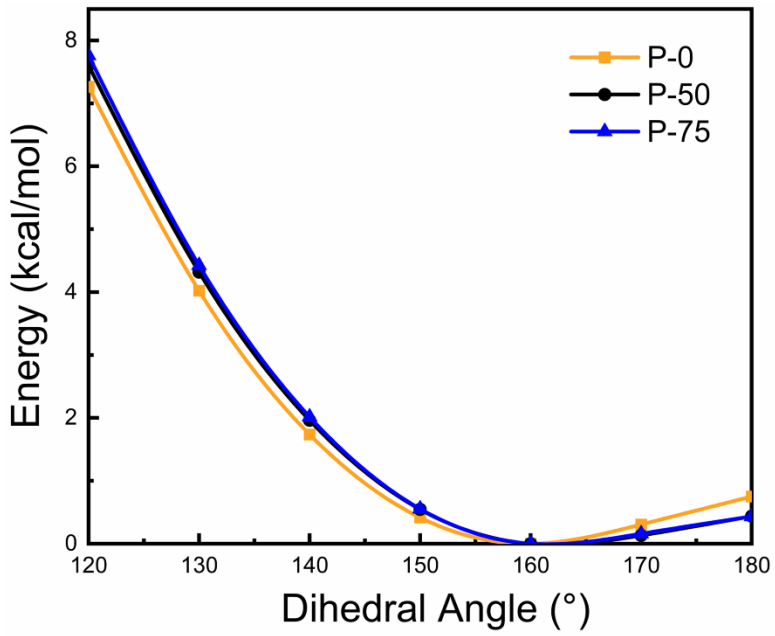


**Figure S27.** Torsional potentials around the centermost C=C bond in the neutral tetramers of P-0, P-50, and P-75 focusing on the 120−180° region.

### 5.2.12 References


1. B. Fu, J. Baltazar, A. R. Sankar, P.-H. Chu, S. Zhang, D. M. Collard and E. Reichmanis, *Advanced Functional Materials*, 2014, **24**, 3734-3744.
2. Y. R. Cheon, Y. J. Kim, J.-j. Ha, M.-J. Kim, C. E. Park and Y.-H. Kim, *Macromolecules*, 2014, **47**, 8570-8577.
3. L. V. Ganapatibhotla, J. Zheng, D. Roy and S. Krishnan, *Chemistry of Materials*, 2010, **22**, 6347-6360.
4. N. M. Randell, P. C. Boutin and T. L. Kelly, *Journal of Materials Chemistry A*, 2016, **4**, 6940-6945.
5. A. Onwubiko, W. Yue, C. Jellett, M. Xiao, H. Y. Chen, M. K. Ravva, D. A. Hanifi, A. C. Knall, B. Purushothaman, M. Nikolka, J. C. Flores, A. Salleo, J. L. Bredas, H. Sirringhaus, P. Hayoz and I. McCulloch, *Nat Commun*, 2018, **9**, 416.
6. P. Singla, N. Van Steerteghem, N. Kaur, A. Z. Ashar, P. Kaur, K. Clays, K. S. Narayan and K. Singh, *Journal of Materials Chemistry C*, 2017, **5**, 697-708.
7. Y. Deng, B. Sun, Y. He, J. Quinn, C. Guo and Y. Li, *Chem Commun (Camb)*, 2015, **51**, 13515-13518.
8. Z. Jiang, Journal of Applied Crystallography, 2015, 48, 917-926.


## 5.3 Supplementary information for chapter 4

### 5.3.1 Methods

#### Time resolved spectroelectrochemistry

Spectroelectcrochemistry was performed using a home-built system composed of a gas tight three glass electrochemical cell used in a three-electrode configuration. Ag/AgCl was used as a reference, Pt mesh as counter and a drop cast organic film on ITO as working electrode. The electrolyte was 0.1 M NaCl. The sample was illuminated using a 10 mW tungsten halogen source (Ocean Optics), which was collimated, transmitted through the sample and refocused using 5 cm planoconvex lenses (Edmund). A spectroscope and GaAS CCD camera (Ocean

optics IR quest) was used to resolve spectra and detect changes in intensity. Potentials were applied using a IVIUM VERTEX potentiostat. Both the CCD camera and potentiostat were controlled using custom built LABVIEW code (available at https://github.com/BenjaminSMoss). Spectroelectrochemistry was performed using a linear sweep voltammogram and recording intensities at each potential in the sweep. Potential Decay spectroscopy was performed by applying a step potential step holding for a set time then opening the circuit to resolve the decay kinetics of the system in the absence of a driving bias and recording spectra every 30 ms. Step potential Spectroscopy was performed by applying a square wave and recording spectra. In all cases the starting potential was chosen as 0.2 V vs Ag/AgCl, with a step of -0.6 V.

## Energy level measurements

Ultraviolet photoelectron spectroscopy (UPS) and low energy inverse photoelectron spectroscopy (LE-IPES) measurements were conducted in a single UHV multi-probe chamber (ScientaOmicron) operating at 10-10 mbar. UPS was conducted with a Helium discharge lamp (focus) He(1) 21.22 eV and a hemispherical electron analyzer Sphera II with a multiple channelton detector. LE-IPES measurements were conducted in isochromatic bremsstrahlung mode using a home built set up consisting of a mono-energetic (0.25 eV-0.5 eV) incident electron source (STAIB) directed normal to the sample biased at -20 V, emitted photons were collected using an assembly of internal and external focusing lens (Thorlabs) through an optical band pass filter (280 nm) and detected with a photo multiplier tube (PMT) (Hammatsu). All other light in the chamber was excluded. Calibration was achieved with reference to an evaporated Au film fermi level for UPS. The calibration of LE-IPES was performed in accordance with literature with reference to the 0 eV kinetic energy point E0 assigned to the centre of a Gaussian fitted to the turn on drain current with linearly increased beam energy.

The spectra onset are then referenced to the Evac position at E0 + hυ (4.43 eV). Samples were prepared by spincoating from dilute solutions in chloroform (5 mg/mL) on evaporated Au substrates. Processing and fitting of the data was achieved using Origin, removing a small 2% He(1) β 23.09 eV satellite from the UPS and arbitrary intensity normalization for ease of comparison with fitting.

## Cyclic Voltammetry (CV)

CV measurements were performed in ambient air atmosphere using a Autolab PGSTAT101 with a three-electrode setup. CV cycles in organic electrolytes were performed by using a Ag/Ag+ non-aqueous reference electrode (BAS, RE-7) filled with 0.01 M $AgNO_3$ and 0.1 M TBAP solution and calibrated against the ferrocene/ferrocinium redox couple (Fc/Fc+). Pt mesh was used as the counter electrode (active area 25 × 35 mm). Thin films were prepared by spin coating on indium-doped tin oxide (ITO) glass substrates, as the working electrode. An electrolyte is composed of 0.1 M solution of tetrabutylammonium hexafluorophosphate ($TBAPF_6$) in acetonitrile. The Ferrocene/Ferrocenium ($Fc/Fc^+$) redox couple was used as a reference, and all potentials were reported versus this couple using 4.8 V as ionization energy of $Fc/Fc^+$. CV measurements in aqueous electrolyte was performed in 0.1 M NaCl electrolyte, with Ag/AgCl aqueous reference electrode (BAS, RE-1B), and Pt mesh as the counter electrode, and polymers were spin-coated on ITO substrate as the working electrode.

## In-situ superoxide detection by electron paramagnetic resonance (EPR)

For the detection of superoxide formation through spin trapping, two solutions were prepared separately in dry chlorobenzene (CB): a 1 mg/ml solution of each polymer and a 0.8 M solution of DMPO (Sigma Aldrich, for ESR spectroscopy). For the EPR measurements, 50 µL of each solution were mixed and transferred to 2.9 mm OD, 2.0 mm ID EPR tubes.

Oxygen gas was bubbled through the solutions before transferring them to the EPR tubes and performing the EPR measurements. Prior to the EPR measurements on the polymers, the DMPO was tested by recording EPR spectra of the pure DMPO solution in chlorobenzene in the dark and under illumination, giving no appreciable EPR signal beyond a small contribution of a three-line pattern attributed to degraded DMPO. Successful spin-trapping of superoxide radicals by DMPO under the conditions of the experiments performed here was verified using the non-fullerene acceptor FBR following a previously published approach.[1] (See Fig. S11).The continuous-wave EPR experiments were performed on a Bruker EMXmicro spectrometer. The sample was centered vertically with standard PTFE supports in the cylindrical TE011 mode of a super-high sensitivity Bruker probe head (ER4123-SHQE-W1) at room temperature. Light-induced radical species were measured by in-situ illumination of the solution through the optical window of the resonator (optical grid with eight 2x5 mm slits over a height of 23 mm) using a Schott KL 2500 LED cold light source with a liquid light guide (luminous flux ca. 1100 lm). The EPR spectra were recorded at a microwave frequency of around 9.75 GHz using a microwave power of 1 mW and a modulation amplitude of 0.1 mT. A field calibration was performed with a standard solid $N@C_{60}$ sample with a known *g*-value.[2] Spectral simulations were performed using the EasySpin[3] toolbox. The experimental spectra were simulated as a single contribution of an isotropic EPR line for the dark measurements, accounting for the polymer signal, and as a sum of contributions of this signal and the DMPO–superoxide adduct for the measurements under illumination (Figure. S9c). The polymer signal was simulated as an isotropic line at *g*-values of 2.0032, 2.0031, 2.0031, for P-0, P-50 and P-75, respectively, and the contribution of the DMPO–superoxide adduct was simulated using an isotropic *g*-value of 2.0059, an isotropic $^{14}N$ hyperfine coupling of 1.29 mT and an isotropic proton hyperfine coupling of 0.75 mT. For quantitative measurements, the experimental spectra were simulated as a sum of contributions from the polymer signal and the DMPO-

superoxide adduct and the number of spins for each contribution were estimated from the double integral of the corresponding simulated spectrum using the resonator calibration parameter set provided by the manufacturer. For the monitoring of the spin concentration as a function of time, the amplitudes of simulated spectra for the polymer signal and the DMPO-superoxide adduct were automatically fitted to the experimental spectrum recorded at each time point.

## OECT Fabrication of intrinsic polymers

OECT substrates were fabricated photolithographically, OMIEC channel materials were deposited by drop casting from 5 mg/mL chloroform solutions, and OECT patterned channels were defined using a parylene peel-off process.[4] Resulting channels were 100 um wide and 10 um long with varied channel thickness (1 um). OECTs were gated with aqueous 100 mM NaCl using an Ag/AgCl pellet as the faradaic gate electrode.[5] Electrical characterization (output, transfer, and pulsed stability) of the OECTs were carried out using NI source-measure units controlled by custom LabView code. Capacitance was determined via EIS on similarly patterned 600 um x 600 um OMIEC coated Au electrodes using a Metrohm potentiostat with frequency response analyzer with an Ag/AgCl pellet functioning as a combined reference and counter electrode.

## Spectroelectrochemical procedure

OMIEC materials were spin-coated from 5 mg/mL chloroform solutions Indium tin oxide (ITO) coated glass (15-20 ohm sq-1) (University Wafer) that prior to spinning had been successively sonicated in acetone and isopropyl alcohol, and cleaned with UV-ozone exposure. Spectroelectrochemistry measurements were carried out in 100 mM aqueous NaCl in a PMMA cuvette with an Ag/AgCl pellet (Warner Instruments) reference/counter electrode. Potential control and current measurement were carried out with a potentiostat (Ivium). Simultaneous

absorption spectroscopy was recorded with a halogen white light source (Ocean Optics, DH-2000-BAL) and an optical fiber light path split to separate UV-visible (Ocean Optics, FLAME-S) and near-infrared (Ocean Optics, NQ512) spectrometers, with 30 ms and 120 ms integration times, respectively. Electrochemical and spectroscopic data were recorded with Iviumsoft and OceanView software, respectively.

## OECT Fabrication of doped polymers

OECTs were fabricated on glass substrates with gold source and drain contacts using photolithography. 10nm/40nm of Cr/Au was thermally evaporated on glass substrates followed by deposition of two layers of parylene C. The layers were separated by micro-90 antiadhesive (4% in water). A 9 μm layer of photoresist (AZ4620) where used on top of parylene layers to define the channel area photolithographically and etched in the last step of the fabrication. Then the semiconducting solution was spun cast onto the substrates at 500 RPM for 45s. Polymer solutions were made at 10mg/ml concentration from chloroform and left at 45° C for an hour. The N-DMBI dopant solution was made at 0.5 mg/ml concentration from chlorobenzene and added to the polymer solution with different ratios and left overnight. For all the doped solutions the volume of the added dopant solution at maximum percentage was considered as the reference. Therefore, for lower percentages, chlorobenzene in the amount of the difference to the reference, was added to the solutions to make sure all the doped solutions contain the same amount of chlorobenzene.The OECTs were characterized in a three terminal setup using an Ag/AgCl pellet (Harvard Apparatus) as the gate electrode and 0.1 M NaCl aqueous solution as the electrolyte. Electrical characterization was carried out by Keysight B2912B source and measure unit on six devices with channel length and width of 50μm and 500 μm respectively. A potentiostat (Metrohm Autolab, PGSTAT128N) was employed for impedance measurements while the Ag/AgCl pellet was used as the reference electrode and a

Pt wire served as a counter electrode. The AC voltage amplitude applied on the gate was set to 10 mV on top a DC bias at which the transconductance peaked and the measurements were taken over the range of 100KHz to 0.1 Hz. Thickness measurements were taken by Bruker DektakXT profilometer.

## In situ electrochemical resonant Raman spectroscopy (ERRS)

Polymers were dissolved in in chlorobenzene at a 5 $mgml^{-1}$ at 80°C. The solutions were spin coated on to cleaned FTO substrates at 1000 rpm/40 s. Deposited films were dried in a desiccator and stored in $N_2$. A Renishaw in Via Raman microscope with InGaAs detector was used to collect Raman spectra and with a 50x objective in a backscattering configuration. Spectra were collected using a HeNe laser (633 nm) with laser power and acquisition time optimised to give the best spectra. Calibration of the filter and grating was performed using the well-defined 520 $cm^{-1}$ peaks of a Si reference. Ex situ measurements were measured in a $N_2$ environment in a Linkam THMS600 stage. In situ measurements degradation high stress measurements were taken in 0.1 M NaCl electrolyte without bias before and after a constant bias of -0.8 V for 10 minutes followed by +0.2 V reverse voltage for 30 s. Raman peak assignment and geometry analysis was simulated using density functional theory (DFT) on the Imperial College High-Performance Computing service using GAUSSAIN09 software.[6] All simulations were performed on single molecules in the gas phase using B3LYP level of theory and basis set 6-31G(d.p).[7, 8, 9] Frequency of vibrations were identified from simulations of Raman spectra using empirical scaling factor of 0.97,[10] and peak assignments were visualised using GaussView 6.0.16 software.

## Electron Paramagnetic Spectroscopy of N-DMBI doped P-75 film

Electron paramagnetic resonance (EPR) measurement were recorded using an X-band (9.84 GHz) Burker EMXMICRO, with a microwave power of 1.002 mW. The number of scans was set to 10, and the sweep width and sweep time of the magnetic field were 120 G and 72.19 s, respectively. Pristine and doped polymer films were spin coated on Quartz substrate (10 mm x 6 mm), which were placed inside a sealed cylindrical quartz ESR tube prior to measurements.

## 5.3.2 Supplementary Tables

Table S1. Summary of energy level measurements[11]

| | Computational calculations [a] | | | UPS & LE-IPES [b] | | | PESA & UV-vis [c,d] | | | | CV[e] | |
|---|---|---|---|---|---|---|---|---|---|---|---|---|
| **Polymer** | IP[a] [eV] | EA[a] [eV] | $E_g$[a] [eV] | IP[b] [eV] | EA[b] [eV] | $E_g$[b] [eV] | $\lambda_{max,film}$[c] [nm] | I'[d] [eV] | EA[d] [eV] | $E_g$[d] [eV] | $E_{red.onset}$ [V] | EA[e] [eV] |
| **P-0** | 5.69 | 3.44 | 2.25 | 5.55 | 4 | 1.55 | 823 | 5.21 | 4.09 | 1.12 | -0.22 | 4.51 |
| **P-50** | 5.72 | 3.61 | 2.11 | 5.55 | 4.2 | 1.35 | 973 | 5.29 | 4.30 | 0.99 | 0.11 | 4.84 |
| **P-75** | 5.77 | 3.68 | 2.09 | 5.55 | 4.3 | 1.25 | 998 | 5.30 | 4.37 | 0.93 | 0.30 | 5.02 |

[a] Calculated by Density functional theory (DFT) simulations.
[b] IP is Measured by ultraviolet photoelectron spectroscopy (UPS) and EA by low energy inverse photoelectron spectroscopy (LE-IPES)
[c] Thin film and solution absorption onset.
[d] Estimated optical gap calculated using onset of absorption spectra ($E_{opt.gap}$ =1240/$\lambda_{onset}$), IP is measured by photo electron spectroscopy in air (PESA) and EA is calculated from $E_{opt.gap}$ and IP
[e] EA was measured by cyclic voltammetry of polymer thin films on ITO substrates in 0.1 M tetrabutylammonium hexafluorophosphate ($TBAPF_6$) in acetonitrile

Table S2. Summary of EA values by cyclic voltammetry reported in literature

| | CV[a] | |
|---|---|---|
| Polymer | EA [eV] | Reference |
| p(gNDI-gT2) | 3.85 | [12] |
| P-90 | 4.10 | Measured here |
| $BBL_{152}$ | 4.38 | [13] |
| PgNaN | 4.28 | [14] |
| PgNgN | 4.35 | [14] |
| f-BTI2TEG-FT | 3.82 | [15] |
| f-BTI2g-TVTCN | 3.81 | [16] |
| p(g7NC10N) | 4.23 | [24] |
| PBFDO | 5.18 | [17] |
| PBDF | 5.15 | [18] |
| **P-0** | **4.51** | **This work** |
| **P-50** | **4.84** | |
| **P-75** | **5.03** | |

[a] 0.1 M tetrabutylammonium hexafluorophosphate ($TBAPF_6$) in acetonitrile.

Table S3. Energy levels measured herein for state-of-the-art polymer series

| | **UPS & LE-IPES [b]** | | |
|---|---|---|---|
| **Polymer** | IP[b] [eV] | EA[b] [eV] | $E_g$[b] [eV] |
| **p(gNDI-gT2)** | 4.81 | 3.83 | 0.98 |
| **P-90** | 5.52 | 4.05 | 1.47 |
| **PgNaN** | 5.02 | 3.90 | 1.12 |
| **p(g7NC10N)** | 5.05 | 3.83 | 1.22 |
| **BBL[19]** | 6.33 | 4.15 | 2.18 |

[b] IP is Measured by ultraviolet photoelectron spectroscopy (UPS) and EA by low energy inverse photoelectron spectroscopy (LE-IPES). BBL energy level data using the same techniques were adapted from literature.

Table S4. OECT performance summary of N-DMBI doped P-75 with an average over 6 devices

| **Doping level** | $V_T$ $[V]$ | $\frac{g_m}{Wd/L}$ $[\mathbf{S\ cm^{-1}}]$ | $g_m$ $[uS]$ | $\mu$ $[\frac{cm^2}{Vs}]$ | $\mu_{transient}$ $[\frac{cm^2}{Vs}]$ | $C^*$ $[Fcm^{-3}]$ | $\mu_{transient} * C^*$ $[Fcm^{-1}V^{-1}s^{-1}]$ | $\mu * C^*$ $[Fcm^{-1}V^{-1}s^{-1}]$ |
|---|---|---|---|---|---|---|---|---|
| P-75 (0%NDMBI) | $-0.024$ | 4 | $210 \pm 0.07$ | 0.035 | 0.0034 | 250 | 0.8 | 9 |
| P-75 (0.1%NDMBI) | $-0.026$ | 8 | $300 \pm 0.1$ | 0.052 | 0.0021 | 418 | 0.9 | 22 |
| P-75 (0.25%NDMBI) | $-0.011$ | 4 | $290 \pm 0.07$ | 0.028 | 0.0015 | 346 | 0.5 | 10 |

## 5.3.3 Supplementary Figures

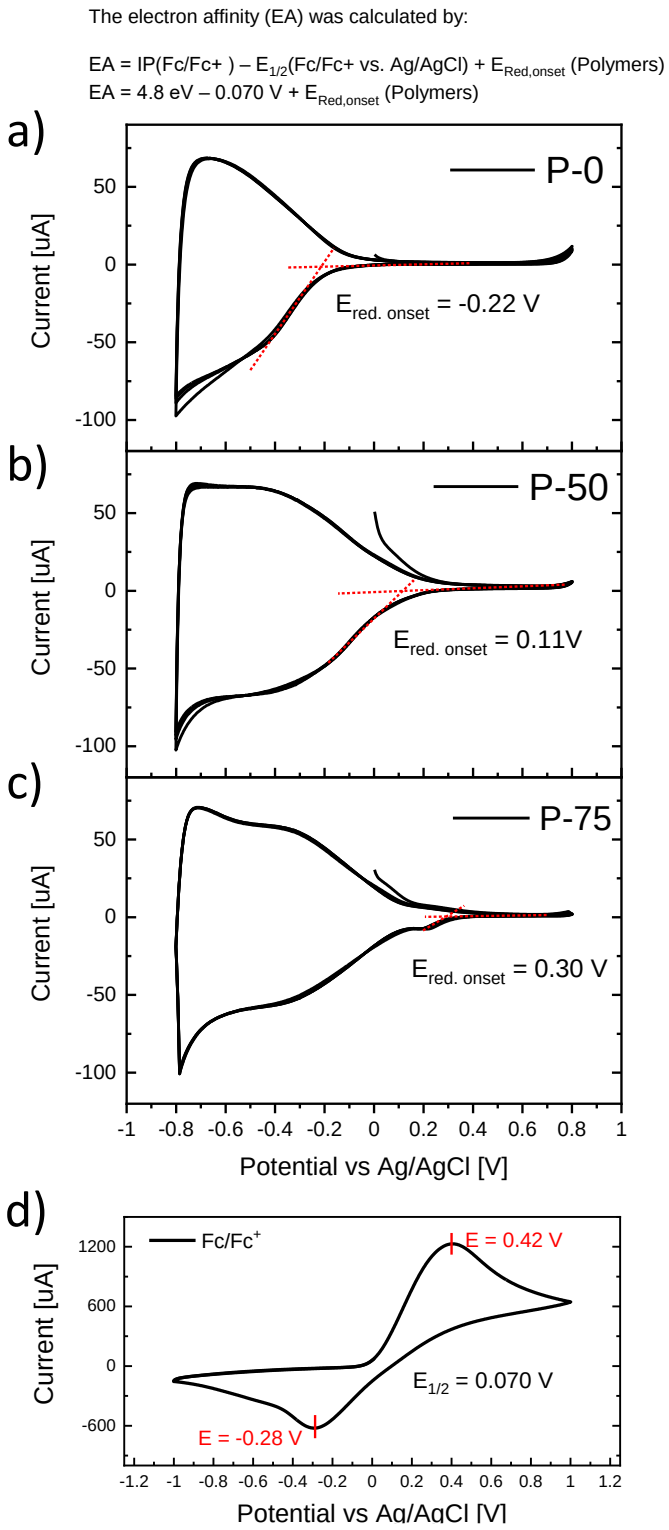


Fig. S1 CV measurements in 0.1 M $NBu_4PF_6$ with a scan rate of 100 mV/s shown three scans of a) P-0 [EA = 4.51 eV], b) P-50 [EA = 4.84 eV], c) P-75 [EA = 5.03 eV] and d) Ferrocene.

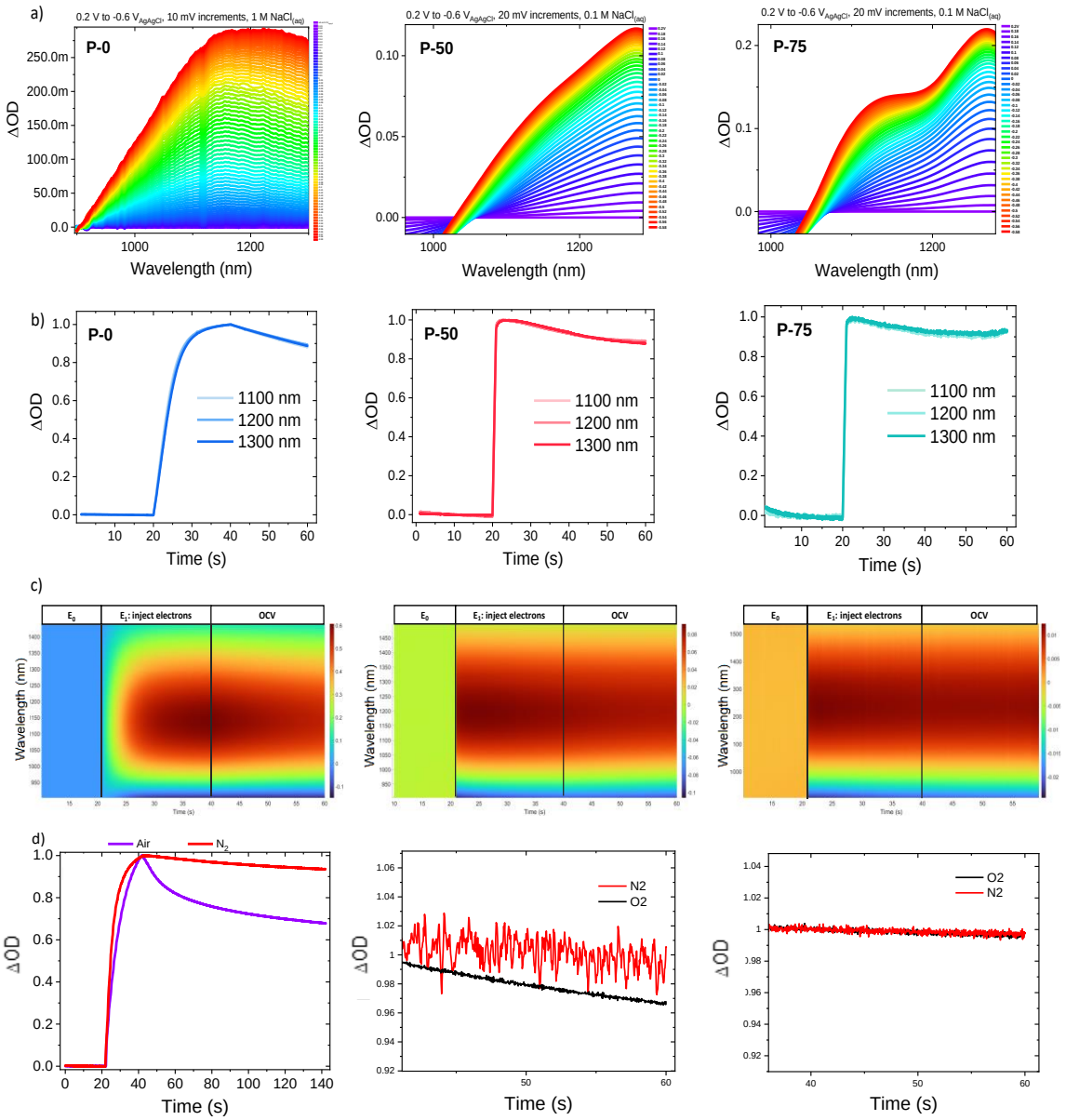


Fig. S2 a) Electrochemical spectrums of the three polymers composed of a ground state bleach and an absorption in the near IR. b) Absorption of anionic species kinetic decay at open circuit performed after injecting at -0.8 V. All kinetics are identical indicating a single species monitored. c) An example of the data obtained from step potential a step potential-potential decay experiment. d) Step-potential decay kinetics for negative polarons in air and introducing nitrogen.

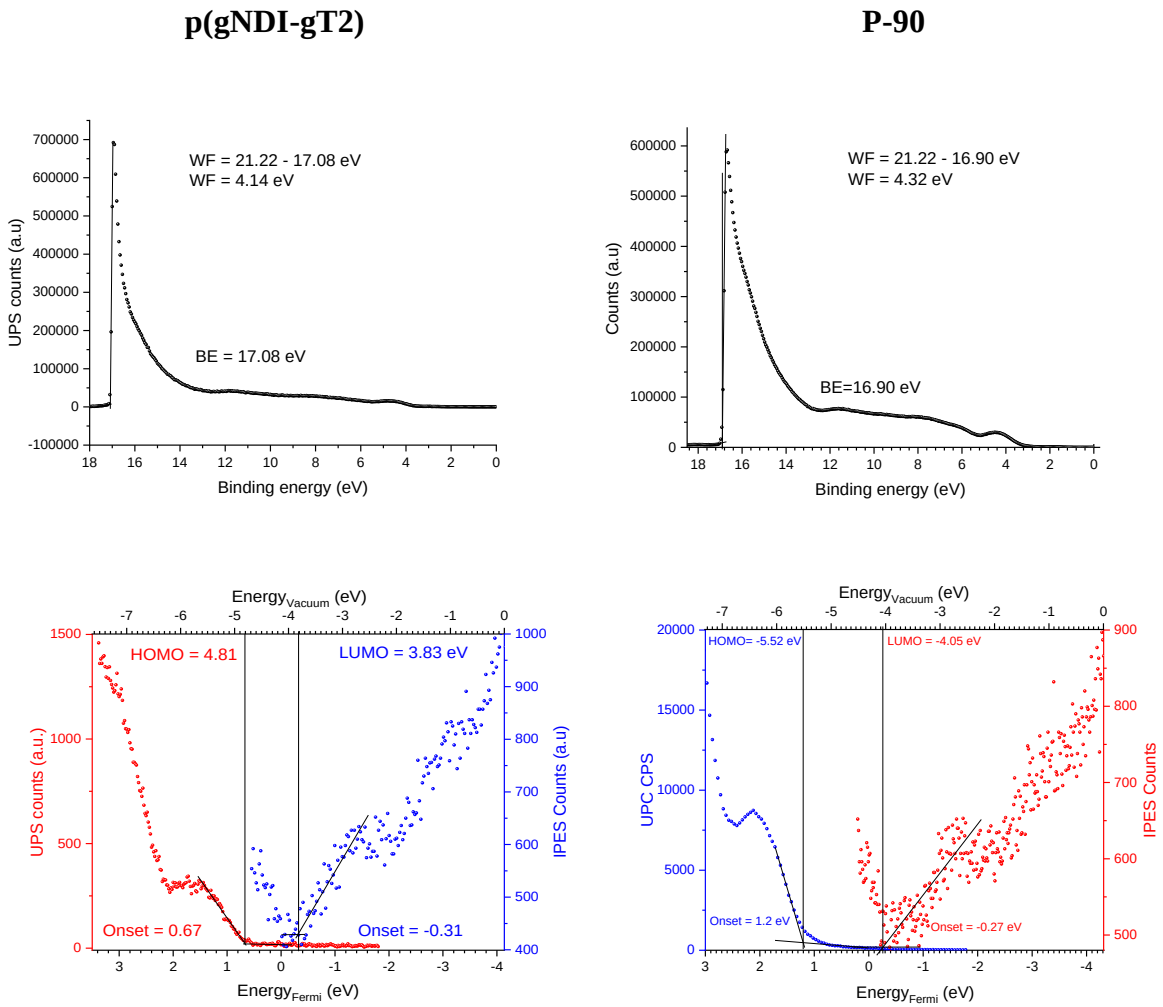


Fig. S3 UPS and LE-IPES measurements of thin 10-20 nm spin-coated pristine films of p(gNDI-gT2), and P-90. comprising UPS Secondary electron cutoff (SECO) determining the work functions (on the top), and Unified plot of the UPS (on the bottom) HOMO region spectra and LE-IPES from which the relative positions of the HOMO and LUMO to the $E_f$ position and to $E_{vac}$ are shown providing IP and EA.

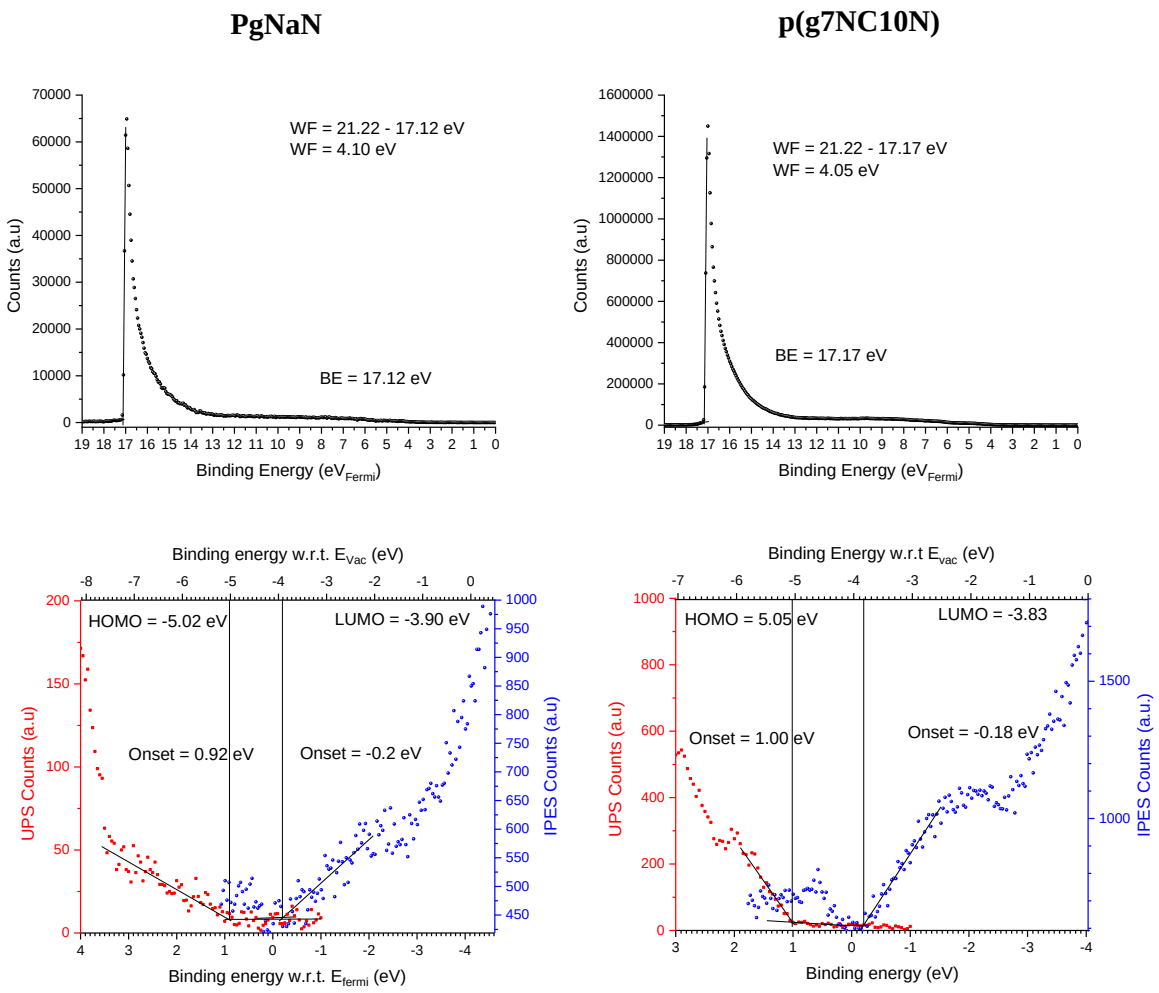


Fig. S4 UPS and LE-IPES measurements of thin 10-20 nm spin-coated pristine films of PgNaN and p(g7NC10N). comprising UPS Secondary electron cutoff (SECO) determining the work functions (on the top), and Unified plot of the UPS (on the bottom) HOMO region spectra and LE-IPES from which the relative positions of the HOMO and LUMO to the $E_f$ position and to $E_{vac}$ are shown providing IP and EA.

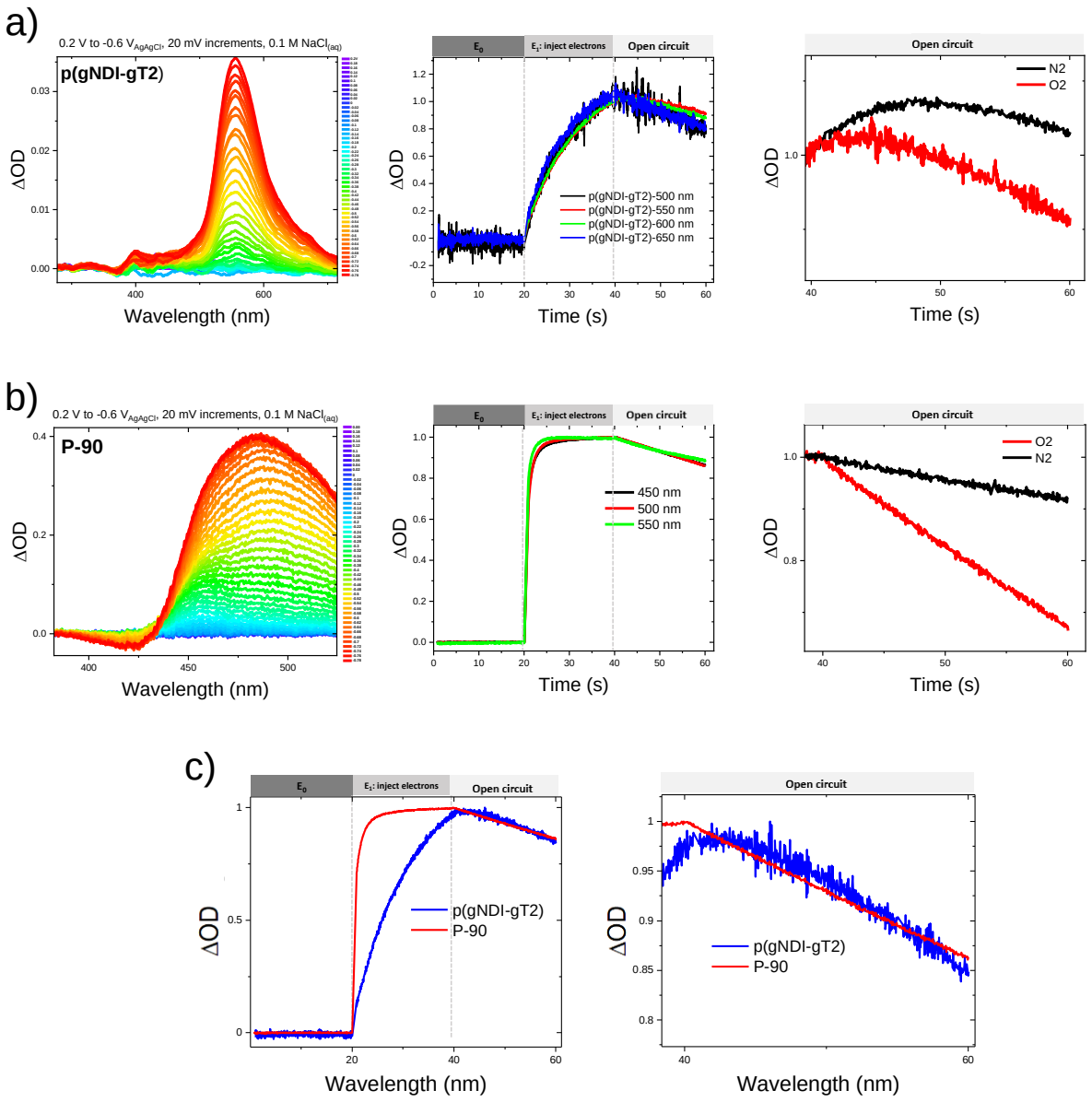


Fig. S5 Electrochemical spectra, absorption of anionic species kinetic decay at open circuit time-resolved spectra, and step potential-potential decay kinetics for anions in the presence and absence of oxygen of a) p(gNDI-gT2) and b) P-90.

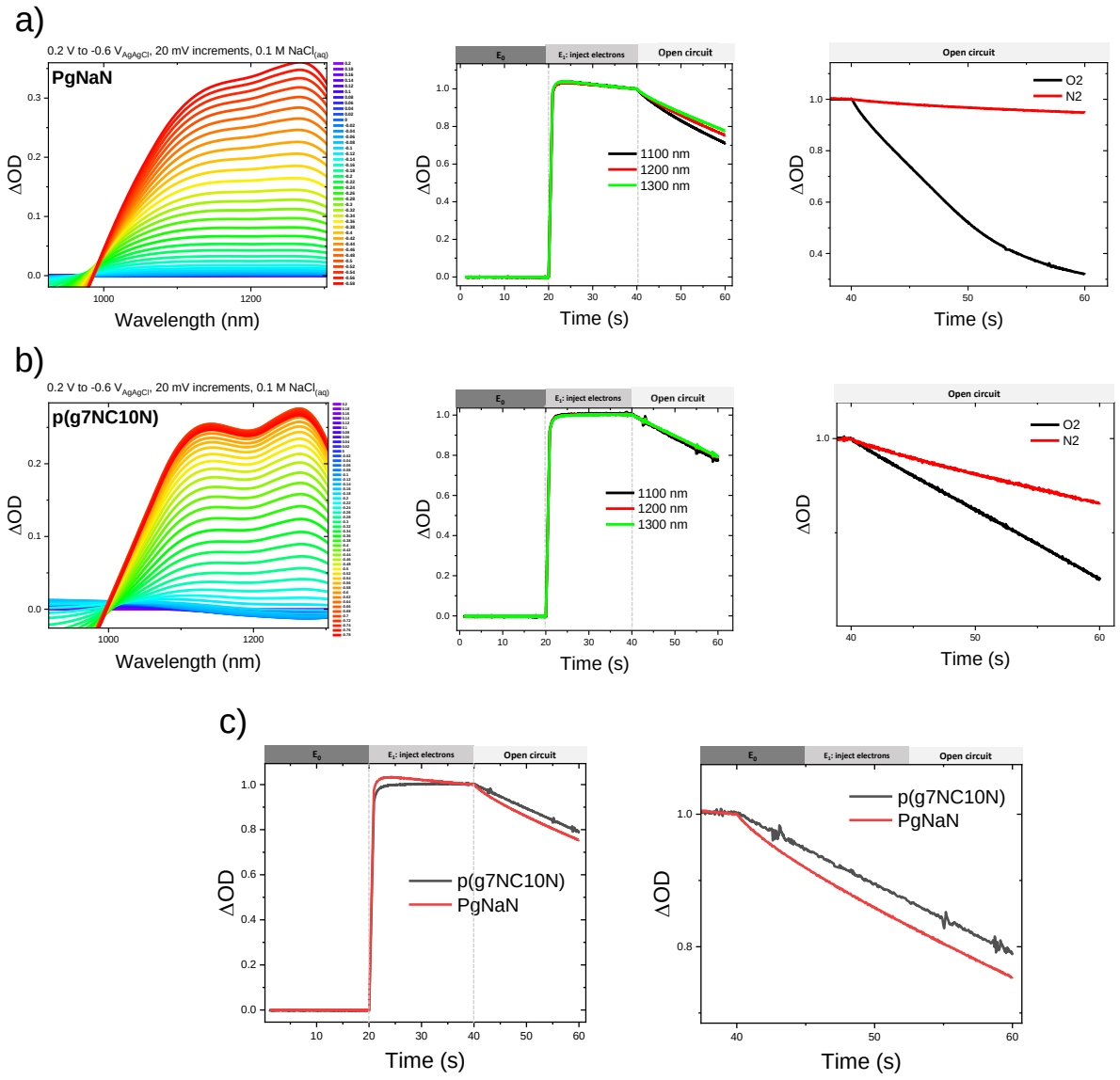


Fig. S6 Electrochemical spectra, absorption of anionic species kinetic decay at open circuit time-resolved spectra, and step potential-potential decay kinetics for anions in the presence and absence of oxygen of a) PgNaN and b) p(g7NC10N).

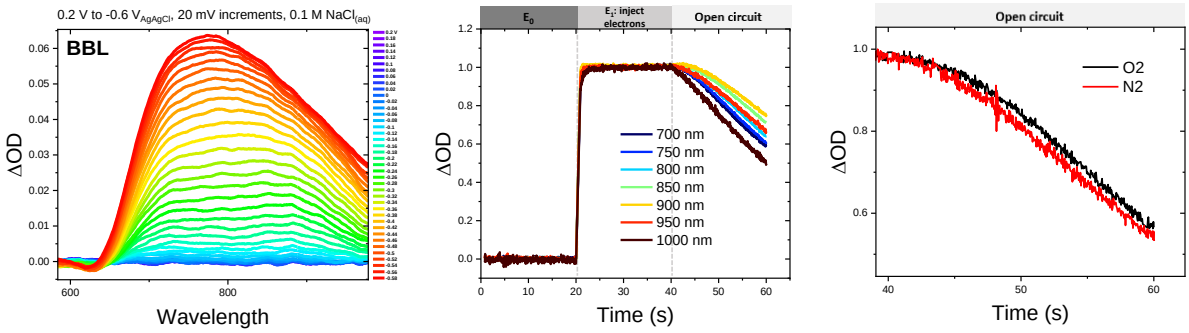


Fig. S7 Electrochemical spectra, absorption of anionic species kinetic decay at open circuit time-resolved spectra, and step potential-potential decay kinetics for anions in the presence and absence of oxygen of BBL.

The durability of negative polarons over a broad range of state-of-art n-type OECT materials was further tested in air, namely NDI-based polymers, p(gNDI-gT2),[20] and P-90,[21] ladder polymer BBL,[22] fused lactam polymers, PgNaN,[23] and p(g7NC10N).[24] The polymer EAs were measured using LE-IPES, similar to the study polymers, and found to be–3.83, -4.05, -3.90, and –3.83 eV, for p(gNDI-gT2), P-90, PgNaN, and p(g7NC10N), respectively. EA of BBL is -4.15 eV as previously determined by LE-IPES[19] The corresponding UPS/LE-IPES plots can be found in Supplementary Figures. S3 and S4. Similarly to the study polymers, the spectra of radical anionic species were resolved using spectroelectrochemisry (SEC), and their kinetics were then probed at open circuit potential. All the polymers showed a decay of the negative polaron absorption in air, with the decay being retarded under nitrogen. These results further affirm the crucial need for deep LUMO energies towards an air stable electron transport.

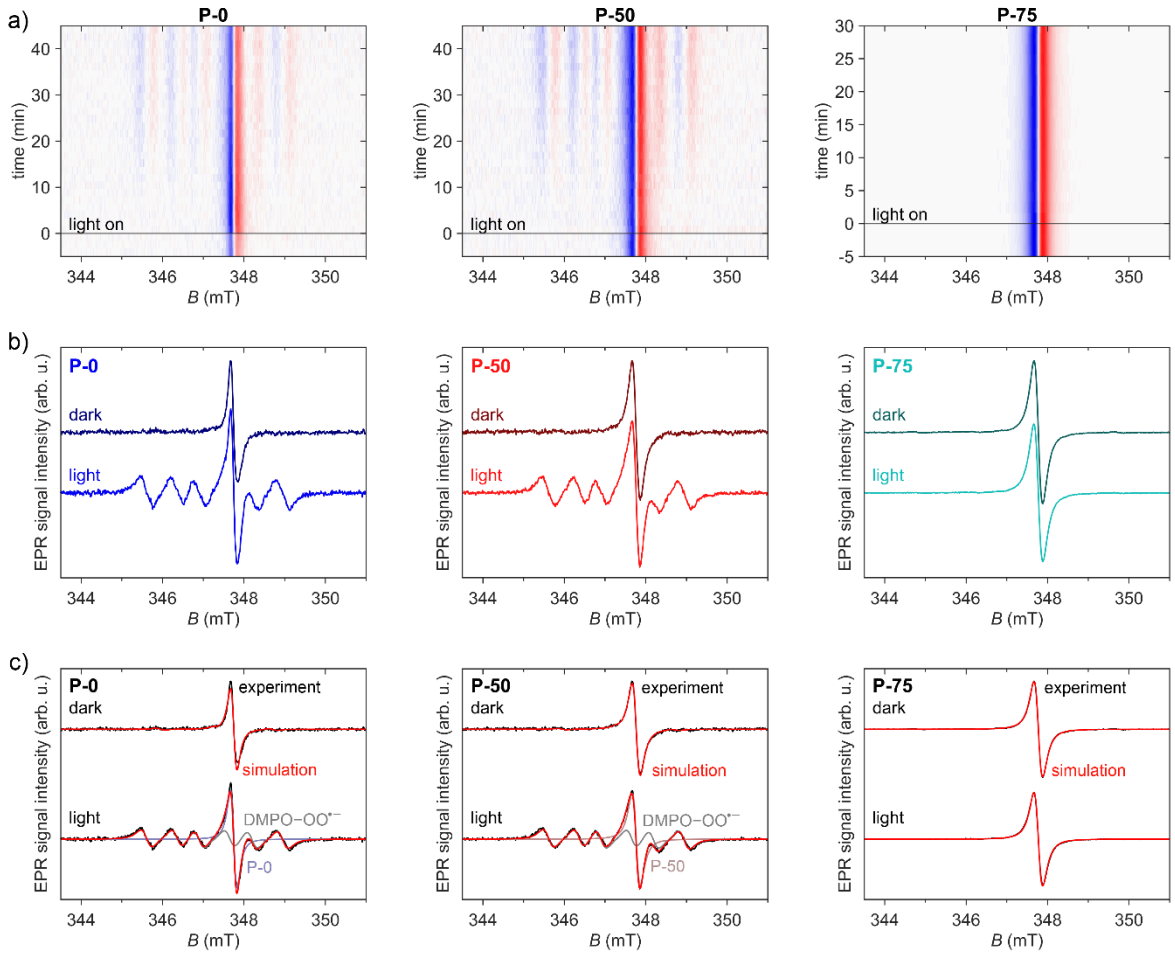


Fig. S8 a) EPR spectra recorded on oxygenated solutions of the polymers P-0, P-50 and P-75 in chlorobenzene with an excess of DMPO spin trap as a function of time in the dark and under white light illumination (blue = positive, red = negative signal contributions). b) EPR spectra averaged over 15 min in the dark and after ca. 30 min of constant illumination. c) Comparison of the experimental EPR spectra (black) with simulations (red), taking into account a polymer signal centred at g-values of 2.0032, 2.0031, 2.0031 and the contribution of the DMPO–superoxide adduct with a g-value of 2.0059, a $^{14}N$ hyperfine coupling of 1.29 mT and a proton hyperfine coupling of 0.75 mT

Closer inspection of the time-dependence of the observed EPR signals also reveals changes of the central EPR signal assigned to the polymer, with *g*-values of 2.0032, 2.0031 and 2.0031 for P-0, P-50 and P-75, respectively. For P-0, white-light illumination leads to a rapid increase of the polymer EPR signal is detected (reaching a maximum corresponding to about 1.8 times the initial intensity after about 3 min and then slowly decreasing), in agreement with

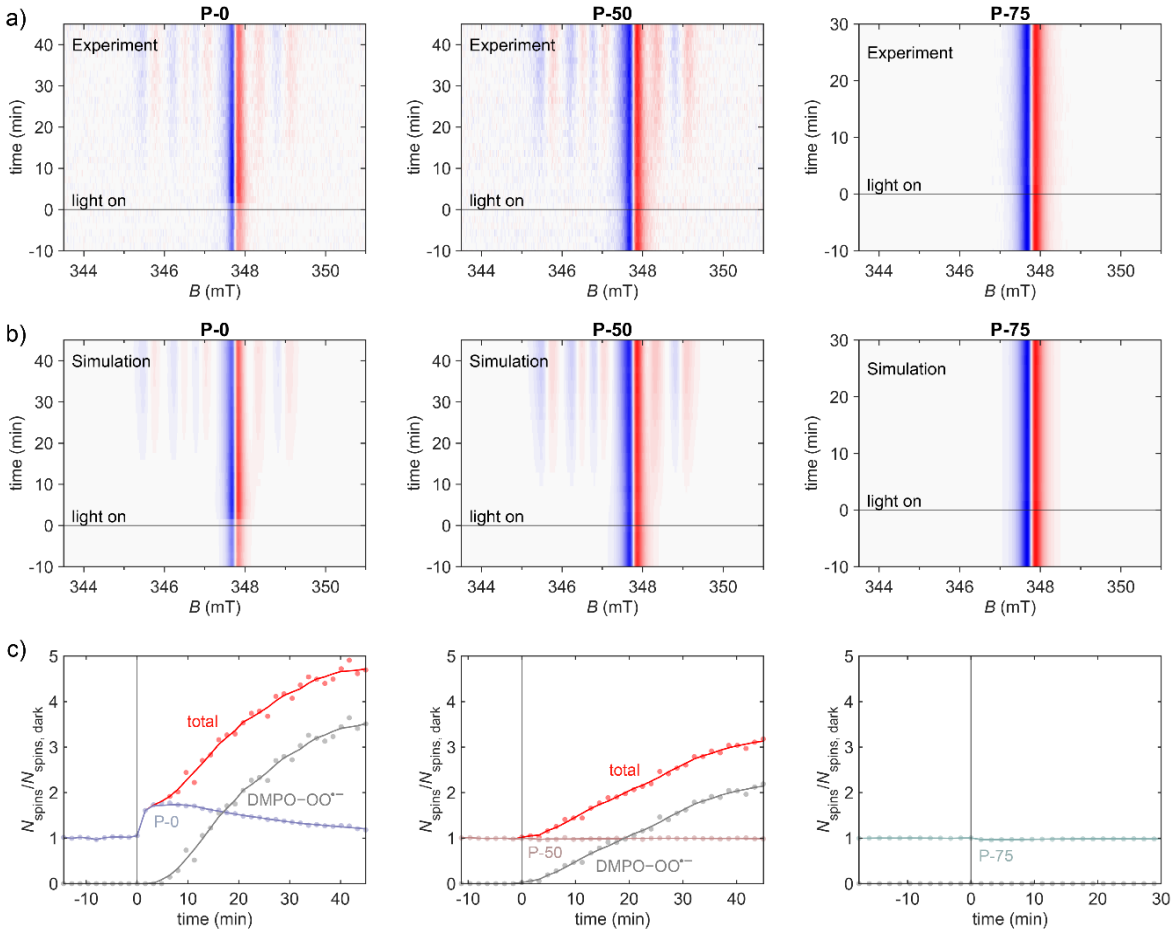


Fig. S9 a) EPR spectra recorded on oxygenated solutions of the polymers P-0, P-50 and P-75 in chlorobenzene with an excess of DMPO spin trap as a function of time in the dark and under white light illumination (blue = positive, red = negative signal contributions). b) Corresponding simulation obtained by fitting the amplitudes of each contributions to the experimental data at each time point. c) Relative spin count as a function of time before and after illumination determined from the double integral of the individual contributions to the simulated spectra shown in b). The number of spins determined for the polymers in the dark amount to 2.5 $10^{13}$, 5.6 $10^{13}$ and 3.9 $10^{14}$ spins for P-0, P-50 and P-75, respectively.

a prior observation in a molecular doping study.[11] The EPR signal of the DMPO-superoxide adduct grows in on a slower timescale as shown in Figure S8. When illumination is stopped, the signal of the DMPO-superoxide adduct decays over a time period of several hours (Figure S10 in the SI). The time-dependent EPR data recorded for the P-50 polymer shows a small decrease (−2.4% after about 3 min) in the intensity of the polymer EPR signal at short times after the start of the illumination, in qualitative agreement with the observation of a decrease in EPR signal intensity in molecularly doped P-50 films, attributed to bipolaron formation. Again, the change in intensity of the polymer EPR signal occurs on a faster

timescale compared to the slower increase in concentration of the DMPO-superoxide adduct (see Figure S8). For P-75, where no superoxide formation was detected, the only response to illumination was a small decrease in intensity of the EPR signal assigned to the polymer (−3.8% after about 5 min), in agreement with previous observations.

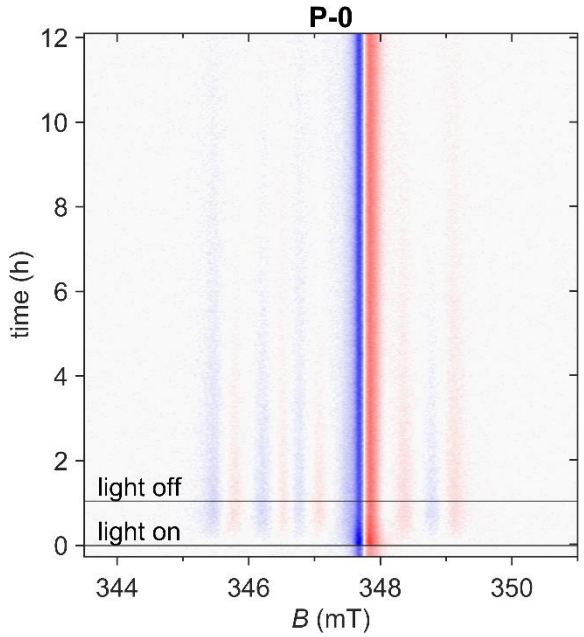


Fig. S10 EPR spectra recorded as a function of time on a solution of the P-0 polymer in chlorobenzene with an excess of DMPO spin trap in the dark, under white-light illumination and after switching off illumination.

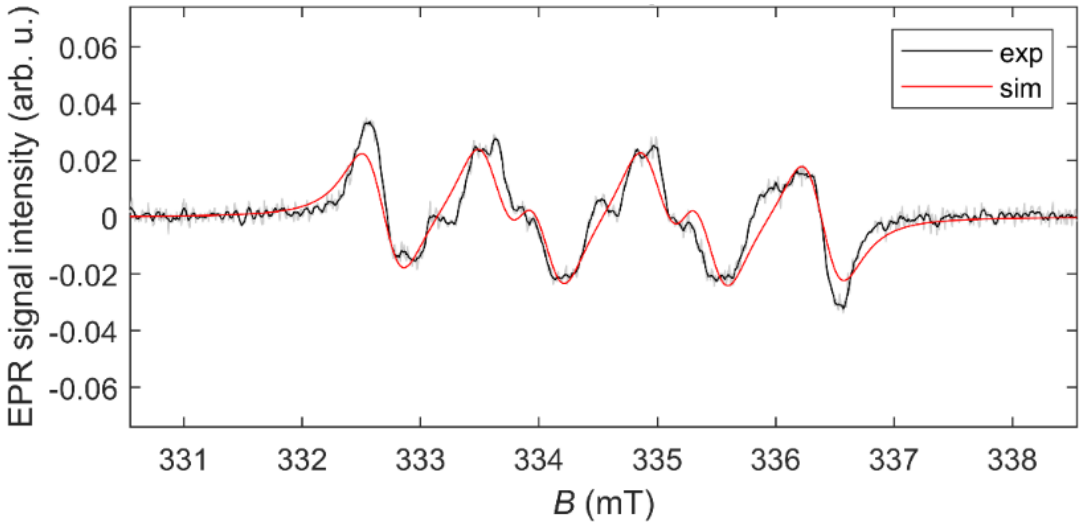


Fig. S11 Experimental spectrum and simulation of the DMPO-superoxide formed after light-induced polaron formation in a solution of the non-fullerene acceptor, 5,5′-[(9,9-Dioctyl-9H-fluorene-2,7-diyl)bis (2,1,3-benzothiadiazole-7,4 diylmethylidyn-ne)] bis[3-ethyl-2 thioxo-4-thiazolidinone], (FBR).

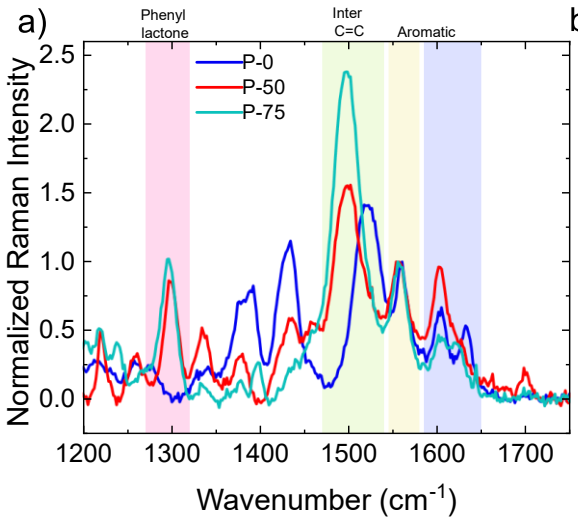


| Peak ($cm^{-1}$) | Assignment |
|---|---|
| 1297 | Phenyl lactone breathing |
| 1434-1458 | Naphthalene |
| 1498-1518 | Inter ring C=C |
| 1555-1560 | All naphthalene and phenyl units *Normalised to |
| 1603 | Naphthalene lactam |
| 1620 | Phenyl lactone and lactam |
| 1632 | Naphthalene lactone |

Fig. S12 a) Normalized steady state Raman spectroscopy of P-0, P-50 and P-75 at 633 nm excitation, normalized to 1560 $cm^{-1}$ and b) Raman peak assignment.

The steady state resonant Raman spectra with 633nm excitation and peak assignment of the three polymers carried out by comparison to DFT simulations and published literature, (Supplementary Fig. S12).[25, 26, 27, 28] Aromatic phenyl and naphthalene peaks are located in the regions of 1580 – 1650 $cm^{-1}$, the peak at 1560 $cm^{-1}$ is shared across all monomeric units, thus spectra are normalised to this all backbone peak. At the higher wavenumbers there is a peak splitting between the different monomeric units. In P-0 the furan flanked naphthalene (herein named as core-flanking rings ie naphthalene lactone) mode at 1632 $cm^{-1}$, followed by the naphthalene lactam mode at 1604 $cm^{-1}$. In P-50, this peak split is maintained between the phenyl lactone (1627 $cm^{-1}$) and the naphthalene lactam (1603 $cm^{-1}$) and the relative peak intensity of the naphthalene peaks increases suggesting a greater proportion of π electron density is localised to the naphthalene rings compared to the phenyl rings in the neutral polymer. In P-75, both the phenyl lactone and the phenyl lactam vibrations overlap at 1620 $cm^{-1}$, increasing the relative intensity with respect to the remaining naphthalene unit (1603 $cm^{-1}$). There are further naphthalene aromatic peaks in the region of 1350-1480 $cm^{-1}$ followed by the

appearance of the phenyl breathing mode for the phenyl lactone units of P-50 and P-75 at 1297 $cm^{-1}$.

Interestingly, the most intense vibrational peak is observed at around 1500 $cm^{-1}$ which originates from the C=C inter-ring bond between fused lactone ring units. The relative intensity of the C=C inter-ring peak increases with increased phenyl units, indicating a greater distribution of π-electron density between the fused rings, suggesting a more delocalized and planar backbone. This peak shows a significant red shift (20 $cm^{-1}$) from 1518 $cm^{-1}$ in P-0 to 1498 $cm^{-1}$ in P-75, corresponding to a lower energy inter-ring stretch between the smaller and more flexible phenyl units. DFT geometry analysis shows a more planar dihedral angle of 7° between phenyl containing units compared to 12° between a phenyl and a naphthalene unit and 15° between two naphthalene containing units, further indicating a softening of C=C inter-ring vibration and less steric hindrance with phenyl units.

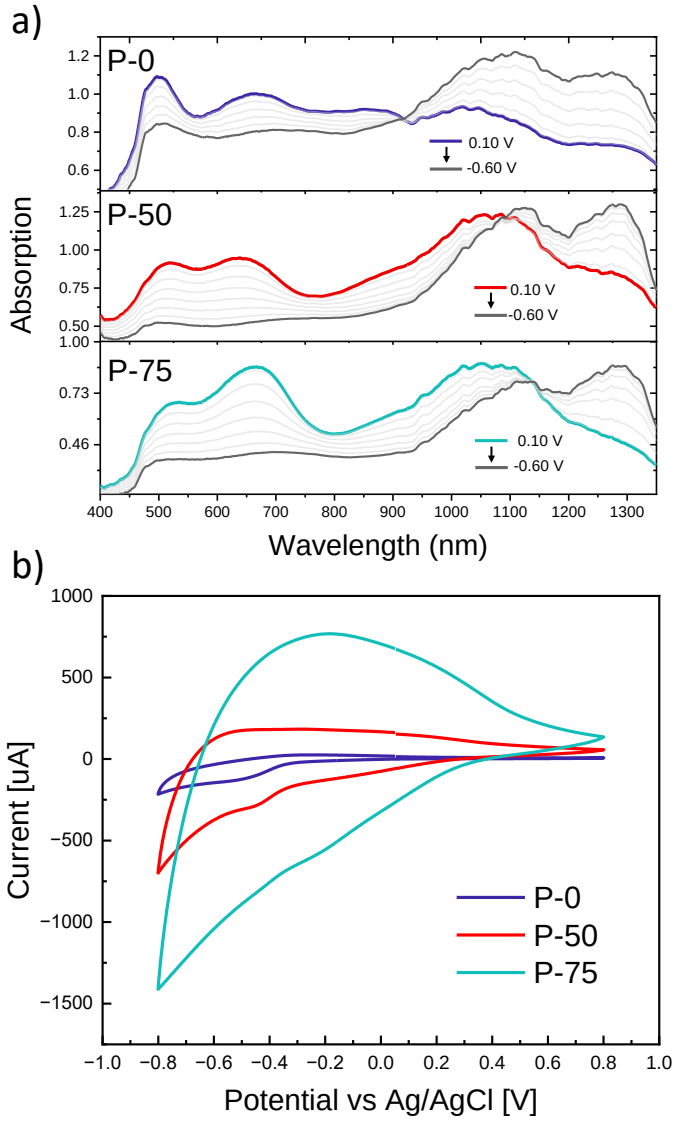


Fig. S13 a) UV–vis–NIR spectroelectrochemical measurements of the three polymers in thin films in 0.1 m NaCl aqueous solution at different bias against Ag/AgCl reference, b) Cyclic voltammograms aqueous electrolyte The polymers were deposited by spin coating on ITO-coated glass substrates and measured with a scan rate of 50 mV/s. Cyclic voltammograms of polymer thin films showed typical n-type behavior in P-0, with reduction potentials in the negative scan, (ERed.aq= -0.32 V). A decrease in reduction onset is noticeable in P-50 (ERed.aq= 0.19 V), which decreases further in P-75 (ERed.aq= 0.29 V). Lower reduction potentials in aqueous electrolytes may indicate improved ion penetration during redox electrochemical reactions, as shown by the increasing area enclosed by the CV curve, indicating an increase in charge carriers.

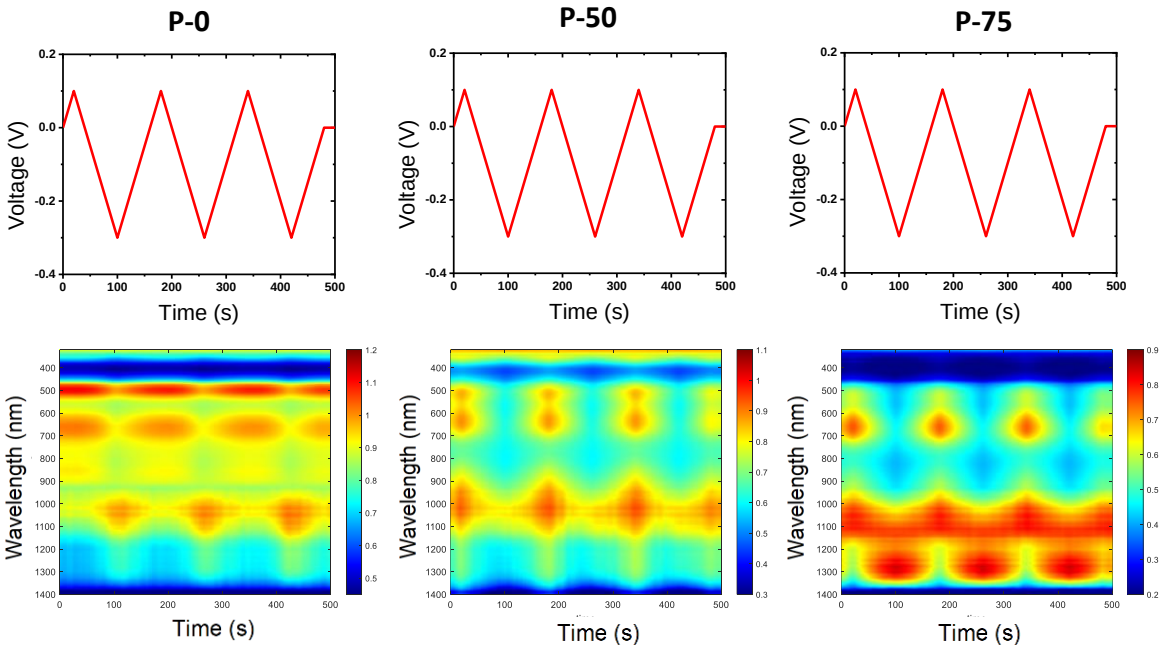


Fig. S14. Spectroelectrochemistry: Potential dependent UV/Vis-NIR absorption spectra. Voltage profiles and absorption color maps of the three polymers at low reductive stress.

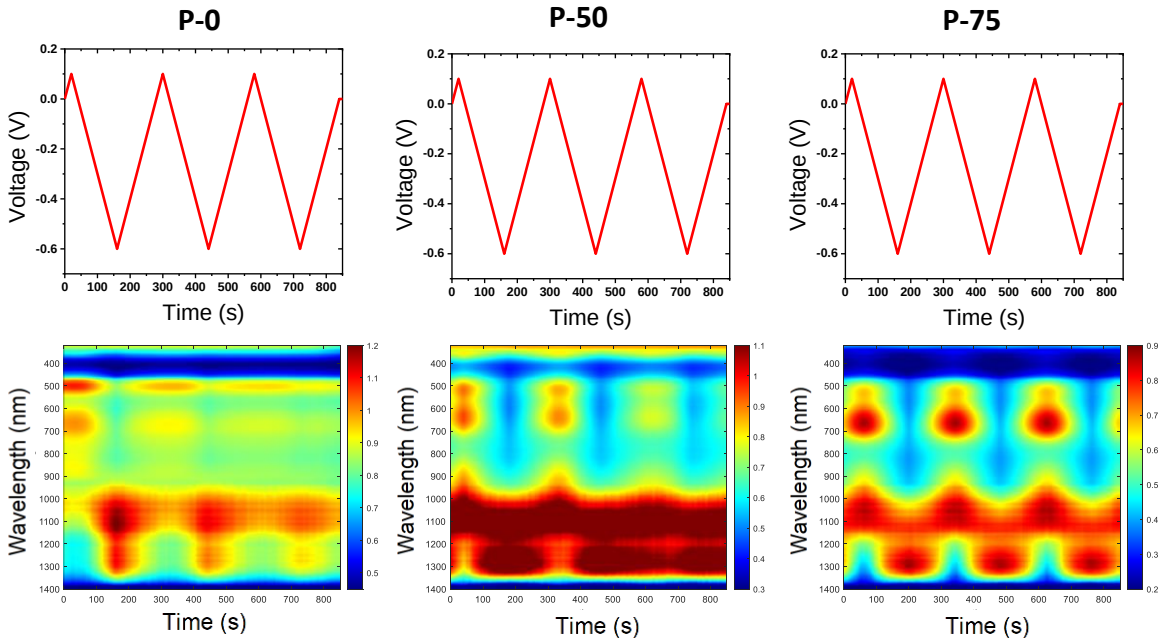


Fig. S15. Spectroelectrochemistry: Potential dependent UV/Vis-NIR absorption spectra. Voltage profiles and, and absorption color maps of the three polymers at high reductive stress.

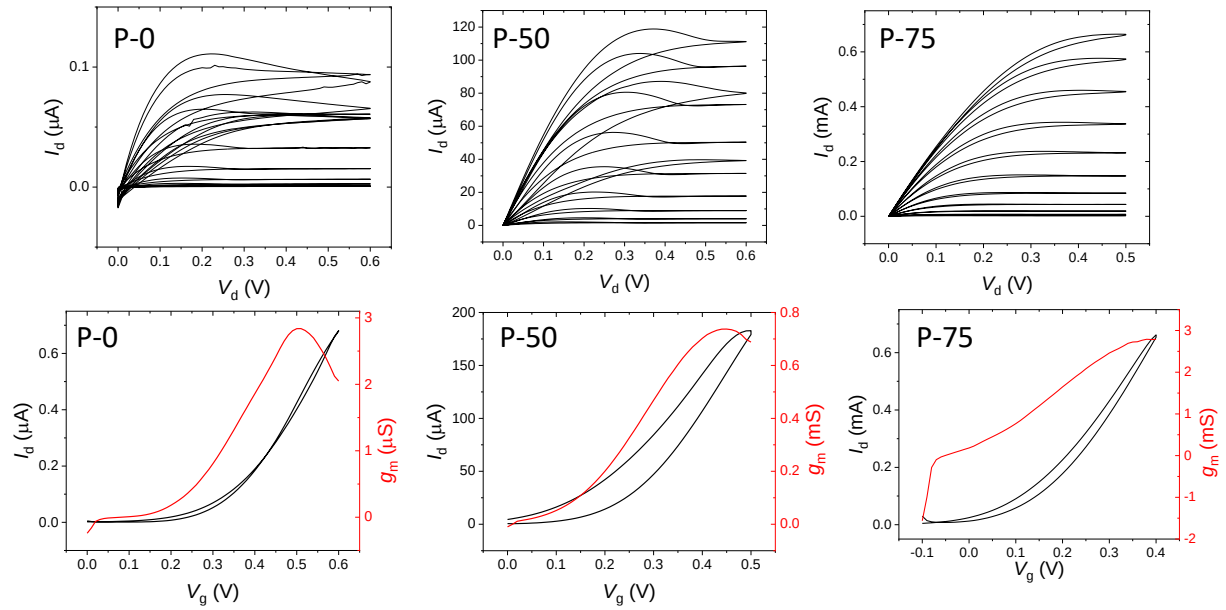


Fig. S16. Output and transfer characteristic curves of drop-casted pristine polymers.

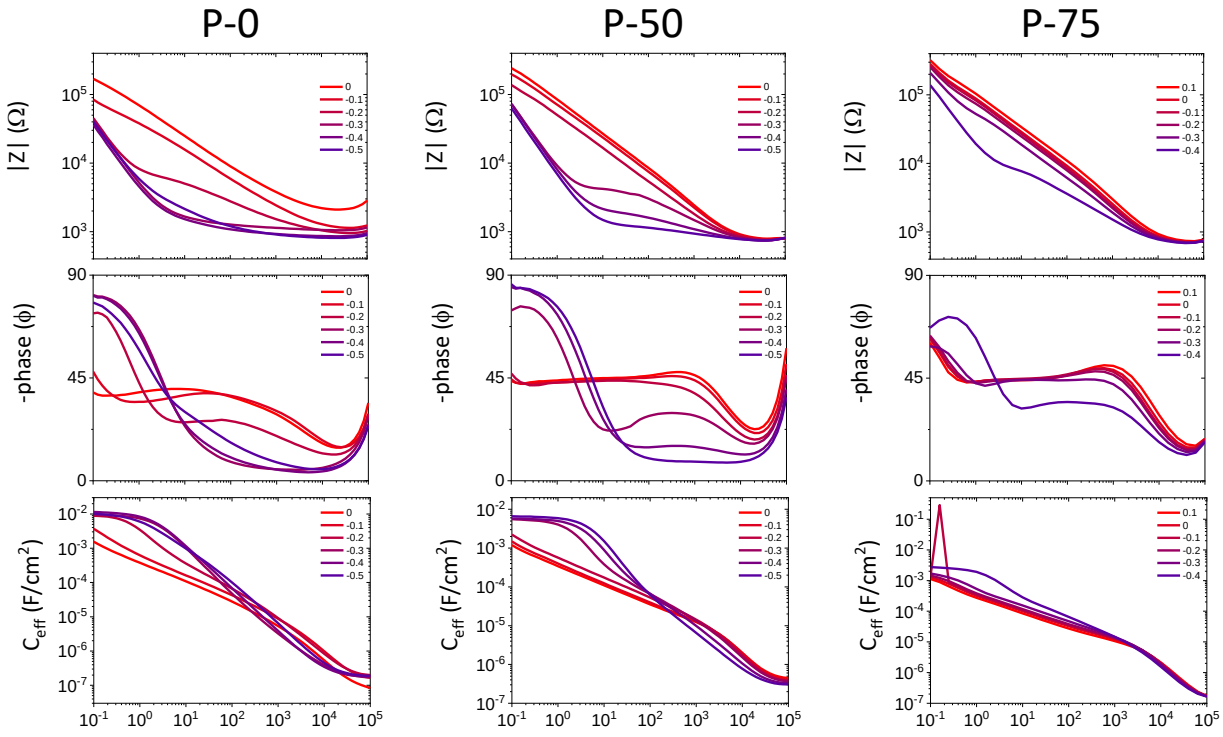


Fig. S17. Electrochemical Impedance Spectroscopy: impedance, phase angle, and effective capacitance of P-0, P-50, and P-75

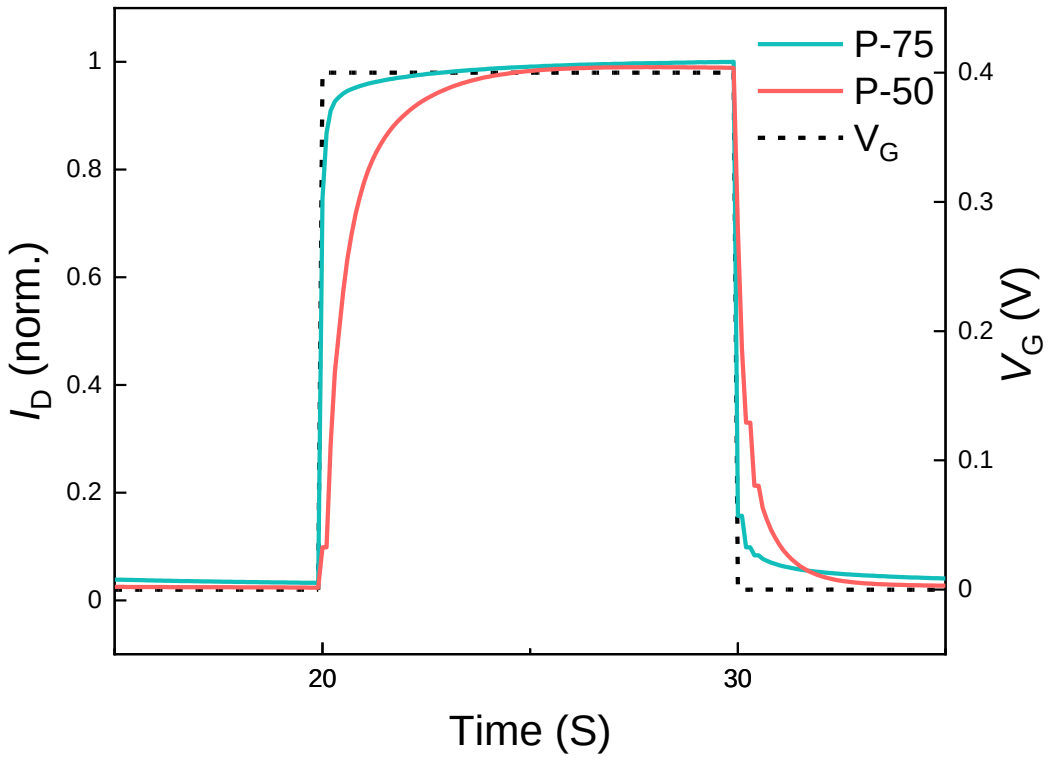


Figure S18. Transient response measurement during pulse operation for P-50 and P-75. The transient response of the drain current in OECT devices is an important parameter for fast bio electronic devices and circuits. The switching speed of P-50 and P-75-based OECTs was determined by pulsing $V_G$ between 0 and 0.4 V and measuring changes in $I_D$. P-50 shows response times of $\tau_{ON}$ = 800 ms and $\tau_{OFF}$ = 450 ms. An enhanced switching speed is observed for P-75, with $\tau_{ON}$ = 90 ms and $\tau_{OFF}$ = 60 ms , reflecting a facile ion injection and electron extraction at the source/drain contacts. Due to low and unstable drain currents of P-0, it was difficult to obtain transient response.

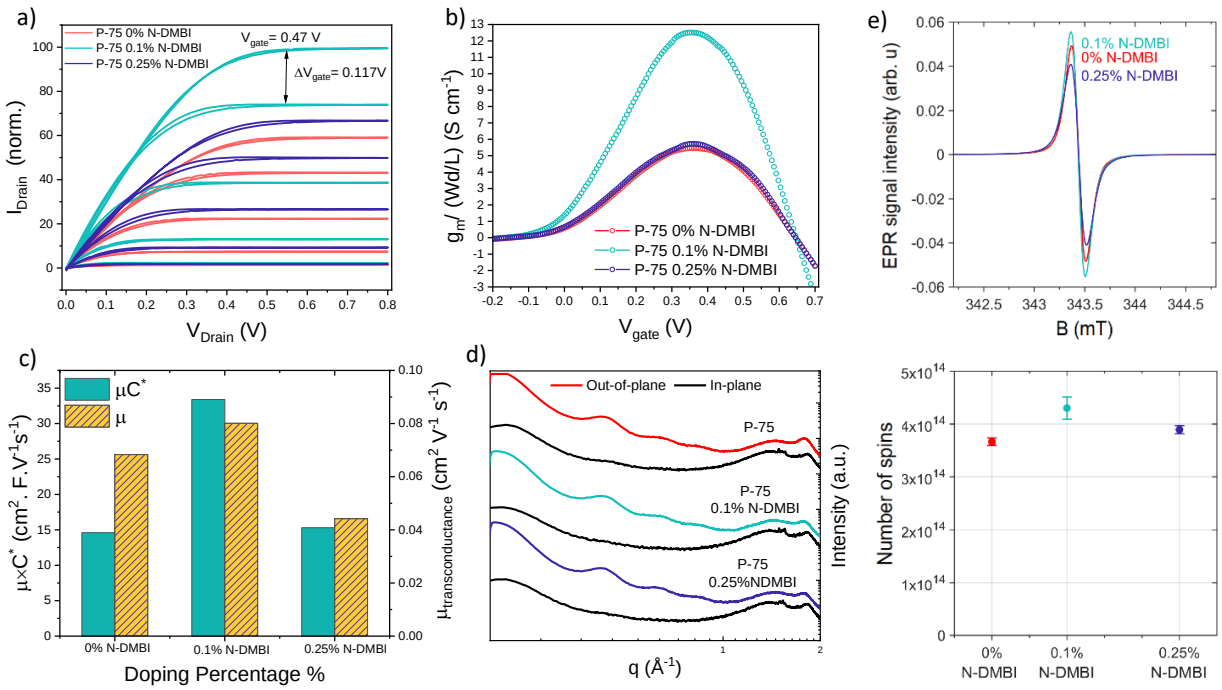


Figure. S19. a)-b) Normalized output and transconductance curves obtained for undoped and two doping percentage (0.1% NDMBI and 0.25%NDMBI) of P-75 polymer using transistors with W=500 μm and L= 50μm. Data for transfer curves was collected at $V_D$=0.7 V and output curves were obtained for different gate voltages starting from $V_{gate}$= 0 and increasing in 0.117V steps up to $V_G$= 0.47 V. $g_{m,norm}$. 12.5 S $cm^{-1}$.c) μC* and $\mu_{OECT}$ of undoped and doped P-75 calculated from the OECT transfer characteristics, with $\mu C^*$ of 33.44 F $cm^{-1}V^{-1}s^{-1}$. d) GIWAXS Scattering profiles of in-plane and out-of-plane for pristine and doped P-75. Lamellar and π-π distances showed negligible changes, indicating an undisturbed polymer microstructure despite NDMBI's large size and π-system, contrary to the substantial disturbance in the polymer ordering that has been noted in heavily doped polymers. e) EPR spectra recorded for undoped and doped P-75 polymer and detected number of spins as a function of doping concentration. Doping with N-DMBI at low concentrations (0.1 wt.%) increased the EPR signal, confirming an increase in charge density, as confirmed by spin quantification. However, at higher doping concentration (0.25 wt.%), the EPR signal decreased in amplitude. The presence of 0.1 wt.% dopant represents a threshold level for decreasing polaron concentration due to bipolaron formation through polaron-polaron interactions, and matches a previous report on P-75 films with high dopant concentrations.

An n-dopant, N-DMBI, has been shown to efficiently n-dope a wide class of n-type conjugated polymers improving electrical conductivity, charge carrier concentration, and electrical performance.[29] P-75, the highest performing semiconducting polymer in the series, was doped with N-DMBI in solution, and NaCl electrolyte gated OECT were tested over a range of dopant concentrations (0, 0.1, and 0.25 wt.%).). The output and transconductance curves are shown in Figs. S19a and b. (P-75-0.1% N-DMBI) displayed the best performing device with an

extremely low threshold voltage of -0.025 V, an enhanced volumetric capacitance of 418 F $cm^{-3}$, a normalized transconductance of 12.5 S $cm^{-1}$ and $\mu C^*$ of 33.44 F $cm^{-1}V^{-1}s^{-1}$. OECT results of the highest performing devices are summarized in Extended Data Table.1.

The trend in performance with varying doping percentage is consistent with the reported thermoelectric performance, with the polymer reaching its maximum conductivities of 12 S $cm^{-1}$ at low doping percentages and declining with higher doping levels.[11] In Fig. S19c, the effect of varying the dopant concentration on electron mobility and $\mu C^*$ is presented. It should be emphasized that we employed ultra-low dopant concentrations in contrast to the reported doping percentages for thermoelectrics (0%, 10%, and 50%). It is remarkable to observe that ultra-low doping concentrations can substantially improve the OECT characteristics to enable an enhanced performance. OECT performance summary of N-DMBI doped P-75, with an average over 6 devices can be found in (Supplementary Fig.. S120 and Table S4).

Grazing incidence wide angle X-ray scattering (GIWAXS) was used to investigate the impact of N-DMBI on P-75 microstructure and morphology. As shown in Fig. S19d and Supplementary Fig. S22, P-75 with 0, 0.1 and 0.25 wt.% NDMBI, show an isotropic amorphous scattering ring centered near 1.5 $Å^{-1}$. At 0.1% doping , significant differences were observed on i) the film texture, as it transitions from face-on orientation to a preference for edge- and face-on orientation, ii) π-π coherence length (Lc) (extracted from FWHM of (010) peak), which expanded from 35.79 to 41.27 Å, both observations are aligned with the improved OECT performance at 0.1% doping level. Lamellar and π-π distances showed negligible changes, indicating an undisturbed polymer microstructure despite NDMBI's large size and π-system, contrary to the substantial disturbance in the polymer ordering that has been noted in heavily doped polymers[30]. Overall, the GIWAXS results show no negative effects on the polymer's microstructural order at these ultra-low doping levels.

Electron paramagnetic spectroscopy (EPR) was used to monitor doping-induced changes in spin concentration in polymers. Most polymers have charge carriers, polarons, which can be detected and quantified by EPR.[31, 32] Doping with N-DMBI at low concentrations (0.1 wt.%) increased the EPR signal, confirming an increase in charge density, as confirmed by spin quantification. (Fig. S19e) However, at higher doping concentration (0.25 wt.%), the EPR signal decreased in amplitude. The presence of 0.1 wt.% dopant represents a threshold level for decreasing polaron concentration due to bipolaron formation through polaron-polaron interactions, and matches a previous report on P-75 films with high dopant concentrations. Both GIWAXS and EPR results suggest that ultra-low doping concentrations do not disturb film microstructure, resulting in improved OECT performance.

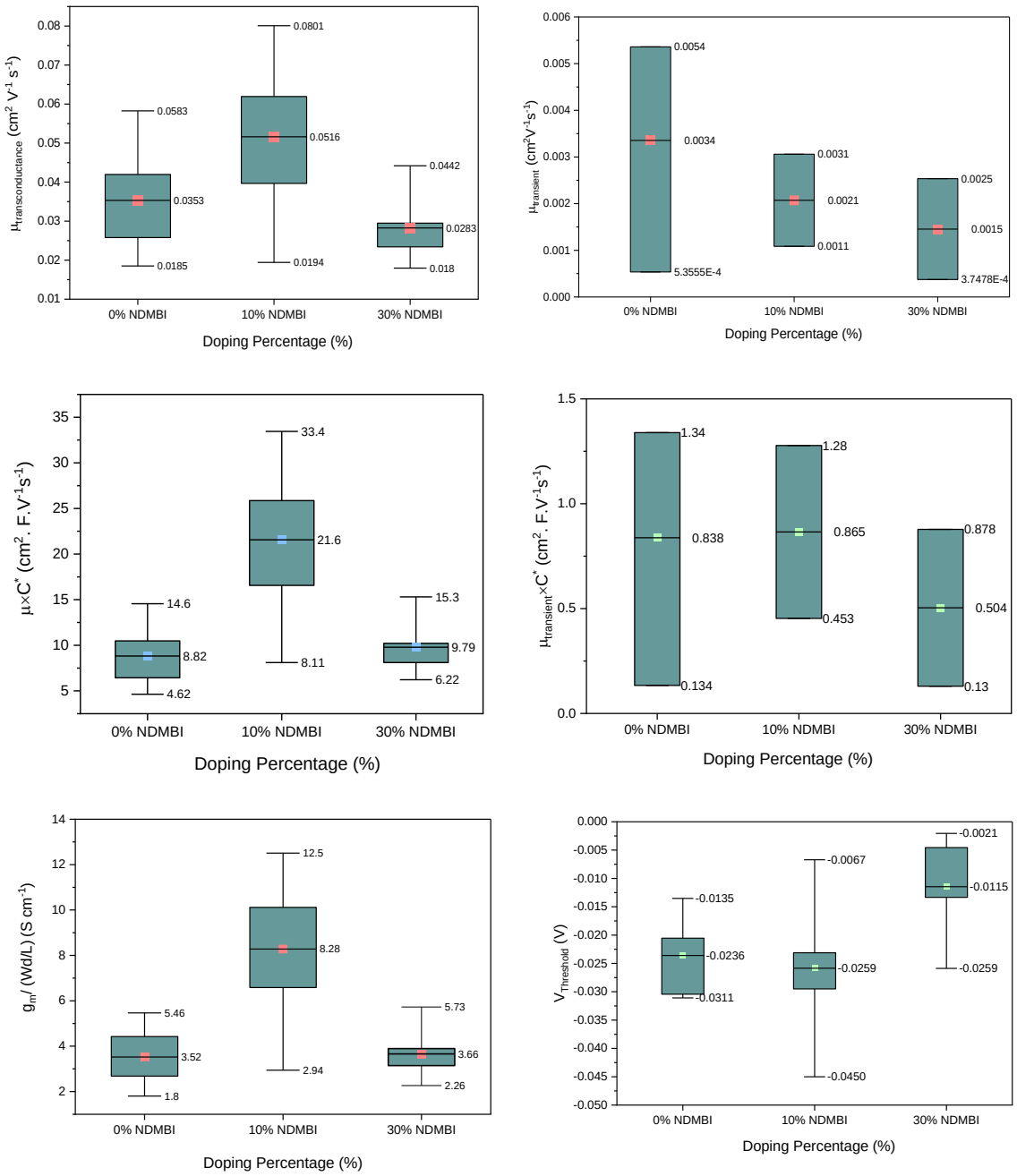


Fig S20. OECT performance summary of N-DMBI doped P-75, with an average over 6 devices.

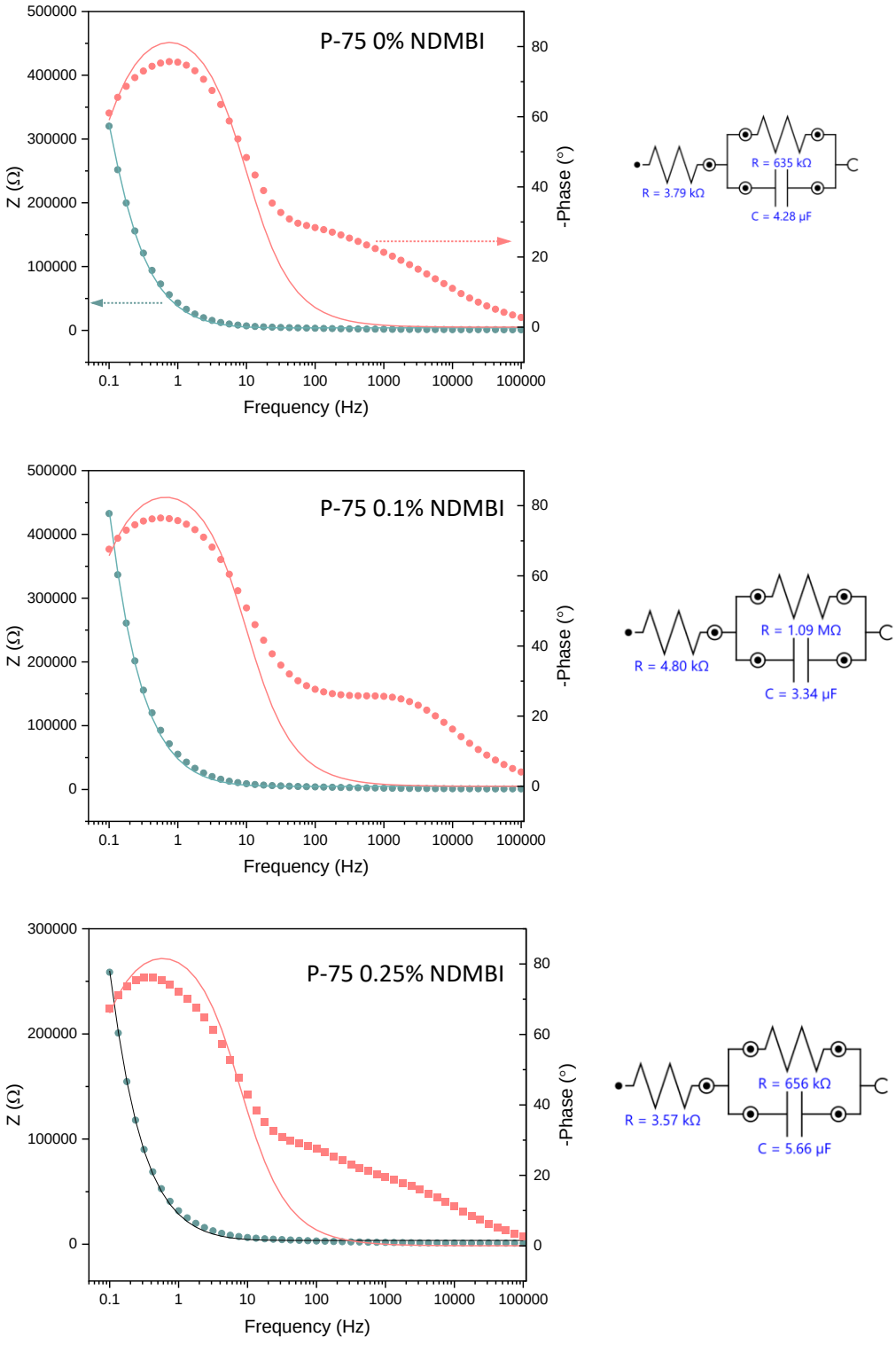


Figure S21. Electrochemical Impedance Spectroscopy of N-DMBI doped P-75.

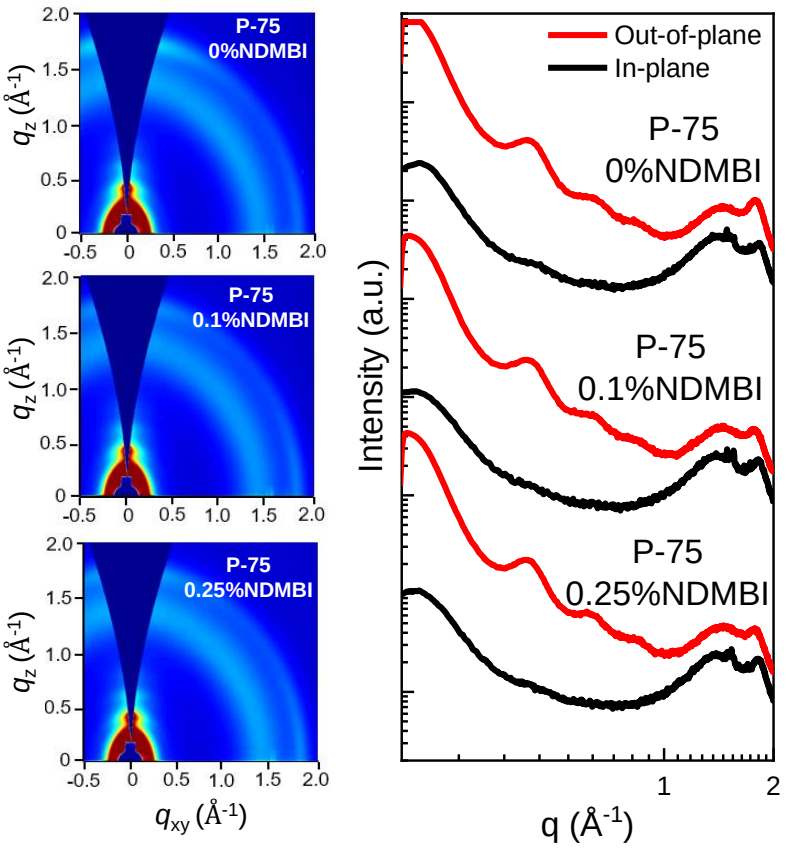


| Polymer | Lamellar Stacking | | | | $\pi-\pi$ Stacking | | | |
|---|---|---|---|---|---|---|---|---|
| | $q_{(100)}$ [Å$^{-1}$] | $d$ [Å] | FWHM [Å$^{-1}$] | $L_c$ [Å] | $q_{(010)}$ [Å$^{-1}$] | $d$ [Å] | FWHM [Å$^{-1}$] | $L_c$ [Å] |
| P-75 | 0.19933 | 31.52 | 0.04889 | 117.80 | 1.81297 | 3.47 | 0.15847 | 35.79 |
| P-75- 0.1% NDMBI | 0.19933 | 31.52 | 0.04598 | 125.66 | 1.7785 | 3.54 | 0.13719 | 41.27 |
| P-75- 0.25% NDMBI | 0.19708 | 31.88 | 0.04305 | 131.50 | 1.80533 | 3.49 | 0.13743 | 41.14 |

Figure S22. GIWAXS Patterns: Two-dimensional grazing incidence X-ray scattering map, GIWAXS linecuts, and a summary table of pristine and NDMBI doped P-75.

## 5.3.4 References


1. Sudakov I, Van Landeghem M, Lenaerts R, Maes W, Van Doorslaer S, Goovaerts E. The Interplay of Stability between Donor and Acceptor Materials in a Fullerene-Free Bulk Heterojunction Solar Cell Blend. *Advanced Energy Materials* 2020, **10**(46)**:** 2002095.

2. Wittmann J, Can T, Eckardt M, Harneit W, Griffin R, Corzilius B. High-precision measurement of the electron spin g factor of trapped atomic nitrogen in the endohedral fullerene N@ C60. *Journal of Magnetic Resonance* 2018, **290:** 12-17.

3. Stoll S, Schweiger A. EasySpin, a comprehensive software package for spectral simulation and analysis in EPR. *Journal of magnetic resonance* 2006, **178**(1)**:** 42-55.

4. Parr ZS, Rashid RB, Paulsen BD, Poggi B, Tan E, Freeley M, *et al.* Semiconducting Small Molecules as Active Materials for p-Type Accumulation Mode Organic Electrochemical Transistors. *Advanced Electronic Materials* 2020, **6**(6)**:** 2000215.

5. Tarabella G, Santato C, Yang SY, Iannotta S, Malliaras GG, Cicoira F. Effect of the gate electrode on the response of organic electrochemical transistors. *Applied Physics Letters* 2010, **97**(12)**:** 205.

6. Gaussian09 RA. 1, mj frisch, gw trucks, hb schlegel, ge scuseria, ma robb, jr cheeseman, g. Scalmani, v. Barone, b. Mennucci, ga petersson et al., gaussian. *Inc, Wallingford CT* 2009, **121:** 150-166.

7. Becke A. Density-functional thermochemistry. III. The role of exact exchange (1993) J. *Chem Phys*, **98:** 5648.

8. Petersson a, Bennett A, Tensfeldt TG, Al-Laham MA, Shirley WA, Mantzaris J. A complete basis set model chemistry. I. The total energies of closed-shell atoms and hydrides of the first-row elements. *The Journal of chemical physics* 1988, **89**(4)**:** 2193-2218.

9. Stephens PJ, Devlin FJ, Chabalowski CF, Frisch MJ. Ab initio calculation of vibrational absorption and circular dichroism spectra using density functional force fields. *The Journal of physical chemistry* 1994, **98**(45)**:** 11623-11627.

10. Laury ML, Carlson MJ, Wilson AK. Vibrational frequency scale factors for density functional theory and the polarization consistent basis sets. *Journal of computational chemistry* 2012, **33**(30)**:** 2380-2387.

11. Alsufyani M, Stoeckel MA, Chen X, Thorley K, Hallani RK, Puttisong Y, *et al.* Lactone Backbone Density in Rigid Electron-Deficient Semiconducting Polymers Enabling High n-type Organic Thermoelectric Performance. *Angewandte Chemie* 2022, **134**(7)**:** e202113078.

12. Giovannitti A, Nielsen CB, Sbircea DT, Inal S, Donahue M, Niazi MR, *et al.* N-type organic electrochemical transistors with stability in water. *Nat Commun* 2016, **7:** 13066.

13. Wu HY, Yang CY, Li Q, Kolhe NB, Strakosas X, Stoeckel MA, *et al.* Influence of Molecular Weight on the Organic Electrochemical Transistor Performance of Ladder-Type Conjugated Polymers. *Adv Mater* 2021**:** e2106235.

14. Chen X, Marks A, Paulsen BD, Wu R, Rashid RB, Chen H, *et al.* n-Type Rigid Semiconducting Polymers Bearing Oligo(Ethylene Glycol) Side Chains for High-Performance Organic Electrochemical Transistors. *Angew Chem Int Ed Engl* 2021, **60**(17)**:** 9368-9373.

15. Feng K, Shan W, Ma S, Wu Z, Chen J, Guo H, *et al.* Fused Bithiophene Imide Dimer-Based n-Type Polymers for High-Performance Organic Electrochemical Transistors. *Angew Chem Int Ed Engl* 2021, **60**(45)**:** 24198-24205.

16. Feng K, Shan W, Wang J, Lee JW, Yang W, Wu W, *et al.* Cyano-Functionalized n-Type Polymer with High Electron Mobility for High-Performance Organic Electrochemical Transistors. *Adv Mater* 2022, **34**(24)**:** e2201340.

17. Tang H, Liang Y, Liu C, Hu Z, Deng Y, Guo H, *et al.* A solution-processed n-type conducting polymer with ultrahigh conductivity. *Nature* 2022, **611**(7935)**:** 271-277.

18. Ke Z, Abtahi A, Hwang J, Chen K, Chaudhary J, Song I, *et al.* Highly Conductive and Solution-Processable n-Doped Transparent Organic Conductor. *J Am Chem Soc* 2023, **145**(6)**:** 3706-3715.

19. Xu K, Sun H, Ruoko T-P, Wang G, Kroon R, Kolhe NB, *et al.* Ground-state electron transfer in all-polymer donor–acceptor heterojunctions. *Nature Materials* 2020, **19**(7)**:** 738-744.

20. Giovannitti A, Nielsen CB, Sbircea D-T, Inal S, Donahue M, Niazi MR, *et al.* N-type organic electrochemical transistors with stability in water. *Nature communications* 2016, **7**(1)**:** 1-10.

21. Giovannitti A, Maria IP, Hanifi D, Donahue MJ, Bryant D, Barth KJ, *et al.* The role of the side chain on the performance of n-type conjugated polymers in aqueous electrolytes. *Chemistry of Materials* 2018, **30**(9)**:** 2945-2953.

22. Sun H, Vagin M, Wang S, Crispin X, Forchheimer R, Berggren M, *et al.* Complementary logic circuits based on high-performance n-type organic electrochemical transistors. *Advanced Materials* 2018, **30**(9)**:** 1704916.

23. Chen X, Marks A, Paulsen BD, Wu R, Rashid RB, Chen H, *et al.* n-Type Rigid Semiconducting Polymers Bearing Oligo (Ethylene Glycol) Side Chains for High-Performance Organic Electrochemical Transistors. *Angewandte Chemie International Edition* 2021, **60**(17)**:** 9368-9373.

24. Marks A, Chen X, Wu R, Rashid RB, Jin W, Paulsen BD, *et al.* Synthetic nuances to maximize n-type organic electrochemical transistor and thermoelectric performance in fused lactam polymers. *Journal of the American Chemical Society* 2022, **144**(10)**:** 4642-4656.

25. Preuss M, Bechstedt F. Vibrational spectra of ammonia, benzene, and benzene adsorbed on Si (001) by first principles calculations with periodic boundary conditions. *Physical Review B* 2006, **73**(15)**:** 155413.

26. Hewett KB, Shen M, Brummel CL, Philips LA. High resolution infrared spectroscopy of pyrazine and naphthalene in a molecular beam. *The Journal of chemical physics* 1994, **100**(6)**:** 4077-4086.

27. Razzell-Hollis J, Wade J, Tsoi WC, Soon Y, Durrant J, Kim J-S. Photochemical stability of high efficiency PTB7: PC 70 BM solar cell blends. *Journal of Materials Chemistry A* 2014, **2**(47)**:** 20189-20195.

28. Wood S, Wade J, Shahid M, Collado-Fregoso E, Bradley DD, Durrant JR, *et al.* Natures of optical absorption transitions and excitation energy dependent photostability of diketopyrrolopyrrole (DPP)-based photovoltaic copolymers. *Energy & Environmental Science* 2015, **8**(11)**:** 3222-3232.

29. Zhao W, Ding J, Zou Y, Di CA, Zhu D. Chemical doping of organic semiconductors for thermoelectric applications. *Chem Soc Rev* 2020, **49**(20)**:** 7210-7228.

30. Lu Y, Yu ZD, Liu Y, Ding YF, Yang CY, Yao ZF, *et al.* The Critical Role of Dopant Cations in Electrical Conductivity and Thermoelectric Performance of n-Doped Polymers. *J Am Chem Soc* 2020, **142**(36)**:** 15340-15348.

31. Tsutsui Y, Okamoto H, Sakamaki D, Sugiyasu K, Takeuchi M, Seki S. Landscape of charge carrier transport in doped poly (3-hexylthiophene): noncontact approach using ternary combined dielectric, paramagnetic, and optical spectroscopies. *The Journal of Physical Chemistry Letters* 2018, **9**(13)**:** 3639-3645.

32. Wegner B, Lungwitz D, Mansour AE, Tait CE, Tanaka N, Zhai T, *et al.* An organic borate salt with superior p-doping capability for organic semiconductors. *Advanced Science* 2020, **7**(17)**:** 2001322.

# Chapter 6

## Conclusions, discussion and outlook

In brief, the research conducted in this thesis focuses on addressing key challenges in the performance of n-type conjugated polymers, specifically their low electrical conductivities and poor air stability. Herein, these limitations are approached exclusively through a chemical design perspective. Our chemical design target is to develop semiconducting polymers that are electron-deficient and possess the highest possible electron affinity (EA). With this goal in mind, we took notes from the benchmark n-type materials, identified the don'ts and dos, and then formulated preliminary candidate polymers with the potential to overcome the limitations of the benchmark n-type materials.

The chosen polymer class for investigation is the fused lactam rigid polymers. These polymers fall under the category of all acceptor or (A-A) polymers, due to the presence of the electron withdrawing bis-lactam functional groups (good for high EA), and feature a rigid backbone achieved through double bond linkage between the monomer units (good for charge transport). These characteristics render this class of polymers suitable with the objectives of our research.

From a synthetic perspective, the selected polymer class comes with a second advantage, as it involve the use of metal-free aldol polymerization. Differently from the widely used transition metal-mediated cross-coupling polymerizations, this polymerization route has only water as the byproduct, whereas metal-catalyzed polymerization requires extensive purification steps to isolate a pure polymer free of residual metals used as catalysts in the synthesis, such as palladium.[1, 2] The polymers presented in this thesis are therefore synthesized using metal-free, acid-catalyzed aldol condensation only, making polymer isolation much simpler.

**In chapter 2**, the lactone incorporation into fused lactam polymers was first tested, and it resulted in enhancing the EA of the resulting lactone-containing polymers (P1, P2 and P3),

compared to all-lactam derivatives.[3] Based on the observed trends in the EA and electrical conductivity trends in P1, P2, and P3, which are -4.68, -4.68, -4.52 eV and 0.20, 0.30, and 0.008 S $cm^{-1}$, respectively, it is possible to conclude that the dominant factor in increasing conductivity is energy level offset, which drives electron transfer. Further investigations conducted using GIWAXS have provided insights into polymers film microstructure and charge transport behaviour. Despite the similar EA of P1 and P2, which mirror their similar structures, they exhibited slightly different microstructures, differing in the ratio of crystallite orientation, with P1 having a predominantly face-on orientation, and P2 exhibiting a mixture of face-on and edge-on orientations. The more uniform orientation of crystallites in P1 might explain the higher OFET mobility, while, mix of edge-on and face-one orientated crystallites in P2 may have contributed to the improved electrical conductivity, suggesting that the dominant factor in optimizing the electrical conductivity is the doping density, which seems to be better in P2, perhaps because the longer side chains in P1 could hinder the dopant penetration within the polymer. In addition, a combination of edge-on and face-on orientations could create free space at the polymer matrix's boundaries, thereby facilitating the accommodation of dopant molecules.[4] Compared to P1 and P2, P3 exhibited a lower EA and a less crystalline microstructure, and both collectively have compromised its thermoelectric performance. The slight differences in thermoelectric performance between P1 and P2 suggest the important role of side-chain size, which in turn affect the microstructure and the final thermoelectric performance by either favoring charge transport in P1 or favoring dopant intercalation in P2. The significant difference however, in thermoelectric performance of P1/P2 and P3, suggest the EA as the dominant factor in optimizing the thermoelectric performance than the film microstructure. Despite the lower thermoelectric performance of the best performing polymer (P2) compared to literature materials, this work provided chemical design guidelines by demonstrating that extending the lactone aromatic core in (P3), reduced the electron affinity,

due to reducing the density of electron withdrawing groups (Carbonyl groups) along the backbone and subsequently the electrical conductivity reduced by almost two orders of magnitude. These results were striking to us as they contradicted the common notion in the field, in which the more extended conjugation was found to facilitate interchain interactions and therefore charge transport.[3, 5, 6]However, our results provided new insights in which that the advantages of extending the conjugated backbone are not always guaranteed, and that a planarized polymer structure is necessary to fully exploit the benefits of aromatic core extension. These results therefore highlight the effect of aromatic ring size expansion in the final thermoelectric performance and suggest electron affinity as the dominating factor in determining the thermoelectric performance of this class of rigid n-type conjugated polymer. These findings provided useful insights into the design of a second set of polymers (P-0, P-50, and P-75), **in chapter 3**, in which our design targeted aromatic core contraction instead of extension, in an attempt to maximize the EA by maximizing lactone backbone density. This was achieved by systematic reduction in aromatic size from naphthalene to benzene. Experimental and theoretical energy level investigations demonstrated that increasing the lactone group density by increasing the benzene ring ratio along the backbone from 0%, to 50% and 75% result in i) progressively larger electron affinities (up to 4.3 eV), ii) higher backbone coplanarity due to less twisting between benzene based building blocks, which has in turn enabled iii) extended negative polaron distribution along the polymer backbone. As a result the polymer with the largest lactone density, P-75 has shown remarkable intrinsic conductivities of up to 0.5 S $cm^{-1}$ and upon doping with N-DMBI, high electrical conductivities (σ) of 12 S $cm^{-1}$ have been achieved, demonstrating one of the few polymers reported with electrical conductivities > 10 S $cm^{-1}$. Therefore, high power factors (PF) were achieved of up to 13.2 $\mu W m^{-1} K^{-2}$, among the highest performing n-type thermoelectric materials published that year. Overall, the experimental techniques used in this study has provided us with a deeper

understanding of the nature of the study polymers, and aided in explaining the observed trends in thermoelectric performance. Theoretical modelling together with experimental activation energies provided insight into the extent of charge delocalization along the polymers backbone. UV-vis-NIR and EPR spectroscopy provided insights into the doping behaviour and spin density of the pristine and doped polymers. Aside from these findings, this study raised new questions that remain unresolved. For example, the underlying cause of the intrinsic conductivity of the three polymers remains elusive, (which is more pronounced in P-75), and is evident by a signal in EPR spectroscopy. Furthermore, the underlying cause for the inverse correlation between the EPR signal intensity and electrical conductivity remains unclear. Typically, a decrease in EPR intensity suggests a reduction in the number of spins, which in turn may lead to a decrease in electrical conductivity. However, an opposite pattern was observed in P-50 and P-75, in which a decrease in EPR intensity corresponded to an increase in electrical conductivity. The decrease in EPR intensity upon increasing the dopant concentration in P-50 and P-75 can be explained by the formation of bipolarons (EPR silent) through polaron-polaron interactions, which are also evident in UV-vis-NIR spectroscopy by a broad absorption over 2000 nm at high doping levels. However, we still don't know why bipolarons contribute to higher electrical conductivities than polarons in our case, as it has been previously demonstrated that bipolarons are slower than polarons. Nevertheless, the above two studies highlight that replacing the lactam groups with the stronger electron withdrawing lactone group is an effective design strategy to optimize the thermoelectric performance, and offer new insights into material design guidelines for the future development of high-performing n-type organic thermoelectrics. Ultimately, rational design and synthetic modifications of polymer building blocks has enabled the progression from initial electrical conductivities and power factors of 0.28 S $cm^{-1}$ and 0.16 μW $m^{-1}$ $K^{-2}$, respectively, to achieve

state-of-the-art thermoelectric performance values of 12 S $cm^{-1}$ and 13.2 μW $m^{-1}$ $K^{-2}$ for electrical conductivity and power factors, respectively. (See Figure.1)

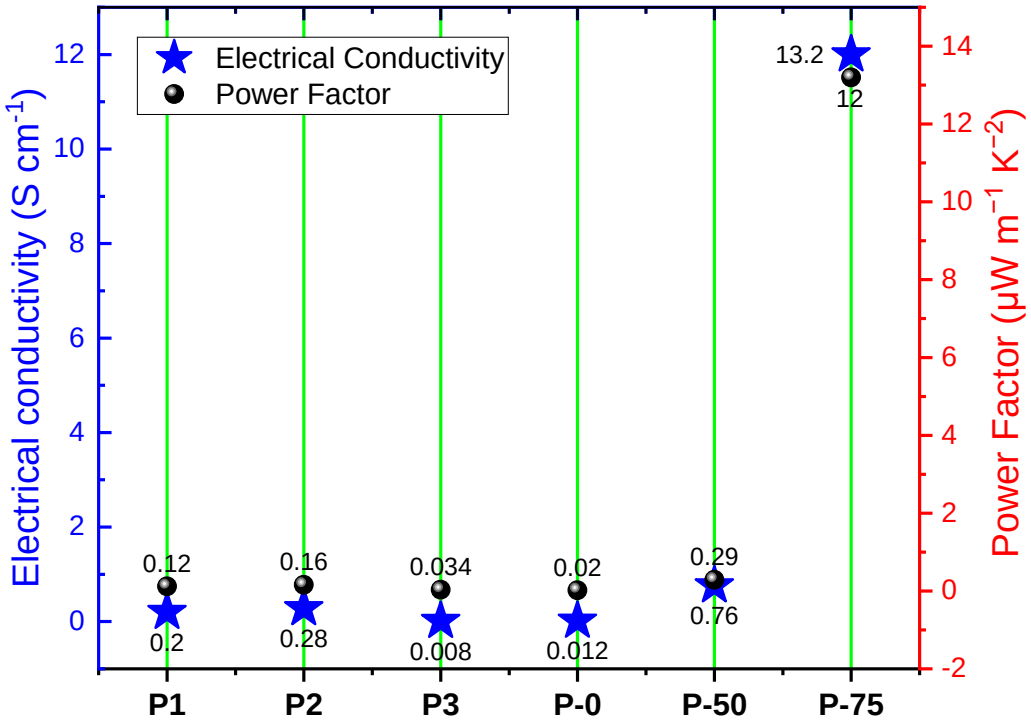


Figure 1. Thermoelectric performance progress of initial and final polymers.

It would be expected that the polymers of **chapter 3** would also find application in n-type OECT devices, with ionic compatibility provided by the hydrophilic side chains. While **chapters 2** and **3** investigated the molecularly n-doped polymers, **chapter 4** was dedicated to exploring the electrical performance of electrochemically n-doped polymers. More specifically, exploring organic mixed ionic-electronic conductors (the polymers of chapter 3) in biologically relevant environments, for use in devices such as organic electrochemical transistors (OECTs), for bioelectronics sensing applications. **Chapter 4** addresses one of the key challenges in the performance of n-type OECTs that is their ambient instability, and in particular, evaluates the effect of one of the reactions of electrons with molecular oxygen,

namely the formation of superoxide radical anions, on organic electrochemical transistors (OECTs) performance. The investigated polymers P-0, P-50, and P-75 are suitable candidates for this study due their distinct LUMO levels that are situated around the thermodynamic threshold for superoxide formation. We commenced this investigations by evaluating the durability of the electrochemically generated electrons in aqueous electrolytes using time resolved spectroelectrochemistry, and interestingly, the trend in lifetime of negative polarons observed in the three polymers in air are consistent with the trend in EA. By performing nitrogen controls, we confirmed that the observed decay of negative polarons is oxygen induced, involving a reduction of oxygen through an electron transfer from the n-doped polymers to molecular oxygen. Since the product of this one-electron reduction is superoxide radical anion, our next step was to confirm the occurrence of this reaction by detecting its product, the superoxide radical, using EPR spin trapping technique. Indeed, EPR results demonstrated the absence of superoxide formation from photoinduced polarons of P-75 and its presence in P-50 and P-0, with increased generation of superoxide arising from the P-0 polymer, with the smallest EA. The trend of persistence in the electrochemically generated electrons in air seem to reflect on their redox reversibility and structural recovery as evidenced by spectroelectrochemistry and in-situ electrochemical resonant Raman spectroscopy, respectively. Ultimately, all the above trends are in agreement with the polymers OECT performance, which also follow the same trend of OTEs performance, with P-0 exhibiting the lowest performance and P-75 having the highest, demonstrating a state-of-the-art n-type OECT performance (it was the highest n-type OECT material in the field in 2021). Overall, this work provide a general design methodology to avoid detrimental parasitic reactions under ambient conditions, and the benefits that arise in the OECT performance. N-DMBI is a widely used n-dopant in organic thermoelectrics due to its air stability and solution-processability, and it was the adopted dopant in the two studies of **chapter 2, and 3**. For the first time herein, in **chapter**

**4**, the performance of N-DMBI doped polymers is investigated in OECTs, where the polymers are doped both chemically and electrochemically. This has resulted in preceding OECT performance with $g_m$ and $\mu C^*$ of 12.50 S $cm^{-1}$ and 33.44 F $cm^{-1}V^{-1}s^{-1}$, respectively.

Following the conducted research, here are several perspectives on how this research assisted me in identifying potential areas for improvement:

1. The first perspective concerns the polymer quality and batch reproducibility. The polymers synthesized in this thesis are step-growth random copolymers. Step-growth polymerization (or polycondensation) can occur via two primary routes: transition-metal mediated cross-coupling condensation (widely used in the field, mostly using Stille, and Suzuki coupling), and acid/base-catalyzed aldol condensation (such as acid-catalyzed aldol condensation used in this thesis). In both cases, and according to the Carothers equation, the polymerization is particularly sensitive to stoichiometry (and thus purity).[7] Molecular weight and molecular weight distribution are also not controlled. Controlling the primary structure of polymeric materials is essential for achieving high-performance applications in organic electrical devices.[8, 9] In transition-metal mediated polycondensation of conjugated polymers, a more controlled route was accomplished by catalyst transfer polymerization, such as Kumada catalyst transfer polymerization (KCTP),[9] and Negishi catalyst-transfer polycondensation (NCTP)[10] systems, proceeding in a chain-growth manner with controlled MW and polydispersity. Conversely, limited attention has been devoted to developing a controlled route for metal-free polycondensation of conjugated polymer synthesis. Attempts by the Tomoya Higashihara group were first taken in 2018,[11] when they reported a transition-metal-free controlled synthesis of a p-type polymer, poly(3-alkylthienylene vinylene), via Horner–Wadsworth–Emmons (HWE) condensation. Their route involves the use of a dithiocarbamate-type thiophene monomer and an organobase, which results in the formation of a deprotonated monomer (which did not undergo self-

condensation due to the resonance effect). This is followed by the addition of an initiator, with an active formyl group. The polymerization proceeded in a chain-growth manner using the HWE condensation reaction and resulted in the formation of the polymer with a controlled molecular weight and molecular weight distribution. Later in 2020, an electron-deficient lactam-based polymer was developed using the same route with a controllable molecular weight. Based on these findings, it is expected that further optimization of the polymerization routes demonstrated by the Tomoya Higashihara group will result in the realization of controllable chain-growth polymerizations, which minimize the drawbacks of random copolymers by step-growth polymerizations and produce high-quality polymers with batch-to-batch consistency. Furthermore, the absence of residual transition metals contributes to the purity of the isolated polymer.

2. The second perspective is related to the air stability of n-type semiconducting polymers in OECT devices. When it comes to assessing the air stability of n-type polymers, all literature reports so far have relied on conclusions drawn from one report by De Leeuw et al. in 1997.[12] The main conclusion of the article by De Leeuw is that in order for a doped n-type polymer to be stable in both oxygen and water, its LUMO must be -4.9 eV or deeper. It is widely acknowledged that achieving such a LUMO level is extremely challenging and presents a concern in the development of ambient stable doped n-type polymers under device operation. Nevertheless, experimentally, a couple of n-type materials with LUMO levels ~ -4 eV were able to show air stable OFET-based device operation.[13, 14, 15] This has been explained by the concept of overpotentials, ranging between 0.9−1.0 V. (overpotentials are explained in Section 1.4.1). Therefore, by accounting for these overpotentials, it was concluded that a LUMO of ~ -4 eV would be sufficient to enable an air-stable electron transport. However, it must be noted that this energetic threshold holds only true in OFET-based transistors. In a typical thin-film OFET, only the interface

between the active channel (an n-type polymer) and the dielectric layer is electrically n-doped, and acts as the conductive channel. The n-type active channel's remaining layers, which are thicker than the conductive channel, serve as a self-encapsulation layer. As a result, n-type polymers with LUMO ~ -4 eV have been found to be air stable under OFET device operation. Conversely, in an OECT device, the bulk polymer films are entirely n-doped and conductive. This suggests that to stabilize the non-encapsulated n-doped polymer in OECTs, deeper LUMO energy levels are necessary compared to OFETs (-4.1 eV). Based on the above discussion and in the context of OECTs, we conclude that the generally accepted energy threshold (~ -4 eV) believed to enable air stability in OECTs must be reevaluated, and that air stability guidelines derived from OFETs should not be applied indiscriminately to OECTs. Our findings in **chapter 4** provide an initial support to this viewpoint, in which n-type polymers with LUMO of $\leq$ -4.2 eV exhibited ambient instability in OECT devices. Moreover, apart from electrochemical degradations driven by energetics (thermodynamic instability), one must also consider chemical degradations that results from the thermodynamic instability. For example, during OECT operation in aqueous electrolytes, latent ORR products such as $H_2O_2$ and hydroxyl radicals (equation 1-4, Section 4.2), could potentially react with the n-doped polymer, leading to its chemical degradation, with potential corrosive damage during OECT operation.[16, 17] This is another example of the differences in operating conditions between OFETs and OECTs, and it encourages OECT researchers to reconsider the energy level diagram air stability for achieving high-performance air-stable n-type OECT materials, rather than relying on conclusions drawn from devices with different operating conditions, such as OFETs.

3. **Chapter 4** aimed to explore the potential effect of molecular oxygen as an electron trap by examining the detection of its one-electron reduction product, the superoxide radical. However, there are other possible electron traps that need to be considered in the future.

For example, reduction of water by the n-doped polymer via $2H_2O + 2e^- \rightleftharpoons H_2 + 2OH^-$, is possible to occur.[12] One method to verify this reaction is to use a hydrogen evolution setup, which enables the detection of low concentrations of hydrogen evolution. Apart from oxygen and water, Ho and coworkers have suggested hydrated-oxygen complexes, $O_2(H_2O)_n$, as a possible candidate for electron traps. Followed by that, recent research suggested that hydrated-oxygen complexes, $O_2(H_2O)_n$, are the most likely source of organic field effect transistor (OFET) performance degradation under ambient conditions,[18] and Therefore, these two electron traps, water, and hydrated oxygen complexes are worth investigating in the context of OECTs.

4. In the context of OTEs, chemical doping of the semiconducting polymer is required to optimize electrical conductivity. Consequently, the air stability of the thermoelectric device is represented not only by the semiconducting polymer but also by the applied dopant, and thus evaluating the air stability of both components independently prior to mixing is critical. However, this is not the case in current literature reports, including the work in this thesis. This is mainly because N-DMBI dopant, which is most commonly used, is regarded as air stable.[19] However, a recent investigation has revisited the air stability of N-DMBI, and found that actually neat solutions of N-DMBI chemically degrade in the presence of oxygen to form $O_2$-mediated side reactions.[20] Based on the above, reporting the air stability of thermoelectric materials should include a separate evaluation of both the host and the dopant, for reliable study conclusions. Moreover, this further emphasizes the need for developing new air stable n-type dopants for a reliable examination of thermoelectric device air stability.
5. Given the promising results shown by P-75, a logical next step would be to undergo further structural optimizations by modifying the side chains and maximizing the mixed conduction properties. In terms of side chain modifications, there's room for enhancing the

interchain packing of P-75 by replacing the branched alkyl side chains with linear side chains, while screening different chain lengths to find a “sweet spot” where solubility and film crystallinity are not compromised. Another side-chain modification attempt would involve exploring P-75 with different alkyl:glycol ratio. This was done in NDI-based polymers for OECTs,[21] where different alkyl and glycol content were screened, with P-90 (10% alkyl, and 90% glycol) found to exhibit the highest volumetric capacitance and OECT performance. Applying similar investigation on P-75 might lead to further optimization in mixed conduction properties. The drawback, however, of synthesizing random co-polymers such as P-0, P-50, and P-75 in this thesis, and the mentioned NDI-based polymers, is the uncertainty in achieving the desired alkyl:glycol ratio, leading to batch-to-batch variations, which adds another disadvantage of synthesizing random polymers. One way to tackle this issue is to have both alkyl and glycol chains attached to one monomer, also called amphipathic side chain. This was examined in NDI-based polymer, p(C6-gNDI-gT2), where an alkyl spacer has been introduced between the NDI core and the ethylene glycol side chain, and it resulted in minimizing detrimental swelling close to the polymer backbone, leading to OECT performance that outperforms the parent p(gNDI-gT2) with no alkyl spacer, with an improved operation stability. This approach can be easily implemented in P-75 with a dual benefit of avoiding the synthesis of random copolymers, and controlling the degree of swelling to obtain a more stable OECT operation.

Further optimization of the polymerization solvent is possible. Toluene was used as the polymerization solvent in all published materials regarding fused lactam/lactone polymers, including the polymers presented in this article. Toluene might be a suitable solvent for alkyl- functionalized polymers. However, glycol-functionalized polymers are expected to have a poor solubility in toluene than of the alkylated polymers. A more polar solvent such as anisole and/or a mixture of toluene and anisole might be a better solvent to enhance

polymer solubility during polymerization. Solubilizing both alkylated and glycolated units during polymerization is also important when synthesizing step-growth random copolymers with different alkyl:glycol ratio, as the poor solubility of either component would affect the attainment of the desired ratio.

6. In a broader context, the insights gained from studying structure-property relationships in this work can potentially extend to designing conjugated small molecules for n-type OECTs. This would streamline the synthesis procedures and eliminate the necessity for extensive optimization of polymerization conditions, as well as avoiding batch-to-batch inconsistencies in polymer production.

# References


1. Durán ADLF, Liang AY-L, Denti I, Yu H, Pearce D, Marks A, *et al.* Origins of hydrogen peroxide selectivity during oxygen reduction on organic mixed ionic-electronic conducting polymers. 2022.

2. Murata T, Kotsuki K, Murayama H, Tsuji R, Morita Y. Metal-free electrocatalysts for oxygen reduction reaction based on trioxotriangulene. *Communications Chemistry* 2019, **2**.

3. Onwubiko A, Yue W, Jellett C, Xiao M, Chen HY, Ravva MK, *et al.* Fused electron deficient semiconducting polymers for air stable electron transport. *Nat Commun* 2018, **9**(1)**:** 416.

4. Yang CY, Jin WL, Wang J, Ding YF, Nong SY, Shi K, *et al.* Enhancing the n-Type Conductivity and Thermoelectric Performance of Donor-Acceptor Copolymers through Donor Engineering. *Advanced Materials* 2018, **30**(43).

5. Thomas TH, Harkin DJ, Gillett AJ, Lemaur V, Nikolka M, Sadhanala A, *et al.* Short contacts between chains enhancing luminescence quantum yields and carrier mobilities in conjugated copolymers. *Nature Communications* 2019, **10**.

6. Coropceanu V, Cornil J, da Silva DA, Olivier Y, Silbey R, Bredas JL. Charge transport in organic semiconductors. *Chemical Reviews* 2007, **107**(4)**:** 926-952.

7. Carsten B, He F, Son HJ, Xu T, Yu LP. Stille Polycondensation for Synthesis of Functional Materials. *Chemical Reviews* 2011, **111**(3)**:** 1493-1528.

8. Himmelberger S, Vandewal K, Fei ZP, Heeney M, Salleo A. Role of Molecular Weight Distribution on Charge Transport in Semiconducting Polymers. *Macromolecules* 2014, **47**(20)**:** 7151-7157.

9. Lu LY, Zheng TY, Xu T, Zhao DL, Yu LP. Mechanistic Studies of Effect of Dispersity on the Photovoltaic Performance of PTB7 Polymer Solar Cells. *Chemistry of Materials* 2015, **27**(2)**:** 537-543.

10. Goto E, Ochiai Y, Lo CT, Koganezawa T, Ueda M, Higashihara T. Synthesis of regioblock copolythiophene by Negishi catalyst-transfer polycondensation using BuZn•2LiCl. *Polymer Chemistry* 2017, **8**(39)**:** 6143-6149.

11. Goto E, Ochiai Y, Ueda M, Higashihara T. Transition-metal-free and halogen-free controlled synthesis of poly(3-alkylthienylene vinylene) the Horner-Wadsworth-Emmons condensation reaction. *Polymer Chemistry* 2018, **9**(15)**:** 1996-2001.

12. deLeeuw DM, Simenon MMJ, Brown AR, Einerhand REF. Stability of n-type doped conducting polymers and consequences for polymeric microelectronic devices. *Synthetic Metals* 1997, **87**(1)**:** 53-59.

13. Jones BA, Facchetti A, Wasielewski MR, Marks TJ. Tuning orbital energetics in arylene diimide semiconductors. Materials design for ambient stability of n-type charge transport. *Journal of the American Chemical Society* 2007, **129**(49)**:** 15259-15278.

14. Zhan XW, Facchetti A, Barlow S, Marks TJ, Ratner MA, Wasielewski MR, *et al.* Rylene and Related Diimides for Organic Electronics. *Advanced Materials* 2011, **23**(2)**:** 268-284.

15. Usta H, Risko C, Wang ZM, Huang H, Deliomeroglu MK, Zhukhovitskiy A, *et al.* Design, Synthesis, and Characterization of Ladder-Type Molecules and Polymers. Air-Stable, Solution-Processable -Channel and Ambipolar Semiconductors for Thin-Film Transistors via Experiment and Theory. *Journal of the American Chemical Society* 2009, **131**(15)**:** 5586-5608.

16. Giovannitti A, Rashid RB, Thiburce Q, Paulsen BD, Cendra C, Thorley K, *et al.* Energetic Control of Redox-Active Polymers toward Safe Organic Bioelectronic Materials. *Advanced Materials* 2020, **32**(16).

17. Jalilov AS, Nilewski LG, Berka V, Zhang CH, Yakovenko AA, Wu G, *et al.* Perylene Diimide as a Precise Graphene-like Superoxide Dismutase Mimetic. *Acs Nano* 2017, **11**(2)**:** 2024-2032.

18. Tietze ML, Rose BD, Schwarze M, Fischer A, Runge S, Blochwitz-Nimoth J, *et al.* Passivation of Molecular n-Doping: Exploring the Limits of Air Stability. *Advanced Functional Materials* 2016, **26**(21)**:** 3730-3737.

19. Wei P, Oh JH, Dong GF, Bao ZN. Use of a 1Derivative as an -Type Dopant and To Enable Air-Stable Solution-Processed -Channel Organic Thin-Film Transistors. *Journal of the American Chemical Society* 2010, **132**(26)**:** 8852-+.

20. Bardagot O, Aumaître C, Monmagnon A, Pécaut J, Bayle PA, Demadrille R. Revisiting doping mechanisms of n-type organic materials with N-DMBI for thermoelectric applications: Photo-activation, thermal activation, and air stability. *Applied Physics Letters* 2021, **118**(20).

21. Giovannitti A, Maria IP, Hanifi D, Donahue MJ, Bryant D, Barth KJ, *et al.* The Role of the Side Chain on the Performance of N-type Conjugated Polymers in Aqueous Electrolytes. *Chem Mater* 2018, **30**(9)**:** 2945-2953.

# Appendix

## A.1. Copyright permissions for literature figures

**Copyright permission for Figures. 2a and 6a**



**Copyright permission for Figure. 2b**

**Copyright permission for Figure. 3b**

"Review—Organic Materials for Thermoelectric Energy Generation" by authors: Lewis M. Cowen, Jonathan Atoyo, Matthew J. Carnie, Derya Baran and Bob C. Schroeder is under Creative Commons License with the below disclaimer:

This is an open access article distributed under the terms of the Creative Commons Attribution 4.0 License (CC BY, http://creativecommons.org/licenses/by/4.0/), which permits unrestricted reuse of the work in any medium, provided the original work is properly cited.

**Copyright permission for Figure. 18c**

"Reversible Electrochemical Charging of n-Type Conjugated Polymer Electrodes in Aqueous Electrolytes " by authors: Anna A. Szumska, Iuliana P. Maria, Lucas Q. Flagg, Achilleas Savva, Jokubas Surgailis, Bryan D. Paulsen, Davide Moia, Xingxing Chen, Sophie Griggs, J. Tyler Mefford, Reem B. Rashid, Adam Marks, Sahika Inal, David S. Ginger, Alexander Giovannitti, and Jenny Nelson is under Creative Commons License with the below disclaimer:

This work is licensed under the Creative Commons Attribution 4.0 International License. To view a copy of this license, visit http://creativecommons.org/licenses/by/4.0/ or send a letter to Creative Commons, PO Box 1866, Mountain View, CA 94042, USA.

**Copyright permission for Figure. 6bc**

**ELSEVIER LICENSETERMS AND CONDITIONS**

Aug 27, 2023

This Agreement between University of Oxford -- Maryam Alsufyani ("You") and Elsevier("Elsevier") consists of your license details and the terms and conditions provided byElsevier and Copyright Clearance Center.

| | |
|---|---|
| License Number | 5617020547108 |
| License date | Aug 27, 2023 |
| Licensed Content Publisher | Elsevier |
| Licensed Content Publication | Polymer |
| Licensed Content Title | Backbone orientation in semiconductingpolymers |
| Licensed Content Author | Itaru Osaka,Kazuo Takimiya |
| Licensed Content Date | Feb 24, 2015 |
| Licensed Content Volume | 59 |
| Licensed Content Issue | n/a |
| Licensed Content Pages | 15 |
| Start Page | A1 |
| End Page | A15 |

| | |
|---|---|
| Type of Use | reuse in a thesis/dissertation |
| Portion | figures/tables/illustrations |
| Number of figures/tables/illustrations | 1 |
| Format | electronic |
| Are you the author of this Elsevier article? | No |
| Will you be translating? | No |
| Title | Thesis |
| Institution name | University of Oxford |
| Expected presentation date | Dec 2024 |
| Portions | Abstract figure |
| Requestor Location | University of Oxford12 Mansfield Roadchemistry research laboratoryOXFORD, Not Applicable OX1 3TAUnited KingdomAttn: University of Oxford |
| Publisher Tax ID | GB 494 6272 12 |
| Total | 0.00 GBP |

**Copyright permission for Figure. 17b**

**JOHN WILEY AND SONS LICENSE TERMS AND CONDITIONS**

Aug 27, 2023

This Agreement between University of Oxford -- Maryam Alsufyani ("You") and John Wiley and Sons ("John Wiley and Sons") consists of your license details and the terms and conditions provided by John Wiley and Sons and Copyright Clearance Center.

| | |
|---|---|
| License Number | 5617270781549 |
| License date | Aug 27, 2023 |
| Licensed Content Publisher | John Wiley and Sons |
| Licensed Content Publication | Advanced Materials |
| Licensed Content Title | Enhancing Molecular n-Type Doping of Donor–Acceptor Copolymers by Tailoring Side Chains |
| Licensed Content Author | L. Jan Anton Koster, Jan C. Hummelen, Siewert J. Marrink, et al |
| Licensed Content Date | Jan 11, 2018 |
| Licensed Content Volume | 30 |
| Licensed Content Issue | 7 |
| Licensed Content Pages | 9 |
| Type of use | Dissertation/Thesis |
| Requestor type | University/Academic |
| Format | Print and electronic |

| | |
|---|---|
| Portion | Figure/table |
| Number of figures/tables | 1 |
| Will you be translating? | No |
| Title | Thesis |
| Institution name | University of Oxford |
| Expected presentation date | Dec 2024 |
| Portions | Figure. 4 |
| Requestor Location | University of Oxford<br>12 Mansfield Road<br>chemistry research laboratory<br><br>OXFORD, Not Applicable OX1 3TA<br>United Kingdom<br>Attn: University of Oxford |
| Publisher Tax ID | EU826007151 |
| Total | 0.00 GBP |

**Copyright permission for Figure. 20b**

**JOHN WILEY AND SONS LICENSE TERMS AND CONDITIONS**

Aug 27, 2023

This Agreement between University of Oxford -- Maryam Alsufyani ("You") and John Wiley and Sons ("John Wiley and Sons") consists of your license details and the terms and conditions provided by John Wiley and Sons and Copyright Clearance Center.

| | |
|---|---|
| License Number | 5617280564285 |
| License date | Aug 27, 2023 |
| Licensed Content Publisher | John Wiley and Sons |
| Licensed Content Publication | Advanced Materials |
| Licensed Content Title | Amphipathic Side Chain of a Conjugated Polymer Optimizes Dopant Location toward Efficient N-Type Organic Thermoelectrics |
| Licensed Content Author | Jian Liu, Gang Ye, Hinderikus G. O. Potgieser, et al |
| Licensed Content Date | Dec 11, 2020 |
| Licensed Content Volume | 33 |
| Licensed Content Issue | 4 |

| | |
|---|---|
| Licensed Content Pages | 9 |
| Type of use | Dissertation/Thesis |
| Requestor type | University/Academic |
| Format | Print and electronic |
| Portion | Figure/table |
| Number of figures/tables | 1 |
| Will you be translating? | No |
| Title | Thesis |
| Institution name | University of Oxford |
| Expected presentation date | Dec 2024 |
| Portions | Figure. 1 |
| Requestor Location | University of Oxford<br>12 Mansfield Road<br>chemistry research laboratory<br><br>OXFORD, Not Applicable OX1 3TA<br>United Kingdom<br>Attn: University of Oxford |
| Publisher Tax ID | EU826007151 |
| Total | 0.00 GBP |

**Copyright permission for Figure. 17a**

# A.2. Copyright permissions to reproduce full articles

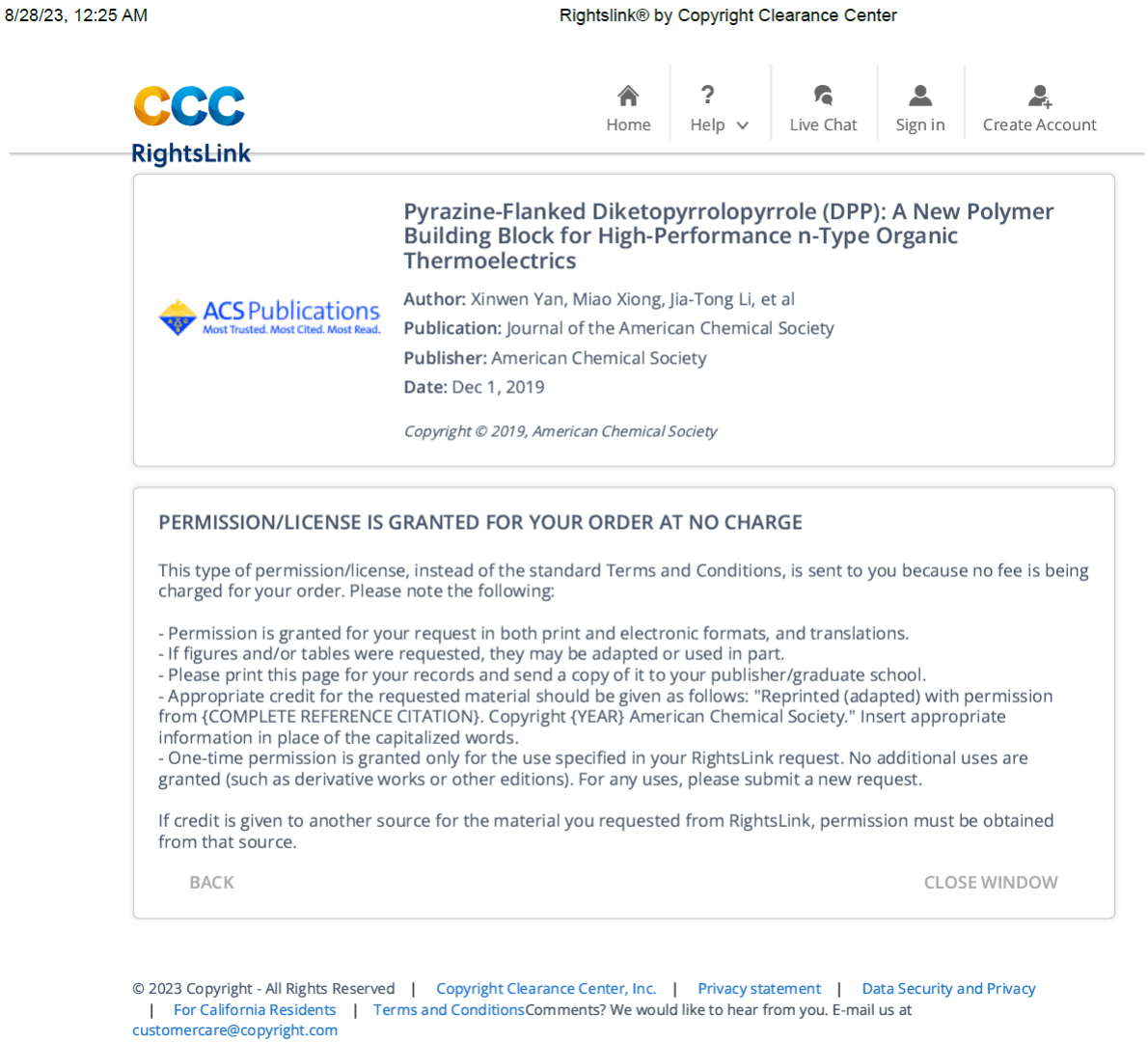


1. Permission to reproduce published article in **chapter 2** was provided by the Royal Society of Chemistry under the following statement in the article website (https://pubs.rsc.org/en/content/articlelanding/2020/TC/D0TC03347B):

"If you are the author of this article, you do not need to request permission to reproduce figures and diagrams provided correct acknowledgement is given. If you want to reproduce the whole article in a third-party commercial publication (excluding your thesis/dissertation for which permission is not required) please go to the Copyright Clearance Center request page".

2. Permission to reproduce published article in **chapter 3** is below:

**JOHN WILEY AND SONS LICENSE**
**TERMS AND CONDITIONS**

Aug 29, 2023

This Agreement between University of Oxford -- Maryam Alsufyani ("You") and John Wiley and Sons ("John Wiley and Sons") consists of your license details and the terms and conditions provided by John Wiley and Sons and Copyright Clearance Center.

| | |
|---|---|
| License Number | 5618311131188 |
| License date | Aug 29, 2023 |
| Licensed Content Publisher | John Wiley and Sons |
| Licensed Content Publication | Angewandte Chemie International Edition |
| Licensed Content Title | Lactone Backbone Density in Rigid Electron-Deficient Semiconducting Polymers Enabling High n-type Organic Thermoelectric Performance |
| Licensed Content Author | Iain McCulloch, Simone Fabiano, Jonathan Rivnay, et al |
| Licensed Content Date | Dec 18, 2021 |
| Licensed Content Volume | 61 |
| Licensed Content Issue | 7 |
| Licensed Content Pages | 9 |
| Type of use | Dissertation/Thesis |
| Requestor type | Author of this Wiley article |
| Format | Print and electronic |
| Portion | Full article |
| Will you be translating? | No |
| Title | Thesis |
| Institution name | University of Oxford |
| Expected presentation date | Dec 2024 |
| Requestor Location | University of Oxford<br>12 Mansfield Road<br>chemistry research laboratory |

| | |
|---|---|
| | OXFORD, Not Applicable OX1 3TA<br>United Kingdom<br>Attn: University of Oxford |
| Publisher Tax ID | EU826007151 |
| Total | 0.00 GBP |